

Hybrid Silicon Optoelectronic Technologies

A thesis submitted for the degree of Doctor of Philosophy
in the Faculty of Engineering, University of Glasgow

by

Andrew J. McLaughlin

September 1998

© Andrew J. McLaughlin

ProQuest Number: 13818706

All rights reserved

INFORMATION TO ALL USERS

The quality of this reproduction is dependent upon the quality of the copy submitted.

In the unlikely event that the author did not send a complete manuscript and there are missing pages, these will be noted. Also, if material had to be removed, a note will indicate the deletion.



ProQuest 13818706

Published by ProQuest LLC (2018). Copyright of the Dissertation is held by the Author.

All rights reserved.

This work is protected against unauthorized copying under Title 17, United States Code
Microform Edition © ProQuest LLC.

ProQuest LLC.
789 East Eisenhower Parkway
P.O. Box 1346
Ann Arbor, MI 48106 – 1346



11403 (copy 1)

This thesis is dedicated to my family,
who just wanted to know,
“Is it finished yet?”



Acknowledgements

First and foremost, I would like thank to my supervisor Dr Stewart Aitchison for his continued help and support throughout this project, for which I am in his debt. Secondly I would like to acknowledge Professor S.P Beaumont for the provision of research facilities in the Department of Electronics and Electrical Engineering.

I am grateful for the excellent technical support provided formerly by Tom Wright, and latterly by Dougie Irons and all his staff, and to the administrative staff for all their assistance.

I would like to extend my thanks to Ian McNicholl, for his continued efforts in maintaining the Flame Hydrolysis Deposition Facility. I thank him especially for his continual supply of bad jokes and seemingly never ending observations on marriage. The cleanroom staff are thanked for their help. In particular Joan Carson whose efforts are gratefully acknowledged. The staff of the dry etch facility are thanked for their excellent support in developing all things RIE. In particular Dave Clifton and Gillian Hopkins. The staff of the mechanical workshop are thanked. In particular, thanks go to Kas Piechowiak for his constant attention in cutting and polishing waveguides. Thanks to Robert Harkins for his assistance in making my masks. Jim Gray is thanked for assistance in laser labs. Robert McDonald in Geology is thanked for his assistance with the Microprobe analysis.

Financial support from the Engineering and Physical Sciences Research Council through a CASE award sponsorship with Lucas Advanced Vehicle Systems Development is gratefully acknowledged. I would also like to thank Alan Jacobs-Cook and Rob Pinnock at Lucas for the provision of equipment, materials, wisdom and technical assistance on all things resonant.

During my extended studies at the University of Glasgow I have made many friends, of all nationalities and cultures. In particular I thank the folks from the office: Daniel Ortega, Fernando Camacho, Paulo Marques, Valentin Loyo and Carolyn McEwan for sharing culture, laughs and beer. Special thanks go to Daniel for standing up in a skirt (kilt) at my wedding. I thank friends made elsewhere in the department for tea-table

chat, the odd game of five-a-side and for sharing beer at most available opportunities. I particularly extend my gratitude to Mike Jubber and Jim Bonar, for their friendship, advice and help to which I am deeply in their debt.

A big thank you goes to my family for their constant support throughout my academic life. In particular I thank my wife Joan, for her love, attention and for constantly nagging me to ‘finish the thing’!

Abstract

The aim of this project was to realise integrated optical interferometers suitable for use in low-coherence optical sensor systems. The research focused on the development of waveguide fabrication techniques and the design of phase tuned interferometers.

The flame hydrolysis deposition technique was employed to produce $\text{SiO}_2\text{-GeO}_2\text{-B}_2\text{O}_3$ glass films. The result was the production of high quality planar waveguide films with a controllable refractive index and thickness. A high degree of dopant homogeneity was observed between depositions, and across deposited glass films.

Ridge waveguide fabrication was facilitated through the use of photolithography and reactive ion etching (RIE). Photolithography was used to define waveguide patterns in NiCr etch masks. A reproducible, high rate, high selectivity CHF_3 reactive ion etch process was developed which reduced the typical RIE process time to approximately 1 hour for a $6 \mu\text{m}$ waveguide structure. The result of the processing was the fabrication of ridge waveguides with low sidewall roughness, and a sidewall angle $>89^\circ$.

Passive design and active tuning were explored as techniques controlling phase. Beam Propagation Method (BPM) techniques were used to design and fabricate asymmetric waveguide interferometers with fixed phase shifts, where experimental phase shifts were accurate to $\pm 2\%$ of the BPM simulations. Active phase control was implemented through the use of the thermo-optic effect, where waveguide phase modulators were produced which exhibit a fast response ($\sim 150 \mu\text{s}$) and low operating powers ($< 0.9\text{W}$).

Preliminary measurements were made on interferometers with designed optical path differences (OPD) of $250 \mu\text{m}$. Experimental results indicated that biasing a device at its quadrature point via the thermo-optic effect is stable with time, with a controllable range of 4π . Channelled spectra measurements show a static group OPD of $279 \mu\text{m}$.

Novel techniques for integrating optoelectronic components have been explored. Firstly a technique of dividing a substrate such that incompatible processing can be performed, such as silicon micromachining and FHD, where the recombination of the substrate has been shown to possess sub-micron accuracy. Patterned CVD diamond heatsinks with integral fibre alignment V-grooves have been fabricated.

Index

Acknowledgements

Chapter 1	Introduction	1
2.1	Perspective	1
2.2	MOMS & MEMS	2
2.3	Optically Addressed Microresonant Silicon Sensors	2
2.4	Problem Statement	5
2.5	Project Objectives and Constraints	5
2.6	Synopsis of Thesis	6
	References	7
Chapter 2	Planar Silica Waveguides by Flame Hydrolysis Deposition	8
2.1	A Brief History of Flame Hydrolysis Deposition	8
2.2	Fundamentals of FHD Technology	10
2.3	The FHD Process: Equipment and Function	11
2.3.1	A brief FHD overview	11
2.3.2	Dopant selection and transport	12
2.3.3	Flame hydrolysis reaction	20
2.3.4	Sintering	25
2.3.5	Cleanroom	29
2.4	Planar Silica Waveguide Fabrication Procedure	30
2.4.1	Sample preparation	30
2.4.2	Flame hydrolysis deposition procedure	31
2.5	The SiO ₂ -GeO ₂ -B ₂ O ₃ glass system	32
2.5.1	Dopant Considerations	32
2.6	Process Development	35
2.6.1	Low B ₂ O ₃ Content germanosilicate glass	35
2.6.2	High B ₂ O ₃ Content germanosilicate glass	37
2.6.3	Assessment of doping levels by Electron Microprobe Analysis	40
2.6.4	Glass film measurements	42
2.6.5	Recent developments	42
2.6.6	Photosensitivity of germanosilicate glass	45
2.7	Other Glass Systems	47
2.7.1	Waveguide cladding	47
2.7.2	High softening temperature under claddings	47
2.8	Channel Waveguide Fabrication	48
2.8.1	Design of optical waveguide devices	48
2.8.2	Photolithography	49
2.8.3	Nichrome etch masks	50
2.9	Conclusions	51
	References	52
Chapter 3	Reactive Ion Etching of FHD Silica Glass Films	55
3.1	Introduction	55
3.1.1	Motivation	55
3.1.2	Specification for an optimum etch process	55
3.2	RIE Fundamentals	56

3.3	Preliminary Investigations	58
3.3.1	Increasing the RFpower in CHF ₃ RIE	58
3.3.2	Other etch processes	61
3.3.3	Summary of preliminary work	62
3.4	Development of CHF ₃ , C ₂ F ₆ and SF ₆ RIE processes	63
3.4.1	The Experiment	64
3.4.2	Results	66
3.4.3	Assessment of developed processes	70
3.4.4	Comparison between the developed processes for deep etching	74
3.4.5	Summary	74
3.5	CHF ₃ Optimisation	76
3.5.1	Interaction experiments: flow rate v's pressure, rf power v's pressure	76
3.5.2	Investigation of the influence of dc bias	78
3.5.3	Oxygen addition to CHF ₃ plasma processes	87
3.6	RIE Process Development through Design of Experiments	91
3.6.1	The Experiment	92
3.6.2	Discussion of results	100
3.6.3	Summary of factor influence	107
3.6.4	Process reproducibility and sidewall assessment	108
3.7	Conclusions	111
	References	112
Chapter 4	Integrated Optical Mach-Zehnder Interferometers	114
4.1	Introduction	114
4.2	Integrated Optical Y-junctions	114
4.3	The Single Mode Optical waveguide Y-junction	115
4.4	Integrated Optic Mach-Zehnder Interferometer	117
4.5	Asymmetric Mach-Zehnder Interferometers	119
4.5.1	Asymmetric device design criteria	119
4.5.2	Passive phase shifting through asymmetric device design	122
4.5.3	Asymmetric MZI fabrication and test	132
4.6	Active Phase Control	133
4.6.1	The thermo-optic effect	135
4.6.2	Integrated waveguide thermo-optic phase shifter	138
4.6.3	Overdriven thermo-optic modulation	145
4.7	Finite Element Modelling of a Thermo-optic Modulator	148
4.7.1	Model development	149
4.7.2	Validation of the finite element model	153
4.7.3	Finite element analysis of novel thermo-optic modulators	159
4.8	Conclusions	167
	References	168
Chapter 5	IO Interferometers for Low-Coherence Sensing Applications	171
5.1	Introduction	171
5.2	Basic Principles of Low-Coherence Interferometry	172
5.3	Solutions for Signal Fading	173
5.4	Device Design	174
5.5	Low-Coherence Optical Sources	175
5.6	Interferometer Performance	177
5.6.1	Tuning range and stability	177

5.6.2	Estimation of optical path difference	178
5.7	Conclusions	179
	References	180
Chapter 6	Hybrid Integration of Optoelectronic Components	181
6.1	A Review of Common Integration Techniques	181
6.2	Hybrid Packaging of FHD silica waveguides, laser diodes and optical fibres	184
6.2.1	Mask proximity to silicon surface	185
6.2.2	Waveguide polishing	186
6.3	Integration (1): Silicon Partition Lightwave Integration Technology (SPLIT)	186
6.3.1	Split process	187
6.3.2	Demonstration of SPLIT wafer technique (1)	189
6.3.3	Demonstration of SPLIT wafer technique (2)	191
6.4	Hybrid Processing for Optoelectronic Integration	192
6.4.1	Thermal management of optoelectronic components	192
6.5	Integration (2): Silicon Micromachining	195
6.5.1	Anisotropic wet etching of single crystal silicon	195
6.6	Integration (3) Micromachined Pattern Transfer into CVD Diamond	200
6.6.1	The case for CVD diamond films - Finite Element Modelling	204
6.7	Conclusions	205
	References	206
Chapter 7	Conclusions and Suggestions for Future Work	208
7.1	Conclusions	208
7.2	Suggestions for Future Work	212
	Publications List	214
Appendix		216
I.	Selected Orthogonal Tables	216
II.	Finite Element Models	217
III.	Data for Designing Asymmetric Mach-Zehnder Interferometers	224

Chapter 1 Introduction

1.1 Perspective

In the past decade, photonics technology has been identified by the aerospace industry as an important enabling technology in the design of future avionics systems [1]. During this time, a number of standards for optical fibre based communication systems on aircraft have been developed and adopted in new civil and military avionics systems.

An optical fibre communications network possesses a number of advantages over its electrical equivalent in a harsh aerospace environment, some of which are listed below:

- High Temperature Operation ($> 300^{\circ}\text{C}$)
- Electromagnetic Interference (EMI) Immunity
- High Communications Bandwidth ($>1 \text{ THz}$)
- Low Attenuation ($<0.1 \text{ dB/km}$) with almost zero crosstalk
- Lightweight compared to copper
- High Reliability
- Safe in the presence of flammable and corrosive materials

A typical role for photonics in aircraft is that of data transfer in flight control systems. Example applications include the use of fibre optic strain sensors to monitor the structural health of a composite aircraft fuselage, and the use of fibre optics to deliver flight control information to (from) remote sensors and actuators [1].

Another major motivation for the use of optical fibres is reduced life cycle costs and increased component reliability throughout the life of an aircraft. An example of this motivation can be found in the development of future aircraft engines where increased performance and a reduction in fuel consumption are the ultimate goals [2]. One source indicates that a reduction in the fuel consumption of a Boeing 747 of just 1% can lead to a reduction in operator running costs of upto US\$100,000 per annum [3].

The thesis examines the integration of planar silica integrated optics [4] with micromachined silicon resonant sensors for high accuracy aircraft fuel system temperature and pressure measurements [5].

1.2 MOMS & MEMS

The development of silicon micromachining technology [6] has led to an abundance of ‘micro electro mechanical’, MEMS, and ‘micro opto mechanical’ transducer systems, MOMS [7]. Micromachining has been found to be an extremely precise mechanical fabrication technique resulting in the production of highly accurate and extremely stable transducers. Silicon has also proven to be extremely invaluable in the successful production of microresonant devices, due its extremely low hysteresis.

MEMS transducers usually employ a piezoelectric, piezoresistive or capacitive means to monitor an environment such as temperature, pressure or acceleration. In contrast, MOMS transducers monitor optical intensity, wavelength, polarisation or phase. Phase is typically monitored through an interferometric means, and it is this technique that forms the motivation for this work.

1.3 Optically Addressed Microresonant Silicon Sensors

A microresonant sensor is fabricated through a mixture of photolithography, dopant diffusion and anisotropic wet etching of a single crystal silicon wafer [5]. Photolithography is used to define the resonator structure (for example a simple cantilever or bridge structure) by opening windows on an oxidised silicon wafer where the pattern is accurately aligned to a particular orientation of the silicon crystal planes. A high concentration boron diffusion step is used to dope the exposed silicon surface, where the diffusion depth defines the thickness of the final resonant structure. After the photolithography, the substrate is placed in a KOH/H₂O solution where the un-doped silicon is anisotropically etched along its crystal planes, with the end result being a free resonator structure.

Figure 1.1(a) shows an etched bridge structure and a V-groove for aligning an optical fibre [5], whereas Figure 1.1(b) shows the complete interface structure with the integral optical fibre (Figures taken from Jacobs-Cook et al. [5]).

Figure 1.2(a) and (b) illustrate two different schemes of packaging the optical fibre and resonant structure, where the scheme in the latter figure is regarded as being the most robust design, and is also shown in Figure 1.1(b) (Figures taken from Pinnock [8]).

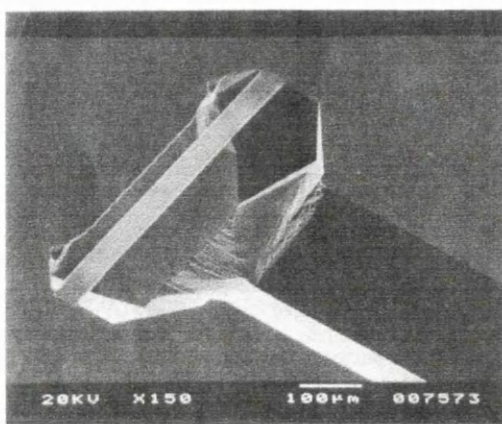


Figure 1.1(a) Resonant Beam Interface

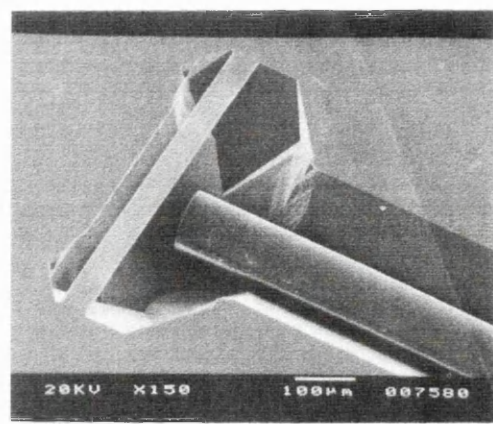


Figure 1.1(b) Interface with Fibre

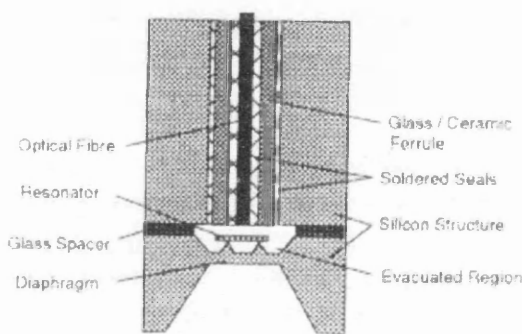


Figure 1.2(a) Basic Optical Interface Structure

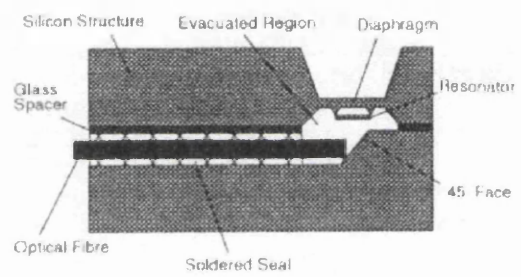


Figure 1.2(b) Robust Optical Interface

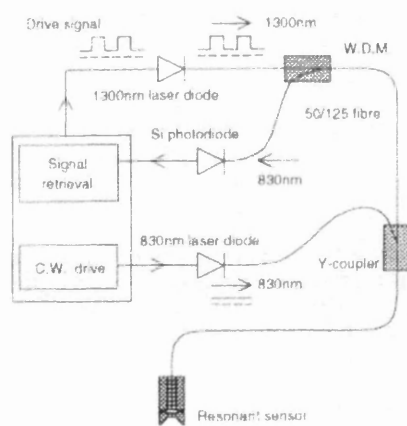


Figure 1.3 Microresonant Optical Sensor System

The device illustrated in Figures 1.1 and 1.2(b) is considered to be more robust as the alignment of the optical fibre to the resonator is defined by the accuracy of the micromachining of the silicon substrate, which is in its self a highly reproducible process. It is also easier to securely integrate the structure and hermetically seal the package, compared to the device shown in Figure 1.2(a).

The operation of this sensor is, as its title describes, based on mechanical resonance of the cantilever or bridge structure (as shown in Figure 1.1(b)). Figure 1.3 illustrates a typical configuration of a microresonant sensor system.

Optical activation occurs as a result of a photothermal mechanism when periodically modulated light from an LED or laser source ($\lambda \sim 1330$ nm) is incident on the silicon surface. The absorption of the light creates a localised heating of the bridge which manifests as flexural vibrations of the silicon structure [9]. The optical source is modulated in a feedback loop at the resonance frequency of the structure.

The amplitude of vibration is of the order of tens of nanometers, so optical detection is performed by interferometry where a continuous wave (CW) light source is incident on the bridge structure. The sensor head effectively operates as a two-beam interferometer, where one beam is derived from the silicon structure, and the other is derived from the fibre face. Typically, ‘white light’ interferometry [10] is employed where the coherence length of the source is chosen to be less than the optical path length of the sensor head. Thus, the two beams propagate back along the addressing fibre to a second, detection interferometer where the resultant interferogram is an oscillating signal at a frequency equal to that of the resonance frequency of the structure.

The resonance frequency of the structure varies with changes in the environment within which the sensor is operating. For example, in the device schematically described by Figure 1.2 (a&b), the resonator is mounted on a diaphragm (also formed by anisotropic etching of the reverse of the silicon wafer). Changes in pressure result in the diaphragm flexing and therefore stress is applied to the resonator, which results in a change in its resonance frequency. From the interference signals that result it remains a simple task to calibrate and deploy the resonator as a pressure sensor.

1.4 Problem Statement

Whilst interferometry provides an elegant and accurate technique for monitoring the small displacements of a resonator (few 10's of nanometers), the sinusoidal response of an interferometer to an applied measurand proves to be its downfall.

It is easy to understand that the diaphragm, and therefore the resonator attached to it, moves with changing pressure. However, over large pressure ranges, the movement of the diaphragm can easily exceed the wavelength of the detection source. Therefore, the optical path length of the sensor head interferometer is not fixed, but variable.

The result is a high frequency, low modulation depth, signal at ~100-200 kHz derived from the resonator which is modulated by the low frequency, large modulation depth signal resulting from the diaphragm movement. Thus, periodically there are points in the pressure range where the output from the sensor system is zero.

This is the effect commonly referred to as ‘signal fading’.

It is obvious that any system where there is a periodic response of the sensor to an applied measurand which results in loss of signal is a particularly undesirable system.

1.5 Project Objectives and Constraints

At the outset of this work, a number of objectives and constraints for the project were identified. Some of these are listed below:

- Develop fabrication technology toward the production of single and multimode planar waveguide interferometer devices
- Examine techniques for overcoming signal fading in resonant sensors
 - Passive optical solutions
 - Single and Dual Interferometers
 - Active optical solutions
 - Tuning via the thermo-optic effect
- Multimode interferometers to be ideally 50/125 μm fibre compatible
- Devices to be implemented in a ‘white light interferometry’ configuration.

1.5 Synopsis of the Thesis

It is the objective of this work to overcome the signal fading problem in interferometric sensors through the hybrid integration of integrated optical components and silicon microresonant sensors.

The technique of Flame Hydrolysis Deposition (FHD) and its application to the fabrication of planar waveguides in the SiO₂-GeO₂-B₂O₃ glass system is discussed in Chapter 2. Toward the end of the Chapter, the latest developments in the glass system preparation and Reactive Ion Etch masks are presented.

The development of fluorine based Reactive Ion Etching (RIE) of FHD glass films is presented in Chapter 3. Particular attention is given to the development of high glass etch rate, high glass:mask selectivity processes for application in the production of multimode waveguide structures.

Passive and active tuning of waveguide interferometers forms the basis of Chapter 4, where experimental results are used to develop a meaningful finite element model for the simulation of thermo-optic controlled waveguide interferometers. Novel waveguide designs are investigated for the optimisation of electrical drive power and optical response time.

Chapter 5 is devoted to the design and testing of interferometric components for use in low coherence interferometric sensor systems. Brief mention is given to the fabrication of low coherence optical sources in GaAs/AlGaAs semiconductors.

Hybrid integration of optical components is investigated in Chapter 6 where a novel technique for accurately aligning optical components through a passive means is presented. The hybrid application of CVD diamond technology and silicon micromachining to heatsinks and optical mounts is also discussed.

Finally, the conclusions of the thesis are contained within Chapter 7, where the author provides suggestions of areas for future investigation and/or development are presented.

References

- [1] The SBAC Technology Committee, "Applications of Photonics in Avionics", Issue 1, February 1996.
- [2] D. Angelides & P. Parsons, *Opt. Eng.*, 1992, **31**, 1641.
- [3] P. Ruffles, *SBAC Farnborough '90 magazine*, 17-19, 1990.
- [4] M. Kawachi, *Opt. & Quant. Elec.*, 1990, **22**, 391.
- [5] A.J. Jacobs-Cook & M.E.C. Bowen, *Sens. and Actuators A*, 1993, **37-38**, 540.
- [6] K.E. Peterson, *Proc. IEEE*, 1982, **70**, 420.
- [7] A.J. Jacobs-Cook, *J. Micromech. Microeng.*, 1996, **6**, 148.
- [8] R.A. Pinnock, *Sensors VI: Technology Systems and Applications*, (Bristol: Institute of Physics), 1993, 141.
- [9] K. Seibert, D. Largeau, B. Bonvalot, D.T. Angelides & P. Parsons, *Sens. and Actuators A*, 1994, **43**, 85.
- [10] Y. J. Rao, D. A. Jackson, *Meas. Sci. & Technol.*, 1996, **7**, 981.

Chapter 2 Planar Silica Waveguides by Flame Hydrolysis Deposition

The application of the Flame Hydrolysis Deposition (FHD) technique to silica waveguide fabrication is presented. The technique is described by examining the FHD equipment used in each stage of the fabrication process. The fabrication process itself is described through illustrative examples where the expected result of each process stage is identified. Toward the end of the chapter, the techniques of photolithography are reviewed, along with some of the developments made in etch mask materials. The last fabrication technique, Reactive Ion Etching (RIE), is discussed briefly, as the developments made form the content of Chapter 3.

2.1 A brief history of Flame Hydrolysis Deposition

The concept of flame hydrolysis was first introduced during the 1930's, and patented in 1942 by J.F. Hyde of Corning Glass, New York [1], where a method for fabricating transparent articles of silica was described. The method involved the vapour phase hydrolysis of volatile halides, primarily silicon tetrachloride (SiCl_4), in an oxy-hydrogen flame. The advantages presented by this technique are numerous, for example:

- the ability to form high purity silica glass,
- ultra-low content of loss inducing transition metals,
- the ability to fabricate multi-component doped glasses.

The technique was adopted and developed by industry during the 1970's to satisfy the growing need for low loss optical fibres suitable for telecommunications applications. As a result, three processes were independently developed by different research groups, namely:

- Modified Chemical Vapour Deposition (MCVD) at Bell Laboratories [2],
- Outside Vapour Deposition (OVD) at Corning Glass Works [3],
- Vapour Axial Deposition (VAD) at NTT [4].

A full description of these techniques can be found in reference [5] by Izawa and Sudo. All of these techniques involve the formation of a cylindrical fibre preform, which is later subjected to a 'drawing technique' to form the optical fibre.

The transfer of this technology to a planar geometry was patented in 1973 by Keck and Schultz [6], again at Corning Glass. However it was not until 1983 that the first planar device was demonstrated by Kawachi *et al.* [7] who reported the fabrication of titanium dioxide doped silica glass films on a silicon substrate. This is the technique described today as Flame Hydrolysis Deposition (FHD).

Since the early work of Kawachi *et al.*, many companies have adopted flame hydrolysis deposition and applied it to the production of silica waveguide devices, although the field is still largely dominated by NTT and Mitsubishi and their associated foundry in the USA, Photonic Integrated Research Inc. PIRI was devised to supply silica planar lightwave circuits (PLC's) on a commercial basis to a worldwide market [8].

Flame hydrolysis has been an area of active research at the University of Glasgow, within the Department of Electronics and Electrical Engineering since the first investigations of Maxwell [9] in the late 1980's. Early work was concerned with the development of an in-house FHD fabrication facility, with the later fabrication of TiO_2 , or GeO_2 silica waveguides, co-doped with P_2O_5 . This led to the first observation of second harmonic generation in planar silica waveguides.

FHD was developed further still by Barbarossa [10], with the fabrication of optical waveguide devices such as three waveguide couplers and the patented vertically integrated channel waveguides [11].

Bebbington [12] provided another major innovation with the introduction of the aerosol doping technique used for the inclusion of rare earth materials such as neodymium into P_2O_5 doped silica glasses, c.f. solution doping used in fibre materials.

Aerosol doping was developed further by the work of Bonar [13], where neodymium and erbium doped silica waveguide lasers were reported for the first time using the aerosol doping technique.

In recent years, the deposition equipment has been refined and upgraded with the introduction of a vertical loading furnace [13] and the aforementioned aerosol doping technique. During the course of this work, the deposition area has been upgraded to clean room status, as well as the introduction of a new load-locked chemical cabinet.

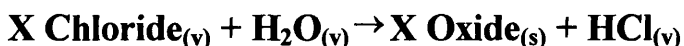
2.2 Fundamentals of FHD technology

High purity silica glass production lies at the heart of the success of the flame synthesis employed in the FHD technique [27]. This is possible due to the fact the reagent metal halides, as listed in Table 2.1, are highly volatile at room temperature. The reagents are carried to the reaction zone, in this case an oxy-hydrogen burner, in a highly pure vapour phase by an inert carrier gas, limiting the final glass composition to that of the intended oxides of the reagent metal halides.

Metal Halide	Resultant Oxide	Influence of Dopant
Silicon Tetrachloride (SiCl ₄)	Silicon Dioxide (SiO ₂)	Host glass
Germanium Tetrachloride (GeCl ₄)	Germanium Dioxide (GeO ₂)	Increase of refractive index
Phosphorous Trichloride (PCl ₃) or (POCl ₃)	Phosphorous Pentoxide (P ₂ O ₅)	Increase of refractive index Reduction of sintering temperature
Boron Tetrachloride (BCl ₃)	Boron oxide (B ₂ O ₃)	Decrease of refractive index Reduction of sintering temperature

Table 2.1 Reagent halide, oxide after hydrolysis and influence on final glass composition

The reaction phase of FHD is a simple hydrolysis process where the reagents are transported to a glass torch by inert nitrogen, and burnt in an oxy-hydrogen flame, thus synthesising a high purity oxide soot which can be deposited onto a substrate, e.g. silicon or silica. The hydrolysis reaction for the various metal chlorides is described by:



where X represents any of the metals described in table 2.1.

Of the many advantages offered by FHD silica waveguides, few are as important as the inherent compatibility with optical fibres [14]. FHD allows accurate control of waveguide parameters such as refractive index (-0.25 to 1% over SiO₂) and thickness (2-200 μm) - enabling the fabrication of both single and multimode components. ‘Silica-on-silicon’ based PLC’s also offer high functionality on a compact and robust substrate, where many integrated optic components can be fabricated and hybridly packaged with other optical components (see Chapter 6).

2.3 The FHD Process: Equipment and Function

The objective of the following section is not to supercede the descriptions given by predecessors, but merely to reinforce the concept of flame hydrolysis by illustrative example. A thorough analysis of the flame synthesis and sintering of silica oxide films is given by Maxwell [9]. Only brief mention is given to the preparation of rare earth doped glasses, as extensive coverage is given by Bebbington [11], and latterly Bonar [12].

Flame hydrolysis deposition of doped silica films can be split into 3 stages, and thus into three main groups of equipment:

- dopant selection & transport, - *Chemical Cabinet and Gas Supply*,
- flame hydrolysis reaction - *Deposition Chamber*
- high temperature sintering - *Consolidation Furnace*.

Each of these stages plays a critical role in the preparation of high purity silica glasses which have a high degree of homogeneity in terms of refractive index and thickness. The purity is guaranteed by the reagent transport stage, whilst the structure of the glass is controlled by the deposition and sintering stage.

2.3.1 A brief FHD overview

The required reagents are collected in a vapour phase and transported to the oxy-hydrogen torch by the inert carrier gas, nitrogen (N_2). A fixed flow rate is used for the main glass former, $SiCl_4$, whilst the flow rate of the other reagents is selected to yield the required glass properties, i.e. refractive index and fusing temperature. The reagents are hydrolysed in a hydrogen and oxygen flame, producing fine glass particles. The substrates are placed on a rotating silicon carbide turntable, over which the torch traverses radially, at a variable rate sufficient to uniformly deposit a fine particle ‘soot’ at a known rate per traversal. The ‘soot’ coated substrates are taken from the reaction chamber to a high temperature furnace where the oxide particles are sintered to form an amorphous glass film. Figure 2.1 is a photograph of the deposition room.

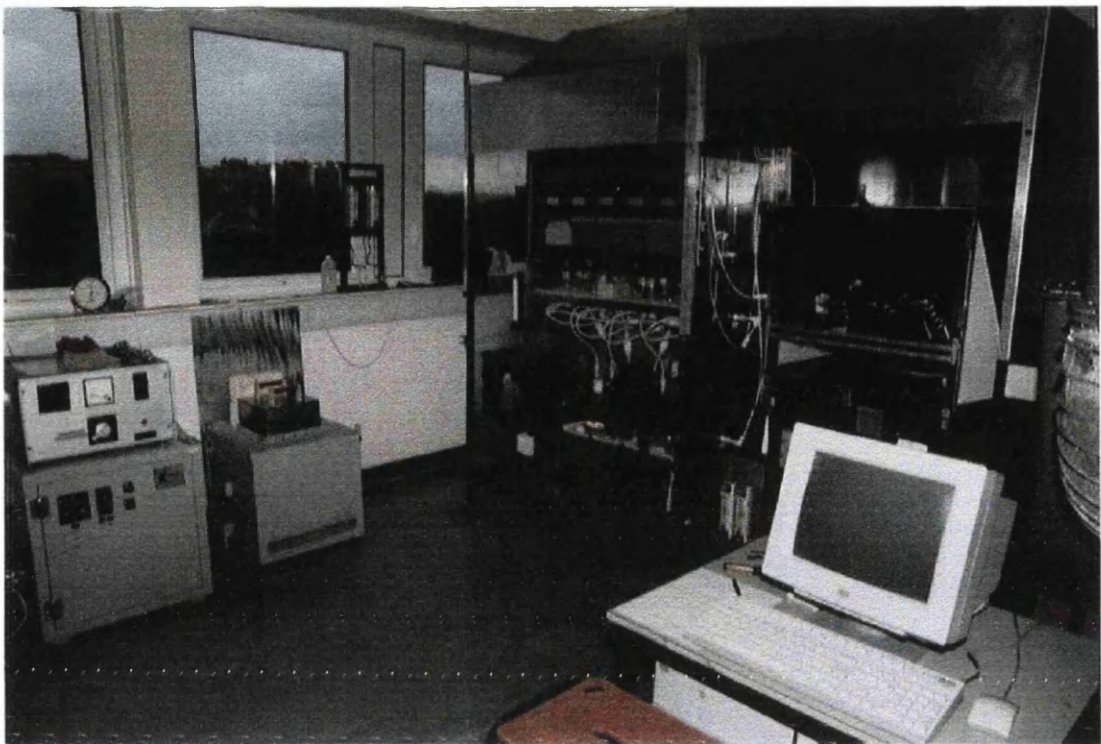


Figure 2.1 Photograph of Flame Hydrolysis Deposition Room

2.3.2 Dopant Selection & Transport

As is the case with optical fibres [5], a number of features must be considered when fabricating amorphous glass films for waveguide applications, for example: the optical loss characteristics and refractive index. Another feature, peculiar to glasses on silicon substrates, is a restriction on the maximum glass softening temperature imposed by the silicon substrate ($\sim 1400^{\circ}\text{C}$).

Amorphous silica glasses are of particular interest in optical communications as they are highly transparent in both the visible and infra-red regions. However, the loss characteristics are restricted by the limits imposed by Rayleigh scattering, a phenomenon intrinsic to amorphous materials arising from random fluctuations in material density and composition.

Of the main dopants used in FHD SiO_2 , GeO_2 and B_2O_3 are commonly referred to as being network formers, as the individual oxides are capable of forming a glass in their own right. P_2O_5 is referred to as a network modifier, and is used in rare earth doping, as P_2O_5 helps increase the solubility of the rare earth ions in the SiO_2 host glass [11].

Refractive index control of SiO_2 based glasses is achieved through the controlled addition of the oxide dopants. As shown in Figure 2.2, TiO_2 and GeO_2 significantly increase the refractive index, whereas B_2O_3 can reduce the refractive index [15].

An amorphous glass is formed by heating the low density oxide ‘soot’ to the point where it exists in a liquid phase. The molten oxide is then cooled until the oxide exists as an amorphous glass in solid solution. Of course the temperature required to liquefy SiO_2 is far higher than that of the melting temperature of the silicon host substrate. The SiO_2 glass is therefore doped with another oxide to reduce the glass softening temperature as illustrated by Figure 2.3 [16].

Another reason for dopant selection is that of the intended application. For example GeO_2 doped SiO_2 results in a glass which exhibits a photosensitive effect under UV exposure, resulting in a semi-permanent change of refractive index. Such an effect can be used in the preparation of Bragg gratings for use in communications and sensing [17, 18]. The effect can be significantly enhanced through co-doping germanosilicate glass with B_2O_3 [19], through flame brushing [20] or hydrogenation [21]. Er^{3+} and Nd^{3+} doping of P_2O_5 doped silica oxide glasses resulted in the development of integrated glass waveguide lasers [22, 23]. More recently, aerosol doping of a phosphosilicate film with thulium resulted in up-conversion in waveguides, resulting in the observation of blue light generation [24, 25].

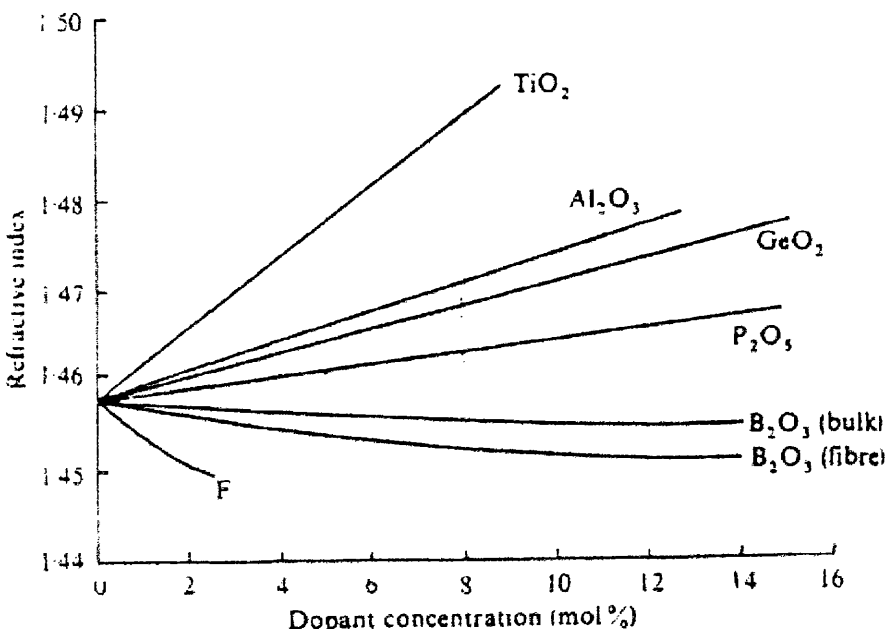


Figure 2.2 Refractive index variation with dopant concentration, for $\text{SiO}_2\text{-}\text{TiO}_2$, $\text{SiO}_2\text{-}\text{GeO}_2$, $\text{SiO}_2\text{-}\text{P}_2\text{O}_5$, and $\text{SiO}_2\text{-}\text{B}_2\text{O}_3$ Binary Glasses (from Beales *et al* [15])

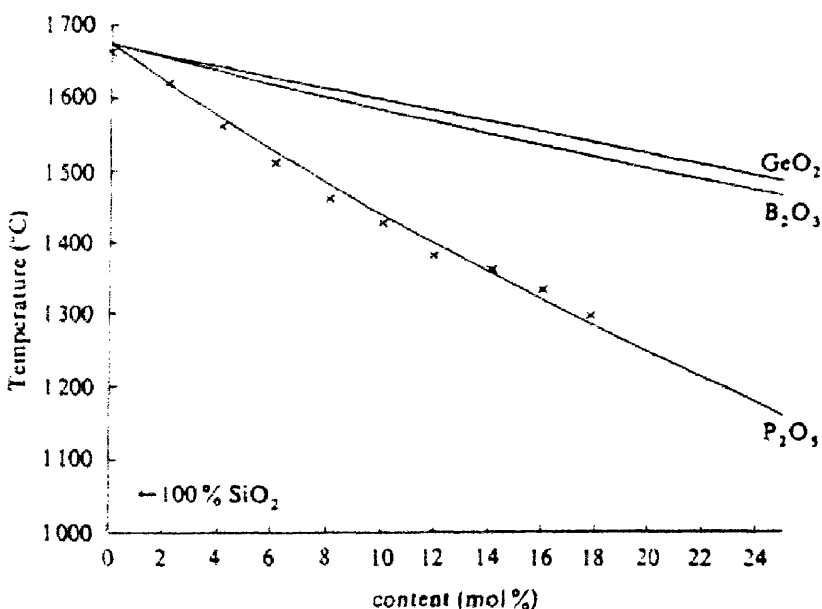


Figure 2.3 Glass softening temperature versus dopant concentration, for $\text{SiO}_2\text{-GeO}_2$, $\text{SiO}_2\text{-P}_2\text{O}_5$, and $\text{SiO}_2\text{-B}_2\text{O}_3$ Binary Glasses (from Hammond [26])

Chemical Cabinet

The reagents used in FHD are stored within a sealed chemical cabinet which is constantly purged with zero grade nitrogen and temperature controlled at 23°C to maintain a dry atmosphere and eliminate condensation in order to prevent hydrolysis within the gas lines..

During the course of this work, the existing 12 year old chemical box was found to have deteriorated with time as a result of exposure to SiCl_4 , due to small leaks from a defective bottle stopper. It was also noted that the Perspex windows were beginning to crack, and owing to the corrosive environment, were becoming opaque. The metal surfaces at the back of the cabinet, as well as the silicone sealant used to seal the panels were also beginning to show signs of corrosion. There was also evidence of deterioration of the Nalgene pipes used for circulating silicone oil. It was considered at this point, that that the cabinet was beginning to show its age, and was likely to become a health hazard in the near future.

A new cabinet was designed and constructed which had many new features which would first and foremost improve safety, but also improve the function and longevity of the cabinet. Some of the new features are mentioned here:

- A ‘Load-lock’ system for easier, and safer, access to the chemical cabinet. This allows for new and old bottles to be moved, without operator exposure to the inner cabinet.
- Welded stainless steel panels on five side sides, again for improved safety, rather than the original silicone sealed Perspex panels of the old design. Glovebox entry is facilitated by retaining a perspex front panel with protective rubber gloves.
- Inspection lamp introduced, for increased visibility.
- Redirected piping, for improved carrier transport.

A photograph of the newly constructed chemical cabinet is shown in Figure 2.4.



Figure 2.4: New and improved chemical cabinet

Dreschel Bottles

Four reagent halides are stored within the chemical cabinet, namely: Optipur grade SiCl_4 , GeCl_4 , PCl_3 and POCl_3 . The chemicals are stored in a liquid form within Dreschel bottles, locally referred to as *Bubbler Jars*. The bubblers are custom made jacketed bottles, where a low viscosity silicone oil can circulate between the inner and outer surfaces of the bottle. The oil temperature is controlled by a heater/refrigeration

unit, such that the temperature of the liquids within each bottle is a constant 20°C, therefore maintaining a constant vapour pressure of the metal chlorides. A photograph of a spare Dreschel bottle is given in Figure 2.5.

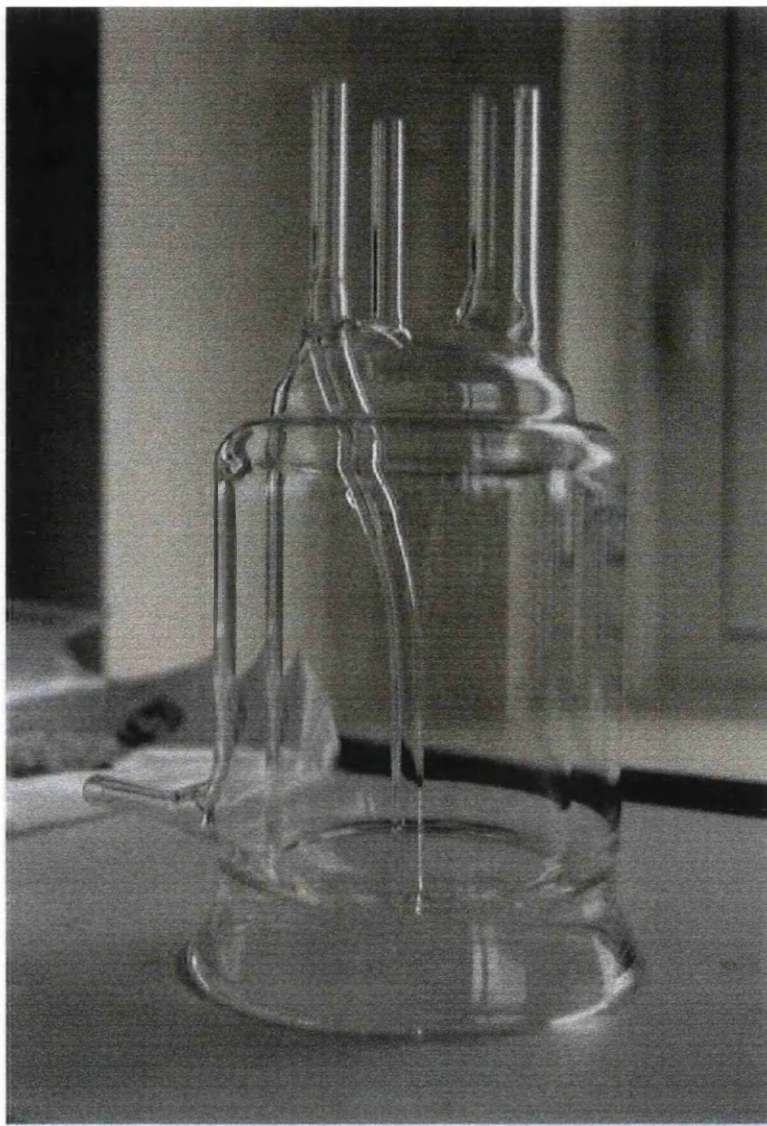


Figure 2.5: Photograph of a custom made Dreschel bottle

The metal chloride vapours are transported to the deposition chamber by the inert N₂ carrier gas by bubbling the gas through the required Dreschel bottles. The flow rate of the N₂ carrier gas to each bottle is controlled using mass flow controllers (MFC's), which are set using potentiometers according to a digital display. The required carrier gas flow rates for a particular glass system are chosen from the relevant calibration chart, which relates refractive index to the carrier flow rate for the commonly used glass systems. The flow path of the carrier gas is controlled via pneumatic bellow valves (PBV) which direct the halide vapours to the oxy-hydrogen torch.

Figure 2.6 demonstrates the bubbling action of the carrier gas through the Dreschel bottles.

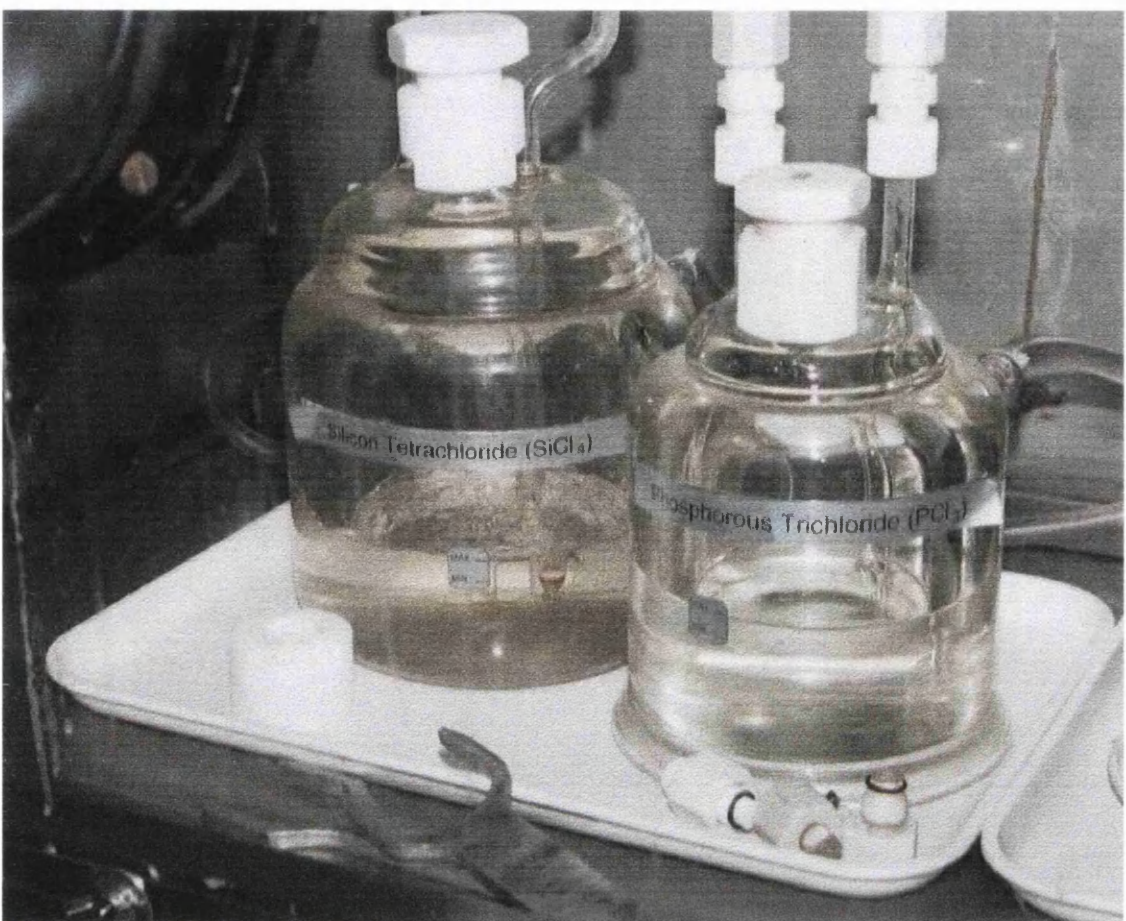


Figure 2.6: Photograph of SiCl_4 bottle, during a deposition. Of note is the vigorous bubbling action.

The interconnecting pipework and fittings within the chemical box are made from polytetrafluoroethane (PTFE), whereas the PBV's are made from polyvinylidifluoride (PVDF), a compound which is chemically inert to chlorides.

There are three PBV's associated with each Dreschel bottle: the waste feed, the bubbler feed and the torch feed. Under normal purging conditions the bottles are isolated with the bubbler and torch feed being normally closed. The waste feed is normally open, directing the carrier gas to the main extract. During deposition the waste feed is closed, the torch and bubbler feeds are opened, and vapour transport to the torch can take place.

A master MFC supplies N₂ to the system continuously through the main torch feed line. This serves three main purposes:

1. To control and maintain a constant flow rate to the torch during depositions. The master flow rate is adjusted after setting the flow of the halides to give a standard 850 sccm flow rate to the torch. This ensures an even deposition rate, by fixing the flow of reagents to the torch.
2. To flush residual halides from the torch feed after deposition.
3. To continually purge the torch supply line (500sccm), therefore maintaining a dry atmosphere within the system when depositions are not in progress to prevent hydrolysis within the lines.

Non-return valves are fitted before the main MFC's, and after the bubbler feeds, to ensure that the halides can only flow to the torch, and thereafter out through the chamber extract. A manometer is fitted adjacent to the torch feed as a means of monitoring pressure within the torch feed line. A ruler is fixed in place, and used to standardise the pressure in particular processes, thus providing a means of monitoring for blockages and other associated problems.

Boron Trichloride

A bottle of gaseous BCl₃ is fitted externally to the system in an independently temperature controlled (26°C), extracted cabinet. The BCl₃ supply system is normally purged by the N₂ gas supply to maintain a dry atmosphere, again to eliminate line hydrolysis. The gas is piped to the torch via stainless steel piping, with a temperature gradient of 3.5°C/m as an aid to gas transport. Originally, the maximum BCl₃ flow rate was MFC restricted to 50 sccm, however during the course of this work a new MFC was fitted to allow higher flow rates upto a maximum of 100 sccm.

N₂ Carrier Gas

Fundamental to the function of the FHD system is the use of an inert carrier gas, zero grade nitrogen (N₂). Zero grade N₂ (H₂O content < 10 ppm) has two functions within the FHD system; carrier gas for reagent transport and purging gas for the reagent

supply lines. The N₂ supply is provided by an external assembly of four gas cylinders, flow regulators, valves and electro-mechanical switches. Two bottles supply the system simultaneously with a constant pressure of 50 psi supplied to the system. At such time as the pressure falls below 20 psi, the electro-mechanical switch transfers the supply to the other two bottles, thus maintaining a constant supply of N₂. The N₂ supply system can also be filtered through gas dryers where a lower grade nitrogen supply or compressor is used, or during routine system maintenance. The N₂ gas supply system is shown in Figure 2.7.

Hydrogen, Oxygen and Helium

Hydrolysis occurs as a result of the reaction of the halide reagents with the hydrogen (H₂) and oxygen (O₂) flame. The required gases are flow meter controlled and supplied via stainless steel pipes, with flash-back arresters fitted as a safety precaution. Helium (He) and oxygen are also used as an aid to sintering, and as such are fed to the furnace by stainless steel pipe via flow meter controls.

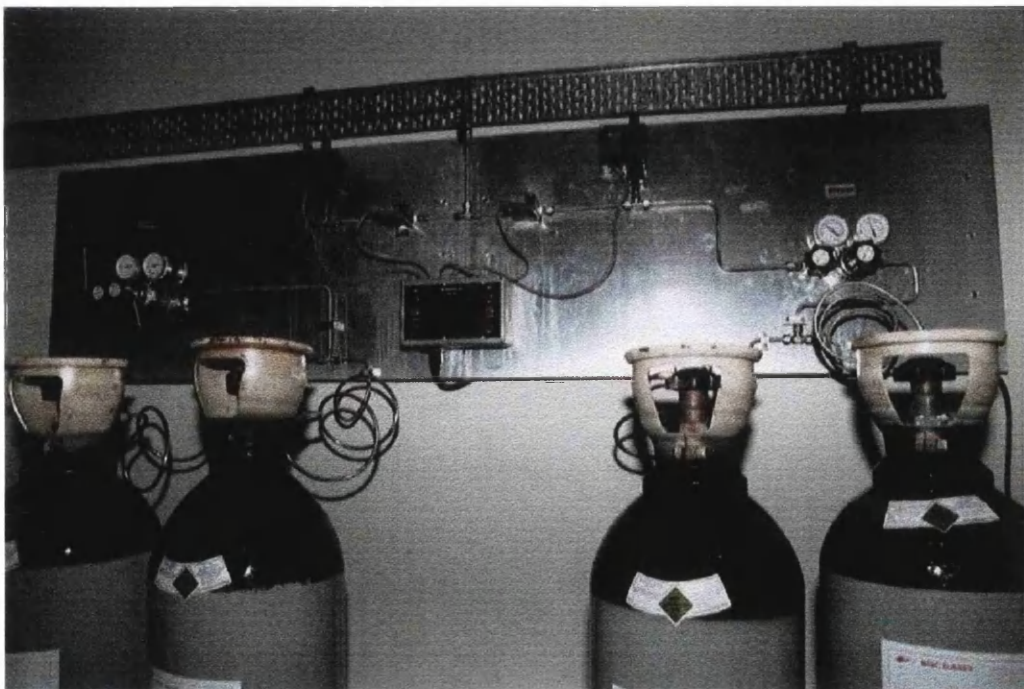


Figure 2.7: Photograph of Nitrogen Supply System.

2.3.3 Flame Hydrolysis Reaction

The essence of FHD is the synthesis of fine glass particles by the hydrolysis of vapour phase halide pre-cursors within a hydrogen-oxygen flame, where the particles are deposited onto a host substrate as a low density oxide ‘soot’. Oxide ‘soot’ deposition occurs in stages: firstly the initial chemical reaction phase, secondly particulate nucleation and growth and finally thermophoretic transport.

The reaction phase of FHD is a rapid process where the high purity halide pre-cursors hydrolyse within the combustion zone of the flame, due mainly to the high temperature flame processing, the low activation energy of hydrolysis processes and the presence of radicals within the flame [27]. Flame temperatures are much greater than the melting point of the forming oxide proto-particles, typically > 2000 K.

As the proto-particles formed in the reaction phase pass through the flame, they condense as the flame cools, where according to the rules set out by Ulrich [28], a proto-particle must exceed a certain critical radius in order to remain stable. Brownian motion dictates the formation of growth where the formation of aggregates depends jointly on the frequency of collision and the concentration of reagents. Where the flame temperature is greater than the oxide melting point, particles fuse together, to form aggregates. Below the melting point, particle bonding is of a physical nature where the formation of large agglomerates is dominant.

Deposition onto the substrate is determined by thermophoresis [29], where the particles formed in the flame are ‘driven’ toward the cooler substrate. Tsai *et al* [30] recently modelled thermophoretic transport mechanisms in FHD, particularly the influence of the target temperature (substrate), where the authors found that the optimum SiO₂ deposition efficiency occurred at a substrate temperature of 900 K.

Turntable temperature is of great importance in determining the deposition efficiency of the FHD process. Edahiro *et al* [31] studied the dependence of deposition properties on the substrate temperature for various binary systems over the temperature range, 200°C - 800°C. The oxides B₂O₃ and GeO₂ were found to exist in a crystalline phase for substrate temperatures below 400°C, whereas above 500°C, an

amorphous form of GeO_2 could be observed. The dissolved concentration of B_2O_3 and GeO_2 was found to increase with increasing substrate temperature. It is suggested that the high saturated vapour pressure of GeO_2 results in vapour phase deposition of the oxide, where it quickly condenses on the cool substrate to form a crystalline phase. However, the presence of micro-crystallites is not considered to affect the refractive index control of the glasses [32], but glass degradation through exposure to moisture is expected. By contrast, TiO_2 , having a low vapour pressure, was found to deposit in a form independent of the substrate temperature, where no crystalline phase was observed, suggesting that solid particulate formation occurred in the flame.

Deposition Chamber

The FHD reaction occurs within an extracted chamber, as shown in the photograph of Figure 2.8. The movements of the torch and turntable are computer controlled.



Figure 2.8: Photograph of extracted deposition chamber.

The deposition chamber consists of 5 main components all of which are listed below:

1 Sealed Deposition Chamber

The chamber walls are manufactured from hard anodised aluminium, where the inner surfaces are coated with HCl resistant Xylan. Access to the chamber is through a hinged Perspex door, where the door itself has a hinged flap to facilitate sample removal, whilst retaining a clean environment.

2 Exhaust and Scrubber

The chamber has an anodised aluminium exhaust to remove waste products such as HCl and excess chloride vapours. The exhaust is located opposite the traversal path of the torch to improve extract efficiency. The scrubber unit consists of alternate baffles and spray bars. The spray bars generate a fine water mist which dissolves and dilutes the harmful HCl bi-product of the flame hydrolysis process. Good working practice dictates that the scrubber unit is drained and refilled on a regular basis to prevent corrosion.

3 Filtered ventilation

A filtered aperture is located opposite the local extract to maintain a laminar air flow through the deposition chamber, which minimises flame turbulence.

4 Deposition turntable

The turntable is manufactured from silicon carbide, making it resistant to both HCl and the high flame temperatures. Machined recesses can hold a maximum of three 3" substrates. The surface temperature is controlled ($T_{max} \sim 200^\circ C$) through the use of a variac controlled 'diff pump' heater located beneath the turntable. The rotation of the turntable is held constant at 30 rev/min.

5 Torch Assembly

The torch assembly is designed to hold the torch at a fixed height and angle above the turntable surface. The Nalgene gas feed lines are held in position on the assembly to minimise stress on the fragile torch ports during each traversal. A modification was

made to the chamber such that gas feed lines have a fixed point of entry on the chamber wall, rather than insertion through the ventilation aperture. A further modification, was the vertical mounting of the aerosol inside the chamber on the torch holder. Uniform deposition occurs through radially traversing the turntable, where the torch speed matches the local velocity of the turntable.

Quartz Burner Torch

The flame hydrolysis reaction for passive glass films occurs through the use of a Baumbach *standard* 4-port quartz torch, see figure 2.9. The torch consist of three main gas paths: a central path through which the halides are carried to the reaction zone, surrounded by first a hydrogen path (H_2) and an oxygen path (O_2). The fourth port is used to carry N_2 , which acts as a shroud to increase flame directionality and to minimise the likelihood of devitrification of the torch due to the high flame temperatures. Other torches such as the *modified* 4-port quartz torch are used to accommodate aerosol transport in rare earth and heavy metal depositions.

The halide vapours, H_2 , O_2 and N_2 are taken to the chamber via PTFE pipes. Inside the deposition chamber the gases are carried to the torch by replaceable Nalgene flexible tubing. Coupling between the Nalgene pipes and the quartz ports on the torch are assisted through the use of PTFE sealant tape to eliminate leakage.

As an aid to troubleshooting deposition problems and as a safety backup, it is useful to know the flame colours associated with the main glass forming reagents. Figure 2.10 (a-c) shows the flame typical of SiO_2 , P_2O_5 and B_2O_3 depositions. All flames have a 150 sccm flow of $SiCl_4$. Germanium doping does not differ from the flame colour associated with $SiCl_4$.

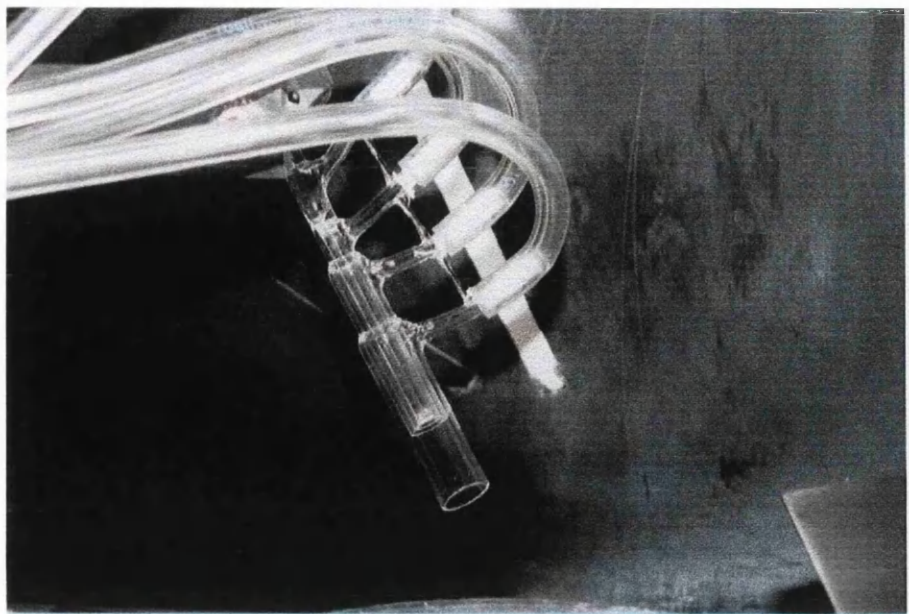


Figure 2.9 Standard 4-port torch used in passive film deposition.

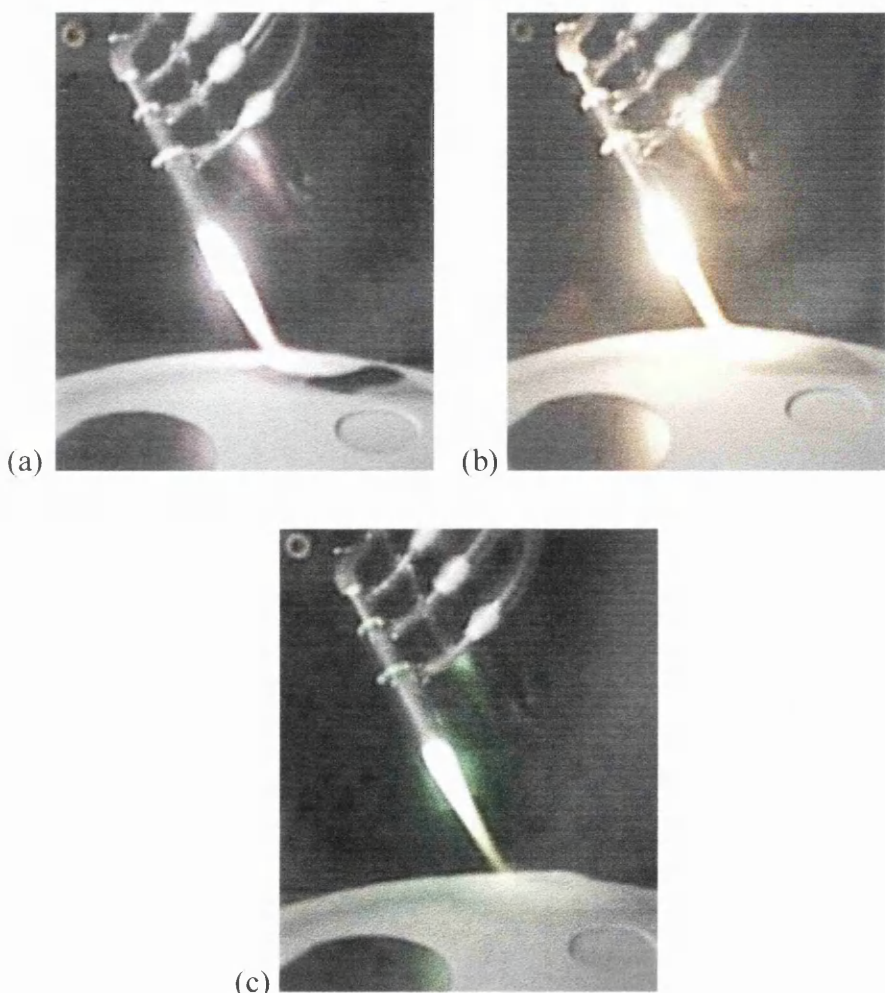


Figure 2.10 Flame colours due to the hydrolysis reaction of (a) SiCl_4 , (b) SiCl_4 & PCl_3 and (c) SiCl_4 & BCl_3 .

2.3.4 Sintering

After the deposition phase of FHD, the low-density fine oxide particles are processed to form a uniform, high density, bubble-free amorphous glass film, through the technique of sintering. In metallurgy terms, sintering is defined as [33]: “the heating of a mixture of powdered metals...to the melting point of the metal in the mixture which has the lowest melting point, the melted metal binding together the harder particles”. For the purposes of glass preparation, sintering is defined to be the process in which the low density oxide particles are heated to temperatures near their melting point [34].

As mentioned previously, the deposited ‘soot’ has the form of a fine powder, albeit with some structural integrity provided jointly by agglomeration in the deposition phase, and through partial sintering as the torch traverses the ‘soot’. At this point, as shown in Figure 2.11 (a), it is clear that the ‘soot’ is more air than glass!

Only by heating the oxide ‘soot’ to near its melting temperature, can the density of the glass be increased. Densification occurs through the formation and growth of interconnecting ‘necks’ between adjoining oxide particles [35], the appearance and growth of such necking is shown in Figure 2.11 (b-d). The growth of these ‘necks’ is described by Frenkel [36] through the theory of viscous sintering. Simply, the energy for viscous flow is provided by a decrease in the surface energy of the sintering structure, as the density of the glass increases. The photographs in Figure 2.11 (a-d) are provided courtesy of Dr J.R. Bonar [13].

The sintering glass can best be described as being an open pore network, where the closure of its pores ultimately determines the successful preparation of a bubble free glass. Pore closure is determined by a number of factors, including: the viscosity and sintering atmosphere. The viscosity of silica glass, as well as its softening temperature (as described in section 2.4), can be reduced by incorporating small amounts of dopant glasses such as B_2O_3 and/or P_2O_5 . The sintering atmosphere can be controlled by introducing gases such as O_2 and/or He, where O_2 can be used as an aid to oxidation particularly in phosphosilicate systems, and He is used as an aid to pore closure [37] due to its high diffusivity in silica.

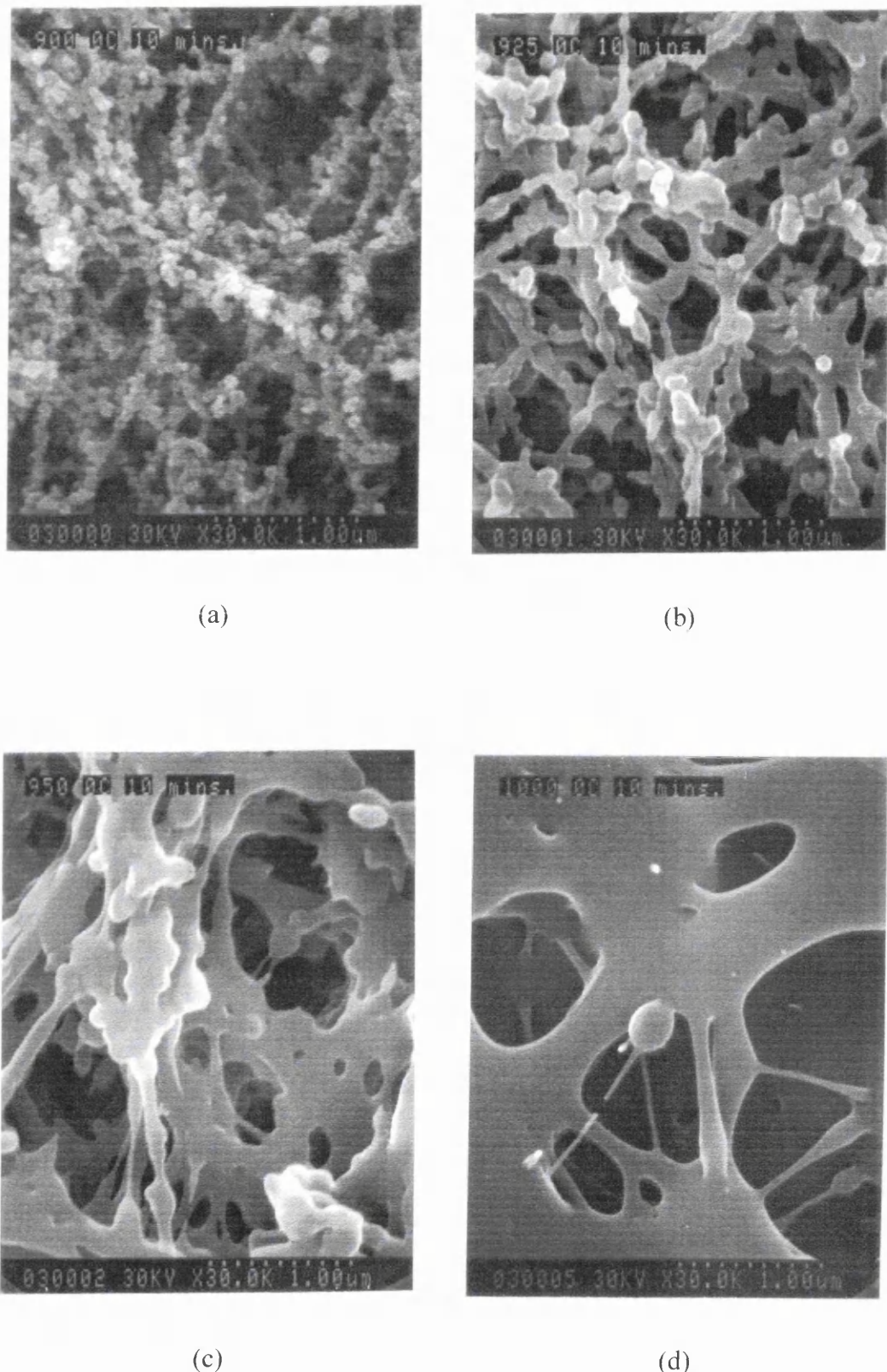


Figure 2.11 Illustration of glass densification by increasing sintering temperature. Samples sintered at: (a) 900°C, (b) 925°C, (c) 950°C and (d) 1000°C, for 15 minutes. Images provided courtesy of Dr J.R Bonar [13].

Consolidation Furnace

Sintering of the low-density soot produced by FHD takes place in a vertical loading MF-206 furnace, a photograph of which is shown in Figure 2.12. The furnace temperature can be adjusted via a programmable Eurotherm controller, which allows the use of multi-step programs, for example temperature ramps and fixed temperature dwells. The maximum operating temperature of the furnace is limited to 1400°C by an alarm controller. Quartz liners are placed within the furnace to minimise the risk of contamination from the ceramic materials used in constructing the furnace. The measurement error of the furnace is nominally less than $\pm 10^\circ\text{C}$.

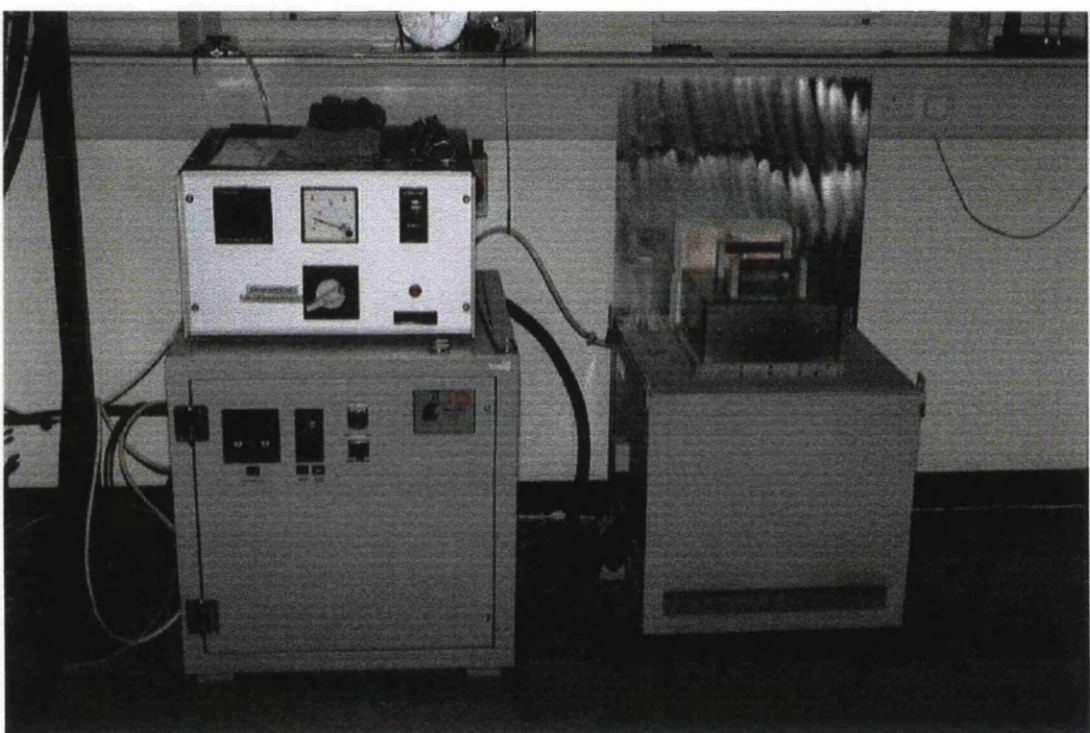


Figure 2.12: MF-206 Consolidation Furnace (Right) and Programmable Controller (Left).

Problems have occurred in the past within the Deposition Room, in that the ambient room temperature was normally in excess of 30°C. This was mainly attributable to the metal exhaust cabinet which surrounded the furnace. During the course of this project a furnace lid was constructed from Syndanyo by the Mechanical Workshop. The lid seals the furnace, which reduces heat loss to the surroundings, therefore reducing power consumption and prolonging the life of the furnace rods. The furnace lid is illustrated in Figure 2.13. Overall the room temperature reduced by 5-10°C.



Figure 2.13: Custom made furnace lid (left of picture) for reduced heat loss.

Substrates are lowered vertically into the furnace using custom made quartz carriages, an example of which is shown in Figure 2.14. The carriages can in principle hold a maximum of 7 substrates, although in reality the number of substrates is restricted to 3 by the size of the deposition turntable.

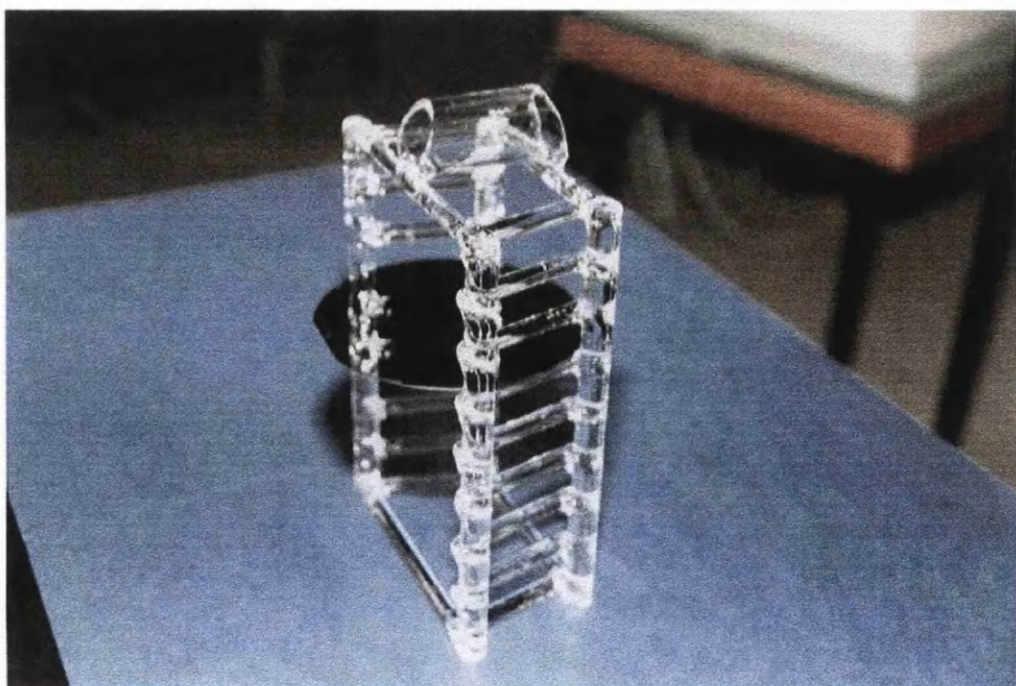


Figure 2.14: Custom made quartz carriage substrate holder.

Recently, the FHD group received a pneumatically loaded vertical furnace from the FHD laboratory at British Telecommunications Research Facility. Pneumatic loading of the substrates from the bottom assists in reducing contamination as the operator is no longer required to stand over the samples during the loading and removal phase. Reductions in electrical power consumption, and room temperature are expected. It is intended that this furnace be adapted for 4" substrate processing.

2.3.5 Cleanroom

One of the major improvements in the FHD facility was the upgrade of the laboratory to cleanroom status. This required extensive re-building of the lab including:

- the roof space was sealed prior to the installation of air filtering units,
- the walls were sealed with custom paint for cleanroom use,
- complete re-wiring of the electrical system,
- construction of a new exhaust hood around the FHD system

An illustration of the improvements [38] in the room are shown in Table 2.2 where a list of the particle count for both 0.5 and 5 micron particles is given.

Location	0.5 μm particles (m^{-3})	5 μm particles (m^{-3})
<i>Before Upgrade</i>		
FHD Laboratory	22,000	240
Deposition Chamber	20,000	N/A
<i>After Upgrade</i>		
FHD Laboratory	130	10
Deposition Chamber	250	30
<i>Comparison</i>		
Outside Corridor	98,000	1080

Table 2.2. Illustration of the improvements made to the FHD laboratory after upgrading

It is clear from the data presented in the table, that the modest sum of money spent on upgrading the FHD lab, has resulted in an substantial improvement, reflected in the change of its cleanroom status from Class 100,000, to Class 1000, although the data shows that it is close to Class 100 standard. The improvements to the FHD lab have resulted in a reduction in the number of defects observed on samples, with an observed defect count of less than 1 per cm^{-2} .

2.4 Planar Waveguide Fabrication Procedure

Throughout the course of this work, 3 inch polished silicon wafers (or smaller cut pieces) were used as the host substrate for the glass film depositions. Silicon substrates were used as they are the preferred material for hybrid integration with other optical components such as fibres, see for example Chapter 6. Other substrates are used, for example fused quartz for the preparation of photosensitive films, and fused quartz slides for bioelectronic applications. All silicon wafers had been thermally oxidised ($\sim 10\text{-}16 \mu\text{m}$) to provide a buffer/undercladding layer for the waveguide film.

2.4.1 Sample Preparation

Prior to each deposition samples should be cleaned to remove any contamination, normally dust. However, in the case of smaller samples cut from full wafers, pieces are typically contaminated by an assortment of waxes and cleaning agents. Samples are also meticulously cleaned prior to each cladding layer deposition, as residual mask material must be removed. The silicon substrates were normally cleaned in an ‘acid bath’ prior to FHD deposition to remove any surface contamination. Cleaning in acid is performed in accordance with the stringent cleanroom regulations, where the details of safe working practice should always be obtained from members of cleanroom staff and considered prior to that presented here. An ‘acid bath’ is prepared by the slow addition of a small amount of hydrogen peroxide (H_2O_2) to a larger amount of sulphuric acid (H_2SO_4) (typically 5-10 ml H_2O_2 per 100ml of H_2SO_4) in a standard beaker. The mixture should be mixed periodically, and the temperature should be monitored using a thermometer until such time as the mixture is at 80°C . A beaker is filled with RO (reverse osmosis) water in readiness for sample rinsing.

The silicon wafers are cleaned through total immersion within the acid mixture, for a period of 5-10 mins. Gentle agitation should be applied periodically to refresh the solution. After completion, the sample should be rinsed in RO water for 5-10 mins, before being blown dry and baked on a hotplate at 90°C . The sample should be examined by microscope to ensure that there is no residual material or drying stains on the surface. The waste acid is disposed of by dilution in copious amounts of water.

2.4.2 Flame Hydrolysis Deposition Procedure

The description that follows is the typical procedure used in flame hydrolysis similar to that found in previous works (for example Maxwell [9]). For more specific deposition procedures involving aerosol and solution doping, interested readers are directed to the work of Bonar [13]. A review of the techniques has been presented elsewhere [39].

1. Clean or replace glassware as required,
2. Clean chamber (IPA) and turntable (water),
3. Locate turntable on spindle,
4. Replace Nalgene tubing as required,
5. Fasten torch at correct height and angle, and clean turntable (IPA),
6. *(Prepare nebuliser with rare-earth/heavy-metal solutions if required)*,
7. Check halide levels, silicone oil temp, cabinet temp extract and scrubber,
8. Switch on computer, check communication with turntable/torch,
9. Open, check, and set H₂ and O₂ flow rates, set N₂ flow rate, vent lines,
10. Switch on turntable heater and stepper motor cooling fan,
11. Set required halide flow rates,
12. Monitor turntable temperature, until required temperature is reached,
13. Load samples at desired temperature,
14. Ignite hydrogen and oxygen flame, adjust to required flow rates,
15. Toggle gas flow switches and adjust master MFC to give 850 sccm,
16. *(Start N₂ nebuliser flow)*,
17. Check manometer and flame colour and begin deposition,
18. After deposition close and purge halide lines, close H₂ bottle and vent,
19. Allow chamber to vent and remove samples to furnace.

2.5 The SiO₂-GeO₂-B₂O₃ Glass system

The objective of this work was to develop a germano-silicate glass deposition process which resulted in a reproducible refractive index and thickness control, such that the glass was of sufficient quality to fabricate optical waveguides. The assessment by the author of the SiO₂-GeO₂-B₂O₃ glass system is restricted to refractive index and thickness measurements, general qualitative observations on macroscopic defects and Microprobe analyses to evaluate the doping levels. Latterly, work in conjunction with the University of Porto, has resulted in significant improvements in the deposition and microscopic properties of the germano-silicate glass system. This included work on photosensitive phenomena, and tentative X-ray diffraction analyses.

The use of the photosensitive GeO₂ glass system is important to future applications of integrated optics in interferometric sensing, as the effect can be used as an elegant solution to path length control. Chapter 5 describes how the success of low coherence interferometry relies on a physical path difference between interferometer arms. UV laser trimming has already been shown to be a valuable technique for controlling the path imbalance of a Mach-Zehnder [40], and thus it is conceivable that photosensitivity can be applied in eliminating fabrication errors. More elegant, is the concept that a path difference (~250μm) could be introduced through UV illumination of one arm, which allows trimming of fixed length interferometers for different path length systems.

2.5.1 Dopant Considerations

The objective of this section is merely to introduce the dopants used in the above mentioned glass system, and to indicate their relevance to this work. Analysis of the dopant characteristics was sufficient for a fundamental understanding of the influence of the individual dopants in the ternary glass system.

The binary system SiO₂ - GeO₂

The phase diagram for the SiO₂-GeO₂ systems is shown in Figure 2.15 (from Schafer *et al* [41]). From this phase diagram, and the evidence of Baret *et al* [42] it is clear that there exists a glass forming region for all doping levels of GeO₂ in SiO₂. The addition of GeO₂ can also be observed to contribute to a reduction of the glass

softening temperature, albeit with a significantly lower magnitude than that of B_2O_3 and P_2O_5 additions (see Figure 2.3). From the work of Edahiro [30], it is known that the phase of GeO_2 is strongly dependant on the substrate temperature, where evidence of a crystalline phase was observed for substrate temperatures less than 400°C.

The thermal expansion coefficient of highly doped GeO_2 films can be as much as an order of magnitude greater than SiO_2 [43]. This is important where silica substrates are used, as there is a positive difference in thermal expansion between the deposited film and the silica substrate [13]. This imposes a tensile stress on the glass after removal from the high temperature furnace, which can lead to cracking of the deposited films [7]. This problem can be alleviated however, through the use of silicon substrates, which exhibit a negative thermal expansion difference relative to the film.

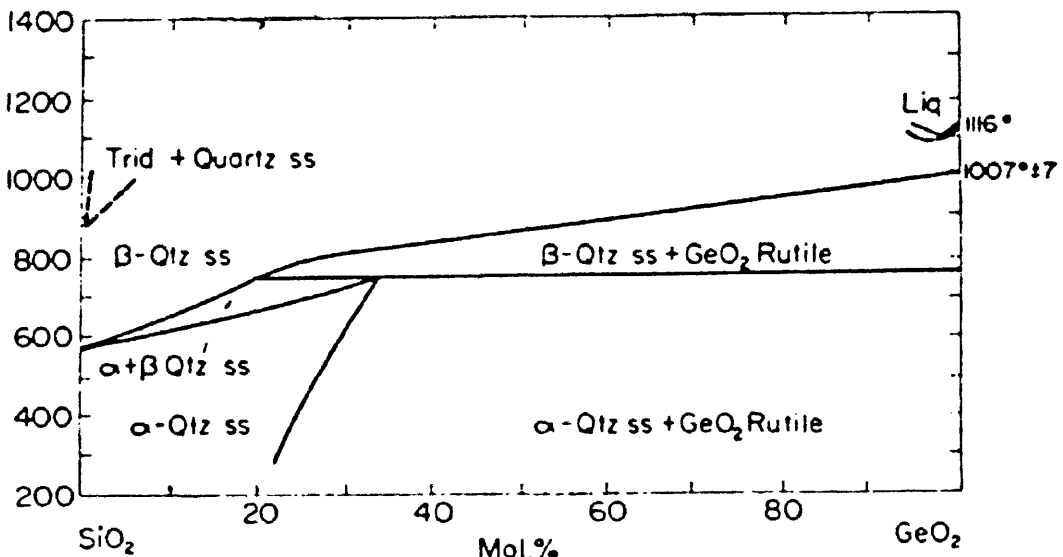


Figure 2.15 Phase diagram for the SiO_2 - GeO_2 binary system (from [39])

The binary system SiO_2 - B_2O_3

The phase relationship of the SiO_2 - B_2O_3 binary glass system was studied by Rockett and Foster [44], and again by Baret *et al* [40] (the latter authors also studied the phase of numerous binary and ternary systems based on SiO_2 , GeO_2 , B_2O_3 , As_2O_3 and P_2O_5).

From the phase diagram shown in Figure 2.16, it is apparent that increasing the doping level of B_2O_3 significantly reduces the glass softening temperature of the binary system,

with no apparent crystalline B_2O_3 phase. The addition of this dopant is also known to significantly reduce the viscosity of the glass.

B_2O_3 is an extremely important dopant in silica glass waveguide fabrication, not least because it reduces the glass softening temperature, but more importantly because it reduces the refractive index, making it ideal for cladding optical waveguides.

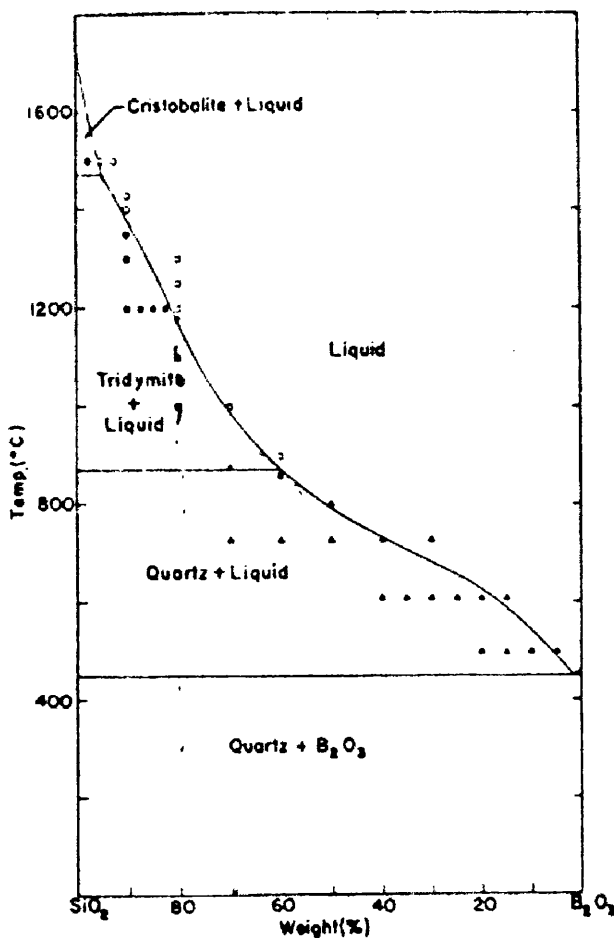


Figure 2.16 The phase diagram for the SiO_2 - B_2O_3 binary system (from [42])

The ternary system SiO_2 - GeO_2 - B_2O_3

Baret *et al* examined the phase relationship of the ternary glass system [40], both experimentally and by analysis where they found that no crystal phase could be observed. Also, the same authors published a detailed analyses for the relationships between the glass transition, liquidus and flow temperatures for this system [45]. Typical temperatures of the order of 850, 1150 and 1300°C respectively for various levels of GeO_2 (4 - 14 mol%) and B_2O_3 (12 - 15 mol%).

2.6 Process Development

A requirement of this work was the production of $\text{SiO}_2\text{-GeO}_2\text{-B}_2\text{O}_3$ glass films of sufficient quality to successfully fabricate optical waveguides. In order to achieve this goal, material analysis was limited to a quantitative assessment of properties relating to optical waveguide design, refractive index and film thickness. A qualitative assessment of macroscopic defects was performed where necessary.

The relative refractive index difference ($\Delta n\%$) at a wavelength of 632.8nm and thickness of the prepared films was assessed through the use of a prism coupler (for a description see Lee [46] and/or previous PhD theses [9, 10, 12, 13]). The prism coupler is also used to visually assess the quality of the waveguide film, where a qualitative assessment of the optical loss is provided by the in-plane and out-of-plane scatter. Periodically the thickness was verified using a DekTak surface profiler after either: a selective etch of the waveguide film or partial removal of the deposited ‘soot’ prior to the sintering stage.

Macroscopic defects are defined as being a restriction on the fabrication of a waveguide. These defects are typically visible under visual inspection of the sample by the naked eye or under an optical microscope, and are of the order of 100 microns in size. A macroscopic defect will typically impede successful waveguide fabrication as it may prevent light propagation. Some examples of macroscopic defects are bubbles, voids and unsintered areas of the sample.

2.6.1 Low B_2O_3 content germanosilicate glass

Initial studies on germanosilicate glass fabrication were performed using the deposition parameters given in Table 2.3. Low values of hydrogen and oxygen were chosen at this stage as it was believed that a lower flame temperature would decrease the likelihood of the germanium dioxide content depositing on the substrate in its vapour phase, and hence prevent vaporisation and/or the formation of a crystal phase.

A 150 sccm flow rate of SiCl_4 is used, forming the bulk glass and hence maintaining a typical thickness of 1 micron per traversal. This is commonly used in the deposition of

other established glass systems, for example $\text{SiO}_2\text{-P}_2\text{O}_5$. The BCl_3 flow rate was chosen to be mid-range of its mass flow controller (MFC).

Deposition Parameter	Value
Hydrogen Flow Rate	1 l/min
Oxygen Flow Rate	2 l/min
Silicon Tetrachloride Flow Rate	150 sccm
Boron Trichloride Flow Rate	30 sccm
Germanium Tetrachloride Flow Rate	60 - 180 sccm

Table 2.3 Preliminary deposition data for germanosilicate glass preparation

Numerous substrates were prepared using a germanium flow rate varied in the range 60 to 180 sccm, and sintered at 1300°C in a He:O₂ atmosphere for one hour. Each sample was assessed in turn using the prism coupler to estimate the refractive index of the glass film, as shown in the graph in Figure 2.17.

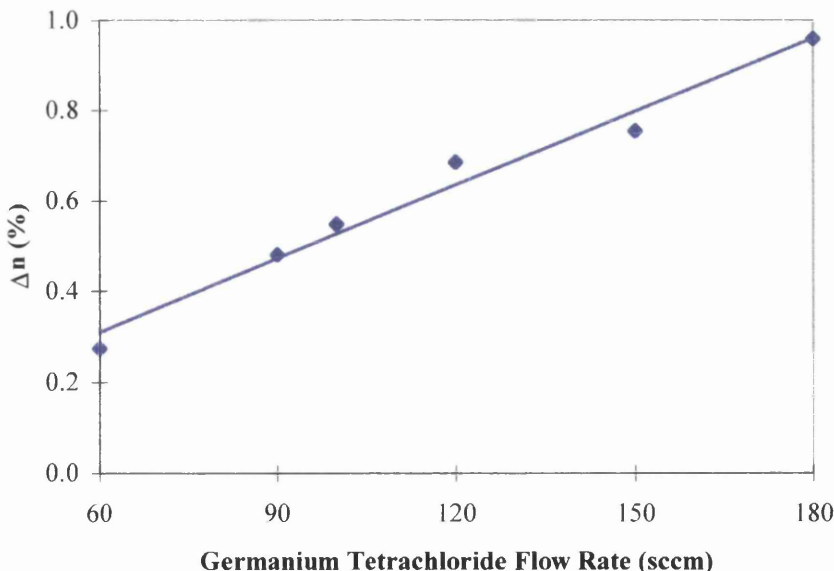


Figure 2.17 Refractive index difference with increasing GeCl_4 flow rate (BCl_3 30 sccm)

Visual inspection of the samples at this stage indicated that the sample was not entirely sintered, a fact which was confirmed by the presence of both in and out of plane scattering, an example of which is demonstrated in Figure 2.18.



Figure 2.18 Photograph showing the presence of in plane scatter (horizontal line across sample) and out of plane scatter (at left edge of sample) in a partially sintered silica film.

2.6.2 High B_2O_3 content germanosilicate glass

More samples were prepared and subjected to higher temperatures (1325-1375°C) for longer times, where it was noted that in general the level of sintering increased. Typically the samples exhibited a glassy appearance on the surface, and a speckled appearance below. On this evidence it was concluded that the sintering point was higher than the maximum temperature permissible by the furnace. The sintering temperature can be reduced by adding more BCl_3 , thus increasing the doping level of B_2O_3 in the silica glass, and as such an MFC with a larger flow rate (0-100 sccm) was installed.

Samples were prepared under the same conditions as listed in Table 2.3, with the exception of higher BCl_3 flow rate (50 sccm). Sintering at 1325°C resulted in an increase of compaction of the glass film, confirmed by both visual assessment and a reduction in the level of both in and out of plane scattering. It is known that increasing B_2O_3 content causes a reduction in the refractive index of the silica film, a fact which

was evidenced in the graph shown in Figure 2.19, where the Δn has fallen by approximately 0.1% compared to the lower B_2O_3 case as shown in figure 2.18.

A new problem was encountered in the appearance of an extremely high density of voids and bubbles on the order of 50 defects per square inch, examples of which are shown in the SEM picture of Figure 2.20 and the microscope image of Figure 2.21.

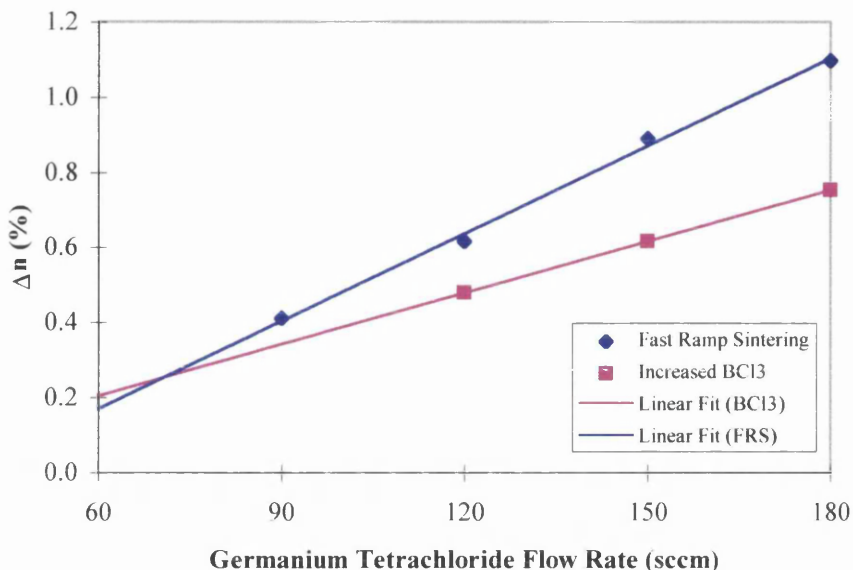


Figure 2.19 Refractive index difference with increasing $GeCl_4$ flow rate (BCl_3 50 sccm). Also shown is the increased refractive index difference under fast ramp sintering conditions.

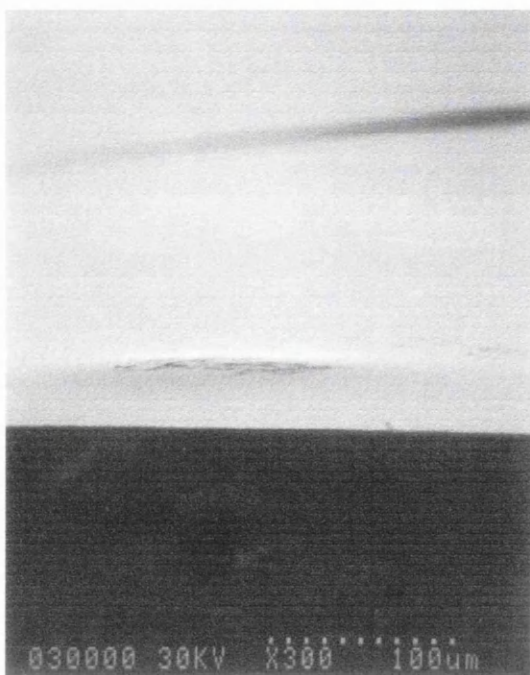


Figure 2.20 SEM micrograph of a bubble

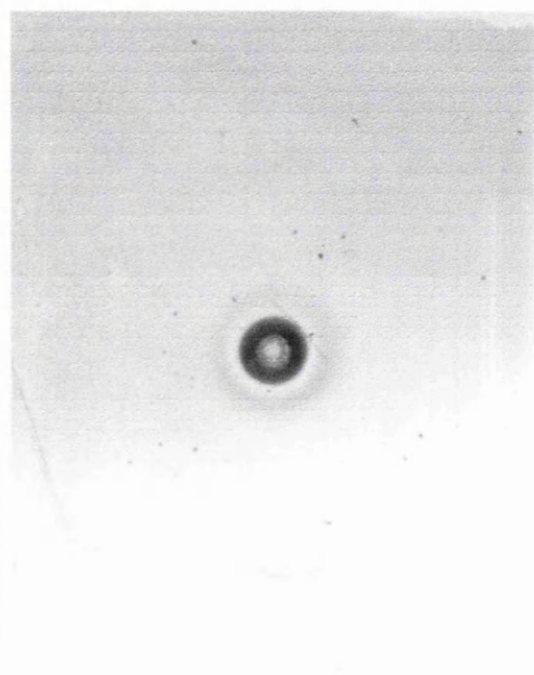


Figure 2.21 Optical micrograph of a void

Initially these defects were thought to be caused by gas trapping, an effect which is partially related to the gas trapped in the compacting pores, and partially related to the fact that the glass may be compacting faster than the trapped gases can escape [36]. Attempts were made to reduce the defect level by introducing temperature ramps to the sintering process in which the temperature is raised from below the glass softening point (in this case 850°C was the start point) to the required sintering temperature (1325°C in this case). This allows sufficient time for the trapped gas to diffuse out from the closing pores. Various ramps were used, ranging from 5 to 20 °C/min, and it was found that slow ramps appeared to be more successful in reducing the number of defects on the sample. However, the difference in defect count was insignificant when compared to the number of defects remaining.

The source of the defects have been attributed to external contamination, particularly where there has been human contact with the substrate. This is most noticeable in regions where the substrates have been handled with tweezers. Despite rigorous cleaning regimes, these defects still remain albeit at low levels (<20 defects per 3" wafer). Evidence that the contamination occurs prior to the sintering phase was provided by locating the substrate outwith the confines of the furnace liner, but sufficiently close that the film begins to sinter. Dark spots in the white 'soot' appeared in a rapid and random nature, and occurred without any sintering of the vast majority of the 'soot'. By mapping the position of these spots as they occurred and comparing them to defects in the final sintered glass it was clear that the contamination had occurred either before or during the deposition phase. To date, no satisfactory explanation for the origin and nature of these spots has been found. Some suggestions include: the presence of organic matter within/under the soot which are vaporising before sintering of the glass can begin, thus creating small bubbles which eventually burst. This is supported by the perfectly circular appearance of the voids (diameter ~ 100 microns) and the concentric distribution of debris within the void.

It was noted during the investigation of temperature ramps that the refractive index of the sintered films was higher under fast ramp conditions, shown in Figure 2.19. The sintering conditions were a 20°C/min. ramp from 850°C to 1250°C, followed by a 1 hour dwell. It is thought that this could be due to an increase of the GeO₂ content

within the glass. It is known that GeO_2 has a high vapour pressure, and it is quite conceivable that under a slow ramp, evaporation of volatile GeO_2 may occur.

2.6.3 Assessment of doping levels by Electron Microprobe Analysis [47]

The doping levels of the sintered boro-germano-silicate glass film was performed by the Electron Microprobe facility of the University Geology Department. The author expresses his gratitude to Mr R. McDonald for his time and assistance in assessing these samples. The machine was a Camebax SX50 Electron Microprobe with a quoted accuracy of ± 1 wt%.

The assessed samples were produced using 150 sccm SiCl_4 , 50 sccm of BCl_3 and various GeCl_4 flow rates. A minimum of 10 measurements were taken across each sample (2 cm width). The averaged results for these analyses are shown in Table 2.4. During the analysis a scan was also performed for the presence of B_2O_3 in the glass system, however owing to the size of the boron atom the scan showed up only trace amounts of B_2O_3 , which fell below the quoted accuracy of the Microprobe. Therefore this data is not presented, and its presence is shown in the error of the total.

Flow Rate (sccm)	SiO_2 (wt%)	GeO_2 (wt%)	Total (wt%)
60	92.69 (S.D. 0.33)	7.08 (S.D. 0.36)	99.77
90	89.65 (1.29)	8.90 (1.46)	98.55
120	86.02 (0.53)	12.65 (0.83)	98.67
150	82.93 (0.45)	16.23 (0.42)	99.16

Table 2.4 Average doping levels and standard deviation of GeO_2 in SiO_2 glass

The standard deviation of the dopants across the 2 cm samples was also less than the machine accuracy, indicating a high degree of dopant homogeneity across the sample.

A further scan was carried out by the operator, Robert McDonald, using matrix correction techniques in an attempt to more precisely evaluate the B_2O_3 co-doping level in the sample prepared using 150 sccm GeCl_4 . This analysis indicated that the B_2O_3 level was approximately 6.49 wt%, compared to 72.53 wt% and 20.98 wt% of

SiO_2 and GeO_2 respectively. The standard deviation across the sample was 0.49, 0.17 and 0.41 wt% respectively. Due to the inherent difficulties in measuring boron emissions, this data is treated with a certain degree of scepticism.

Similar analyses were performed using EDS equipment by P.V.S. Marques at the University of Porto, Portugal on similarly doped samples (150 sccm GeCl_4). In this work the variation in dopant levels was monitored from deposition to deposition, position on the deposition turntable and position in the furnace, refer to Table 2.5.

Sample ID	Average SiO_2 (wt%)	Average GeO_2 (wt%)
41	82.91 (S.D. 0.25)	17.09 (S.D. 0.25)
46	83.20 (0.36)	16.8 (0.36)
48	83.29 (0.00)	16.66 (0.07)
51 (Middle)	82.48 (0.37)	17.52 (0.37)
51 (Top)	82.52 (0.54)	17.48 (0.54)

Table 2.5 Variation of doping levels from deposition to deposition, radial position on turntable and position within furnace. Data courtesy of P.V.S. Marques.

Each sample ID refers to three small pieces, where each piece was co-located within a substrate recess at a specific radial location during the deposition phase. The depositions were spaced by 1 week, with the system being used for other types of deposition during that period. Sample 51 was sintered in two positions within the furnace, some pieces at the middle of the quartz carriage, some at the top of the carriage (a spatial separation of approx. 3 cm)

The average doping levels over all conditions was found to be 82.88 wt% for SiO_2 and 17.11 wt% for GeO_2 with a standard deviation of 0.38 and 0.39 wt% respectively. Again this illustrates the dopant homogeneity across the width of a sample, but more importantly it illustrates the reproducibility of the FHD process from deposition to deposition, indicating that the deposition process is immune to external variation.

The sintering temperature was reduced further by adding more BCl_3 (65 sccm), which led to an appreciable increase in the level of sintering. This was indicated by a large decrease of in-plane scatter, and the elimination of out-of-plane scatter.

2.6.4 Glass film measurements

In the authors experience, the film thickness was found to vary by $\pm 5\%$ from deposition to deposition, and across each sample (3" wafer). This gave an approximate deposition rate of 1 micron per torch traversal (thickness after compaction). Problems were incurred later on in this work where the measured film thickness was less than intended. Typically a film intended to be 8 micron thick, would be 6-6.5 microns thick, an error of 25%. The error arose from a reduction in silica content within the glass, which was caused by a faulty bottle stopper on the SiCl_4 Dreschel bottle. The bottle had been recently been refilled, and due to a bad seal, this led to a reduction of pressure within the bottle during depositions, which causes a reduction in the transported halide vapour, and thus a reduction in SiO_2 content. The problem was alleviated by replacing the faulty component.

Toward the end of this work, owing mainly to increasing commercial interest in FHD, measurements were made on the birefringence of the deposited slab waveguide glass films. It was found that the refractive index difference between the TE and TM polarisations was of the order of 3.9×10^{-4} , comparable with published data on planar silica glasses [14]. This value is due mainly due to the slab nature, rather than the intrinsic birefringence due to the material, of the deposited waveguide film.

2.6.5 Recent Developments

Since the time writing began, the germanium glass system has been optimised further. This was found to be necessary due to a degradation of the deposited glass using standard techniques, occurring after a routine refill of the GeCl_4 bottle. It is thought that the degradation was due to a significant increase in the doping level of GeO_2 in the glass system, which due to the volatile nature of GeO_2 , was manifest in an increased formation of bubbles within the sintering glass.

The problem was alleviated by increasing the H₂ and O₂ flow rates, and hence the flame temperature. This results in a more compact oxide ‘soot’, hence a smaller particle size, and therefore a reduced pore size. It is known, that the pressure of a gas inside a pore is inversely proportional to the pore radius [33]. Pore closure is successful if the outside pressure due to surface tension is greater than the vapour pressure within the closing pore. Thus by depositing a more compact soot, it is conceivable that the conditions for pore closure are satisfied. It was found that subsequent depositions using high H₂ and O₂ flow rates had increased compaction (reduced scattering) and that the bubbles observed previously had been eliminated.

Recalling the “it doesn’t rain but it pours” syndrome, it was found that the depositions using higher GeO₂ doping, resulted in glass films which exhibited large, and randomly orientated cracks. These cracks are not thought to be entirely due to mismatches in thermal expansion characteristic of rapid quenching of the glass, as the cracks are large with smooth edges. Cracks arising from rapid quenching have been demonstrated to have abrupt edges [10]. This problem is illustrated in Figure 2.22.

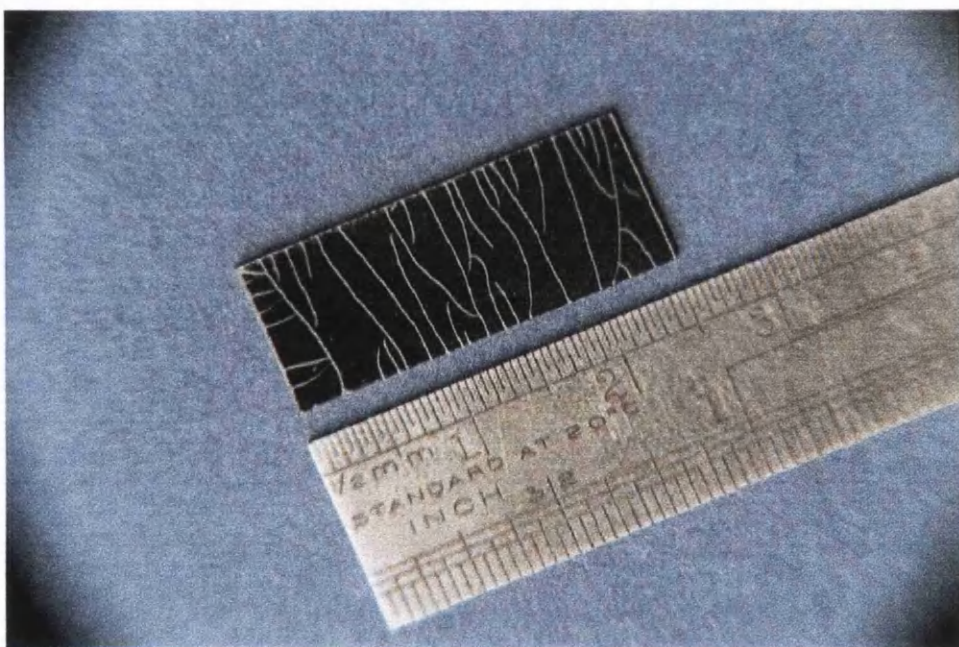


Figure 2.22 Typical example of cracking in highly doped GeO₂ films

Similar problems were experienced by Maxwell [9] in the ternary system, SiO₂-P₂O₅-GeO₂, where the author indicated that higher doping levels could be used, but only through the use of thinner layers. Barbarossa [10] also suggested that the use of

thinner layers would be beneficial in alleviating these cracks. In his analysis of the problem, the author suggested that the cracking most likely occurs as a result of the surface tension of underlying areas pulling apart the soft sintered areas of the superficial layers. The problem of cracking was solved in this work through the observations of P.V.S. Marques, where it was noticed that substrates removed straight from the hot turntable and into the furnace showed little or no evidence of cracking, whereas substrates which are allowed to cool were subject to cracking. It is suggested here that with each torch traversal each underlying layer is subjected to an increased level of partial sintering, to the extent that the underlying layers have greater structural integrity. As the substrate cools after removal from the turntable the underlying layers contract in such a way as to pull apart the softer sintered areas above, as in Ref. [10]. Cracking was only evident using high flame temperatures ($H_2:O_2$).

Now that a stable glass system has been developed, a re-calibration of the refractive index variation with $GeCl_4$ was required, as shown in Figure 2.23. This plot indicates that the GeO_2 content of the glass has increased, most likely through an increased reaction efficiency in the flame, but also through the deposition of a more compact soot, thus reducing any vaporisation of the GeO_2 content.

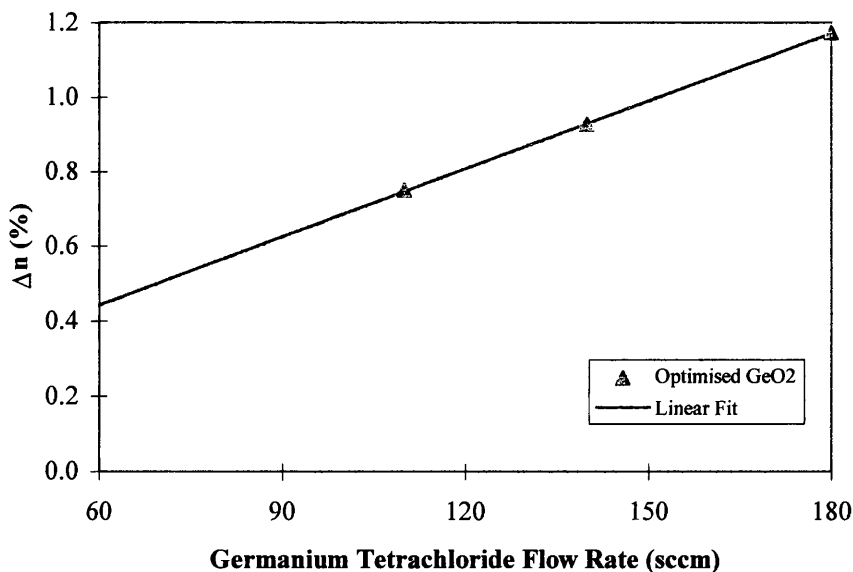


Figure 2.23 Refractive index difference with increasing $GeCl_4$ flow rate (BCl_3 65 sccm, H_2 and O_2 5 and 7 l/min respectively). This data represents a further optimisation of the deposition process. Data courtesy of P.V.S. Marques.

X-Ray Analysis of SiO_2 - GeO_2 - B_2O_3

Preliminary results taken at the University of Porto have indicated that there is no GeO_2 crystalline phase within the compacted ternary glass system. At this stage these results can best be described as interesting, but without further investigation their validity cannot be justified.

2.6.6 Photosensitivity of germanosilicate glass

It was mentioned in Section 2.3.2 that germanium doped glass is known to be photosensitive, where changes in the glass refractive index can be observed during exposure to an external UV laser beam.

Glass films fabricated using the techniques described in this thesis were tested for photosensitivity by P.V.S. Marques at the University of Porto. The glass films were hydrogenated to enhance their photosensitivity [48], and exposed through a quartz phase mask to a KrF excimer laser operating at a wavelength of 248 nm, rate of 20 Hz, and a fluence of 200 mJ/cm².

The resultant grating due to the UV exposure was monitored with increasing exposure time. Figure 2.24 illustrates the increase of the grating reflectivity as a function of the number of pulses, where approximately 13500 pulses (approximately 11 mins.) are required to obtain a grating reflectivity of 100%. Similarly, Figure 2.25 illustrates the evolution of the grating spectra as a function of exposure.

At the time of writing it is clear that the germanium doped glass developed at the University of Glasgow is suitable for fabrication of planar waveguide gratings. Work is ongoing to develop the glass system further, thus improving its characteristics in terms of optical loss and photosensitivity.

Related to the germanium photosensitivity, is the development of photosensitive phosphosilicate glasses. This has been achieved through the use of the aerosol and solution doping techniques to dope the phosphosilicate glass films with tin [49, 50]. This is of particular importance where gratings are to be incorporated with rare-earth doped lasers, where the phosphorus doping aids the incorporation of the rare-earth ions.

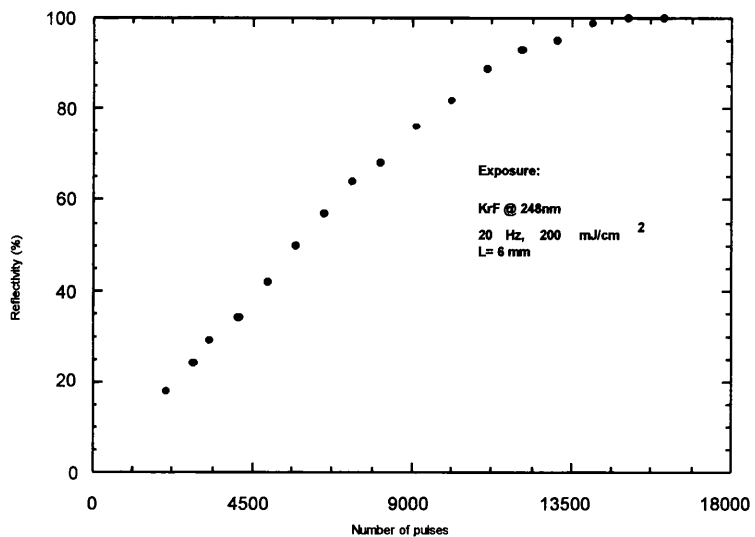


Figure 2.24 (a) Growth of grating reflectivity with time

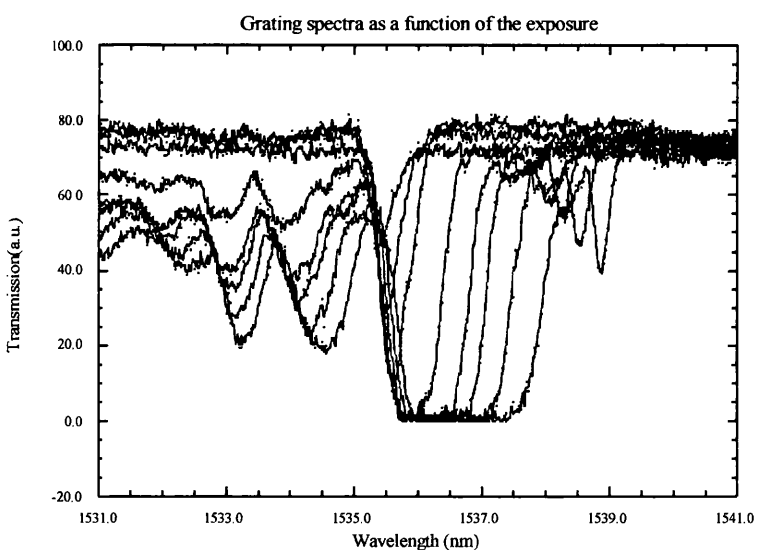


Figure 2.25 Grating spectra as a function of exposure time

2.7 Other glass systems

In this section a brief description of other glasses used or investigated is given.

2.7.1 Waveguide Cladding

The final stage in the preparation of planar silica waveguides, is the deposition of a lower refractive index cladding layer which buries the higher index waveguide core. The cladding must have a lower refractive index than the core, but the same as the thermal oxide buffer layer ($n=1.457 @ \lambda = 632.8 \text{ nm}$). The sintering temperature of this glass must also be lower than the core material (typically $>1300^\circ\text{C}$). The cladding material was formed from the ternary $\text{SiO}_2\text{-P}_2\text{O}_5\text{-B}_2\text{O}_3$, where the function of the phosphorus content is to reduce the sintering temperature, and the purpose of the boron content is to reduce the refractive index to 1.457. The parameters used follow from work on this system by Bonar [13]. Table 2.6 shows the deposition parameters. An example of an index matched buried waveguide is shown in Chapter 3, Figure 3.36.

Parameter	Setting
Silicon Tetrachloride	150 sccm
Phosphorus Trichloride	30 sccm
Boron Trichloride	65 sccm
$\text{H}_2\text{:O}_2$ Flow Rates	1:2 l/min
Furnace Temperature	1215°C

Table 2.6 Cladding deposition data

2.7.2 High temperature under-claddings

During the course of this work, problems were incurred in obtaining thermally oxidised silicon wafers ($T_{\text{ox}} > 10 \mu\text{m}$). As a matter of interest a number of depositions were made to see if it was possible to deposit a high temperature, low index buffer material. SiCl_4 , GeCl_4 and BCl_3 flow rates of 150, 20 and 50 sccm respectively were used to produce a $\text{SiO}_2\text{-GeO}_2\text{-B}_2\text{O}_3$ glass which had a refractive index of 1.457. The minimum sintering temperature of this glass was in excess of 1375°C . Subsequent core layer depositions showed no problems.

2.8 Channel Waveguide Fabrication

Optical waveguides are fabricated using a number of different techniques. The first of these is the FHD deposition of a high index waveguide core layer as described in previous sections. This is followed by photolithography where the waveguide film is patterned with a mask material such as photoresist, or in some cases a thin film metal mask. This mask material is used during reactive ion etching, to define the non-etching areas of the waveguide film, resulting in the formation of a precisely defined rib waveguide structure. The technique and application of reactive ion etching (RIE) is described fully in Chapter 3. After RIE, residual etch mask material is removed and the etched structure is buried with a thick SiO₂-P₂O₅-B₂O₃ using the parameters given earlier in this section. The final stage of fabrication involves cutting and polishing the ends of the waveguides ready for end fire coupling and testing.

2.8.1 Design of Optical Waveguide Devices

The first step in fabricating waveguides is the selection of suitable waveguide refractive indices and thickness. These parameters are selected according to the intended waveguide application using techniques such as: the effective index [46], or more accurately through the use of mode solving software such as Fwave or BPM-CAD.

Perhaps the quickest way is to follow the technique described in reference [46], where the core (n_o) is and cladding (n_c) indices are chosen. Using the plot shown in Figure 2.23, the required deposition parameters can be selected. The required film thickness, d , for a given wavelength (λ) is calculated from the expression for the normalised frequency (v) given by:

$$v = \frac{2\pi}{\lambda} d \sqrt{n_o^2 - n_c^2}$$

The normalised frequency parameter, v , is selected from Figure 2.26 according to the asymmetry parameter, a , and the and normalised guide index, b . The film thickness is obtained using approximately 1 μm per traversal as a guide to the number of traversals.

$$a = \frac{(n_s^2 - n_c^2)}{(n_o^2 - n_s^2)} \quad b = \frac{(N^2 - n_s^2)}{(n_o^2 - n_s^2)}$$

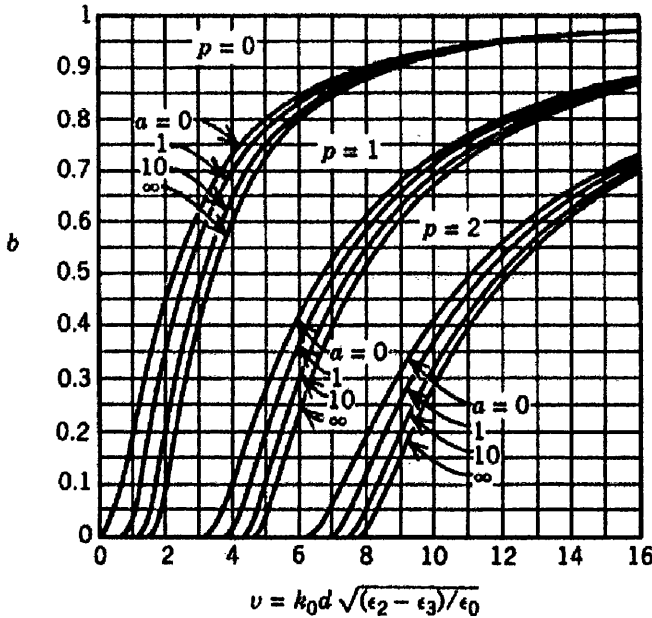


Figure 2.26 Dispersion curves for a step index planar waveguide (from [46])

2.8.2 Photolithography

Photolithography is a technique used to define an optical waveguide pattern on the surface of the FHD silica glass films. Photoresist is spun onto the glass film and exposed through a photomask to UV light. The pattern is developed and then used as a mask for subsequent RIE processing of the glass films, as described in Chapter 3.

Typically, the wafers are taken directly from the consolidation furnace and spin coated with resist primer (Hexamethyl disilazane (HMDS), 4000 rpm, 20 sec) and photoresist (Shipley S1818, 4000 rpm, 30 sec). The coated wafer is then baked at 90°C for 30 min. Exposure is performed on a Hybrid Technology Group (HTG) mask aligner for 10 secs, after which the photoresist is developed in 1:1 Shipley developer : RO water.

If the mask is to be used as an etch mask in RIE, then the sample is postbaked at 160°C for 20 minutes. If NiCr is to be used as an RIE mask, the wafers are coated with NiCr in a thermal evaporator (Evaporation rate < 0.5 nm/s) prior to the spin coat process, and the NiCr is wet etched after the photoresist development stage.

2.8.3 Nichrome Etch Masks

In order to obtain large waveguide etch depths it became necessary to use metal etch masks. Unlike the lift off technique for etch masks described by Bonar [13], the masks used here have been prepared by wet etching in a chrome etch solution.

It became apparent that sidewall roughness could be directly attributed to the technique used to deposit the NiCr films. Figure 2.27 (a) shows an SEM micrograph of a processed NiCr film, 180 nm thick, which had been deposited in a Plassys Electron Beam evaporator. Its rough appearance is in stark contrast to a similar film prepared after evaporation in a thermal evaporator, shown in Figure 2.27 (b). Also shown in Figure 2.28 (a) & (b) is the resulting etch profile after CHF₃ RIE where it is clear that the Plassys evaporated NiCr films are not suitable for silica waveguide fabrication.

It is thought that the difference in quality in the Plassys evaporated film is due to the dissimilar melting temperatures of nickel and chrome, which could result in the evaporation of a crystalline phase. Work performed by Dr A. Glidle on XPS measurements demonstrated that the composition of the NiCr film had changed from 60:40 in the bulk to 40:60 in the evaporated film.

Thus it is recommended that thermally evaporated NiCr should be used as it translates into reproducibly smooth RIE etch processing of silica waveguides

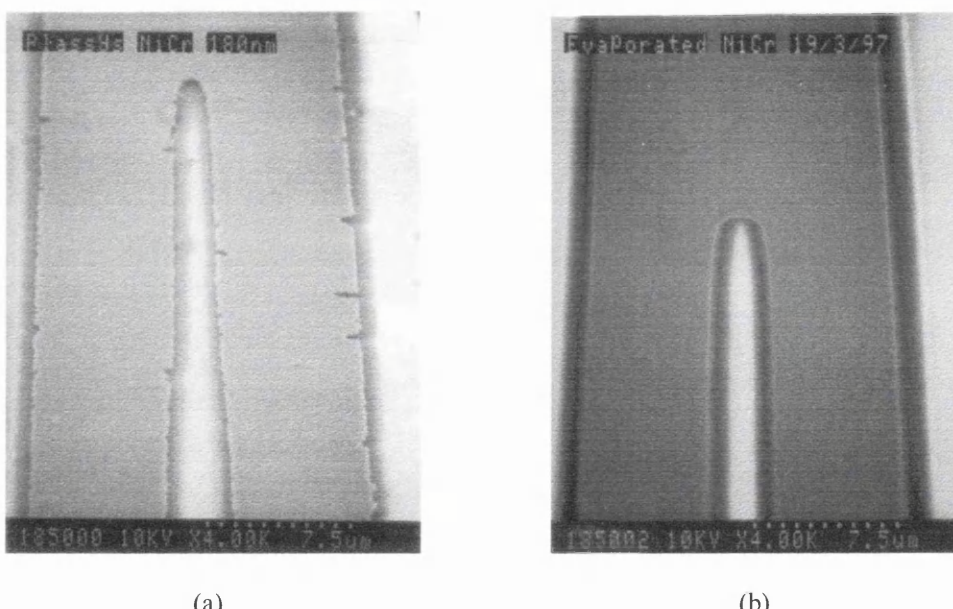


Figure 2.27 (a) Plassys Evaporation of NiCr and (b) Thermal Evaporation of NiCr

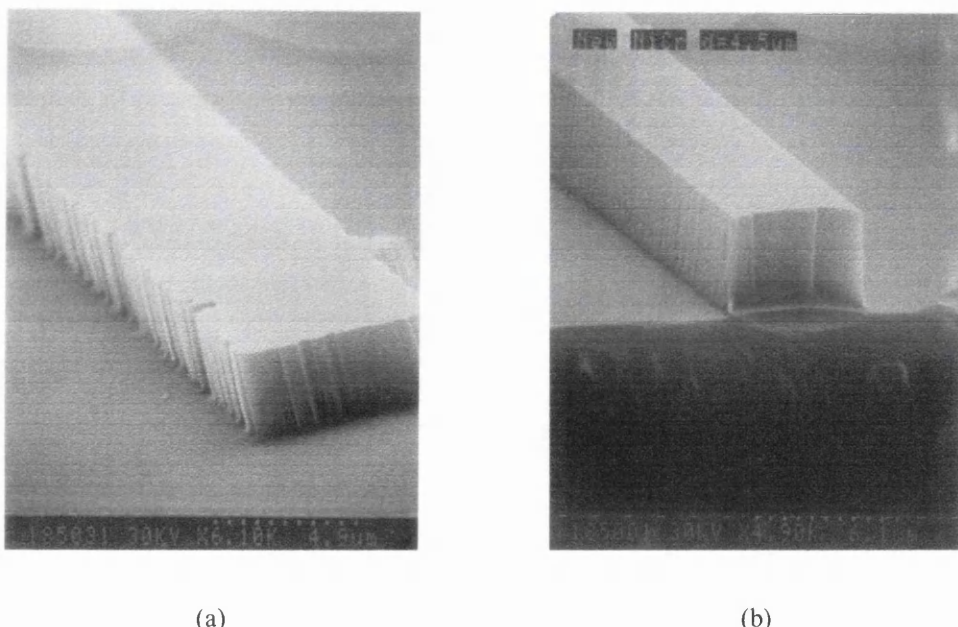


Figure 2.28 (a) Etched Waveguide (Plassys) and (b) Etched Waveguide (Thermal)

2.9 Conclusions

A description of the flame hydrolysis deposition (FHD) technique has been given, with an overview of the functions of the main pieces of equipment used in FHD and some observations on the results of each process stage. The upgrade of the FHD fabrication lab from Class 100,000 to almost Class 100 cleanroom standard has been shown to be a contributing factor in the preparation of low defect count ($<1 \text{ cm}^{-2}$) glass films.

The development of the $\text{SiO}_2\text{-GeO}_2\text{-B}_2\text{O}_3$ glass system has been presented where the importance of the B_2O_3 content has been shown in the preparation of a sintered glass film. Microprobe analysis has confirmed the relationship between refractive index and GeO_2 content. Microprobe scans have also demonstrated the high uniformity of the deposited glass films from wafer to wafer, and across a wafer surface. Glass films with a controllable relative refractive index difference of upto 1.2% have been prepared. Birefringence measurements have shown that the index change between TE and TM polarisation is of the order of 3.9×10^{-4} . The germanium doped films have also been shown to be photosensitive upon exposure to UV radiation.

The importance of NiCr etch mask evaporation techniques have been demonstrated where thermal evaporation of etch masks is preferred to electron beam evaporation.

References

- [1] J. F. Hyde, *United States Patent*, No. 2,272,342, 1942.
- [2] J.B. MacChesney, P.B. O'Connor, F.V. DiMarcello, J.R. Simpson and P.D. Lazay, Proc. *Tenth International Congress on Glass*, Kyoto, 1974.
- [3] D.B. Keck, P.C. Schultz and F. Zimar, *United States Patent*, No. 3,737,292, 1973.
- [4] T. Izawa and N. Inagaki, *Proc. IEEE*, 1980, **68**, 1184.
- [5] T. Izawa and S. Sudo, Optical Fibres: Materials and Fabrication, Tokyo: KTK Scientific, 1987.
- [6] D.B. Keck and P.C. Schultz, *United States Patent*, No. 3,806,223, 1974.
- [7] M. Kawachi, M. Yasu and T. Edahiro, *Electron. Lett.*, 1983, **19**, 583.
- [8] Photonic Integration Research Inc. (PIRI), *Product Catalogue*, Internet Address: <http://www.piri.com>
- [9] G.D. Maxwell, *PhD Thesis*, University of Glasgow, 1990.
- [10] G. Barbarossa, *PhD Thesis*, University of Glasgow, 1991.
- [11] G. Barbarossa and G.D. Maxwell, UK Patent Office Application 9202463.7.
- [12] J.A. Bebbington, *PhD Thesis*, University of Glasgow, 1993.
- [13] J.R. Bonar, *PhD Thesis*, University of Glasgow, 1995.
- [14] M. Kawachi, *Opt. & Quant. Elec.*, 1990, **22**, 391.
- [15] K.J. Beales and C.R. Day, *Phys. & Chem. Glasses*, 1980, **21**, 5.
- [16] C.R. Hammond, *Phys. & Chem. Glasses*, 1978, **19**, 41.
- [17] R. Kashyap, G.D. Maxwell, B.J. Ainslie, *IEEE Photon. Tech. Lett.*, 1993, **2**, 191.
- [18] R. Kashyap, *Opt. Fibre Technol.*, 1994, **1**, 17.
- [19] D.L. Williams, B.J. Ainslie, J.R. Armitage, R. Kashyap and R. Campbell, *Elec. Lett.*, 1993, **29**, 45.

- [20] F. Bilodeau, B. Malo, J. Albert, D.C. Johnson, K.O. Hill, Y. Hibino, M. Abe and M. Kawachi, *Opt. Lett.*, 1993, **18**, 953.
- [21] G.D. Maxwell, B.J. Ainslie, D.L. Williams and R. Kashyap, *Elec. Lett.*, 1993, **29**, 425.
- [22] J.R. Bonar, M.V.D. Vermelho, P.V.S. Marques, A.J. McLaughlin and J.S. Aitchison, *Opt. Comms.*, 1998, **149**, 22.
- [23] J.R. Bonar, J.A. Bebbington, J.S. Aitchison, G.D. Maxwell and B.J. Ainslie, *Electron. Lett.*, 1995, **31**, 99.
- [24] J.R. Bonar, M.V.D. Vermelho, A.J. McLaughlin, P.V.S. Marques, J.S. Aitchison, J.F. Martins-Filho, A.G. Bezerra, A.S.L. Gomes, and C.B. deAraujo, *Proc. ECIO'97.*, Stockholm, 1997.
- [25] J.R. Bonar, M.V.D. Vermelho, A.J. McLaughlin, P.V.S. Marques, J.S. Aitchison, J.F. Martins-Filho, A.G. Bezerra, A.S.L. Gomes, and C.B. deAraujo, *Opt. Comm.*, 1997, **141**, 137.
- [26] C.R. Hammond, *Phys. And Chem. Glasses*, 1978, **19**, 41.
- [27] T.J. Miller, E. Potkay and M.J. Yuen, *Fibre Optics: Processing and Applications*, AIChE Symposium Series, **83**, 1.
- [28] G.D. Ulrich, *Combust. Sci. and Technol.*, 1971, **4**, 47.
- [29] W.H. Gourdin and M.J. Andrejco, *J. Appl. Phys.*, 1982, **53**, 5920.
- [30] H.-C. Tsai, R. Greif and C.K. Wu, *J. Materials Processing and Manufacturing Science*, 1996, **4**, 299.
- [31] T. Edahiro, M. Kawachi, S. Sudo, S. Tomaru, *Jpn. J. Appl. Phys.*, 1980, **19**, 2047.
- [32] E. Potkay, H.R. Clark, I.P. Smyth, T.Y. Kometani and D.L. Wood, *J. Lightwave Technol.*, 1988, **6**, 1338.
- [33] Chambers English Dictionary, 7th Edition, W. R. Chambers Ltd. And Cambridge University Press, 1988
- [34] J.K. Mackenzie and R. Shuttleworth, *Proc. Phys. Soc., London*, 1949, **62**, 833.

- [35] G.W. Scherer, *J. Am. Ceram. Soc.*, 1977, **60**, 236.
- [36] J. Frenkel, *J. Phys. (Moscow)*, 1945, **9**, 385.
- [37] S.Sudo, T. Edahiro, M. Kawachi, *Trans. IEICE Jpn.*, 1980, **E62**, 731.
- [38] Private Communication with Mr I. McNicholl, University of Glasgow.
- [39] P.V.S. Marques, J.R. Bonar, A.J. McLaughlin, A.M.P. Leite & J.S. Aitchison, *Fisica '98*, 11th Physics National Conference, Porto, September 1998.
- [40] R.Kashyap, G.D. Maxwell and B.J. Ainslie, *IEEE Photon. Tech. Lett.*, 1993, **5**, 191.
- [41] E.C. Schafer and R. Roy, *Phase Diagrams for Ceramists*, Ed. E.M. Levine, 1964, 140.
- [42] G. Baret, R. Madar and C. Bernard, *J. Electrochem. Soc.*, 1991, **138**, 2830.
- [43] Y.Y. Huang, A. Sarkar and P.C. Schultz, *J. Non-Cryst. Solids*, 1978, **27**, 29.
- [44] T.J. Rockett and W.R. Foster, *J. Am. Ceram. Soc.*, 1965, **48**, 75.
- [45] G. Baret, R. Madar and C. Bernard, *J. Electrochem. Soc.*, 1991, **138**, 2836.
- [46] D.L. Lee, *Electromagnetic Principles of Integrated Optics*, John Wiley and Sons, Inc., 1986
- [47] S.J.B. Reed, *Electron Microprobe Analysis and Scanning Electron Microscopy in Geology*, Cambridge University Press, 1996.
- [48] P.J. Lemaire, R.M. Atkins, V. Mizrahi and W.A. Reed, *Electron. Lett.*, 1993, **29**, 1191.
- [49] P.V.S. Marques, J.R. Bonar, A. Glidle, A.J. McLaughlin, A.M.P. Leite and J.S. Aitchison, *Proc. QE-13*, Cardiff, 1997.
- [50] P.V.S. Marques, J.R. Bonar, A. Glidle, A.J. McLaughlin, A.M.P. Leite and J.S. Aitchison, *OSA Topical Meeting - 'Bragg gratings, photosensitivity and poling in glass waveguides and fibers; applications and fundamentals'*, Virginia, 1997

Chapter 3 Reactive Ion Etching of FHD Silica Glass Films

3.1 Introduction

Chapter 3 introduces the reader to the basic principles of reactive ion etching (RIE) and examines the use of RIE for silica waveguide fabrication. The chapter details the development of etch processes using CHF₃, C₂F₆ and SF₆ and the subsequent optimisation of the CHF₃ process through the controlled addition of O₂ to the plasma. Finally, development of a very high rate CHF₃ process is presented. Suggestions for future process optimisation can be found in Chapter 7, Conclusions.

3.1.1 Motivation

The scope of this research project was to develop existing silica waveguide fabrication technology for use in aerospace and bioelectronic sensor applications [1]. For aerospace applications, multi-mode optical waveguide devices with core sizes in excess of 10 μm would be required. Bioelectronic devices would require the fabrication of micro-fluidic handling devices with dimensions also in excess of 10 μm.

FHD is capable of producing thick silica films (~200 μm [2]), however practical limitations are imposed by the relatively slow RIE post-processing of thick films. The starting point for this work was a previously developed CHF₃ plasma process [3], which had an etch rate of 1.8 μm per hour. For single-mode waveguide (>6 μm) production, process times of around 4 hours were commonplace.

3.1.2 Specification for an optimum etch process

In order to develop a new process, a number of factors must be taken in consideration:

- Glass etch rate
- Glass to etch mask selectivity
- Sidewall anisotropy (and in some cases control)
- Low sidewall and surface roughness
- Etch uniformity
- Process reproducibility
- Low chamber contamination

The aim of this work is to optimise the glass etch rate in order to reduce the RIE processing time required for each device, whilst maintaining a high selectivity over the etch mask. The combination of these factors permits deep silica etching. The process should also result in smooth etched surfaces and anisotropic sidewalls, key factors in reducing optical insertion losses of the finished device. Finally, the process should be clean and easily reproducible in that the variations across a wafer and from run to run are minimised.

3.2 RIE Fundamentals

Reactive Ion Etching (RIE) is a plasma-based dry etching technique characterised by a combination of physical sputtering with the chemical activity of reactive species. Plasma etching was adopted by the microelectronics industry during the early 1970s [4] as it offered etch directionality and accurate pattern transfer in a clean process, all in an automation compatible process - a factor synonymous with mass production [5].

Figure 3.1 shows a schematic of the Oxford Plasmatechnology RIE80 reactive ion etching machine used during process development. This type of reactor consists of a pair of capacitively coupled parallel electrodes in a low pressure chamber, typically ranging from 0.01 to 1 Torr. The material to be etched is placed on the lower electrode, or cathode. A suitable feed gas is fed into the chamber above the top electrode.

Many gases have been used to etch silica films including CF_4 [6], C_2F_6 [7] and CHF_3 [8]. In the case of fluorocarbon etching, it is generally considered that the CF_3^+ ion is largely responsible for etching SiO_2 , with the formation of the volatile etch product SiF_4 . It is possible however to use other fluorine based gases such as F_2 and SF_6 [9], where the fluorine ion is generally regarded as the etchant species, however this is generally at the expense of selectivity and/or anisotropy as detailed later on.

What follows is a summary of the processes occurring within an RIE etch system [10].

A plasma exists when there are equal numbers of positive and negative charged species within the etch chamber. Such a condition occurs when a high-frequency voltage

(13.56 MHz) is applied across the parallel electrodes. The feed gas undergoes a number of processes such as electron-impact dissociation and ionisation which creates radicals, positive and negative ions, electrons and neutrals. The result is known as a glow discharge. This can be observed as the coloured region of Figure 3.1. (Illustration courtesy of Dr S. E. Hicks)

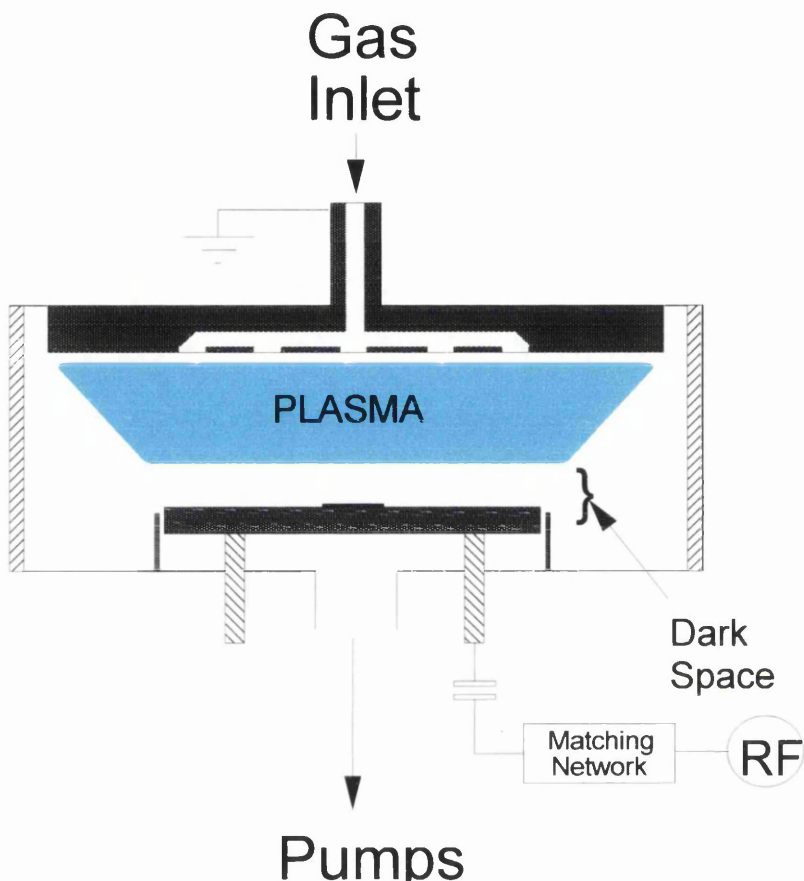


Figure 3.1 Schematic diagram of RIE Chamber.

As electrons have a much higher mobility than the ions, the lower driven electrode quickly acquires a negative charge, leaving the plasma positive. A boundary region, known as the ‘sheath’ or ‘dark space’, occurs between the plasma and the lower electrode, across which there is a potential, commonly referred to as the self-bias voltage. The motion of ions within the plasma is random, however as positive ions drift toward the ‘dark space’ they begin to accelerate under the presence of the dc bias.

The reactive radicals adsorb onto the surface of the material to be etched. This step is followed by a chemical reaction on the surface to form volatile etch products, or their

precursors. The ongoing ion bombardment of the surface enhances the reaction of the adsorbed radicals thus accelerating the etch process.

A critical step in the etch process is the desorption of the etch product into the gas phase. This relies on the etch product having a relatively high vapour pressure at the substrate temperature, which in RIE is typically room temperature.

The volatile etch products are subsequently pumped out of the chamber. If this stage is unsuccessful, the desorbed products can redeposit on the etch surface.

3.3 Preliminary Investigations

3.3.1 Increasing the RF Power in CHF_3 RIE

As mentioned in the introduction, the aim of this work was to increase the etch rate of the low pressure/low flow rate RIE process developed previously [3]. An example of a typical etched waveguide is illustrated in figure 3.2. The obvious way to achieve this, at the time, was to increase the RF power, although with hindsight this was a rather naïve and simplistic approach to take.

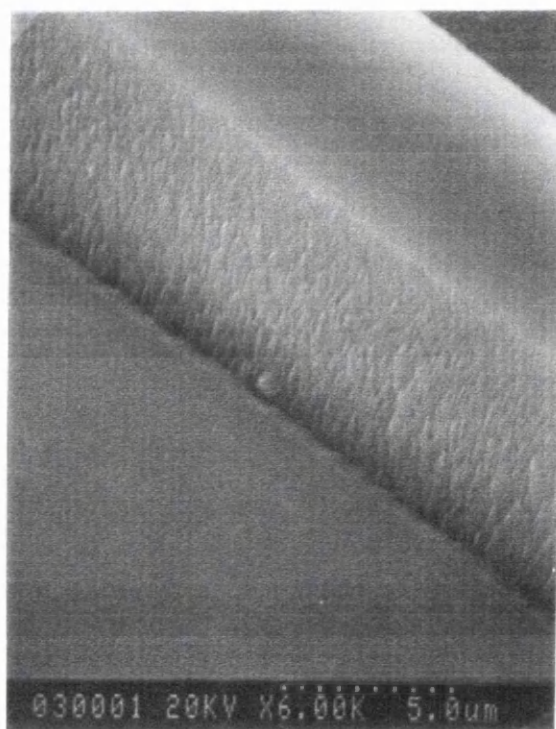


Figure 3.2 Typical etch waveguide using previously developed process (from [3]).

Typically, an increase in RF power leads to an increase of material etch rate [8]. Increased RF power gives rise to a larger voltage drop, and hence an intensified ion bombardment of the material being etched, which in turn increases the etch rate. A number of etch tests were carried out with increased RF power in conjunction with etch mask refinement as described in Chapter 2. The RIE parameters used are illustrated in Table 3.1.

Etchant Gas	CHF ₃	CHF ₃	CHF ₃	CHF ₃
Flow Rate (sccm)	8	8	8	8
Pressure (mtorr)	6.8	6.8	6.5	6.5
RF Power (W)	100	100	140	140
dc Bias (-V)	430	430	510	510
Etch Time (hr x4)	1	1	1	1
Mask	Thin S1818	Thick S1818	Thin S1818	Thick S1818
Glass Etch Rate	1.83	1.93	2.2	2.4

Table 3.1 RIE parameters for preliminary investigation.

Increasing the RF power increased the dc self-bias of the process, from -430 V at 100 W to -510 V at 140 W. This increase was reflected in the increase of the glass etch rate from around 1.8 $\mu\text{m}/\text{hr}$ to 2.4 $\mu\text{m}/\text{hr}$. From the SEM images in Figures 3.3 (a-d), it is clear that by increasing the RF power only, a dramatic effect on the etch profile of the resulting waveguide structures can be observed. This is a consequence of increased resist mask erosion with power, where thicker masks are preferable.

By studying RIE etch technology, it becomes clear that interactions between parameters exist. Simply increasing the RF power increases the degree of dissociation of the feed gas and quite possibly, on the evidence presented here, increases the amount of reactive species in the plasma, i.e. increases the etch rate of the glass and the mask. As will be discussed later on, an important factor in successful fluorocarbon etching of glass is now missing: polymer protection of the sidewalls. As the feed gas flow rate has remained the same at 8 sccm, there is not sufficient CHF₃ to dissociate and form both polymeric and reactive species. Similarly, the pressure has not been adjusted, and as such the likelihood of interactions between species in the plasma is low, thus decreasing the likelihood of creating polymer forming species.

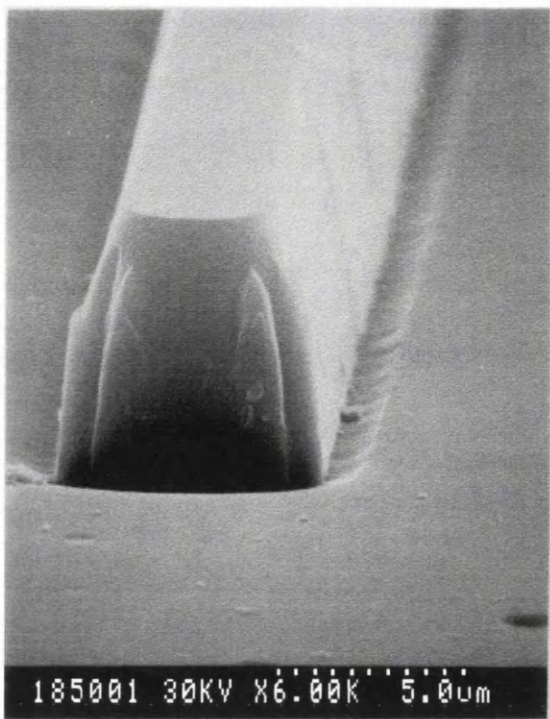


Figure 3.3(a) Low RF Power CHF₃; thin S1818

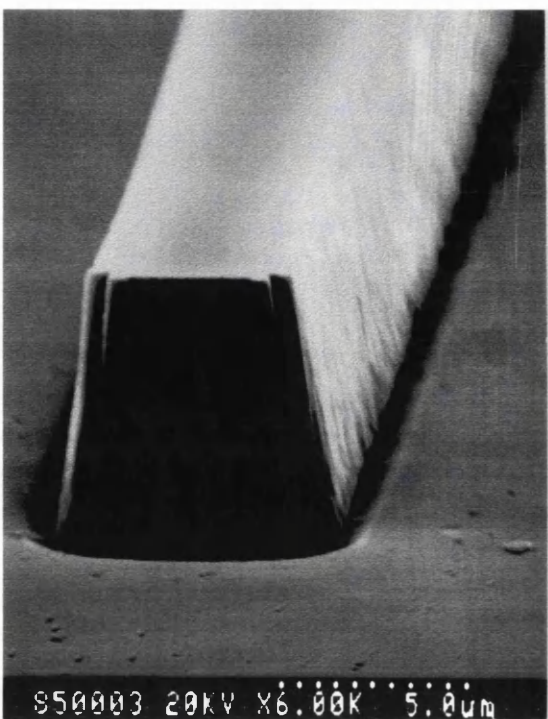


Figure 3.3(b) Low RF Power CHF₃; thick S1818

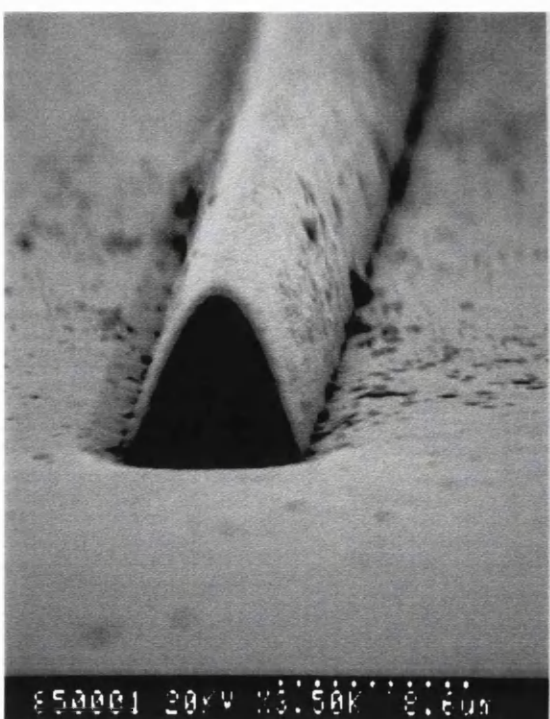


Figure 3.3(c) High RF Power CHF₃; thin S1818

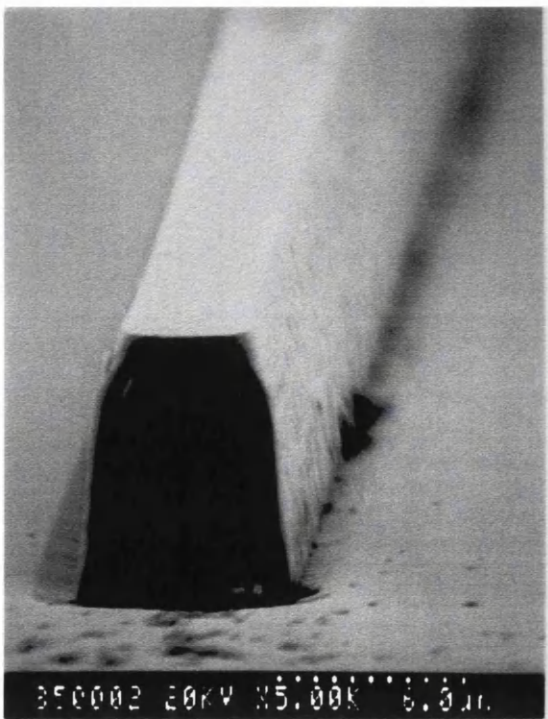
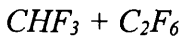


Figure 3.3(d) High RF Power CHF₃; thick S1818

3.3.2 Other Etch Processes



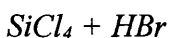
An etch based upon CHF_3 and C_2F_6 had been tested previously [3] using photoresist as an etch mask. However, due to the reactive nature of this process the mask was entirely removed after 30 minutes. To investigate this process further, a sample was metallised with 250nm of evaporated nichrome as an etch mask as described in Chapter 2. Samples were also prepared with resist masks. The etch parameters and the results of the etch tests are shown in Table 3.2.

Etchant Gas	$\text{CHF}_3/\text{C}_2\text{F}_6$	$\text{CHF}_3/\text{C}_2\text{F}_6$	$\text{CHF}_3/\text{C}_2\text{F}_6$
Flow Rate (secm)	45/24	45/24	45/24
Pressure (mtorr)	32	32	50
RF Power (W)	150	190	190
dc Bias (-V)	N/A*	510	510
Etch Time (mins)	30	60	60
Etch Rate ($\mu\text{m/hr}$)	5.6	6.6	6.6

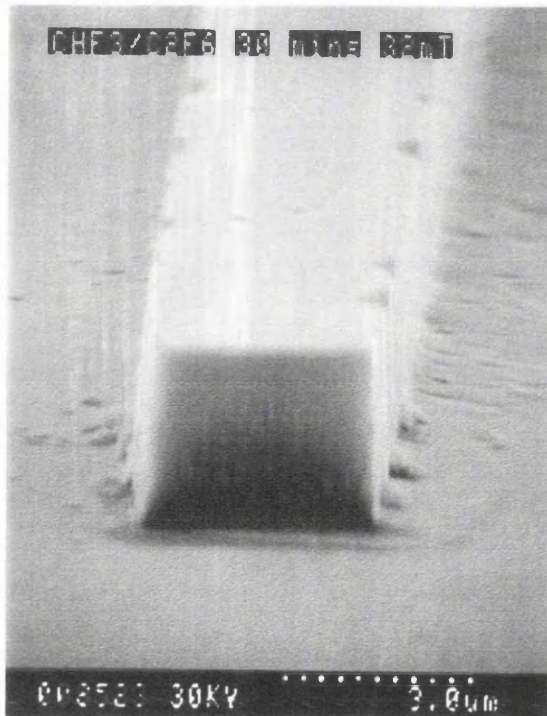
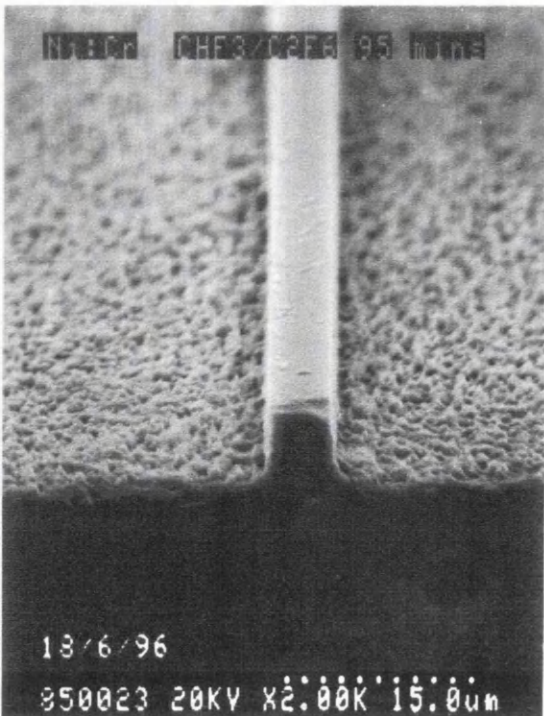
Table 3.2 RIE parameters for preliminary investigation.

* No value of the dc Bias was recorded on the etch run log sheet

It was observed that the resist mask was completely removed by the end of the etch runs, and that the nichrome masks had almost completely been removed, indicating a NiCr mask etch rate of approximately 250 nm/hr. From the SEM images of Figure 3.4 (a-b) we can see that the etch process results in a vertical etch profile. At the time of this work, the mask development process (see Chapter 2) was ongoing, as reflected in the poor sidewall quality. Another problem, illustrated by Figure 3.4 (b), is the presence of micromasking, where NiCr has sputtered and redeposited on the etching surface.



Another process was investigated, which used SiCl_4 and HBr. This process been developed within the department for the purpose of deep *silicon* etching, however, no appreciable etch rate of the silica glass could be observed.

Figure 3.4 (a) $\text{CHF}_3/\text{C}_2\text{F}_6$ Sidewall profileFigure 3.4 (b) $\text{CHF}_3/\text{C}_2\text{F}_6$ micromasking

Summary of Preliminary Work

Whilst it was encouraging to see an increased etch rate in the CHF_3 process with increasing RF power, it was clear from the increased mask and sidewall erosion that more work would be required before a suitable etch process could be found which would be capable of etching large structures with high selectivity and good sidewall quality.

This was also the case with the $\text{CHF}_3/\text{C}_2\text{F}_6$ process, where a high etch rate could be obtained, but only through the use of a nichrome etch mask, a step which will be shown later to be a worthwhile improvement.

3.4 Development of CHF₃, C₂F₆ and SF₆ RIE processes

The results from the work presented in the previous section clearly show that the development of a new RIE process presents a much more complex problem than had been originally envisaged. As a result, it was decided that a more rigorous approach to this work had to be undertaken.

This section reports on the use of CHF₃[11], C₂F₆ and SF₆ as etch gases for deep reactive ion etch processing of SiO₂ based glass films prepared by flame hydrolysis deposition (FHD) [12]. The scope of the study was to identify the benefits and drawbacks of each gas for fabrication of deep structures (>10 µm).

As the objective of the study was to develop an optimised process for each gas, three main goals were selected from the list in section 3.3:

- high FHD glass etch rates,
- high mask selectivity and
- low sidewall damage.

The study examined how selection of reactive ion etch parameters such as etchant gas, etchant gas flow rate, pressure and forward RF power, influence the RIE characteristics of FHD glasses and the potential masking materials.

Deep etching: A published history

Deep etching of silica glass films is not a very well published field. The author found a small number of previous reports, for example using C₂F₆ in electron cyclotron resonance reactive ion beam etching (ECR-RIBE) [13,14,15], and CHF₃/Ar in hollow cathode reactors [16,17]. A detailed analysis of ECR and hollow cathode reactor etching can be found within reference [10]. More recently results have been published on the use of Inductively Coupled Plasma (ICP) machines for deep silica etching [18]. Within the department there exists an ECR capability, however during the course of this research the ECR system remained non-operational.

Investigated Factors

Flow Rate: The gas flow rate allows the control of the feed gas, e.g. CHF₃, into the etch chamber. Too low a flow of gas will mean that there is insufficient material to break down and form a glow discharge. Too high a flow, and there may not be enough time to break down the feed gas, and if there is, there may be a strong dominance of one species over another. The flow rate also places restrictions on the maximum and minimum pressures obtainable in the chamber.

Pressure: The etch pressure determines the level of interaction within the plasma. For example a high pressure would reduce the mean free path for charged particles, thus encouraging the likelihood of an ionisation event within the plasma, possibly leading to an increase in etch rate. Conversely, this increase in residence time could increase the production of polymer forming species. A lower pressure can increase the mean free path, and reduce the likelihood of interactions occurring, thus decreasing the likelihood of etching, possibly favouring polymer deposition. The pressure has a major effect upon both the size of the sheath between the plasma and the electrode, and the magnitude of the potential (dc bias) across it.

RF Power: This has an effect on the dissociation of the feed gas. A low power would, break it down to a lesser degree than at a high power, which in turn would imply that there maybe more, or less, reactive or neutral species within the plasma, dependant on the ionisation potentials of the feed gas products. At high powers the feed gas would have more kinetic energy, possibly increasing the number of ionisation processes, increasing the sheath potential and the ion bombardment energy.

3.4.1 The Experiment

Preparation

A germano-boro-silicate glass film was formed by flame hydrolysis deposition, using the procedure described in Chapter 2. The film composition was estimated by Microprobe analysis to be 83 wt% SiO₂, 12 wt% GeO₂ and 5 wt% B₂O₃. The thickness was measured by prism coupling and found to be ~8 µm. A diamond saw diced the wafer into a sufficient number of pieces for process characterisation.

Prior to each etch test, the etch chamber was pre-conditioned with a 15 minute oxygen clean to remove any thin film contamination on the inner grounded surfaces of the etch chamber. Thin film contamination is more than likely fluorocarbon based, as suggested by Oehrlein [10]. The presence of such films can significantly alter the etching characteristics of the plasma through two processes:

- The electrical characteristics of the chamber change as there is a change in the powered/grounded electrode area ratio through insulation of the chamber walls.
- The chemical characteristics of the plasma change as there can be interactions through consumption/recycling by interaction of the film with reactive species.

Experimental Range

As mentioned earlier, the machine used in these etch tests was an Oxford Plasmatechnology RIE80 etching machine.

The machine had 2 mass flow controllers (MFC) for fluorine based feed gas delivery, where the quoted maximum flow rate for CHF₃ was 50 sccm (in reality 45 sccm), and 20 sccm for both C₂F₆ and SF₆. The flow rate was varied in the range 0-max for all feed gases. During pressure and RF power tests the flow rates were set to 20 sccm.

The pressure was varied in the range 25-100 mtorr where the maximum was determined by the feed flow rate. The pressure was adjusted to 50 mtorr during flow rate and RF power tests.

The forward RF power was varied in the range 50-190 W. The maximum power was generator, rather than machine limited (the machine can be operated at a maximum of 300 W). It was possible to borrow a more powerful generator (250 W) in the latter stages of this work, however this required that another machine was removed from service for the duration of the etch tests. An RF power of 190 W was selected for the pressure and flow rate tests, as more power is generally regarded as beneficial in etching silica based materials.

3.4.2 Results

Process Development

CHF₃ Development

The FHD glass etch rate increased with increasing RF power, as shown in Figure 3.5, above a threshold of 50 W, below which deposition of a thin film was evident. The photoresist mask etch rate decreased with increasing RF power, whereas the etch rate of the nichrome mask increased with increasing RF power, as did the dc bias. The FHD glass etch rate was also found to increase with pressure before saturating above 50 mtorr, as shown in Figure 3.6. Above 50 mtorr a thin film was visible on the etched surface of the sample. The photoresist mask etch rate decreased with increasing pressure whereas the nichrome etch rate remained constant. The dc bias did not vary with pressure. Figure 3.7 illustrates that the glass etch rate increases with increasing flow rate with the maximum etch rate occurring at around 20 sccm. The etch rate was found to decrease as the flow rate increased beyond this point. The optimal process was obtained when the RF power, pressure and flow rate were set to 190 W, 50 mtorr, and 20 sccm respectively. The mask selectivities and glass etch rate using this process are illustrated in Table 3.3.

The increase in glass etch rate (GER) due to increasing RF power can be explained by two factors. Increasing the power generally increases the dissociation of the feed gas, which most likely leads to the creation of more reactive species, which could be backed up by the reduction of thin film formation above 50 W. It is well known that thin film deposition and etching are competitive processes, and from these results, this appears to be the case, as there was an observed threshold to etching. As the RF power increases there is also an increase in the kinetic energy of the ionised plasma species. This can be observed as an increase of dc bias with rf power.

Increased GER's due to increased pressure is also to be expected. Increasing the pressure within the chamber increases the residence time of the feed gas within the chamber, thus increasing the likelihood of dissociation. Increased pressure also decreases the mean free path of the particles within the plasma, which can lead to an increase the likelihood of ionisation processes. However, at too high a pressure, the domination of thin film deposition could be observed, where there was also a decrease

in the GER, as evidenced by Figure 3.6, where the etch rate fell to zero at high pressures and samples were found to be contaminated.

An increase in the flow rate can also increase the GER as there is an increase in the level of feed gas available for dissociation. However increasing the flow rate too much can lead to a reduction in the GER, as there is a reduction in the residence time for the feed gas within the chamber, reducing the likelihood of dissociation and ionisation of the feed gas.

C₂F₆ Development

In C₂F₆ the etch rate of the FHD glass was found to increase with RF power, Figure 3.5, with no observed threshold for etching. The nichrome etch rate also increased as did the dc bias, whereas the photoresist mask etch rate was observed to decrease. From Figure 3.6 we can see that the FHD glass etch rate increased with pressure before saturating above 25 mtorr. The photoresist mask etch rate was found to decrease whereas the nichrome mask etch rate remained constant, again with no change in dc bias. Due to insufficient data in Figure 3.7, it can only be inferred that C₂F₆ is required to etch silica glass. Intuitively we can expect the glass etch rate to drop with increasing pressure for the reasons explained under CHF₃ development. The etch process was optimised where the RF power, pressure, flow rate and dc bias were set to 190 W, 25 mtorr, 20 sccm and -500 V respectively. The mask selectivities and glass etch rate using this process are illustrated in Table 3.3.

SF₆ Development

Using SF₆ the etch rate increased rapidly with increasing RF power, before saturating above 100 W as shown in Figure 3.5. The etch rate of the nichrome mask also increased with RF power, as did the dc bias, however a high photoresist mask erosion rate was evident which increased with RF power. The etch rate of the FHD glass also increased with pressure as shown in Figure 3.6, however the etch rate of the nichrome mask decreased, as did the dc bias. Again the photoresist mask erosion was high and increased with pressure. A thin film was evident on the sample at pressures >50 mtorr and at RF powers >190 W. As was the case with the C₂F₆ flow rate, Figure 3.7 only illustrates that SF₆ is required to etch the glass. The FHD glass etch rate and nichrome selectivity were optimised when RF power, pressure, flow rate and dc bias were set to

190 W, 100 mtorr, 20 sccm and -130 V. The mask selectivities and FHD glass etch rate using this process is presented in Table 3.3.

Gases	FHD Glass Etch Rate ($\mu\text{m/hr}$)	Nichrome (nm/hr)	Photoresist ($\mu\text{m/hr}$)	Sidewall Profile of FHD Glass	Fused silica Etch Rate ($\mu\text{m/hr}$)
CHF_3	5.6	60	0.5	Vertical	3.5
C_2F_6	5.8	150	2	Vertical	5.1
SF_6	7.7	77*	3.9	Undercut	6.5

Table. 3.3. Performance of developed CHF_3 , C_2F_6 and SF_6 etch processes for deep reactive ion etching of flame hydrolysis deposited silica glass films. * The lowest NiCr etch rate measured was 50 nm/hr (GER of 7.1 $\mu\text{m/hr}$) which gave a selectivity of 142:1.

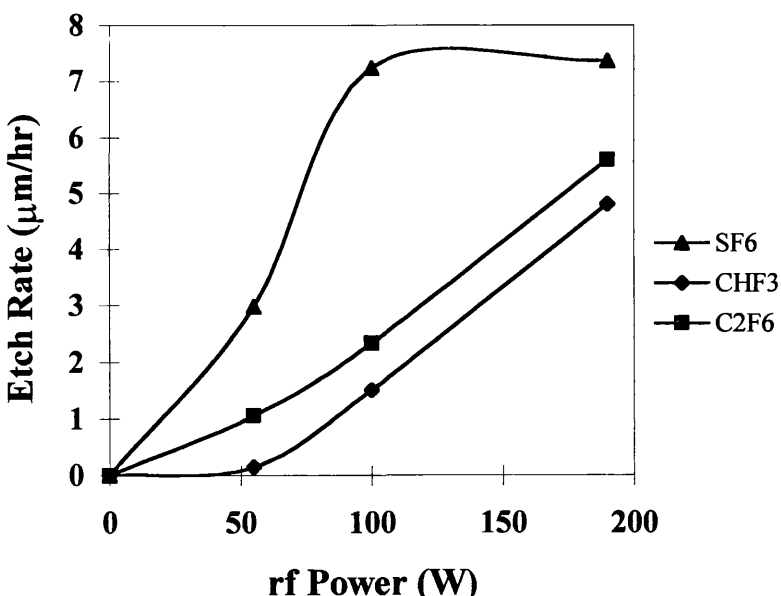


Fig. 3.5. Etch rate of flame hydrolysis deposited glass as a function of forward RF power in CHF_3 , C_2F_6 and SF_6 (Pressure 50 mtorr, flow rate 20 sccm). Thin film deposition was evident above 100 W in SF_6 and below 50 W in CHF_3 .

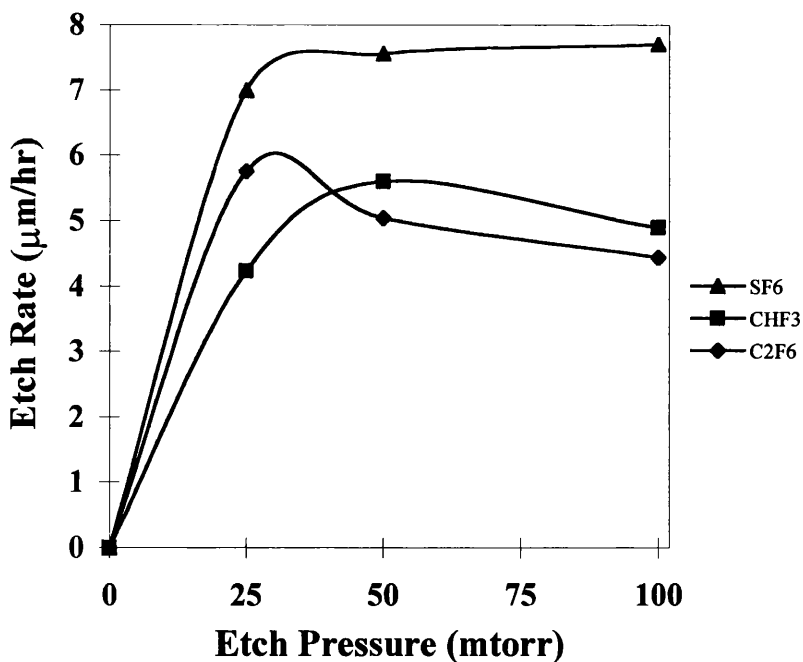


Fig. 3.6. Etch rate of flame hydrolysis deposited glass as a function of etch pressure in CHF₃, C₂F₆ and SF₆ (RF Power 190 W and flow rate 20 sccm).

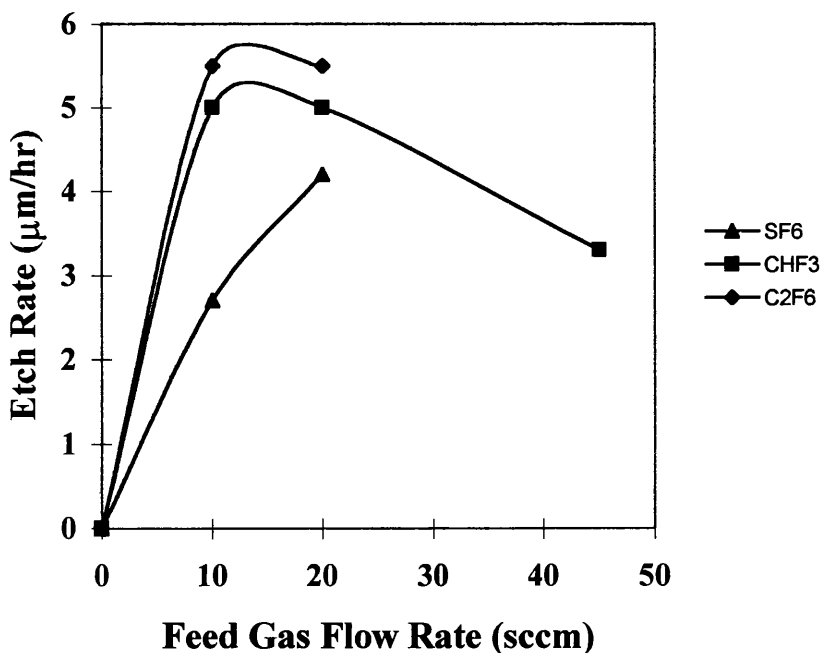


Fig. 3.7. Etch rate of flame hydrolysis deposited glass as a function of feed gas flow rate. (Pressure 50 mtorr, RF Power 190 W).

3.4.3 Assessment of Developed Processes

Sidewall Profile

Samples were prepared with nichrome masks and etched using the optimised processes described in Table 3.3. From the micrograph of Figure 3.8 it can be observed that the CHF₃ process results in a vertical etch profile with no lateral erosion. A similar sidewall profile can also be observed under C₂F₆ etching, Figure 3.9. This lack of lateral erosion indicates the presence of polymer protection of the sidewalls, typical of etching in fluorocarbon etch gases [17]. Sidewall erosion was evident using SF₆ as shown in Figure 3.10. The lateral erosion can be explained by the obvious lack of fluorocarbon protection of the sidewalls. This erosion was minimised under conditions where the dc bias was high.

Sidewall Roughness

The amplitude of sidewall corrugation was estimated by scanning electron microscope investigation to be less than 150 nm using all etch processes, indicating that the sidewall roughness is mask, rather than process limited (confirmed by figures 2.27 and 2.28 In Chapter 2). Additional sidewall roughness is observed when multiple etch runs are performed. This is illustrated in figure 3.11 where a number of lines can clearly be observed along the waveguide. These lines correspond to the number of etch runs carried out, in this case four. This phenomenon has two possible explanations:

- The etch runs are stopped periodically to allow for chamber conditioning, as there is a considerable buildup of a thin film on the chamber walls. There is also, as mentioned above, a thin film on the waveguide walls. During the conditioning step, the samples are exposed to air, which is thought could oxidise this thin film, which could contribute to increase sidewall roughness.
- The bias drops during the etch process, thus the chamber needs cleaned. Possibly, the increase in dc bias during the next etch run serves to damage the metal mask through a sputtering process.

Comparison of Etch Rates with Fused Silica

Fused silica samples were prepared with nichrome masks and etched in the optimised processes to standardise each process as a means of comparison of the FHD glass etch properties. In C_2F_6 and SF_6 RIE the fused silica and FHD glass etch rates were found to drop by only 12 and 13% respectively, whereas in CHF_3 the etch rate was found to fall by 37 %. This illustrates that doped silica glass has a higher etch rate than pure SiO_2 .

Surface Roughness

Any process where a surface is bombarded by reactive ions and neutrals can cause damage in the form of surface roughness. The surface roughness of the samples were measured using the DekTak surface profiler and in all cases the average surface roughness, R_{av} , was found to be less than 10 nm, which was less than the vertical resolution of the machine.

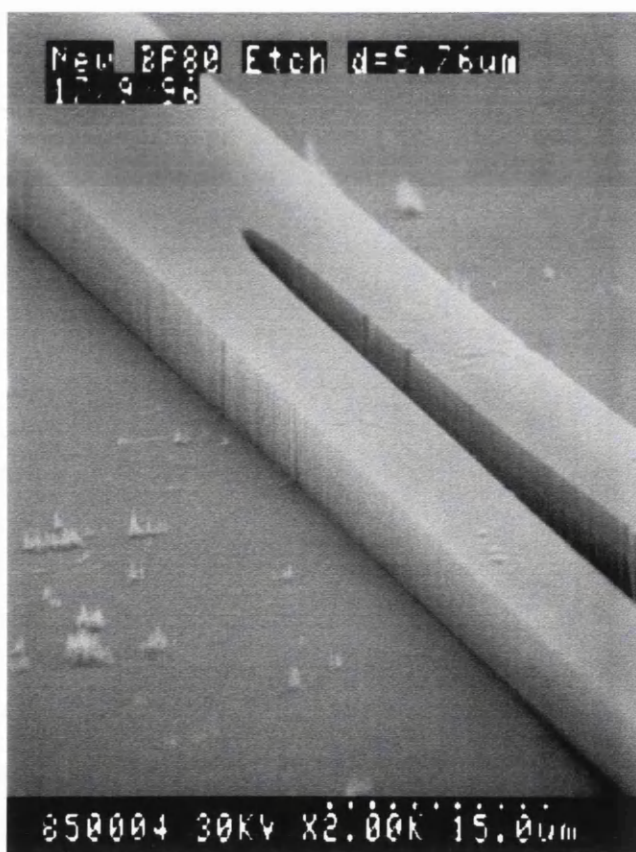


Figure 3.8 FHD glass etch profile using CHF_3 RIE and a thermally evaporated nichrome mask. Note the vertical profile and low lateral erosion of the sidewalls. The etch depth is $5.76\mu\text{m}$.

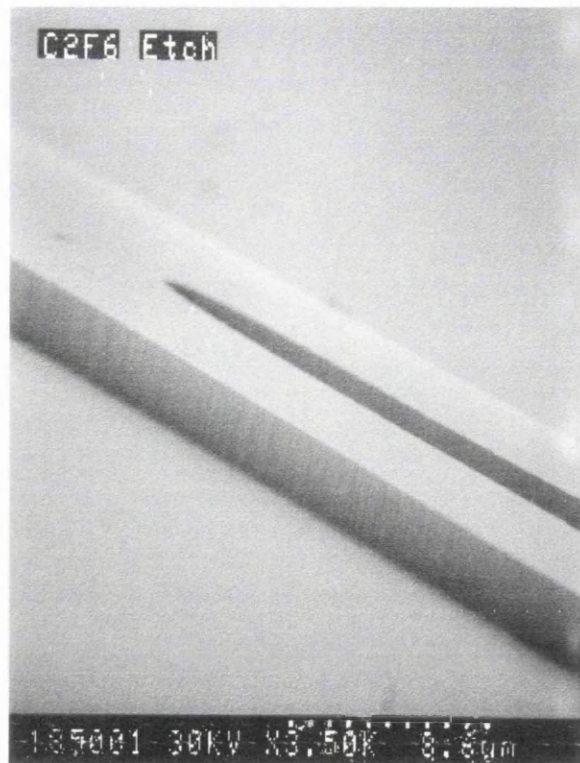


Figure 3.9 FHD glass etch profile using C_2F_6 RIE and a NiCr mask. The etched depth was 5.5 μm .

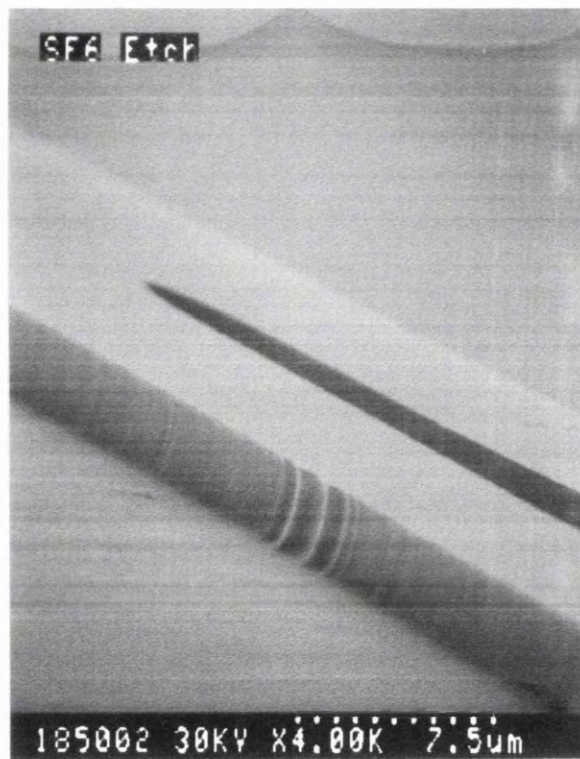


Figure 3.10 FHD glass etch profile using SF_6 RIE and a nichrome mask. Of note is the defect in the mask which illustrates the lateral erosion of the sidewall. The etched depth was 3.9 μm .

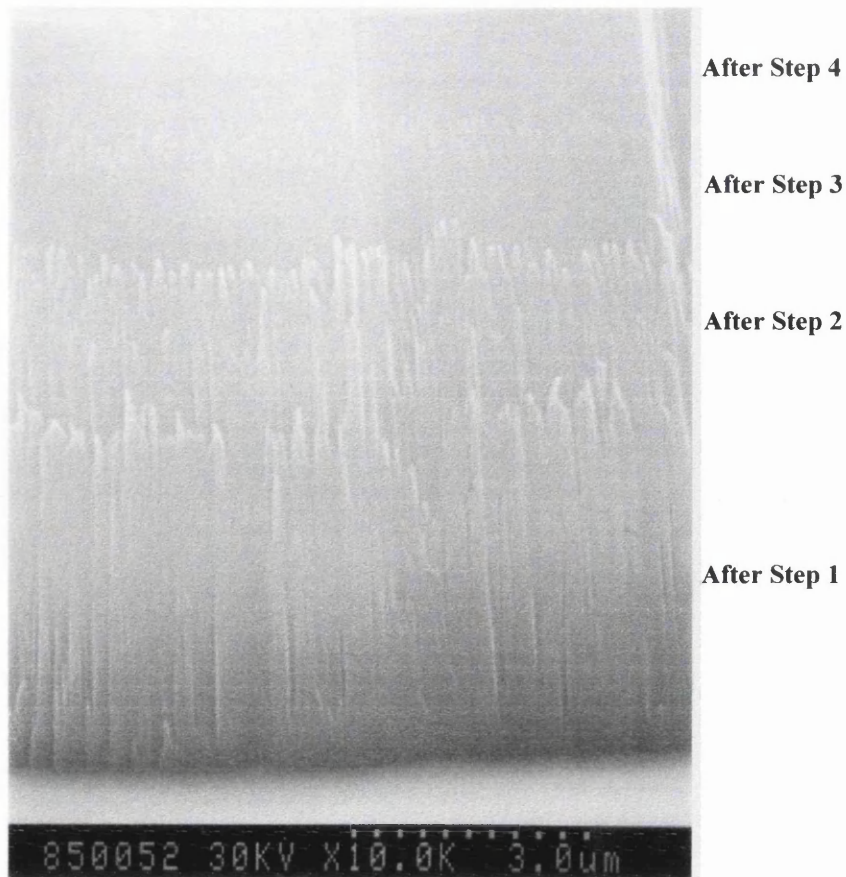


Figure 3.11 SEM image showing the stepped etch profile evident after a multi step CHF_3 plasma process.

3.4.4 Comparison between the developed processes for deep etching

It is clear from the results presented in Table 3.3 that nichrome masks are preferable to photoresist for deep RIE of FHD glass because of the enhanced mask:glass etch rate selectivity, particularly in the case of SF_6 where the nichrome etch rate is very low. The nichrome etch rate is bias, and therefore ion energy dependant, as illustrated by the bias under SF_6 etching of only -130 V, compared to -500 V in CHF_3 and C_2F_6 .

From the results presented here we may deduce that fluorocarbon deposits play an important role in enhancing the mask:glass etch rate selectivity by protecting the mask surface from erosion. We suggest that this is the reason the photoresist mask etch rates were lower in C_2F_6 and CHF_3 RIE than SF_6 RIE. Previous studies have shown that selectivity can be improved through the inclusion of hydrogen in the fluorocarbon process, for example in CHF_3 [19] or through H_2 addition to CF_4 [20]. This is confirmed by the fact that the mask:glass selectivity is higher with CHF_3 compared to

C_2F_6 processing. A fluorocarbon film protects the mask surface as well as the etched sidewalls reducing (or eliminating) the degree of lateral erosion. However, we have observed that too much fluorocarbon deposition leads to a grossly contaminated chamber resulting in a decrease in etch rate with time. Therefore a compromise between mask protection and high etch rates must be found dependant upon the application.

From the work presented here, it is clear that CHF_3 RIE is the most suitable process for deep and vertical etching of FHD glass as it exhibits a high mask:glass etch rate selectivity and results in vertical sidewalls. Figures 3.12 and 3.13 illustrate deep etching in CHF_3 with etched depths of 11 and 14 μm respectively. SF_6 RIE, although having a high etch rate and attractive mask:glass selectivities, suffers from a high degree of undercutting. In optoelectronic applications, this would result in excessive optical losses and a large polarisation sensitivity. Although C_2F_6 RIE of FHD glass results in vertical profiles, it suffers from a low mask:glass etch rate selectivity which limits the depth attainable.

3.4.5 Summary

In summary, the implications for deep etching ($>10 \mu\text{m}$) of flame hydrolysis deposited silica glass using CHF_3 , C_2F_6 and SF_6 as etchant gases have been presented. From the experimental data obtained, CHF_3 presents the most versatile etch process, in terms of FHD glass etch rate and high selectivity over both photoresist and nichrome. However higher etch rates are obtainable with the other etchant gases at the expense of selectivity, and in the case of SF_6 , sidewall quality. Furthermore, it has been illustrated that SF_6 has a high selectivity over nichrome, which could be exploited by using a CF_x ($x \leq 2$) producing gas for increased sidewall protection.

The CHF_3 process, whilst having the lowest etch rates, has the highest mask selectivity. On this basis it is the recommended process for deep waveguide etching. However, it is a dirty process, and as such requires further optimisation. The C_2F_6 process, owing to its high rate of mask erosion, is more suited to single mode waveguide fabrication, using a NiCr etch masks. The SF_6 process is unsuitable for use in waveguide fabrication, however the lateral erosion encountered may be advantageous in fabrication fluid handling channels in bioelectronic applications [21].

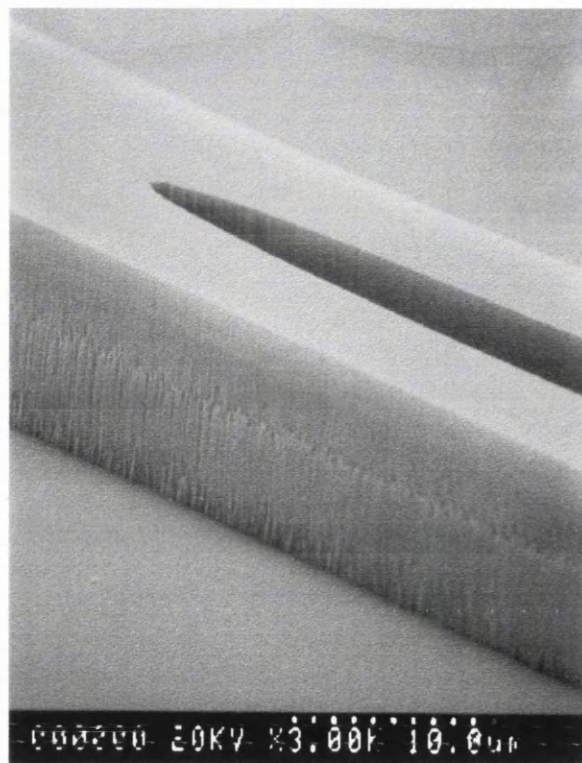


Figure 3.12 Deep etch profile after 2 hours using developed CHF_3 process, etched depth 11 μm .

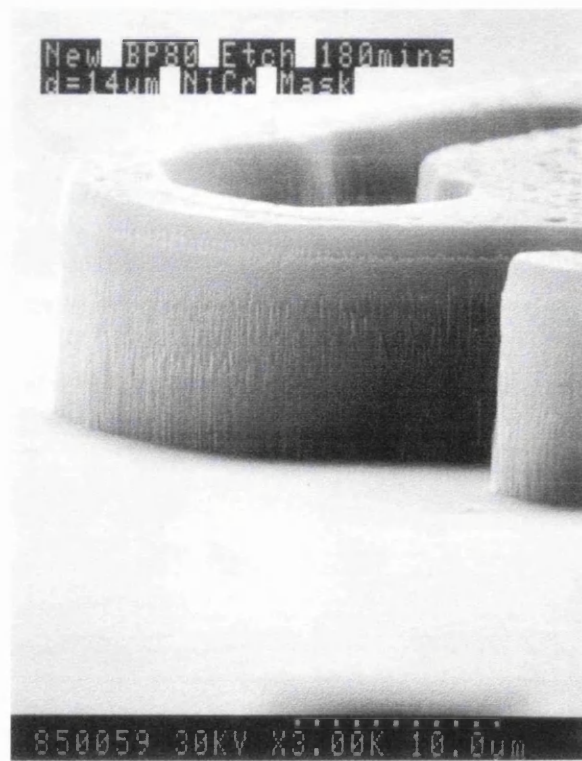


Figure 3.13 Another illustration of deep etching, to a depth of 14 μm .

3.5 CHF₃ Optimisation

From the work of Section 3.6, it was evident that CHF₃ proved to be the most versatile etch process, as it readily could etch deep profiles, >10 µm, using any etch mask material, however it is still limited by the low rate and dirty nature of the process. From this point, four investigations were performed:

- Interaction experiments: flow rate v's pressure, RF power v's pressure
- Investigation of the influence of dc Bias
- Oxygen addition to CHF₃ plasma processes
- Robust process development by Taguchi experimental design (Section 3.8)

3.5.1 *Interaction Experiments: flow rate v's pressure, RF power v's pressure*

It is known, both intuitively and from experimentation, that the parameters involved in RIE, e.g. flow rate, pressure and RF power, can interact with each other. In this study the aim is to optimise these parameters to obtain the key desires of Section 3.3. To achieve this we need to investigate what the major factors in the experiment are, which up to this point is what we have been doing. However, it is also important to know how the factors vary with each other, or in other words interact. It may be the case that as two parameters are varied simultaneously, their combined effect may influence the desired output more so than the individual parameter on its own.

What follows is an examination of the variation of etch rate through the interaction of flow rate (A) and RF power (B), with increasing pressure.

(A) *Variable Pressure & Flow Rate, Fixed RF Power*

In this experiment the RF power was kept constant at 190 W, the etch pressure was varied from 0 to 100 mtorr at a flow rate of both 20 and 45 sccm. The results of the experiment are illustrated in figure 3.14. We can clearly see that there is an interaction between flow rate and pressure. In the case of the higher flow rate, 45 sccm, the etch rate of the glass was lower, and large levels of thin film formation were observed within the etch chamber. In particular, at 100 mtorr, the surface of the sample was

heavily contaminated with a thin film, more than likely a fluorocarbon film, and after mask removal, it was found that this film was 284 nm thick!

Clearly from these results for an optimum etch rate at 190 W we require a flow rate of 20 sccm and an etch pressure of 50 mtorr. This of course is the developed CHF₃ process from Section 3.5.

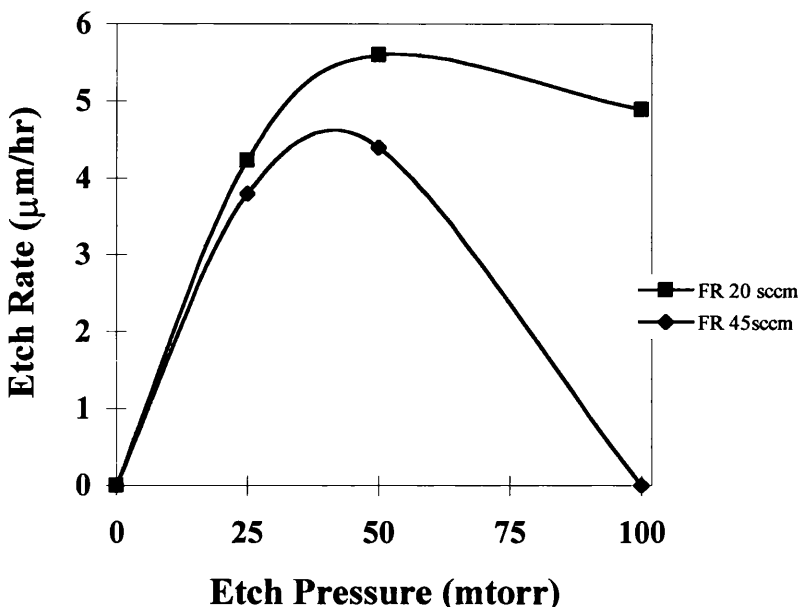


Figure 3.14 Etch Pressure variation, Flow Rate of 20 and 45 sccm, at an RF power of 250 W.

(B) Pressure v's RF Power

The flow rate during this experiment was maintained at 20 sccm, after which the pressure was varied from 0 to 100 mtorr at RF power levels of 190 W and 250 W. The experimental data is plotted in figure 3.15. The plot indicates that there is little interaction between pressure and RF power. However, the saturation of the plots at high pressure suggests that this maybe a gas flow rate limited process, as there maybe insufficient feed gas for increased reactive or neutral product formation.

This experiment is similar to every other experiment in that the optimum etch rate at 190 W occurs with a flow rate of 20 sccm and an etch pressure of 50 mtorr. The experiment also shows the importance of higher RF powers, and as will be shown in the next section, a high dc bias.

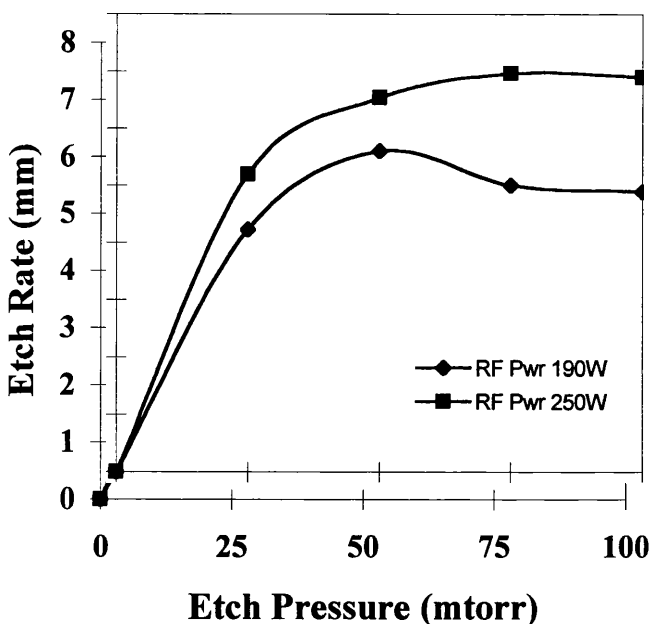


Figure 3.15 Etch Pressure variation, Flow Rate of 20 sccm, RF power set at 190 W and 250 W.

3.5.2 *Investigation of the influence of dc Bias*

We are unable to further increase the pressure or flow rate, therefore higher etch rates can only be obtained through the use of another different etch parameter. One parameter, thus far neglected, is that of the self bias voltage obtained between the plasma and the base electrode, upon which the material to be etched is placed. Whilst we are unable to vary this parameter directly, it can be varied by other means, for example by varying the pressure or by varying the RF power. In the case of Figure 3.15 at 250 W, the bias dropped with increasing pressure from -560 V to -470 V. Figure 3.16 illustrates the variation of FHD glass etch rate with increasing dc bias. In this case the bias was increased by increasing the RF power applied to the system from 50 to 250 W at a constant flow (20 sccm) and pressure (50 mtorr).

This obvious variation with bias led us to investigate another etching machine, the ElectroTech ET340. Unlike the RIE80 etching machine used in the previous section which has floating potential sidewalls, this machine has earthed sidewalls, which increases the self bias voltage of the discharge. The machine is illustrated schematically in figure 3.17. (Schematic courtesy of Dr S. E. Hicks)

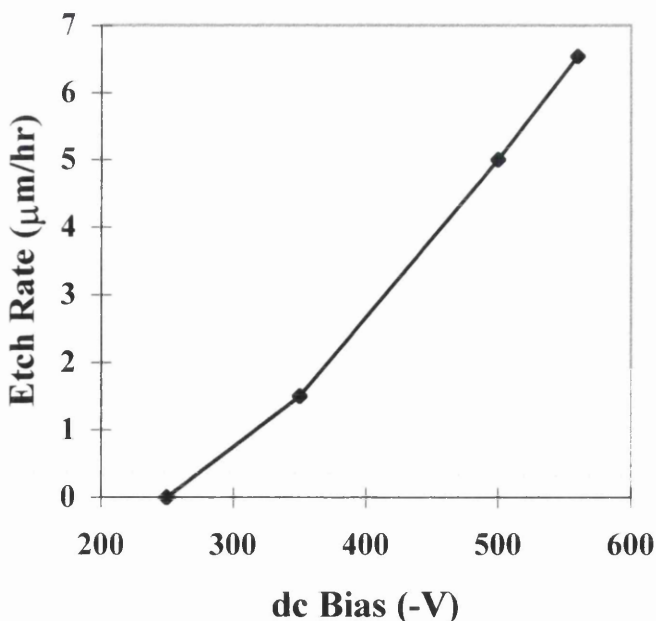


Figure 3.16 Variation of glass etch rate with increasing dc bias.

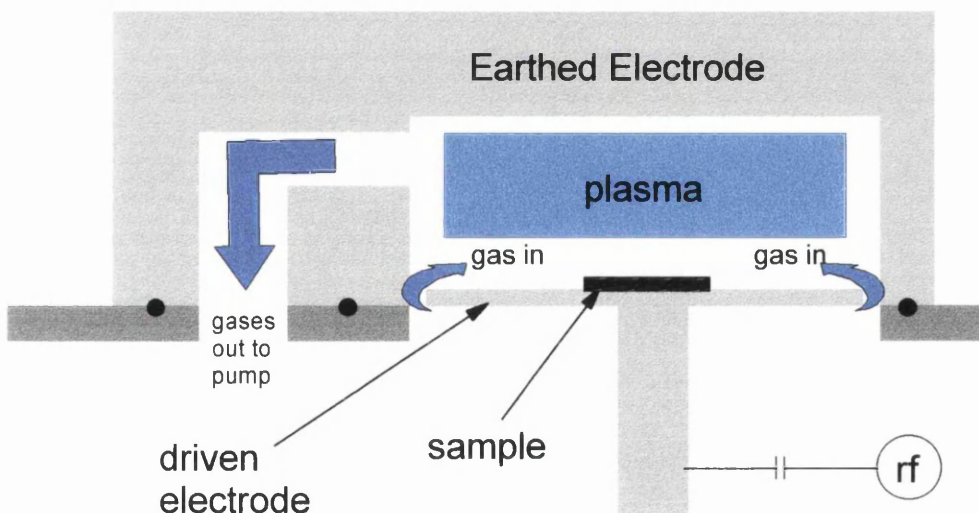


Figure 3.17 Schematic of the ElectroTech ET340 etching machine.

As in the previous sections, the etch rate of the FHD glass was studied as a function of RF Power, Etch Pressure and Flow Rates. The only feed gas under examination was CHF₃ as this was the only fluorine containing gas available on the machine.

Etch tests were limited to 10 minutes as the machine was quite heavily used, and the CHF₃ processes were also shown badly contaminate the chamber sidewalls. As a

result, the etch rates presented are scaled with time in compare the etch rates with those obtained with the RIE80 machine . Samples were prepared with resist masks.

Effect of Pressure

The glass etch rates were measured as a function of pressure over the range 25-120 mtorr with a fixed low rate of 20 sccm and an RF power of 190 W. The measured dc bias was found to be -815 V. The results of this test are illustrated in Figure 3.18 where we can see that the etch rate clearly increases with increasing pressure. A significant problem was noted after the 10 minute etch tests at 190 W in that there was complete removal of the resist mask, except at 25 mtorr where the mask etch rate was found to be in excess of 5 $\mu\text{m}/\text{hr}$. At 125 W the mask etch rate averaged 2.9 $\mu\text{m}/\text{hr}$.

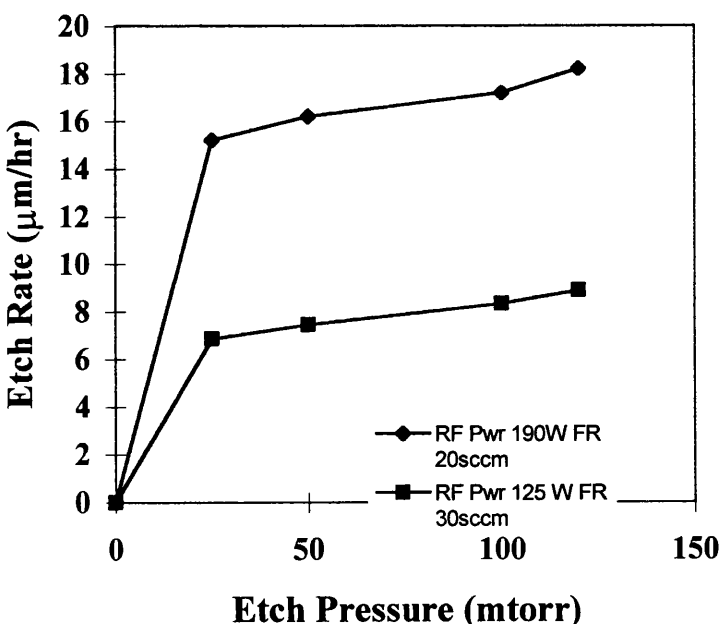


Figure 3.18 Variation of glass etch rate with pressure at an RF power of 190 W and 125 W.

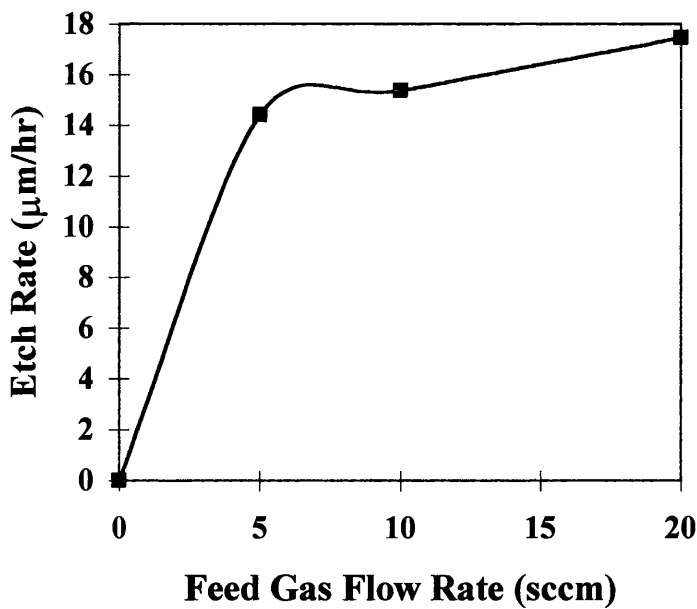


Figure 3.19 Variation of glass etch rate gas flow rate, with RF Power 190 W, etch pressure 50 mtorr.

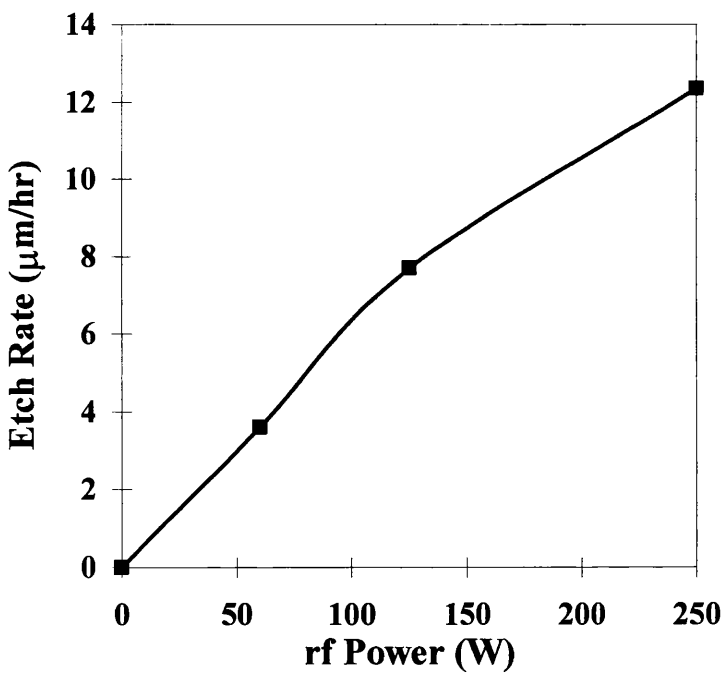


Figure 3.20 Glass etch rate as a function of RF power, gas flow rate set at 20 sccm and etch pressure 50 mtorr.

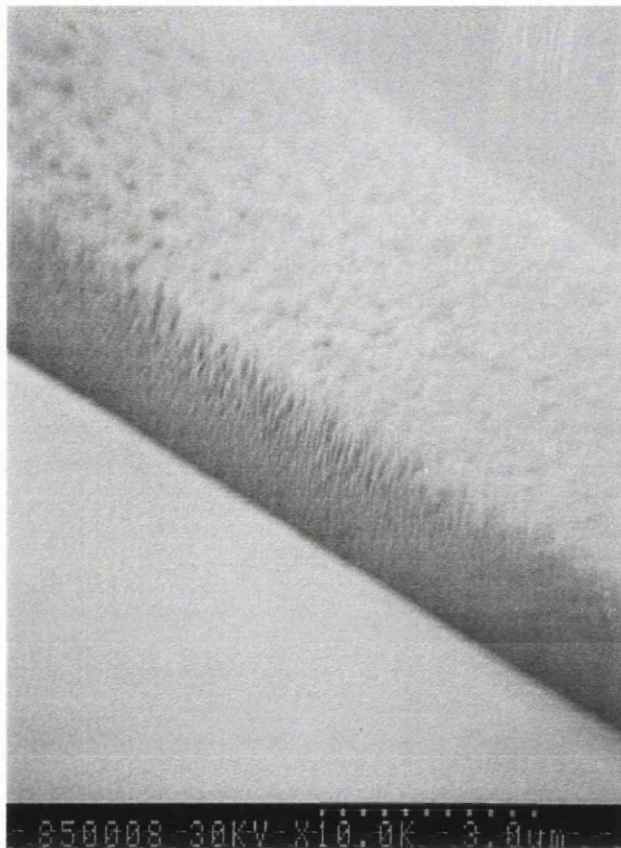


Figure 3.21 SEM image illustrating the mask damage inflicted after 10 minutes etch in ET340.

Effect of Pressure cont.

At both power levels a maximum glass etch rate was obtained at 120 mtorr. At 190 W this was estimated to be 18.2 μm in one hour. This is based upon an etch depth of 3.04 μm in 10 minutes with complete removal of the resist mask observed, as illustrated by the damage in Figure 3.21. As a result the etch rate could be higher as the mask erosion rate is unknown. At 125 W the glass etch rate was estimated to be 8.9 $\mu\text{m}/\text{hr}$ with a resist mask erosion rate of 2.94 $\mu\text{m}/\text{hr}$. Again this is based upon 10 minute observations where the glass etch depth was measured at 1.48 μm with a residual mask thickness of 1.31 μm , (1.8 μm at start). It should be noted that the etch rate increased with increasing pressure at 125 W, whilst the mask etch rate remained constant. The dc Bias fell with increasing pressure from -820 V at 25 mtorr to -630 V at 120 mtorr. This possibly suggests increased feed gas dissociation, as there are more species in the plasma which could contribute to increased etch rate, even at the reduced dc Bias. The lower mask erosion also suggests that the mask is getting the same level of protection with increasing pressure, however it was noted that CHF_3

processes are very dirty regardless of the etch conditions, so it is irrelevant whether or not there are more thin film forming species.

Effect of Feed Gas Flow Rate

At the outset of the project the maximum flow rate of CHF₃ was MFC limited to 20 sccm. The flow rate was subsequently varied over the range 5 -20 sccm, with an RF power of 190 W and constant pressure of 50 mtorr. Figure 3.19 illustrates that the etch rate increases with increasing flow rate, however as was the case with pressure total mask erosion was encountered after 10 minutes, thus the etch rates are estimated. The maximum etch rate was estimated to be 17.46 μm in one hour, based upon an etch depth of 2.91 μm after 10 minutes. As before, the unknown mask erosion rate tells us little about what the true etch rate is.

Effect of RF Power

By doubling the RF power the estimated glass etch rate increased from 3.6 to 7.7 to 12.36 $\mu\text{m}/\text{hr}$, see Figure 3.20. This corresponds to an increase in dc Bias from -530 to -730 to -950 V. It is worth noting that under similar etching condition on the BP80, an RF power of 50 W would give little or no etch rate, however a dc Bias of -510 V would give an etch rate of around 5 $\mu\text{m}/\text{hr}$, compared to 3.6 $\mu\text{m}/\text{hr}$ here, possibly confirming the concept of bias, rather than RF power dependence. Again the etch rates are based upon etch depths measured after 10 min, however in this case the mask etch rates were obtainable as total mask erosion was not encountered. The mask etch rates rose from 1.4 $\mu\text{m}/\text{hr}$ at 60 W to 2.52 $\mu\text{m}/\text{hr}$ at 125W to 7.62 $\mu\text{m}/\text{hr}$ at 250 W.

Further Work on the ET340

It was clear from the results of these tests that for a maximum etch rate we ideally want a high RF Power and a high flow rate. However from the results of pressure variation at 125 W it was clear that it may be possible to create an etch which had not only a high glass etch rate, but also a low mask erosion etch rate.

The Mass Flow Controller (MFC) was changed to increase the maximum flow rate from 30 sccm to 70 sccm. This also allowed a greater range of pressure variation.

In the first instance four etch tests were carried out at 250 W, at a low flow rate (30 sccm) and at a high flow rate (70 sccm), under which conditions, two pressure levels were tested. The results of these tests are tabulated in Table 3.4.

Conditions	Flow Rate (sccm)	Pressure (mtorr)	RF Power (W)	dc Bias (-V)	Glass Etch Rate (μm/hr)	Mask Etch Rate (μm/hr)
Low Flow Low Pressure	30	50	250	980	11.22	6.6
Low Flow High Pressure	30	90	250	850	12.96	7.8
High Flow Low Pressure	70	100	250	800	14.1	6
High Flow High Pressure	70	200	250	650	13.9	4.8

Table 3.4 Variation of pressure under low and high flow rates at 250 W.

At low flow, a 15% increase in the etch rate of the mask and the glass was observed by doubling the pressure. At the higher flow rate, a small decrease in the glass etch rate was observed, with a 20% decrease in the mask etch rate. As the dc Bias dropped with increasing pressure, we can infer that the etch rates have changed due to change in the plasma chemistry, rather than the drop in ion energy associated with the dc bias. It was also noted that the ET340 chamber was badly contaminated after the etch runs.

Conditions	Flow Rate (sccm)	Pressure (mtorr)	RF Power (W)	dc Bias (-V)	Glass Etch Rate (μm/hr)	Mask Etch Rate (μm/hr)
Low Flow Low Pressure	30	50	125	820	6.86	6.6
Low Flow High Pressure	30	100	125	720	8.9	7.8
High Flow Low Pressure	70	100	125	660	4.6	1.3
High Flow High Pressure	70	200	125	630	4.7	0.66

Table 3.5 Variation of pressure under low and high flow rates at 125 W.

As had been shown in the previous section, the etch rates of the glass, and more notably the photoresist mask was much lower when the RF power was reduced. At this point there was more interest in developing an etch process which would compete with the existing CHF₃ process on the BP80. As a result the same etch tests were performed at 125 W. The results of these tests are illustrated in Table 3.5.

Similar to the last section the etch rate increased under low flow conditions, with an increase of 15% and 22% for the mask and glass respectively. At 70 sccm, the glass etch rate was not found to vary, however the mask etch rate was found to fall by 50%

ET340 Etching with NiCr Etch Masks

Four samples were prepared with nichrome masks, and etched under the same conditions as in the previous section, except at 190 W RF power. In this case we were unable to measure the etch rate of the masks under high pressure conditions due to substantial buildup of a thin film on the samples. The results are tabulated in table 3.6.

Conditions	Flow Rate (sccm)	Pressure (mtorr)	RF Power (W)	dc Bias (-V)	Glass Etch Rate ($\mu\text{m/hr}$)	Mask Etch Rate (nm/hr)
Low Flow Low Pressure	20	50	190	894	13.6	250
Low Flow High Pressure	20	100	190	776	NA	NA
High Flow Low Pressure	70	100	190	774	9.2	500
High Flow High Pressure	70	200	190	602	15.5	NA

Table 3.6 Etch Rates of glass and nichrome mask with variation of pressure under low and high flow rates at 190 W.

From the data, it is apparent that a low flow rate and low pressure are preferable conditions, as they result in a high glass etch rate and a low mask etch rate, and as shown in Figure 3.22 results in a vertical profile. Conversely, the high flow, high pressure process results in a lower etch and poorer sidewall quality as shown in Figure 3.23. It is true however that the perspective of the images do not give this impression.

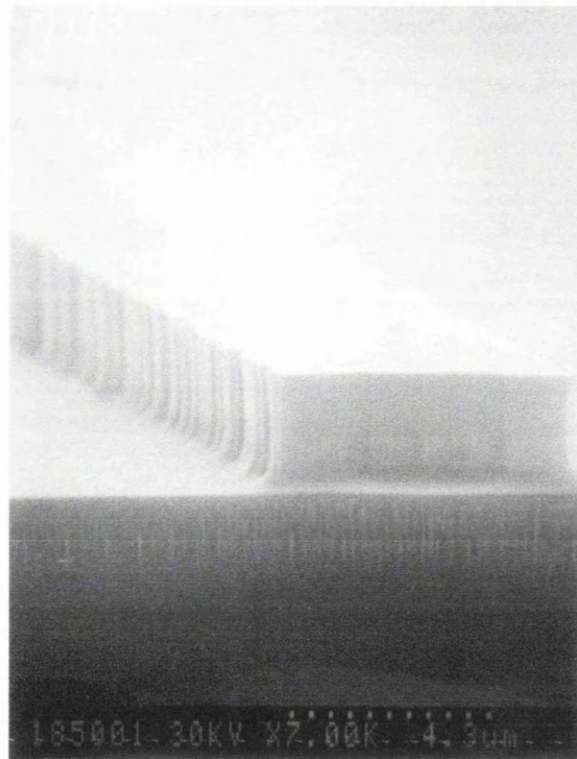


Figure 3.22 Vertical profile from the low CHF_3 flow rate, low pressure process.

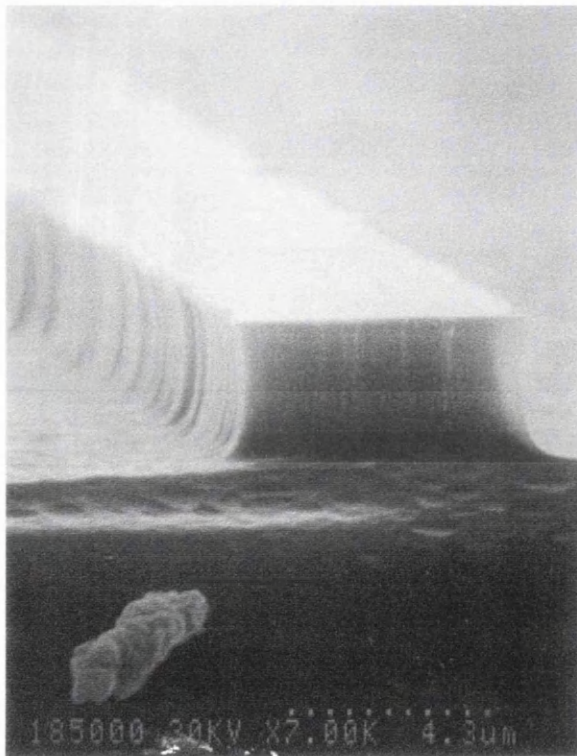


Figure 3.23 Undercut profile from the high flow, high pressure CHF_3 process.

3.5.3 Oxygen Addition to CHF₃ Plasma Processes (RIE80)

It is well known that the addition of gases to plasmas can enhance etch processing, for example: CH₄ to C₂F₆, H₂ to C₂F₆ and Ar to CHF₃ [10]. In general the additive gas increases the etch rate of the material, increases the selectivity over the mask material or helps to increase the efficiency of feed gas dissociation.

It is also known that controlled addition of oxygen to CHF₃ processes can reduce the dirty nature of the etch process [10]. This happens as the oxygen scavenges for and oxidises carbon based molecules within the plasma. This can lead to a reduction of the level of thin film formation, through a reduction in polymer forming CF_x (x<3) molecules. However, the decrease in CF products can also lead to an increase in free atomic fluorine, and a decrease in the level of protection afforded to the sidewalls and mask by polymer deposition. This decrease in CF products can manifest itself in the form of increased mask and sidewall erosion.

To investigate the effects of oxygen addition a simple test was carried out. Two GBSG samples were prepared with NiCr masks and etched under the conditions listed in Table 3.7.

Conditions	Flow Rate (sccm)	Pressure (mtorr)	RF Power (W)	Etch Time (mins)	Comments
Standard Process	20	50	190	2 x 30	Process interrupted for O ₂ chamber clean after 30 minutes
Standard plus Oxygen	20	50	190	2 x 30	2 sccm (10%) of O ₂ introduced during CHF ₃ etch process

Table 3.7 Etch Parameters in the controlled addition of oxygen to CHF₃ etch process

The main objective in this test was to investigate the influence, if any, of O₂ on the etched sidewalls. The standard CHF₃ RIE process was the process developed in Section 3.6. After the first 30 minute etch run the process was interrupted and the etch chamber was conditioned with an oxygen plasma clean (30 minutes, 100 W, 21 mtorr, 30 sccm O₂). Normally the sample is removed at this point as resist etch mask oxidised. In this work samples have nichrome masks, which would remain largely untouched by the O₂ process, and as such were left in the chamber during cleaning.

Figure 3.24 illustrates the roughness of the sidewall, whilst Figure 3.25 illustrates the interface on the sidewall which occurs as a result of the etch process. Unfortunately conditioning the sample with the etch chamber had no effect upon the sidewall roughness, indicating that the roughness occurs during the process and cannot be improved by post processing.

In the second process 2 sccm of O₂ was added to the standard process, with the added oxygen accounting for approximately 10% of the CHF₃ flow rate. Figure 3.26 illustrates that the inclusion of oxygen within the plasma process gives rise to lateral erosion of the sidewalls, as suggested in the introduction to this section. One point, worthy of note, is illustrated in figure 3.27, where we can see a reduction in sidewall roughness, when compared to figure 3.24.

From the results presented in this section it is evident that a certain degree of sidewall roughness can now be attributed to the etch process itself and that it can, in principle, be controlled through the addition of oxygen to the CHF₃ etch process. However, the advantages of using oxygen to control sidewall roughness must be balanced with the disadvantage of lateral sidewall erosion.

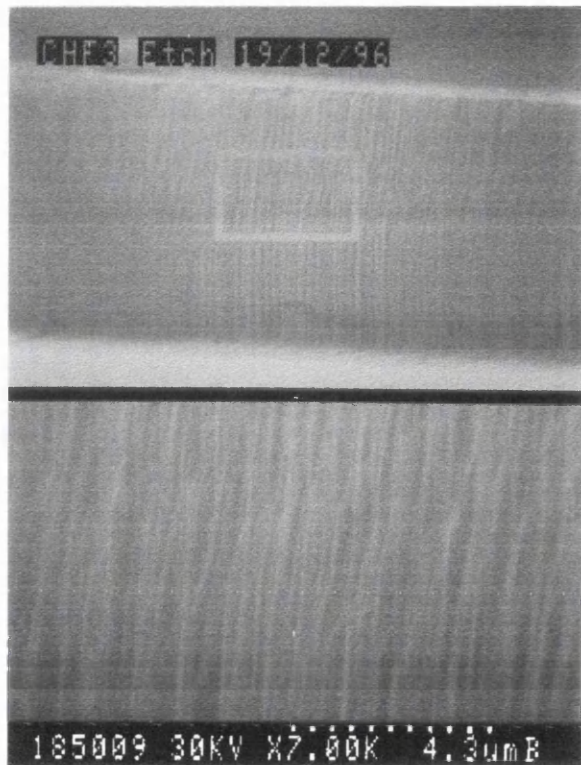


Figure 3.24 Illustration of the sidewall typical of CHF₃ plasma processing.

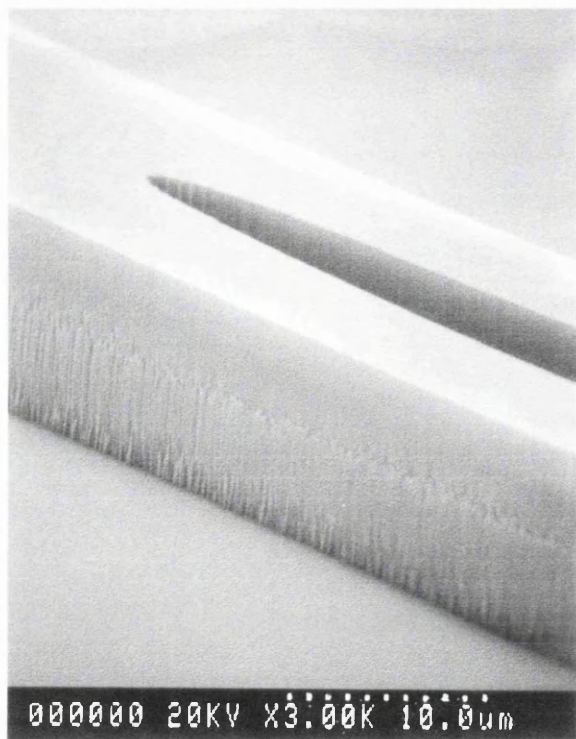


Figure 3.25 Figure to illustrate the interface occurring during the etch process interruption for chamber conditioning .

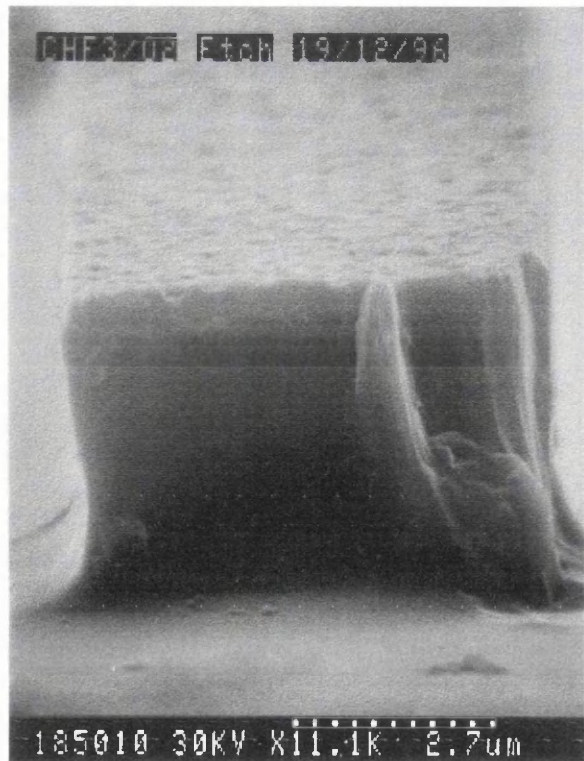


Figure 3.26 SEM image illustrating the increasing in sidewall erosion arising after the addition of O₂ to the standard CHF₃ etch process.

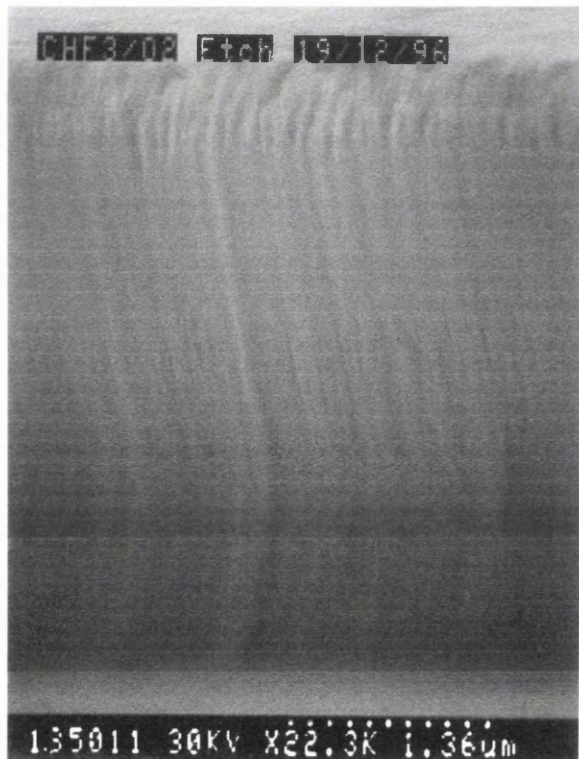


Figure 3.27 Etched sidewall illustrating the reduction in sidewall roughness in O₂, c.f. Fig 3.24

3.6 RIE Process Development through Design of Experiments

Introduction

During the course of the work it became apparent that a lot of RIE experiments had been performed, with the majority of the work pointing towards the one developed process. It became clear that a more structured and rigorous approach was required to fine tune the etch process. Towards the end of the project a concept known as experimental design was explored (often referred to as Design of Experiments, Orthogonal or Factorial Design.) This concept allows the investigator to best develop a systematic experiment which allows a more detailed, and robust, study of the experiment or process requiring development.

Historically, engineers and scientists have been educated in the school of experimentation which dictates that one factor at a time is varied [22]. This technique is simple, but can be described as being a one dimensional search. In this search, one factor is varied, whilst the other factors are held constant, and the experimental output is recorded. This is repeated for every other factor in the experiment. The one factor at a time approach has a number of disadvantages:

- If the optimum point for a factor is determined, it is not known if it remains the optimum point as the other factors are varied. In other words it is difficult to analyse the interaction between factors.
- This approach ignores a large proportion of the experimental space, leaving an unexplored region which may contain useful information.
- The large number of experiments can be a drain on resources, be it time, money or equipment.

The Origin of Robust Design

After the Second World War, Japan suffered from a shortage of resources in the form of workers, materials and equipment. During the 1950's Dr. Genichi Taguchi of NTT in Japan set about developing methodologies for the purpose of improving quality control in Japanese Industry which would help to make more efficient use of the depleted resources.

Applications of Experimental Design

A large number of experimental designs exist which can be used in the development of processes in the semiconductor industry, for example:

- Flores & Norbury [23] compared the use of various models in the development of a photolithography process. Models include linear screening design, factorial design and a quadratic design model.
- Lin et al [24] developed an equipment characterisation and modelling methodology for an LPCVD furnace for polysilicon deposition.
- Guo et al [25] developed a multiple response surface methodology for application to plasma etching, silicon epitaxy, tungsten CVD and simulation of polysilicon CVD.
- May et al [26] examined a plasma etch process for polysilicon using a screening factorial design to identify and isolate the significant factors in the process, before applying a response surface model to optimise the polysilicon etch process.

3.6.1 The Experiment

In this work we use a technique of orthogonal design based upon the Taguchi techniques [27]. An advantage of this technique is that, in the case described here, an experiment with 4 factors at 3 level settings would require 81 experiments to investigate the full parameters (full factorial design), whereas this Taguchi design only requires 9 experiments. Of course, there is a drawback. This technique does not allow us to statistically examine the interactions between factors, however it does give us a good indication of the main effects of each individual factor.

Step 1: Factor Selection

An important feature in correct experimental procedure, is the prior knowledge which the engineer should have with regards to the experiment. There should be a basic knowledge of the main influential factors in the process. In the case presented here, the main factors in silica have been investigated, e.g. CHF₃ flow rate, etch pressure and RF power. The work carried out in the last section also illustrates that O₂ maybe

influential in the successful development of an RIE process for silica films, which gives us a fourth factor: O₂ flow rate.

Step 2: Experimental Range

Before defining the experiment it is important to know the range over which factors can be varied. This comes from prior working knowledge of the process, which in this case has arisen from a myriad of experiments described previously. It is important that the experimental range is neither too narrow, thus making the effects of the factors seem insignificant, nor too broad thus masking any maximum or minimum points in the process. The likelihood of this occurring is thus reduced through some basic experimental knowledge on the part of the experimenter. In general it is acceptable to have a maximum and minimum level with an equally spaced mid-point in between.

The factor levels used in this experiment are illustrated in Table 3.8.

Level Setting	(1) CHF ₃ Flow Rate (sccm)	(2) O ₂ Flow Rate (sccm)	(3) Etch Pressure (mtorr)	(4) RF Power (W)
1	5	0	20	60
2	25	5	60	120
3	45	10	100	190

Table 3.8 Input Parameters and Level Settings used in the optimisation of the CHF₃/O₂ RIE process

Step 3: Experimental Runs

The final stage in the experiment design is the selection of an orthogonal table, a selection of which can be found in the Appendix I. A table is deemed to be orthogonal if the following conditions are met [27]:

- The number of occurrences of each level setting must be equal within each column.
- All rows having identical level settings in a given column must have an equal number of occurrences of all other level settings in other columns.
- The matrix for a given number of columns must be the one with the minimal number of rows that satisfy the above conditions.

In our case we have 4 input factors with 3 level settings. A full factorial design for this case would require 81 experimental runs, however we can use an orthogonal table named, L_93^4 , where 9 is the number of experimental runs, 3 is the number of level settings and 4 is the number of factors. The orthogonal design used in this experiment is illustrated in Table 3.9. Table 3.10 illustrates the actual experiment to be carried out through the re-tabulation of the orthogonal table with the factor level settings as defined in Table 3.8.

Also shown in Table 3.10, are two additional experiments, 4' and 4''. These experiments are included to investigate random variation within the process arising from sample variation, operator effects, machine anomalies etc. Run 4 was selected as the repeat as it was thought that this would be the most likely to provide a reasonable etch process, similar to the previously developed process. Experiment 4' was performed after run 6, with 4'' occurring after run 9.

Run	Input Number			
	1	2	3	4
1	1	1	1	1
2	1	2	2	2
3	1	3	3	3
4	2	1	2	3
5	2	2	3	1
6	2	3	1	2
7	3	1	3	2
8	3	2	1	3
9	3	3	2	1

Table 3.9 Orthogonal Table designated L_93^4 , for 4 factors, 3 level settings and 9 runs.

Run	CHF ₃ Flow Rate (sccm)	O ₂ Flow Rate (sccm)	Etch Pressure (mtorr)	RF Power (W)
1	5	0	20	50
2	5	5	60	120
3	5	10	100	190
4	25	0	60	190
5	25	5	100	50
6	25	10	20	120
7	45	0	100	120
8	45	5	20	190
9	45	10	60	50
4'	25	0	60	190
4''	25	0	60	190

Table 3.10 The full experiment including actual factor levels and duplicate runs (reproducibility).

Step 4: Output Definition

The output functions for this experiment are as follows:

- Glass Etch Rate (GER)
- Mask Etch Rate (MER)
- dc Bias

The GER and MER have already been explored previously and do not require further explanation. During the developed CHF₃ etch process (Section 3.6), it was noticed that the dc Bias dropped with time, which upon further investigation, seemed to be linked to chamber contamination. This was also reflected by a change in the etch rate with time. To investigate this further, the dc Bias was recorded at the beginning and end of each experiment, with the purpose of monitoring any changes.

Step 5: Experiment Preparation

As was the case in all other experiments, a germano-boro-silica glass (GBSG) film was deposited on a silicon wafer by flame hydrolysis deposition and patterned with nichrome. The wafer was diced to provide a sufficient number of samples for successful completion of the experiment.

Prior to **every** experiment the etch machine was subjected to a pre-conditioning process consisting of an O₂ clean to remove any contamination from the chamber sidewalls and electrodes (30 minutes, 100 W, 21 mtorr, 30 sccm O₂).

It was intended that one operator would perform all the experiments, however the experiment ran over two weeks, and as such was subject to operator work-sharing. This provided some justification for the use of repeat experiments.

The thickness of the nichrome mask was measured prior to each run using the DekTak surface profiler. The etched sample was subsequently measured before and after mask removal to give an indication of the glass etch rate and mask etch rate.

In order to further assess each run, a questionnaire was left with the dry etch technician, in which they had to note the dc bias at the start and end of each etch run. The operator was also asked to assess the condition of the etch chamber in their opinion, from the options: **Clean, Average or Dirty**. The condition of each sample was also appraised in terms of its appearance, e.g. dirty from appearance of a thin film, or clean.

Step 6: Experiment Results

In Table 3.11, the results of the 9 runs and the 2 repeat runs are tabulated. The table contains the raw data for the runs, and indicates the assessment of both the etch chamber and the samples after the completion of each run.

Initially, from first examination of the data, there is no apparent trend, however we can make a few observations on the data.

Run Number	1	2	3	4	5	6	4'	7	8	9	4''
Mask (nm)	183.6	176	183	188.8	185.7	184.8	188.9	186	186	189.5	185.4
After RIE (μm)	0.989	2.09	1.66	3.54	3.11	0.189	3.62	0.1630	2.35	0.81	2.14
After Mask Removal (μm)	0.796	2.02	1.66	3.39	2.95	0	3.48	0.163	2.26	0.641	NA
Glass ER (μm/hr)	1.692	4.04	3.32	6.78	5.9	0	6.96	0	4.52	1.282	NA
Mask ER (nm/hr)	0	200	183	77.6	40	0	80	0	180	20	NA
Initial dc Bias (-V)	300	400	490	510	310	460	500	340	550	220	500
Final dc Bias (-V)	290	400	490	500	305	460	500	300	540	220	480
Bias Change (V)	-10	0	0	-10	-5	0	0	-40	-10	0	-20
Chamber Assessment	Clean	Clean	Clean	Dirty	Ave.	Clean	Ave.	Ave.	Dirty	Ave.	Dirty
Sample Assessment	Dirty	Clean	Clean	Clean	Clean	Clean	Clean	Dirty	Clean	Clean	Dirty

Table 3.11 The experimental results in full. The data of interest is highlighted, GER in green, MER in magenta, dc Bias in blue and repeat runs in red. Etch time 30 minutes.

From the evidence of runs 4 and 4' there appears to be little variation in the process over time. We can see that there is a very small change in the glass etch rate (2.6%), with a similarly small change in the mask etch rate (3%). The magnitude of the etch rate was not surprising, as it was expected that this process would have the highest etch rate, as it is similar to the CHF₃ developed in previous sections ref. Table 3.3.

There was however quite a difference between these runs and run 4'' which proved to be a very dirty process. A high level of chamber contamination was reported in runs 4

and 4' which taken in the same context as run 4'' may illustrate that there is a fine line between deposition and etching, rather than operator error being of importance.

In general the runs were clean, except for the high CHF₃ flow runs, 7-9, where the chamber was typically dirty. This correlated with flow rate variation in Section 3.5.

Similarly the runs at 190 W, and hence high dc Bias exhibited the highest etch rates in general. However it was interesting to note that there was a surprisingly high etch rate at 50 W, a result which could be considered bizarre based on the early results presented, which indicated that high powers were optimum. This observation, coupled with the low mask etch rate suggests that a 50 W process could be developed.

Step 7: Data Analysis

The objective of the orthogonal table is to ensure that for each level and process factor, there is a randomisation of the settings for the other factors within each level setting. For example for each CHF₃ flow rate level, each level for the other factor only appears once. Using this property we can isolate the effect of changing flow rate.

Factor Effects

In the first instance we wish to evaluate the factor effects. The technique of evaluating the factor effects is quite often referred to as **Analysis of Means** (or ANOM). We do this by first calculating the overall mean value for each output using equation 3.1 [28]:

$$m = \frac{1}{9} \sum_{i=1}^9 n_i \quad \text{Eq. 3.1}$$

$$= \frac{1}{9} (n_1 + n_2 + \dots + n_9) \quad \text{Eq. 3.2}$$

where m is the overall mean for the output over the experimental range, and n_i is the output value for the ith run of the experiment.

The next step is the evaluation of the effects of the factors. The effect of a factor level is defined as the deviation it causes from the overall mean value. We calculate the average value of the output, n, by working out the mean of the output for each level.

Example: The effect of the O₂ flow rate set at level 2, 5 sccm on the mask etch rate

A flow of 5 sccm O₂ was used in runs 2, 5 and 8 where the mask etch rate was found to be 200, 40 and 180 nm/hr respectively. We work out the average value of the mask etch rate due to this O₂ flow rate using Equation 3.3:

$$MER(O_{l2}) = \frac{1}{3}(n_2 + n_5 + n_8)$$

$$MER(O_{l2}) = \frac{1}{3}(200 + 40 + 180) \quad \text{Eq. 3.3}$$

$$= \underline{\underline{140 \text{ nm / hr}}}$$

So we can now say that the average mask etch rate with the oxygen flow rate at level 2, 5 sccm, is 140 nm/hr.

Similarly the average glass etch rate arising when the pressure is set to level 1, 20 mtorr, is calculated from the data from runs 1, 6 and 8, where the glass etch rate was 1.692, 0 and 4.52 μm/hr respectively, thus using Equation 3.4:

$$GER_{P1} = \frac{1}{3}(n_1 + n_6 + n_8)$$

$$GER_{P1} = \frac{1}{3}(1.692 + 0 + 4.52) \quad \text{Eq. 3.4}$$

$$= \underline{\underline{2.07 \mu\text{m / hr}}}$$

So the average glass etch when the pressure is at level 1 is found to be 2.07 μm/hr. This procedure is performed for all factors, at every level setting, for each of the outputs of the experiment.

The results of these calculations can be found in Tables 3.12 to 3.15 for the CHF₃ flow rate, O₂ flow rate, etch pressure and RF power respectively.

At this point we are now in the position to evaluate the factor effects for each level and each output, where we use Equation 3.5:

$$\text{Effect} = (m_{F_l} - m) \quad \text{Eq. 3.5}$$

Where m_{F_l} is the average output arising for a factor at a given level, and m is the overall mean output over the experimental range.

Figures 3.28 to 3.31 graphically illustrate the effects of varying the different process factors on the Glass Etch Rate (a), Mask Etch Rate (b), dc Bias Drop (c) and the initial dc Bias (d).

3.6.2 Discussion of Results

We can use the data plotted in Figures 3.28-31 to select the optimum settings for each input factor used in the RIE process. Each factor is examined individually to identify the optimum level setting for improving each output function.

1. CHF₃ Flow Rate (Figure 3.28 (a-d))

The low flow rate setting has both a low GER and bias drop, however the MER is at its highest level, almost double the minimum MER. The net result is that the selectivity is reduced to 24:1. We could infer from these results that there is too little gas to enable both glass etching and mask protection through polymer deposition, which due to the high dc bias enables sputtering of the mask to occur.

Conveniently, we see from Figure 3.28(a) that the medium flow rate (25 sccm) results in both the highest mean GER and the lowest mean MER, Figure 3.28(b)). These combine to give the highest glass to a mask selectivity of 108:1. However, using a medium flow rate can be a slightly dirtier process, compared to lower flow rates, as reflected in the bias drop which shows a 34% increase over the minimum, Figure 3.28(c). This flow rate is acceptable as the optimum condition for the process.

Increasing the flow rate to its maximum setting minimises the mean GER, whilst slightly increasing the MER, however the low GER reduces the selectivity to just 28:1. There is also a large drop in the bias with time, as shown in figure 3.28(c) where the

bias drops by a mean of 16.7 V. In general the samples etched at high flow rates were coated with a thin film, as was the etch chamber. The reduction in the dc bias illustrates that there may be a drop of ionised species in the plasma, Figure 3.28(d).

From these results alone, we can infer that increasing the flow rate, provides more reactive and polymer forming species. At higher flow rates, the residence time within the chamber is too short to allow efficient breakdown of the feed gas.

The optimised process uses a medium CHF₃ flow rate, which offers a high glass etch rate and high selectivity over the mask whilst remaining a relatively clean process.

2. O₂ Flow Rate (Figure 3.29 (a-d))

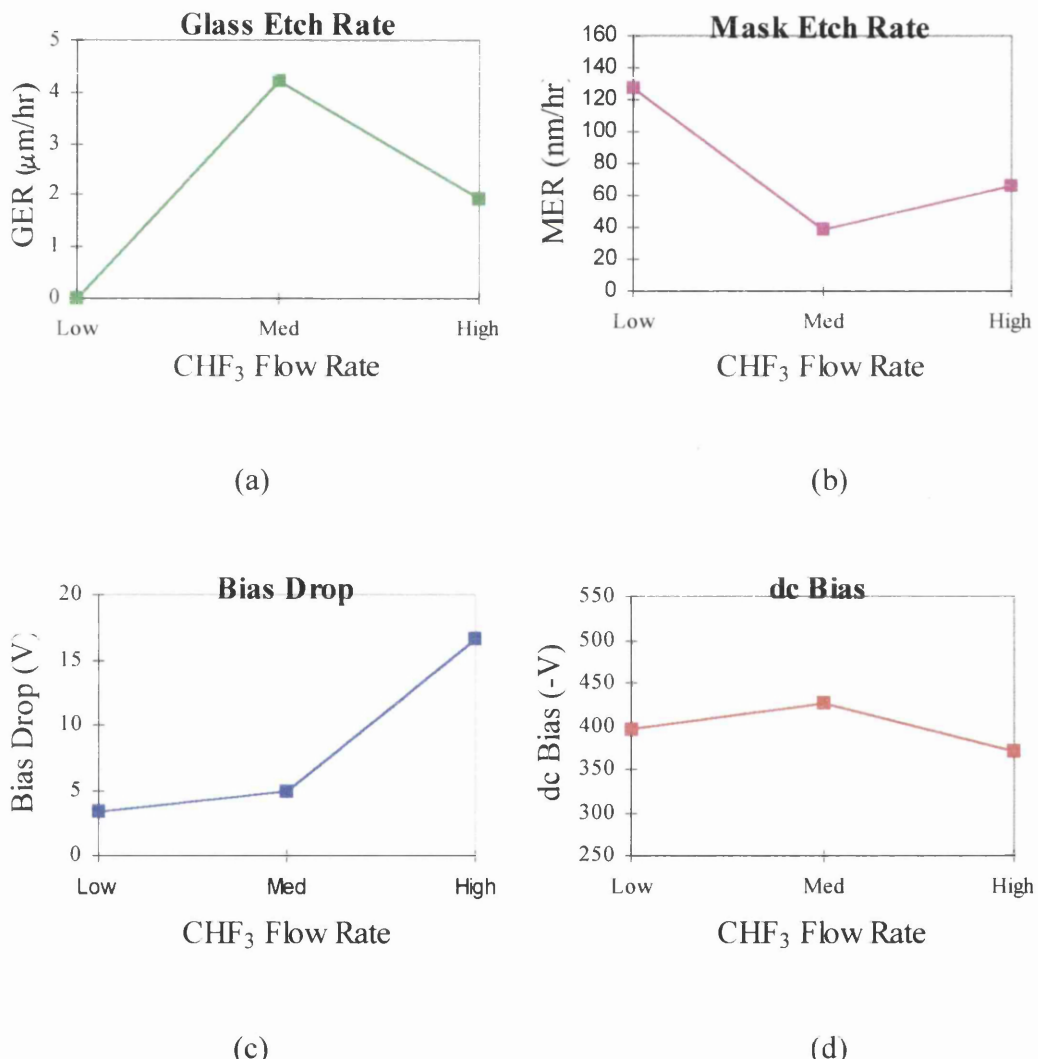
The MER can be minimised if no oxygen is used in the process, however this also reduces the GER and greatly increases the drop in dc bias. This indicates that thin film forming species are commonplace in a typical CHF₃ plasma process.

As was the case with CHF₃, the maximum GER occurs at the medium flow rate, unfortunately the mean MER is also at its greatest. The mean dc bias is at a maximum at this level which implies that there is an increase in ionised species which is reflected in both the maximum MER and GER. Overall, setting the O₂ flow rate to 5 sccm gives a mean selectivity of 34:1.

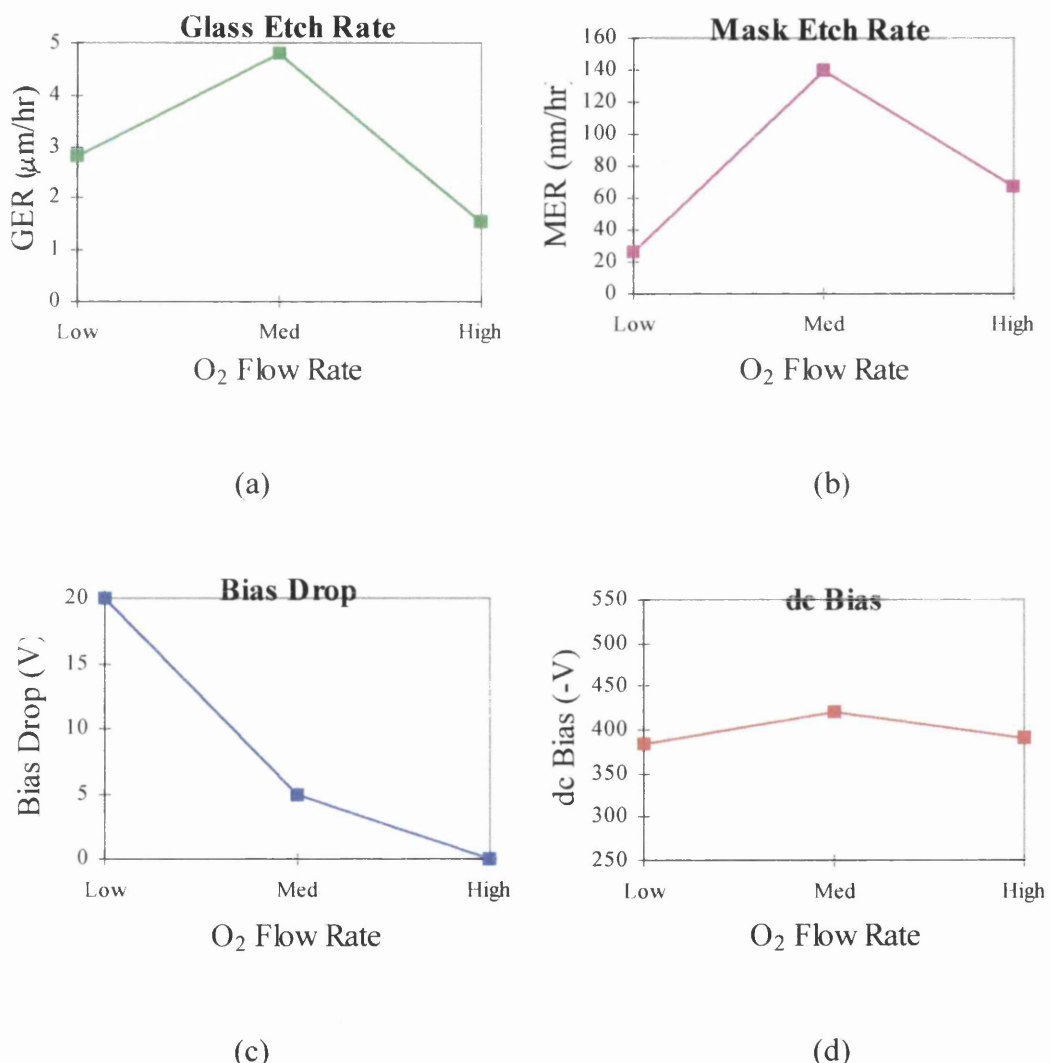
Increasing the oxygen flow rate reduces the mean bias drop to 0 Volts, indicating that there has been a reduction in thin film forming species, a fact which is confirmed by the operator report where a clean chamber and samples was observed. There was, however, a large drop in the GER and a smaller drop in the MER, which reduced the glass to mask selectivity 23:1. This is consistent with a drop in etching species.

Unfortunately oxygen addition does not appear to have an optimum setting where we can maximise the etch rate and selectivity whilst remaining a clean process. Here, oxygen addition does not seem advantageous, however it could be examined again.

Level Setting	Mean GER ($\mu\text{m/hr}$)	Mean MER (nm/hr)	Mean Bias Drop (V)	Mean Initial Bias (-V)
Low (5 sccm)	3.017	128.0	3.3	396.7
Medium (25 sccm)	4.226	39.2	5	426.7
High (45 sccm)	1.934	66.7	16.7	370

Table 3.12 The mean effects of setting the CHF_3 flow rate to its low, medium and high settingFigure 3.28 Influence of CHF_3 flow rate on the (a) glass etch rate (GER), (b) mask etch rate (MER), (c) dc bias drop and (d) dc Bias

Level Setting	Mean GER ($\mu\text{m/hr}$)	Mean MER (nm/hr)	Mean Bias Drop (V)	Mean Initial Bias (-V)
Low (0 sccm)	2.824	25.9	20.0	383.3
Medium (5 sccm)	4.82	140	5	375.6
High (10 sccm)	1.534	68.0	0	390

Table 3.13 The mean effects of setting the O₂ flow rate to its low, medium and high settingFigure 3.29 Influence of O₂ flow rate variation on the (a) glass etch rate (GER), (b) mask etch rate (MER), (c) dc bias drop and (d) dc Bias

Level Setting	Mean GER ($\mu\text{m/hr}$)	Mean MER (nm/hr)	Mean Bias Drop (V)	Mean Initial Bias (-V)
Low (20 mtorr)	2.07	60	6.7	436.7
Medium (60 mtorr)	4.034	99.2	3.3	376.7
High (100 mtorr)	3.073	74.6	15	516.7

Table 3.14 The mean effects of setting the Etch Pressure to its low, medium and high setting

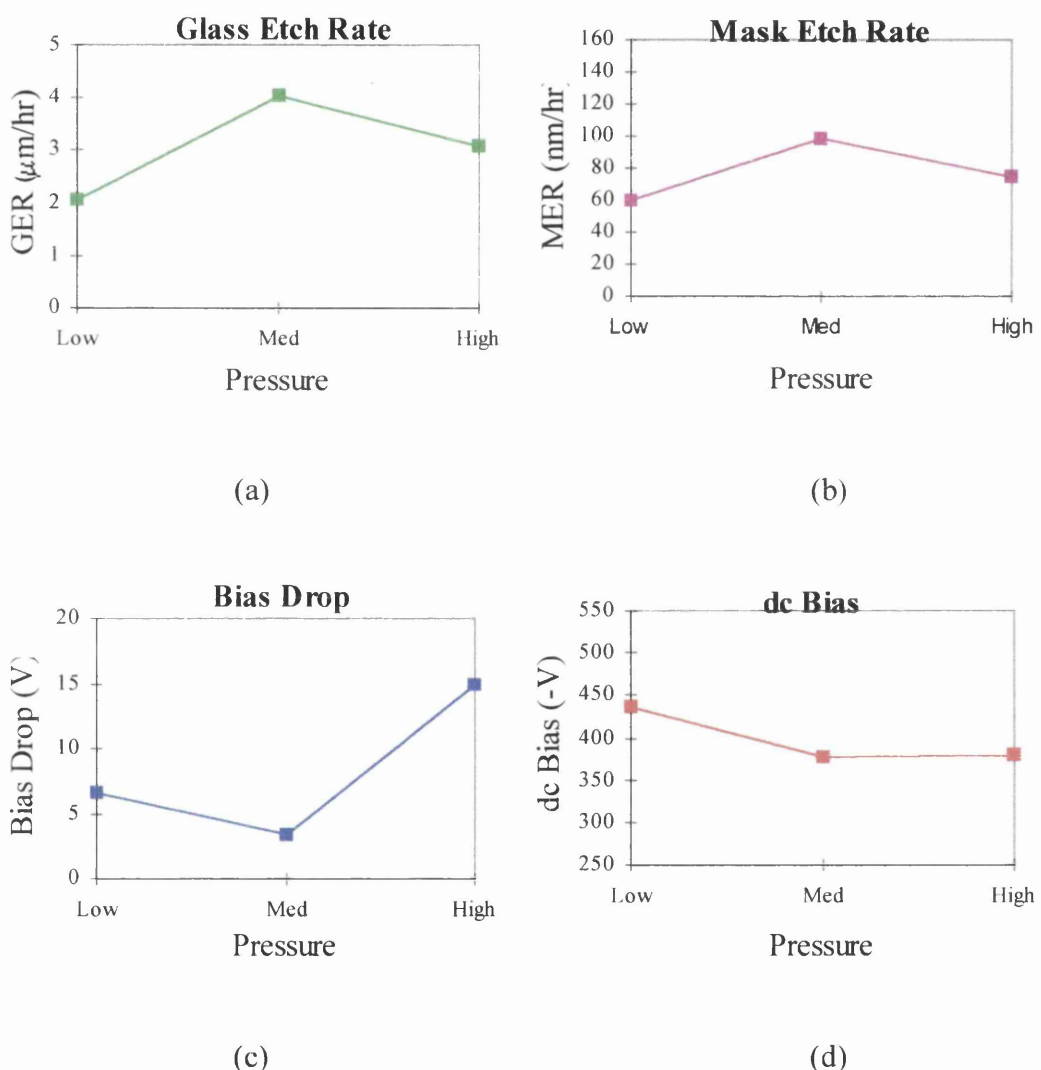


Figure 3.30 Effect of Etch Pressure variation on the (a) glass etch rate (GER), (b) mask etch rate (MER), (c) dc bias drop and (d) dc Bias

Level Setting	Mean GER ($\mu\text{m/hr}$)	Mean MER (nm/hr)	Mean Bias Drop (V)	Mean Initial Bias (-V)
Low (50 W)	2.958	20	5	276.7
Medium (120 W)	1.346	66.7	13.3	395.6
High (190 W)	4.873	147.2	6.7	516.7

Table 3.15 The mean effects of setting the RF Power to its low, medium and high setting

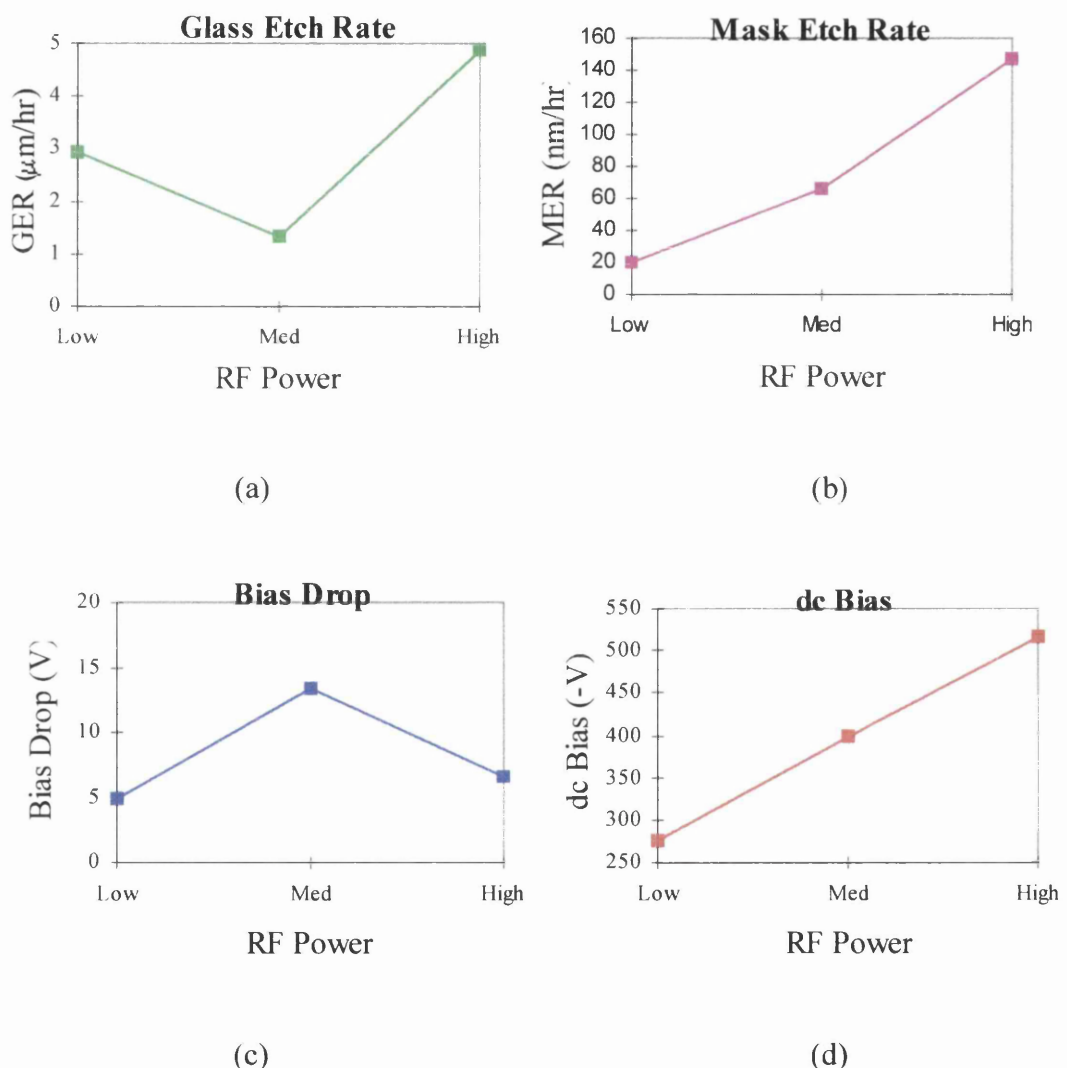


Figure 3.31 Influence of varying RF Power levels on the (a) glass etch rate (GER), (b) mask etch rate (MER), (c) dc bias drop and (d) dc Bias

3. Etch Pressure (Figure 3.30 (a-d))

At low pressure both the mean MER and GER are minimised, as is the mean glass to mask selectivity ~35:1. The bias drop is low, but not minimised.

As we increase the pressure its medium setting the GER and the MER are maximised, however the selectivity does not change much, rising to 41:1. The bias drop is minimised to ~3.3 V. We would expect this to happen as the residence time of the gas within the plasma increases which encourages an increase in the number of interactions within the plasma, i.e. we would expect a higher etch rate as more dissociation would occur.

Unfortunately, the net effect of increasing the pressure further still, is to reduce the GER and MER, whilst maintaining a selectivity of 41:1. However the mean dc bias falls considerably at higher pressures, which is again further evidenced by the appearance of a thin film on the chamber and samples.

It was noted that the mean dc bias dropped with increasing pressure, indicating that there is a drop in the number of ionised species, which correlates with the observed drop in the GER, and increased chamber contamination.

4. RF Power (Figure 3.31 (a-d))

Until this point, it was believed that high RF powers are required in order to etch flame hydrolysis deposited glass films. The reasons for this were justifiable in that a higher RF power would help increase the level of dissociation, whilst encouraging the formation of ionised species due to interactions. This in turn would increase the dc bias, which would typically lead to an increase in the ion energy which serves to enhance the sputtering processes normally associated with oxide RIE.

At low power we observed a high mean GER with a correspondingly low MER. The net result of this is a mean selectivity of 148:1, which to date has only been achieved with SF₆ etching. The mean bias drop was also low at 5 V over 30 minutes. However run 1 at 50 W resulted in heavy sample condition whereas run 5 was recorded as being clean with a high GER (5.9 µm/hr) and a low MER (40 nm/hr).

Strangely, the mean GER decreased when the medium power setting was used. At first it was thought that this may be due to one of the other factors being at a less than optimum level, but based on the other results presented here, this was not the case. The MER increased which led to a reduction of the selectivity to just 20:1.

The highest RF power gave rise to the highest GER and MER albeit at a lower selectivity of just 33:1, but with what looked to be a relatively clean process.

It was surprising to find an etch process with vastly different mask etch rates but similar glass etch rates, compared with higher RF Power etch processes. This leads us to believe that the etching of FHD silica is more of a chemical process, rather than the reactive ion sputtering process as first thought.

The last point to make here is that the dc bias increased linearly with increasing rf power, as did the MER which confirms the generally held belief that the etching of nichrome films is predominantly a sputtering process.

3.6.3 Summary of Factor Influence

The greatest variation in the mean glass etch rate was obtained under RF power and O₂ flow rate variation where the max:min ratio was found to be ~3:1. This is an acceptable result as it is generally thought that O₂ addition helps increase the number of etching species, as does an increase of RF Power.

Mask etch rate variation was found to be greatest under RF power variation (7:1), followed closely by O₂ flow rate (5.4:1). In the case of RF power it is thought this is largely due to the self bias voltage of the process, whereas in oxygen addition it is attributed to the decrease, and subsequent increase of polymer and reactive species respectively. Understandably, variation of CHF₃ had a reasonable influence (3.3:1).

Varying the feed gases and pressure (>4:1) had the greatest effect on the drop in the self bias voltage with time, where in the case of increasing CHF₃ and pressure the effect was to increase the drop, whereas O₂ addition improved things as expected.

The only other output that was examined was that of the initial self bias voltage, which exhibited little variation with the feed gases and pressure (~1:1), although it decreased

with increasing pressure which was expected as the dark space between the electrode and plasma would shrink with increasing pressure. Also, as expected, the dc bias increased rf power.

3.6.4 Process reproducibility and sidewall assessment

In order to assess the robustness (or reproducibility) of the etch tests, repeat runs were carried out. It was anticipated that run 4, which had similar characteristics to the previously developed CHF₃ process, would be the most likely experiment to succeed. As such the experiment was repeated in runs 4' and 4''. The data collected from these runs are presented in Table 3.16.

	Run 4	Repeat Run 4'	Repeat Run 4''
GER (mm/hr)	6.78	6.96	NA
MER (nm/hr)	77.6	80	NA
Sample	Clean	Clean	Dirty
Chamber	Dirty	Average	Dirty

Table 3.16 Illustration of process reproducibility from repeat runs 4' and 4''

We can see that there was a 3% increase in both the glass etch rate and the mask etch rate from run 4 to run 4'. We can see that there is no change in the sample cleanliness, however the chamber remained dirty. It is thought that run 4'' was carried out directly after run 9, without any pre-conditioning of the etch chamber which gave rise to a lot of contamination which indicates that there is a dependence on the operator.

After the experiments it was found that only runs 4, 4', 5 and 8 were suitable for SEM examination. In the other runs the samples had too low an etch rate to make a suitable etch process assessment, where anisotropy (or lack of it) could be assessed. It can be observed from Figure 3.32 that etching under the conditions of run 4, results in a vertical profile. Figure 3.33 illustrates that this process is repeatable as the same resultant profile is obtained using run 4''. Figure 3.34 shows the curved profile after low power etching with oxygen in run 5, whereas Figure 3.35 illustrates that O₂ addition on its own during run 8 results in a curved sidewall profile, c.f. Figure 3.26.

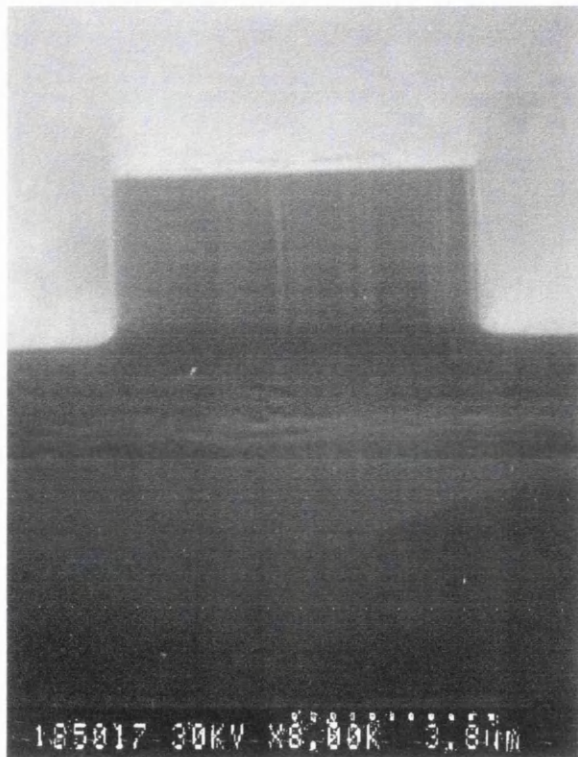


Figure 3.32 Etch profile after Run 4 of CHF₃/O₂ optimisation experiment.

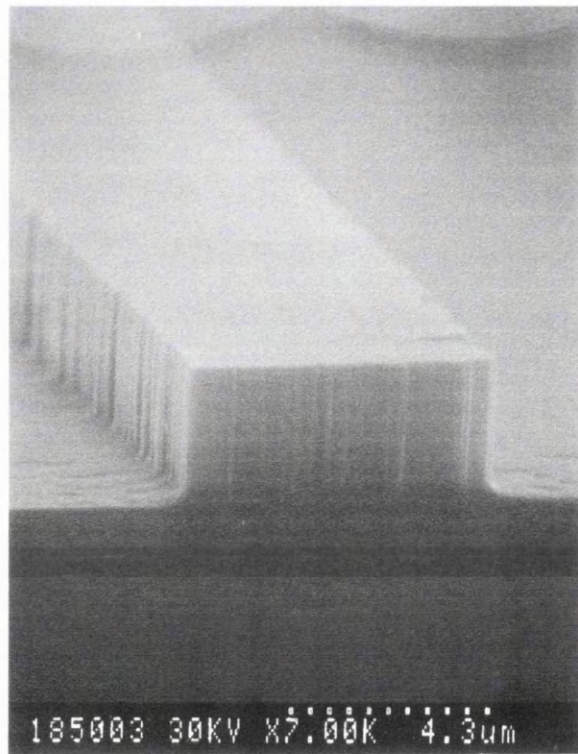


Figure 3.33 Illustration of etch profile reproducibility after run 4'.

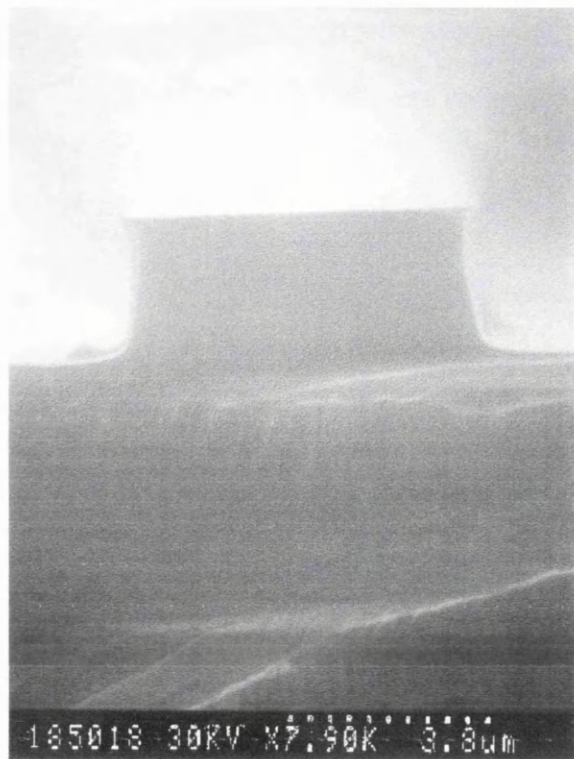


Figure 3.34 SEM showing sidewall erosion during arising due to low power and oxygen addition.

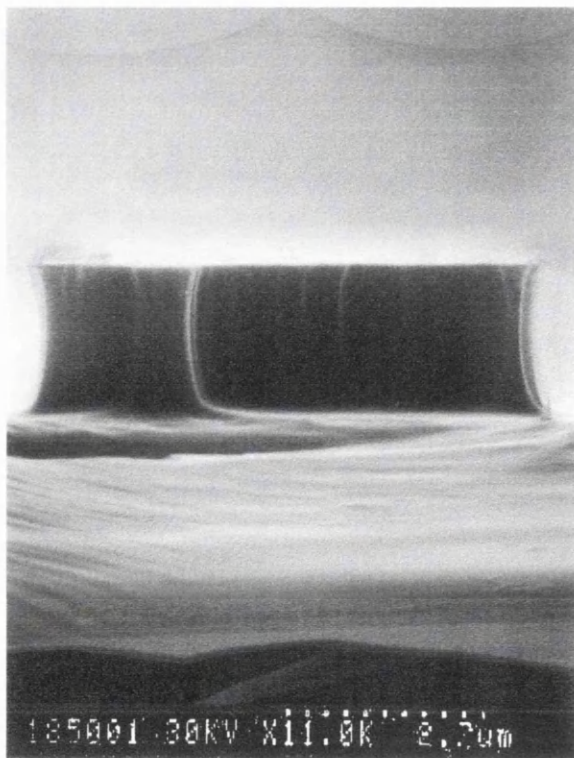


Figure 3.35 SEM illustrating the sidewall erosion occurring due to oxygen addition only (compare with Figure 3.26).

3.7 Conclusions

Reactive Ion Etch (RIE) processing of germanium doped silica glass films has been studied. Throughout the study it became evident that etch mask selection is critical to achieving large etch depths, with NiCr masks being preferable to photoresist masks. A comparison between etch processes using three fluorine based gases was performed where it was found that CHF₃ is preferable to C₂F₆ and SF₆ for deep reactive ion etching as it exhibited a significantly higher mask:glass etch ratio. The CHF₃ process was investigated further where the influence of dc Bias and O₂ addition to the plasma was examined. The study showed that there is a tradeoff between etch mask erosion, sidewall erosion and glass etch rate. Advanced process development procedures were used to fine tune the CHF₃/O₂ process. The fine tuned process results in a highly reproducible glass etch with a high glass etch rate (~7 μm/hr) and a high mask selectivity (~90:1) which produces waveguide core structures with a well defined anisotropic square cross-section. A cross-section of an index matched, buried waveguide is shown in figure 3.36, where virtually no core deformation is evident.

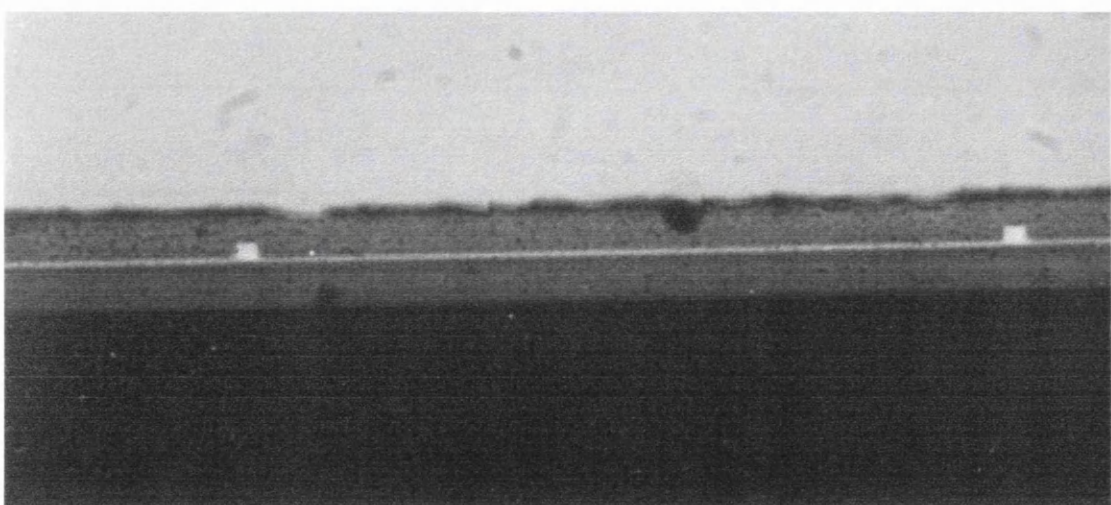


Figure 3.36 Waveguide cross-section after CHF₃ RIE and cladding layer deposition. Of note is the relatively square core shape. This figure is referenced back to Chapter 2, cladding layer deposition.

References

- [1] G.L. Duveneck, E. Verpoorte, P. Oroszlan, M. Pawlak, C. Erbacher, A. Spielmann, D. Neuschäfer and M. Ehrat, *Anal. Methods & Inst. Special Issue μTAS'96*, 158, 1996.
- [2] M. Kawachi, *Opt. & Quant. Elec.*, 1990, **22**, 391.
- [3] J.R. Bonar, *PhD Thesis*, University of Glasgow, 1995.
- [4] S.R. Irving, *Solid State Technol.*, 1971, **14**, 47.
- [5] J.W. Coburn, *Short Course 23*, SPIE, San Jose 1990.
- [6] C.J. Magab, C. A. Adams and D. L. Flamm, *J. Appl. Phys*, 1978, **49**, 3796
- [7] B.A. Ruby, *J. Vac. Sci. Technol.*, 1980, **23**, 1717
- [8] Ch. Steinbrüchel, H.W. Lehmann, K. Frick, *J. Electrochem. Soc.*, 1985, **132**, 1985
- [9] K.R. Williams and R.S. Muller, *IEEE J. Microelectromech. Syst.*, 1996, **5**, 256.
- [10] G.S. Oehrlein, *Chapter 8, Handbook of Plasma Processing Technology*, Editors S.M. Rossnagel, J.J. Cuomo and W.D. Westwood, Noyes Publications, 1990.
- [11] A.J. McLaughlin, J.R. Bonar, M.G. Jubber, P.V.S. Marques, S.E. Hicks, C.D.W. Wilkinson and J.S. Aitchison, *Conference on Lasers and Electro-optics*, 11, OSA Technical Digest Series, 1997, 508.
- [12] A.J. McLaughlin, J.R. Bonar, M.G. Jubber, P.V.S. Marques, S.E. Hicks, C.D.W. Wilkinson and J.S. Aitchison, *J. Vac. Sci. Technol. B*, 1998, **16**, 1860.
- [13] A.K. Dutta, *Jpn. J. Appl. Phys.*, 1995, **34**, 365.
- [14] A.K. Dutta, *Jpn. J. Appl. Phys.*, 1995, **34**, 1663.
- [15] A.K. Dutta, *J. Vac. Sci. Technol. B*, 1995, **13**, 1456.
- [16] M.V. Bazylenko and M. Gross, *App. Phys. Lett.*, 1996, **69**, 2178.
- [17] M.V. Bazylenko and M. Gross, *J. Vac. Sci. Technol. A*, 1996, **14**, 2994.

-
- [18] S.-T. Jung, H.-S. Song, D.-S. Kim and H.-S. Kim, *AESPE '97, 1st Asian-European International Conference on Plasma Surface Engineering*, Seoul, 1997.
 - [19] G.S. Oehrlein and H.L. Williams, *J. Appl. Phys.*, 1987, **62**, 662.
 - [20] H.W. Lehmann and R. Widmar, *J. Vac. Sci. Technol.*, 1978, **15**, 319.
 - [21] J.M. Ruano, D.Ortega, J.R. Bonar, A.J. McLaughlin, M.G. Jubber, J.M. Cooper and J.S. Aitchison, to be presented at *MNE'98*, Belgium, 1998.
 - [22] Matrex LT Users Guide, RSD Associates, 1996.
 - [23] G.W. Flores and D.H. Norbury, *IEEE/SEMI Advanced Semiconductor Manufacturing Conference*, Paper CH3042, 1991.
 - [24] K.L. Lin and C.J. Spanos, *IEEE Trans. Semicond. Manufact.*, 1990, **3**, 216.
 - [25] R.S. Guo and E. Sachs, *IEEE Trans. Semicond. Manufact.*, 1993, **6**, 41.
 - [26] G.S. May , J. Huang and C.J. Spanos, *IEEE Trans. Semicond. Manufact.*, 1991 **4**, 83.
 - [27] G.Z. Yin and D.W. Jillie, *Solid State Technol.*, 1987, 127.
 - [28] Quality Engineering using Robust Design, M. S. Phadke, Prentice Hall, 1989.

Chapter 4 Integrated Optical Mach-Zehnder Interferometers

4.1 Introduction

As mentioned in Chapter 1, the integrated optical (IO) Mach-Zehnder interferometer (MZI) is the key to successful implementation of a phase quadrature optical detection system. The aim of this chapter is to investigate techniques of introducing small phase shifts ($<90^\circ$) between the arms of the interferometer.

In the first instance the design and fabrication of passive phase tuned devices is discussed, where the phase shift is achieved by a physical difference in the optical path length. The fabrication of an active phase shift device utilising the thermo-optic effect is described. The spectral and temporal response of this device to applied electrical power is also presented. Finally, Finite Element Modelling is used to analyse novel waveguide structures which could be used to minimise the electrical power consumption and thermal rise times.

4.2 Integrated Optical Y-junctions

Y-junctions are the preferred choice as an optical power splitter in this application, since there is a requirement for broadband illumination of the sensing device. Originally, this device was to be incorporated into a low-coherence optical sensing system for silicon resonant sensors which typically utilises two optical sources; a short coherence laser diode for optical detection of resonance ($\lambda \sim 850$ nm) and a laser diode source to illuminate and excite resonance of the silicon structure ($\lambda \sim 1.3$ μm).

It is also suggested that Y-junctions would be preferred in a wavelength multiplexed sensor environment where a flat wavelength response is required to maintain an even signal to noise ratio (SNR) over all of the multiplexing wavelengths.

However, it may be the case in the future that a switching action or add/drop wavelength multiplexing may required in the system to address multiple sensors [1]. In these situations it would be necessary to use wavelength flattened directional couplers [2]. This would be ideal in a single wavelength application, for example the use of self-resonant optical sensors using a single optical source for both drive and sensing.

4.3 The Single-mode optical waveguide Y-junction

In order to understand the operation of the integrated single mode MZI, the operating mechanism of the integrated Y-junction must first be examined.

The optical Y-junction can be described in terms of a branching, tapered and straight guide section [3], as shown in Figure 4.1. Assuming that the branching angle, θ , is sufficiently small, the mechanism of the Y-junction combiner can be explained using the concept of ‘local normal modes’ as described by Marcuse [4]. Local normal modes allow us to describe the propagation of the electric field though waveguides with geometrical variations, such as waveguide tapers and Y-junctions.

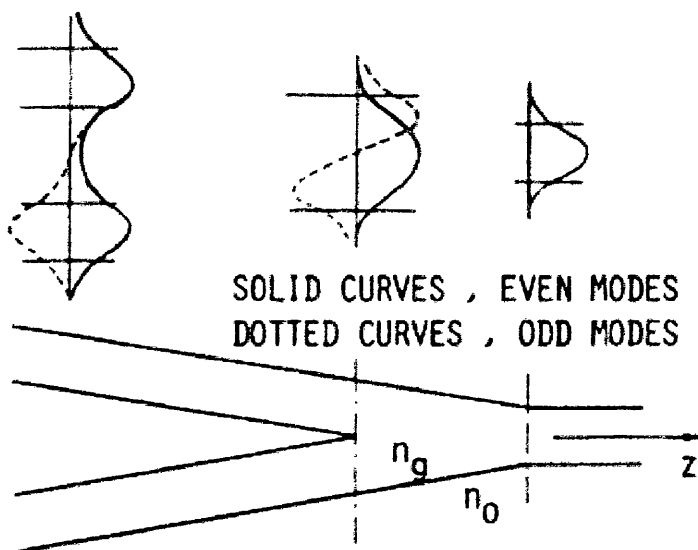


Figure 4.1 Schematic illustration of the optical Y-junction (after [3]).

It is known, that two types of local normal mode exist: even and odd. In the case of the single mode Y-junction discussed here, the branching waveguides only support the even, fundamental mode. At the beginning of the tapered section, the waveguide is wide enough to support the fundamental even mode and the first order odd mode. As the waveguide tapers in width, there comes a point where the higher order becomes non-propagating and is converted into a radiation mode, i.e. at the cut-off width for that mode. From this point on, only the fundamental even mode is supported, and propagates on into the straight waveguide section.

Figures 4.2 (a-c) illustrate the operation of the Y-combiner, where each case shows the creation of both the even (propagating) and odd (non-propagating) modes.

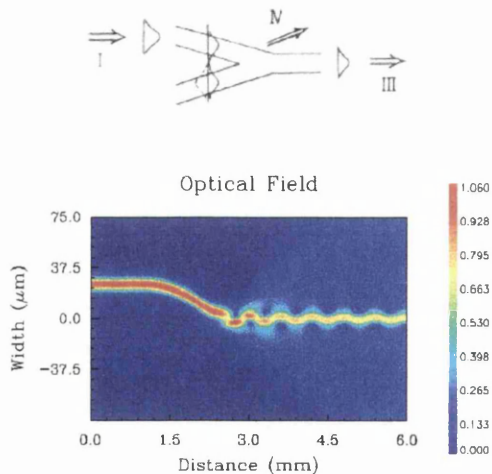


Fig 4.2 (a) Operation of the Y-combiner, one arm excited (after [3])

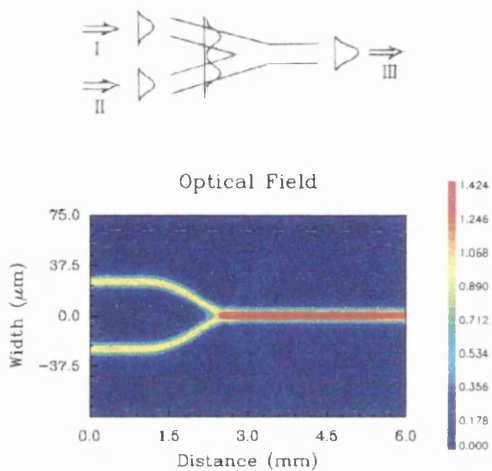


Fig 4.2 (b) Operation of the Y-combiner, both arms excited, 0° phase difference (after [3])

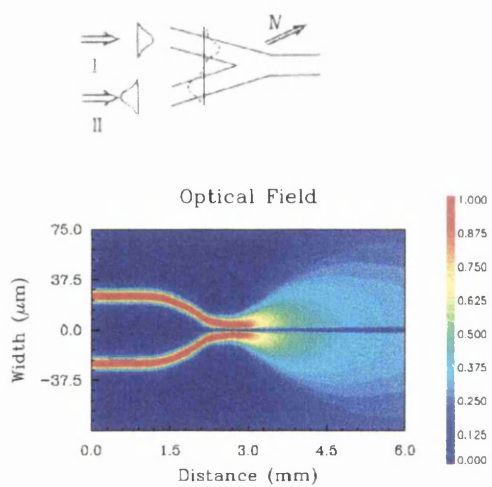


Fig 4.2 (c) Operation of the Y-combiner, both arms excited, 180° phase difference (after [3]).

4.4 Integrated Optic Mach-Zehnder Interferometer

In this section the operation of a Y-junction based Mach-Zehnder interferometer is considered. A model is developed to include loss contributions arising from optical power splitting in the first Y-junction.

The operation of the Mach-Zehnder interferometer can be described in terms of a loss-less 4 port Y-junction, where the configuration of this device is illustrated in Figure 4.3. The device consists of two singlemode input waveguides, port 1 and port 2, where the optical power in these ports is represented as P_1 and P_2 respectively. The waveguides combine and taper, to form a singlemode output waveguide, port 3, optical power P_3 . A fourth port is included to account for the radiation loss due to interference at the waveguide taper. The four port device assumption allows us to follow the scattering matrix formalism as presented by Rediker and Leonberger [5].

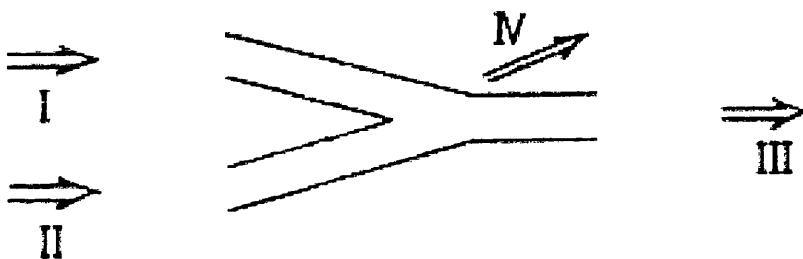


Figure 4.3 Schematic of a lossless 4 port Y-junction

If the device is considered to be a loss-less 3dB coupler then the relationship between the output fields \underline{E}' and the input fields \underline{E} can be represented as:

$$\begin{bmatrix} \underline{E}'_1 \\ \underline{E}'_2 \\ \underline{E}'_3 \\ \underline{E}'_4 \end{bmatrix} = \begin{bmatrix} 0 & 0 & \sqrt{\frac{1}{2}} & \sqrt{\frac{1}{2}} \\ 0 & 0 & \sqrt{\frac{1}{2}} & -\sqrt{\frac{1}{2}} \\ \sqrt{\frac{1}{2}} & \sqrt{\frac{1}{2}} & 0 & 0 \\ \sqrt{\frac{1}{2}} & -\sqrt{\frac{1}{2}} & 0 & 0 \end{bmatrix} \begin{bmatrix} \underline{E}_1 \\ \underline{E}_2 \\ \underline{E}_3 \\ \underline{E}_4 \end{bmatrix} \quad (4.1)$$

where \underline{E}_i represents a complex field of the form:

$$\underline{E}_i = E_i \exp(j\phi_i) \quad (4.2)$$

and E_i and ϕ_i represent the amplitude and phase of the field respectively.

We are primarily interested in the output from port 3, \underline{E}_3' , thus from the matrix we can say that:

$$\underline{E}_3' \exp(j\phi_{3,1}) = \sqrt{\frac{1}{2}} [E_1 + E_2 \exp(j\phi_{2,1})] \quad (4.3)$$

where $\phi_{3,1}$ represents the phase between the input and output field and $\phi_{2,1}$ represents the phase between the two input fields.

Equation 4. 3 can be used to evaluate the optical power in port 3, P_{out} as a function of the optical power in ports 1 and 2 where:

$$P_{out} = \sqrt{\frac{1}{2}} [\sqrt{P_1} + \sqrt{P_2} \exp(j\phi_{2,1})] \sqrt{\frac{1}{2}} [\sqrt{P_1} + \sqrt{P_2} \exp(-j\phi_{2,1})] \quad (4.4)$$

which simplifies to become:

$$\underline{P_{out}} = \frac{1}{2} [P_1 + P_2 + 2\sqrt{P_1 P_2} \cos(\phi_{1,2})] \quad (4.5)$$

Ideally $P_1 = P_2 \equiv P_{in}$, simplifying equation 4.5 to:

$$\underline{P_{out}} = P_{in} [1 + \cos(\phi_{1,2})] \quad (4.6)$$

However, in the real world waveguide devices are imperfect, either by error or design, and as such a mismatch in optical power can occur, therefore Equation 4.5 represents a more realistic model of the interferometer.

Until now the matrix description of the Mach-Zehnder has been assumed to be constructed from lossless and symmetrical Y-junctions. In reality we need to account for reflection and loss, for example; reflection at the Y-junction splitter, propagation loss due to fabrication errors, poor photolithography and sidewall definition. Equation 4.5 already accounts for power mismatch between port 1 and port 2.

However, in order to compensate for loss at the optical power splitter, the coefficient of optical power is rewritten as:

$$\underline{P_{1,2}} = \frac{P_1 + P_2}{2} \quad (4.7)$$

4.5 Asymmetric Mach-Zehnder Interferometers

The objective of this work was to design and fabricate parallel configurations of phase quadrature interferometers. In such a configuration, there needs to be a $\pi/2$ (or 90°) phase difference between the transfer functions of each interferometer.

In silica waveguides, there are two methods for introducing small phase shifts, either by passive design and/or active tuning. Both of these techniques involve altering the optical path length of one arm of the interferometer and thus the phase difference between the propagating beams.

In this section the design, Beam Propagation Method (BPM) simulation and the subsequent fabrication and test of *passive* asymmetric interferometers is examined.

4.5.1 Asymmetric Device Design Criteria

When designing singlemode asymmetric interferometers, a number of factors must be taken into account, for example:

- Type of branching waveguide
- Minimum separation between the branched waveguide arms
- Minimum length of interferometer arms
- Overall device size

Branching Waveguide Design

The type of branching waveguide used is very important to the overall design of the asymmetric interferometer. The branching section should introduce minimum excess loss into the system, whilst allowing the design of compact devices.

Y-junction based devices are typically constructed using straight waveguide branching sections, which *can* give rise to an abrupt change in the direction of propagation at the intersection between the input waveguide and branching section and the following intersection with the straight output section, as shown previously in Figure 4.1. The branching angle between these sections is a contributing factor to the excess loss in the

system. As the branching angle increases, the overlap integral between the fundamental modes of the waveguides decreases, leading to increased radiation loss.

The loss due to straight branching waveguides can be reduced by using smaller branching angles. This solution however, due to the restrictions imposed by the minimum arm separation, imposes a restriction on the minimum device size. Other techniques exist which serve to reduce the branching angle, e.g.: coherently coupled bends [6] where the angle is controlled using multiple straight waveguide sections.

In this work, devices were designed which use S-bends as the branching waveguide. This leads to an effective reduction in the branching angle of the waveguides, as the guides branch while parallel to the direction of propagation, and separate at a rate determined by the radius of curvature of the bend. Similarly, when the S-bend section meets a straight waveguide, it does so parallel to the direction of propagation, leading to better overlap with the fundamental mode of the straight guide.

As S-bends separate slowly, compared to abrupt straight waveguides, there can be problems with crosstalk between the waveguides. In the case of symmetrical branching waveguides, power transfer will be uniform. However, it will be shown later in this section, problems arise in asymmetric device design which can be most likely attributed to non-uniform power transfer. In the case of directional couplers, the coupling in the branching guides can be applied in reducing the size of integrated optical components. Such devices have been reported in silica waveguides [7] where directional couplers have been demonstrated with a coupling length of $l + \Delta l$, where Δl represents the additional coupling length due to the S-bends.

Consideration must also be given to the propagation losses incurred. Loss in bends arises from radiation of the optical mode and increases with decreasing radius of curvature. An analysis can be found in most integrated optics texts, for example Reference [8] or [9]. The minimum radius of curvature which can be used is defined by the relative refractive index difference (Δn) between the waveguide core and cladding. For example, a waveguide with a small radius of curvature and a low Δn will typically exhibit higher propagation loss than a similar high Δn waveguide. Novel techniques exist for reducing bending loss, for example the use lateral offsets [10].

Bending loss in waveguides prepared by flame hydrolysis deposition, has been assessed [7] and reviewed [11] as a function of radius and relative refractive index difference Δn . The minimum bending radius was defined as the lowest radius of curvature which resulted in 0.1 dB loss in a 90° arc at a wavelength of 1.55 μm. Table 4.1 summarises these results.

	Low Δn	High Δn
Relative Refractive Index Difference Δn (%)	0.25	0.74
Core Size (μm)	8 x 8	6 x 6
Loss (dBcm ⁻¹)	<0.05	0.5
Minimum Bending Radius (mm)	25	5

Table 4.1 Summary of loss characteristics of FHD prepared silica films (from Ref [11]). Minimum radius defined from a maximum bending loss of <0.1dB in a 90° arc.

Interferometer Arm Separation

An important feature of dielectric optical waveguides is the optical coupling which occurs when adjacent waveguides are placed in close proximity to each other. In some applications this can be advantageous, for example when used as an optical power splitter/combiner for wavelength division multiplexing (WDM) and in optical switching components. However, in our application, the interferometer arms are discrete optical components, and as such, optical coupling would be disadvantageous as any crosstalk between the waveguides would degrade the performance of the device.

Another important factor is that of thermal crosstalk. Silica has a temperature dependant refractive index. When heat is applied to one arm of the interferometer there is an increase in the optical path length, thus creating a phase difference between propagating optical fields. If the heat is applied for long enough, the temperature in the adjacent arm will tend to increase thus reducing the phase difference between the fields, which would again, degrade the performance of the interferometer.

A combination of BPM and finite element analysis (from Section 4.7) was used to analyse the optical and thermal characteristics of the interferometer. From this it was clear that the minimum separation between the waveguide arms should be 50 μm.

Minimum Arm Length

The arm length is chosen to satisfy two criteria: mode recovery after the intersection with the S-bend, and a minimal length to enable low power thermo-optic control.

After the optical field enters the straight waveguide section, there is a minimum propagation length over which the field will beat before settling into the fundamental mode of the straight waveguide. The BPM was to estimate the minimum propagation length for the fundamental mode to stabilise, which is approximately 1000 μm .

Given that the thermo-optic coefficient of silica, $\delta n/\delta t$ is approximately 1×10^{-5} [7], the minimum optical path length for a 2π phase shift at $\lambda \sim 1.55 \mu\text{m}$, would be approximately 5000 μm , if the core temperature increased to 30°C over ambient.

Using this information the physical path length of the arm was chosen to be 5000 μm (optical path length $\sim 7250 \mu\text{m}$, for $n \sim 1.45$).

4.5.2 Passive Phase Shifting through Asymmetric Device Design

The phase shift is introduced by designing the interferometer such that one arm is physically longer than the other. The interferometers are designed such that they possess sufficient symmetry which allows an approximate 50/50 power split. As such, making one arm longer than the other is not as straightforward as it seems, at least, not for small path differences of the order of $\lambda/4$. It is not possible to insert an additional length of waveguide at the inflexion point of the S-bend.

The transverse width of the S-bend is approximately 25 μm , whilst the longitudinal length is approximately 2000 μm , giving a branching half-angle of only 0.72° from centre. Thus inserting an extra portion of waveguide at the inflexion point, would result in a longitudinal lengthening of the arm, i.e. the y-combiner would have offset arms, degrading its interferometric performance. If the angle was 45°, there would be no problem as the insertion would occur in the transverse direction, making the device wider, but not altering the length. This technique has been used to fabricate optical multiplexors at 5GHz in FHD silica waveguides [7].

Thus, to introduce small path changes, it is necessary to alter the arc-length of the S-bend itself, whilst retaining the same longitudinal length. This is accomplished by adjusting the radius of curvature of the bend and its transverse width.

Length of an S-Bend

The S-bend waveguide is formed by the combination of two symmetrical arcs, with a smooth transition at their intersection. When describing the waveguide we use three physical dimensions: length, L , width, W , and the radius of curvature, r . A schematic illustration of an S-bend is shown in Figure 4.4.

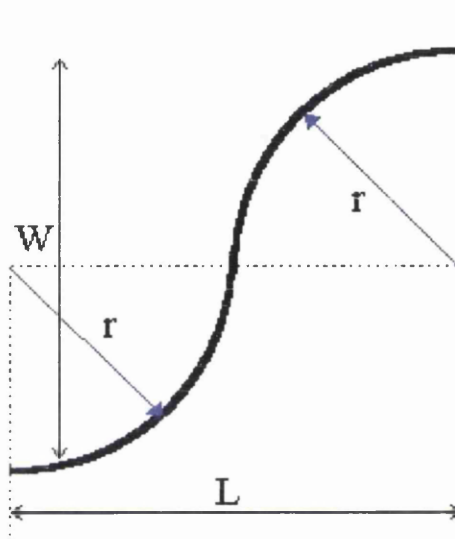


Figure 4.4 Schematic illustration of an S-bend, radius r , length L and width W

In order to calculate the length of the S-bend arc, the length of the arcs that make the bends are calculated using standard expression for the length of an arc:

$$L = r\theta \quad (4.8)$$

To correctly evaluate the arc length, a value for the angle, θ , that the arc sweeps through must be obtained, in terms of the physical dimensions described previously. To do this it is assumed that the width of the waveguide remains constant throughout the arc. The path length is evaluated at the centre of the waveguide, which in a singlemode waveguide is assumed to be the centre of the fundamental mode.

θ can be evaluated by approximating the length of the arc to be the straight line length, B , from the start point to the end of the arc, where B is equal to:

$$B = \frac{\sqrt{W^2 + L^2}}{2} \quad (4.9)$$

Now we calculate the angle, for the arc such that:

$$\theta = 2 \sin^{-1} \left(\frac{\sqrt{W^2 + L^2}}{4r} \right) \quad (4.10)$$

where the arc angle, θ , is in radians.

Recalling equation 4.8, and the fact that an S-bend is made up to two arcs, we can say that the path length of the S-bend, L_{S-Bend} , is:

$$L_{S-Bend} = 4 \cdot r \cdot \sin^{-1} \left(\frac{\sqrt{W^2 + L^2}}{4 \cdot r} \right) \quad (4.11)$$

Path Difference between the Interferometer Arms

The path length of one arm can be defined by the following expression:

$$L_{path} = L_{straight} + 2L_{S-Bend} \quad (4.12)$$

In the device under examination, both the upper and lower straight sections have the same physical path length, thus they can be neglected in the calculation of the path difference.

The path lengths of the total S-bend length in the upper and lower arms can be denoted, $L_{S-upper}$ and $L_{S-lower}$ respectively. Thus the physical path difference between the two arms is simply:

$$L_{Phys} = L_{S-upper} - L_{S-lower} \quad (4.13)$$

Phase Shift of the Propagating Optical Mode

As an optical mode propagates through a waveguide, the phase it propagates with varies with distance. In the Mach-Zehnder interferometer, the phase difference between the interferometer arms can be precisely controlled by adjusting the optical path length of one arm. Interferometers are designed in accordance with the following relationship:

$$\delta = \frac{2 \cdot \pi \cdot L_{\text{diff}}}{\lambda_0} \quad (4.14)$$

where δ represents the required phase difference between the optical modes in the interferometer arms (in radians) and λ_0 is the freespace wavelength (in μm). L_{diff} represents the optical path difference (in μm), which is calculated by multiplying the freespace (or physical) path difference, L_{phys} by the effective index of the propagating optical mode, as such:

$$L_{\text{diff}} = n_{\text{eff}} \cdot L_{\text{phys}} \quad (4.15)$$

The effective index, n_{eff} , of a optical mode within a given waveguide structure can be evaluated analytically [8] or through the use of mode-solver software such as those found in commercial packages like BPM-CAD [12].

Using the expression shown in Eq.4.14, the optical path difference required for a $\pi/2$ (90°) phase shift at $\lambda=1.5\mu\text{m}$, would be $0.375\ \mu\text{m}$. Thus the quadrature point is obtained when an optical path difference equal to $\lambda/4$ is realised. This corresponds to a physical path difference of $0.259\ \mu\text{m}$ in a waveguide with an n_{eff} of 1.448.

Interferometer Response as a function of S-Bend width

The table in Appendix III contains the values of; W , L , r and L_{diff} , the calculated optical path length difference between the interferometer arms.

It was decided that the first S-bend in Table 4.1, of width $25\ \mu\text{m}$ and radius $40,000\ \mu\text{m}$, would be used as the primitive arm in the device structure. The phase shifts

would be implemented in the other arm by reducing the radius of curvature, thus increasing the transverse width of the device. This would maintain the minimum required arm separation of 50 μm for the reasons as described earlier in this section.

The phase difference, δ , between the propagating optical beams was calculated using the expression in Eq. 4.14 and used in evaluating the interferometric output function (Eq. 4.5) as a function of the transverse S-Bend width, W . The device is modelled at a wavelength of 1.55 μm , and an effective index of 1.448. A plot of the interferometer output function is illustrated in figure 4.5.

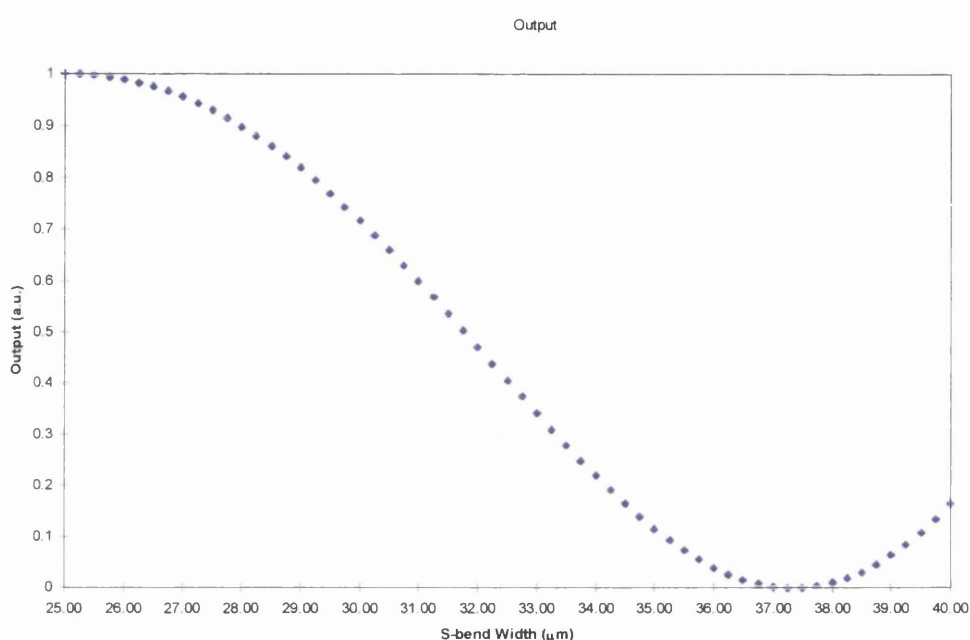


Figure 4.5 Theoretical output function of integrated Mach-Zehnder interferometer as a function of the transverse S-Bend width. The function is derived by comparison of the optical path length, with the primitive S-Bend structure, of width 25 μm .

From the plot it is clear a 90° phase shift occurs when the transverse S-bend width of the arm is approximately 32 μm . A 180° phase shifted device could be designed in principle by implementing an S-bend width of 37.75 μm , although such a device may have a somewhat limited functionality.

Theory versus BPM Simulation

The interferometer function modelled in the previous section provides useful information, with regards estimating the approximate device design. However, at best,

the expression used is simplistic, as effects such as polarisation sensitivity and propagation loss are neglected. The model also assumes ideal interference conditions in an exactly singlemode waveguide, thus limiting it to an approximation of the interferometer.

For this reason, the Beam Propagation Method (BPM) is used to more precisely evaluate the optical response of the waveguide interferometer. The BPM is more accurate in that it accounts for phase changes which arise as the mode propagates through the device. BPMs also account for differences in propagation loss and optical power between the interferometer arms, where such factors can influence the final device response. Inherent to the BPM technique, is modal analysis, where the BPM program precisely calculates the effective index as the mode propagates, unlike the theoretical model which assumes a constant refractive index. All these factors allow for more precise design and simulation of an interferometer.

BPM Simulation of Asymmetric Mach-Zehnder Interferometers

BPM simulation was carried using the BPM 2D program, which forms part of the BPM-CAD software package developed by the Optiwave Corporation [12]. The BPM 2D program simulates light propagation in a two-dimensional (2D) waveguide device. Provided that the waveguide has step like changes in refractive index, 2D simulation is an efficient and accurate method of evaluating waveguide performance.

The transverse dimension, or x-direction, represents an approximation of the X-Y cross-section of the waveguide, calculated using the effective index method [4]. The second dimension represents the direction of propagation, commonly referred to as the z-direction.

Table 4.2 illustrates the data used in simulating the waveguide device. The key parameters involved are the waveguide parameters, the wavelength and the propagation and transverse step sizes.

The simulation step sizes were selected by modelling the devices with a number of different step sizes and checking for convergence in the results.

BPM Model Parameter	Value
Wafer Length (μm)	15000
Wafer Width (μm)	150
Base Refractive Index (Buffer)	1.444
Waveguide Width (μm)	7.5
Waveguide Refractive Index	1.448*
Starting Field Type	Modal
Polarisation	TE or TM
BPM Solver	Paraxial
Boundary Conditions	Simple TBC
Wavelength	1.55 μm
Transverse Mesh Points	1500
Propagation Step	0.5 μm

Table 4.2 BPM simulation parameters and their values.

* The waveguide refractive index parameter can be swept by the software, thus allowing multiple simulations to be performed and recorded. However, at $\lambda=1.55 \mu\text{m}$, the refractive index of singlemode silica waveguides was calculated to be 1.448, and can be explicitly defined in this case.

Mach-Zehnder interferometers were designed using the data given in the Appendix, and constructed using the BPM_CAD drawing tools. The S-Bends in the structure were implemented using the software S-Bends Arcs Waveguide function. Figure 4.6 illustrates a typical asymmetric interferometer as designed using this package.

The optical power in the output waveguide is measured by monitoring the power overlap integral (POI) between the propagating optical field and the fundamental waveguide mode, where the POI is globally normalised to the input optical field.

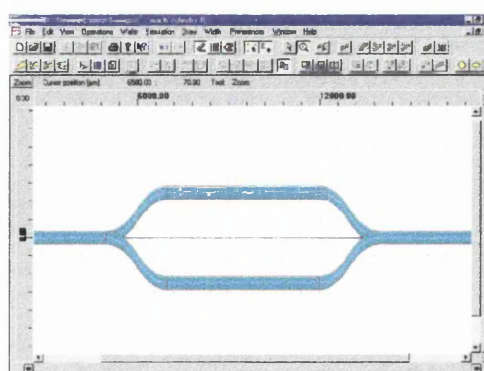


Figure 4.6: Schematic of an asymmetric interferometer (created using BPM-CAD [12])

Figure 4.7 (a-c) illustrates the output of 0, 90° and 180° phase shifted interferometers. These images give a graphical representation of optical propagation in waveguides. Image ‘b’ illustrates that there is some radiation loss at the combining Y-junction, where the resultant optical power in the output waveguide has clearly reduced. In the case of image ‘c’ it is clear that there is no propagating optical power within the waveguide which is confirmed by obvious increase in the scattered optical field. Both of these images confirm the concept of interference due to the introduction of an optical path difference between the waveguide arms.

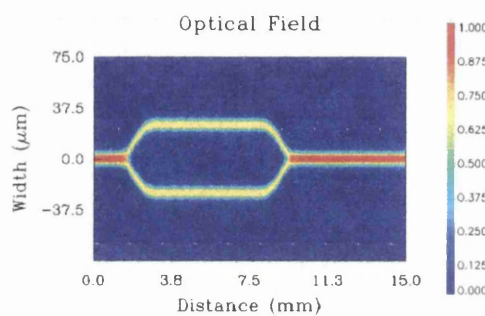
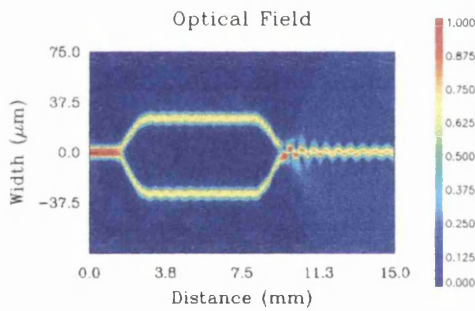
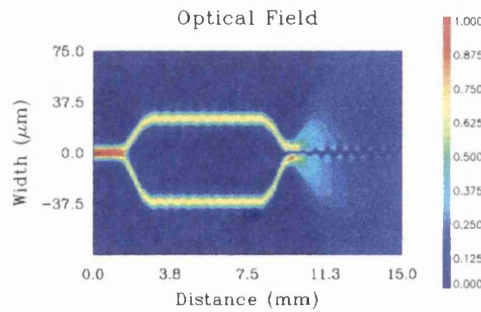


Figure 4.7 (a): Optical power propagating through the symmetrical interferometer (0°)



(b): Optical power propagating through the 90° shifted interferometer



(c): Optical power propagating through the 180° shifted interferometer

The path monitors for these devices further illustrate the interference due to passive phase shifting, where there is a 50% and 100% drop in propagating optical power for the 90° and 180°shifted devices respectively.

Path Length Difference Simulation

The BPM was used to simulate the performance of the symmetrical Mach-Zehnder interferometer, using the 25 μm S-Bend primitive. The path monitor indicated that the transmission of the interferometer was 0.9498061, which can be used to normalise the phase shifted interferometers, as this value gives us the intrinsic optical loss of the basic waveguide component.

Simulations were performed on whole number transverse width S-bends, i.e. 26, 27...31...39 and 40 μm . The path monitor outputs for these devices were normalised to the primitive device. The normalised output function is illustrated in Figure 4.8. Also shown in the plot is the theoretical output, as calculated using the expression in Equation 4.5. It is clear that a discrepancy exists between the theoretical and BPM output functions.

Further analyses were performed to investigate the source of the error.

- *Power imbalance between the interferometer arms.* This effect was estimated using the power split arising in a Y-junction, formed by a primitive S-bend and increasing the asymmetry of the junction. (Max error ~1 %).
- *Inaccuracy of path differences.* This was evaluated using asymmetric combiners (for 90 and 180° devices), and varying the phase of the optical field in the asymmetric arm (-45 and -90° respectively.). The phase was adjusted to maximise the Y-combiner output. (Max error ~1.5%)
- *Refractive index variations.* The refractive index was varied to change the optical path length, but it was found that the error was negligible for small path differences but increased with increasing path difference. (Max error ~3%).

These simulations ruled out the source of error being attributable to design errors. This led us to believe that the discrepancy may be related to the increasing asymmetry

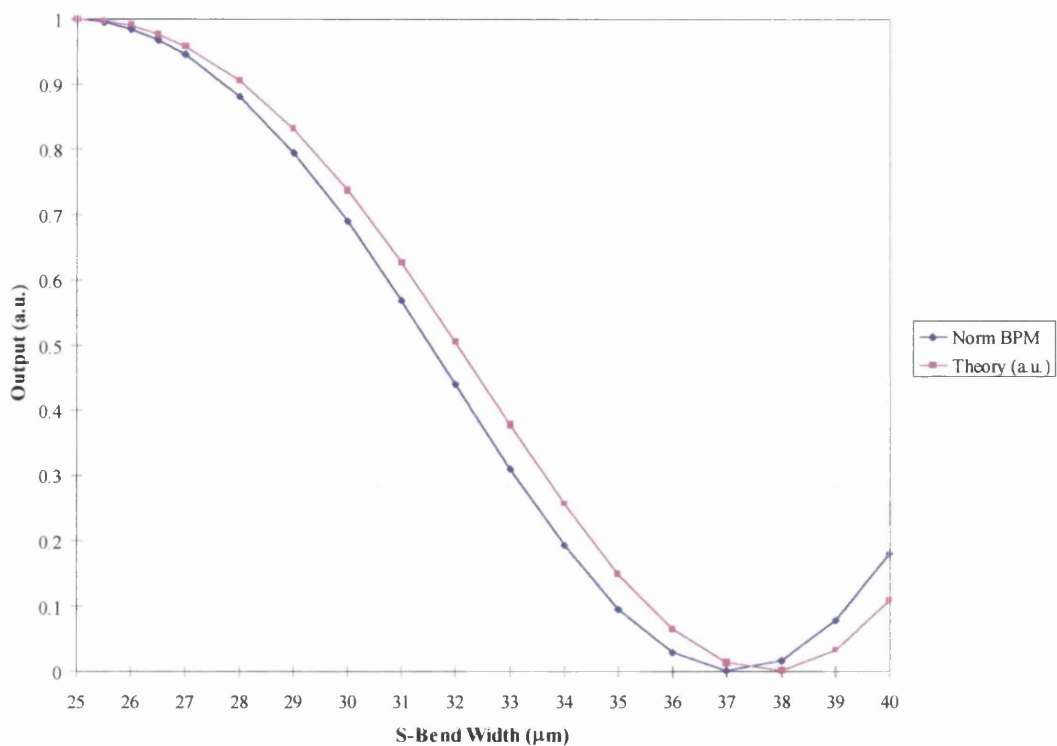


Figure 4.8 Normalised interferometer response as a function of increasing S-Bend width (simulated)

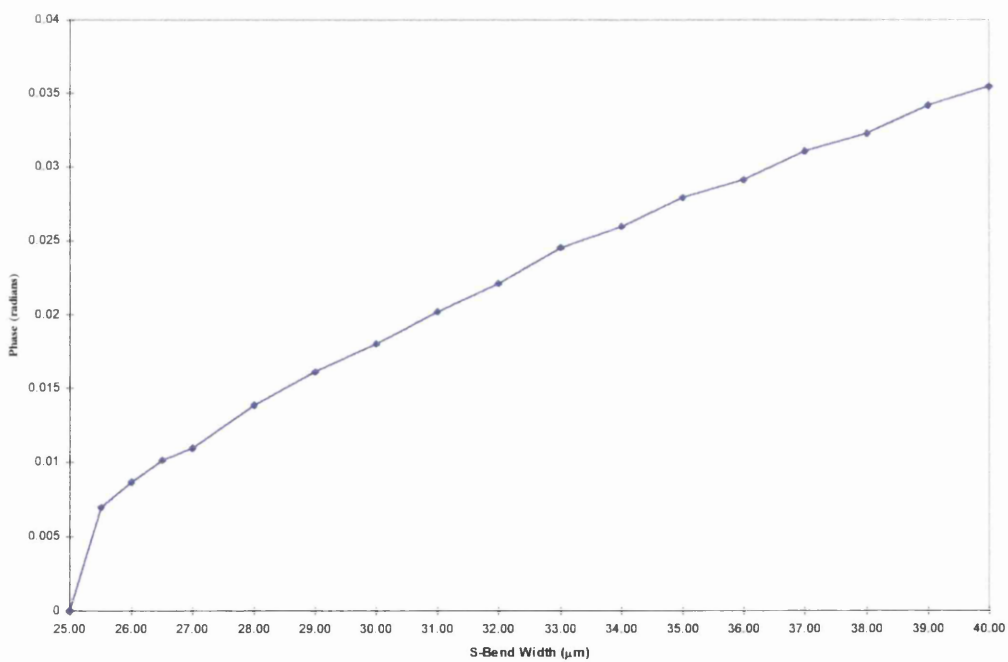


Figure 4.9 Phase error between BPM simulations and interferometer expression of Equation 4.5

of the Y-junctions. The phase difference that would give the same value as the BPM output was estimated theoretically. The phase error between BPM and the expected phase is plotted in Figure 4.9 as a function of transverse width. We can see that there is a jump in phase between the symmetrical device, at 25 μm , and the first asymmetric device at 26 μm . Increasing the asymmetry, or transverse width, further causes the phase error to increase.

This leads us to believe that the discrepancy between the theoretical and simulated output may be attributable to a phase shift which increases due to optical coupling in the asymmetric Y-junctions as they branch [13]. At this point, the available information is sufficient to design and fabricate passively phase shifted devices.

4.5.3 Asymmetric MZI Fabrication and Test

The core layer was formed from an $\text{SiO}_2\text{-GeO}_2\text{-B}_2\text{O}_3$ glass film fabricated using Flame Hydrolysis Deposition. The film had a thickness of 8 μm and an refractive index of 1.461 at $\lambda=632.8\text{ nm}$, corresponding to an index of 1.448 at $\lambda=1.55\text{ }\mu\text{m}$. The glass was patterned and etched using the original low power RIE process (Chapter 3,), where the etch mask was Shipley S1818 photoresist postbaked at 120°C.

Four different Mach-Zehnder interferometers were fabricated:

- Symmetrical MZI (transverse S-bend width of 25 μm)
- 80° Phase Shifted MZI (25 and 30.75 μm)
- 90° Phase Shifted MZI (25 and 31.25 μm)
- 100° Phased Shifted MZI (25 and 31.75 μm)

The symmetrical MZI is intended for use as a reference device to normalise the transmission of the other interferometers. The 80° and 100° interferometers are fabricated to bracket the 90° phase shifted device to examine the implications of fabrication tolerances, if any.

The devices were tested at wavelengths of 1.3 and 1.55 μm , using a loss measurement system. The operation of the system is described elsewhere, for example see the PhD thesis of Dr. J. R. Bonar [14]. The data is was normalised to the symmetrical MZI response. The collected data is illustrated in Table 4.3.

$\lambda=1.55\mu\text{m}$		Normalised Interferometer Output (a.u.)			
Phase Shift (°)	Theory	BPM	Set 1	Set 2	Mean
0	1.00	1.00	1.00	1.00	1.00
80	0.63	0.63	0.62	0.62	0.62
90	0.53	0.54	0.57	0.59	0.54
100	0.44	0.47	0.45	0.35	0.40
$\lambda=1.3\mu\text{m}$		Normalised Interferometer Output (a.u.)			
Phase Shift (°)	Theory	BPM	Set 1	Set 2	Mean
0	1.00	1.00	1.00	1.00	1.00
80	0.50	0.5	0.42	0.64	0.53
90	0.39	0.39	0.35	0.33	0.39
100	0.28	0.32	0.25	0.26	0.26

Table 4.3: Experimental interferometer response at $\lambda= 1.3$ and $1.55 \mu\text{m}$.

From the table it is clear that it is possible to design and fabricate asymmetric interferometers to within 2 or 3% of the intended function. Testing at $1.3 \mu\text{m}$ gives rise to slightly larger errors than at $1.55 \mu\text{m}$, which can be expected as the waveguide is not exactly singlemode, thus reducing the interference efficiency of the Y-junction.

The errors themselves can be attributed to two main factors: poor optical loss characteristics, ~ 5 dB, and experimental tolerances. The symmetrical interferometers typically exhibited a higher optical loss than an equivalent straight waveguide. Better fabrication processes would most likely reduce the magnitude of these errors, thus providing the motivation for the process optimisation described in earlier chapters.

4.6 Active Phase Control

In the previous section, small optical phase shifts have been introduced through passive design. These devices, whilst performing well, do have a number of disadvantages.

Firstly, the operating point of the device is limited by the fabrication tolerances inherent to the processes used. From Table 4.3, variation between sets of devices is small, but still sufficient to alter the performance of the device.

Secondly, the device function is influenced by atmospheric conditions. These devices are intended for use in hostile aerospace environments, where extremes of temperature and pressure are common. Interferometers designed for low-coherence operation are

necessarily large (>1 cm arm separation), and it is conceivable that a temperature gradient could occur across the device, shifting the operation point.

Lastly, and most importantly, the designed optical path difference (OPD) will only provide an 90° phase shift for optical fields at a precise wavelength, i.e. the intended wavelength of operation. In the multiple wavelength application that this device is intended for, this would require the design and fabrication of wavelength specific devices, increasing cost and complexity.

These problems can be overcome by actively controlling the OPD (expressed as $n\Delta L$) by varying the refractive index of one arm of the interferometer.

Silica based glass, in common with most dielectric optical materials, exhibits a phenomenon known as the Thermo-optic (TO) effect, that is, it possesses a temperature dependant refractive index. Understandably, thermal phase control has not received a lot of attention, as thermo-optic modulators and switches generally exhibit a slow response time (~ 0.5 ms), a characteristic of thermal effects.

By contrast, silica can exhibit another phenomenon, the Electro-optic (EO) effect. Unlike other optical materials such as LiNbO_3 and GaAs, silica glass films do not naturally possess an EO effect. However, through the techniques of thermal poling [15], and UV assisted thermal poling [16] it is possible to induce an the EO effect with a coefficient of upto 6 pm/V. Recently, the first demonstration of EO switching in thermally poled silica was reported by [17] where responses times of less than 100 ns were observed.

Optical phase tuning need not be particularly fast for optical sensing applications as the typical rate of change of a temperature or pressure sensor system is less than the typical thermo-optic response. In telecommunication applications, where high communication speeds are the norm, it is easy to see why the thermo-optic effect is so commonly ignored in place of its faster rival. However, it should be noted that the control voltages required for EO phase control are typically much greater than 1kV [17], approximately 10-20 times that required for TO control.

For these reasons, the TO effect is the preferred method of phase control in silica waveguides for interferometric sensing applications as it satisfies both the response and electrical power criteria. However, as understanding of the electro-optic effect in silica develops, lower voltage EO operation may be realised, making the EO effect the preferred method in the future.

4.6.1 The Thermo-optic Effect

The thermo-optic coefficient (dn/dT) of glass is of practical importance in both optical and optoelectronic systems [18]. For example, in bulk optic systems the temperature dependence of the refractive index of a lens should be considered, particularly where high optical powers are used, as the focusing characteristics will change. However, in optoelectronic systems it can be applied as a means of controlling the propagation of optical beams, for example thermally induced mode confinement in silica glass films [19] and thermally tuneable filters/switches [7].

The Physical Origin of the TO effect in silica glass

Few authors have contributed much in the way of information to explain the origin of the thermo-optic effect in glass. Published works have mainly taken the form of device analysis and or fabrication, where the TO effect is merely regarded as something that is generally understood, and is thus left unexplained. It is not the intention of the author to provide an analysis of this effect here, but rather to indicate its origin by reference to relevant literature.

Tsay et al [20] published one of the earliest works on the “temperature derivative of refractive index” for various semiconductor and ionic crystals in their transparent regime. The effect of temperature on the optical bandgap was considered as a function of electronic effects (arising from band-band transitions) and lattice contributions. They found that in semiconductor crystals electronic effects dominate, thus giving a positive dn/dT , whereas in largely ionic crystals they discovered that lattice effects were important resulting in negative coefficients.

In 1991, Matsuoka et al [21] published one of the first papers directly examining the temperature dependence of the refractive index of SiO_2 in the UV and visible regions

(238 to 546 nm) over the range -165 to 83°C. In their work they measured the refractive index of an SiO₂ prism over the given wavelength range for each temperature, where in their analysis they found that the energy shift of the second term of their Sellmeier equation closely correlated with the experimentally observed shift in the exciton peak. They also indicated that the thermo-optic effect in silica glass is dominated by electronic changes, rather than changes in material volume, which agrees with the generally accepted view that the TO coefficient in silica is largely positive.

Ghosh [22] extended the analysis of silica glasses, in 1994, to cover the ultra-violet to 1.7 μm wavelength range. This provided a physically meaningful model for the temperature derivative of refractive index which is accurate in the fibre optic communication windows at 0.85, 1.3 and 1.55 μm, and at shorter UV wavelengths.

Later in the same year, Ghosh [23] put forward a more complete analysis which examined the temperature dependent Sellmeier coefficients and chromatic dispersion for fused silica, Vycor and aluminosilicate glasses. These coefficients are useful in the optimal design of fibre optic communication systems.

Equation 4.16 describes the expression for the temperature derivative of refractive index (dn/dT) in silica glasses, in terms of the energy gap variation with temperature (dE_g/dT) and the linear expansion coefficient, α, from [22]:

$$2n \frac{dn}{dT} = \chi_e \left[-3\alpha - \frac{1}{E_g} \frac{dE_g}{dT} \frac{E_g^2}{(E_g^2 - E^2)} \right] \quad (4.16)$$

where n, χ_e, E and E_g are the room temperature refractive index, the electronic susceptibility, photon energy and a suitable bandgap in the vacuum ultraviolet region.

The term involving the bandgap dependence with temperature is generally large and negative (typically -10⁻⁴ eV/°) compared to the linear expansion term (typically 10⁻⁶/°) and thus tends to make the refractive index dependence with temperature positive. The latter term can be neglected in finite element modelling as its contribution to the thermal response is negligible.

Typically, dn/dT varies from 3×10^{-5} at UV wavelengths to around 1×10^{-5} at longer wavelengths. Figure 4.10 illustrates the variation of $2n \cdot dn/dT$ with wavelength where Ghosh's model is compared to the experimental results of various authors [references contained within Ghosh reference [22]].

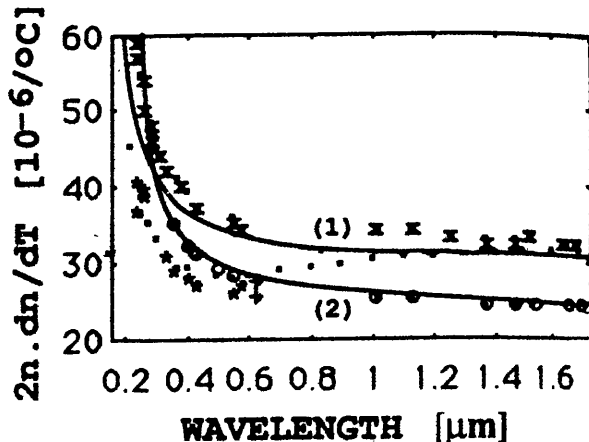


Figure 4.10: Variation of $2n \cdot dn/dT$ with wavelength (after Ghosh [22])

Preliminary observations of thermo-optic modulation

As a first attempt at observing the thermo-optic effect in FHD silica, heat was applied to a symmetrical Mach-Zehnder interferometer, of the type described in the previous section. The heat was applied to the device by locating a standard laboratory soldering iron in close proximity to the waveguide surface.

The tip of the soldering iron was located approximately 5 mm above the surface of the cladding layer, and approximately 1 cm away from one of the waveguide arms. After the soldering iron is switched on the temperature at the surface of the cladding increases. The heat diffuses through the glass surface until it encounters the first arm of the interferometer. The refractive index of the waveguide begins to increase, and as it does so the phase of the propagating optical beam within the waveguide, thus leading to a cyclic modulation of the output of the interferometer.

The optical response of the interferometer to increasing temperature using an Advantest Optical Spectrum Analyser (OSA). The OSA scanned at a point wavelength of 1.5423 μm. The OSA trace in Figure 4.11 clearly shows an

interferometric response to temperature, eliminating any suggestion of drifting optical coupling arising from thermal expansion and bending of the substrate.

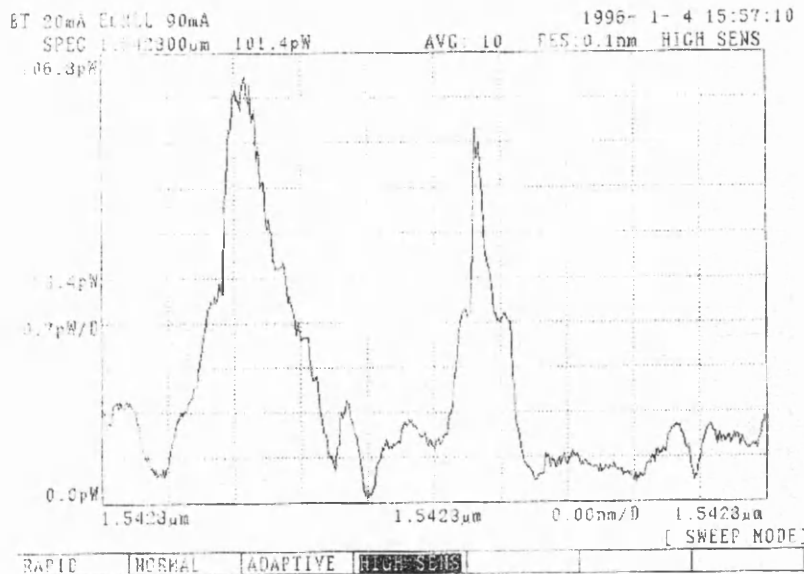


Figure 4.11 Response of interferometer to applied heat from a soldering iron

The fringe contrast was estimated from the plot to be 0.984. This corresponds to an extinction ratio in excess of 18 dB.

4.6.2 Integrated waveguide thermo-optic phase shifter [24]

After the initial confirmation of an interferometric response to applied heat, the next stage was to fabricate thin film electrode heaters which could be used to accurately control the phase of the propagating beams in the interferometer.

In this section a modular waveguide interferometer is presented. The design is compact with an interaction length of 5 mm. The device was designed for use as a modular integrated optical (IO) component for optical sensing applications, where it can be used as a phase tuning device in a fibre optic sensor network. Robust IO components offer increased performance and functionality in a compact, mass producible format, when compared to current fibre optic devices.

The device is modular in that it is capable of operating at multiple wavelengths with a high visibility. The principle function of this interferometer is to compensate for phase drifting between the reflected optical signals from a silicon microresonant sensor which

would normally lead to signal fading. Ideally the device should respond faster than the expected maximum rate of change of the environment in which the sensor is placed (~2ms for aircraft engines). Another specification, is that the device should be capable of applying a low frequency (~1 kHz) modulation to the reflected optical signals. Such a signal would then be processed through a Phase Locked Loop (PLL), where a variable dc signal would be applied to lock the interferometer at its quadrature point.

Device Fabrication

The TO phase shifter module consists of a symmetrical Mach-Zehnder (MZ) interferometer fabricated in glass with a thin film heater over one arm. As described earlier in the chapter, the device has Y-junctions for splitting and recombining the signal thus making the device suitable for use at multiple wavelengths. The waveguide film consisted of a 7.5 μm thick germano-silicate glass layer grown on 1 mm thick oxidised silicon substrates by flame hydrolysis deposition (FHD) [25]. The oxidised silicon surface is 10 μm thick and acts as a buffer for the waveguide structure. Waveguide structures with a 7.5 $\mu\text{m} \times 7.5 \mu\text{m}$ core were defined using a CHF₃ reactive ion etching (RIE) process [26]. A second FHD stage was used to deposit a phospho-silicate cladding layer, index matched to the thermal oxide. The relative refractive index difference between the core and cladding was 0.47 %.

Thin Film Heater Fabrication

Unfortunately, from an photolithography alignment point of view, silica waveguides cores are buried by a thick cladding layer. This makes it difficult to see either the waveguide core or any photo-lithographic alignment marks that may be on the device under microscope examination, (for example, see Chapter 6, Figure 6.2). Whilst it is just possible to see the cores after photoresist coating, it is almost impossible to see the waveguide after evaporation of non-transparent thin film electrode materials.

The natural solution to this problem is to use lift-off photolithography to fabricate the electrodes, but it has been shown [14] that it is difficult to evaporate thick (>50 nm) metal films onto photoresist, where in the experience of the author, residual stress and thermal mismatch caused the metal film to crack and peel.

Thus, it is necessary to use standard photolithography. A technique was developed where a locating pit, was created on the phospho-silicate cladding layer above the waveguide core, by wet etching the darkfield electrode pattern in hydrofluoric acid. The sample is then coated with a metal film, and patterned by a combination of photolithography (on the now visible locating pit) and NiCr wet etching. The process is described below with a photo-graph of the electrode pattern shown in Figure 4.17.

Thin Film Heater Patterning Process

1. Spin coat with Shipley S1818 photoresist (4000 rpm for 30 seconds),
2. Bake at 90°C for 30 minutes,
3. Align **darkfield** copy of electrode mask to the waveguide core,
4. UV expose for 10 seconds (HTG mask aligner), and develop for 75 seconds,
5. Check alignment of pattern under optical microscope,
6. Etch exposed cladding in 10:1 HF acid for approximately 5 minutes,
7. Evaporate 200-300 nm of the electrode metal film (in this case NiCr),
8. Repeat steps 1-4 using **lightfield** copy of electrode mask,
9. Etch metal film in suitable wet etch (Chrome etch if using NiCr film for reasons described in Chapter 2),
10. Check electrode for alignment and continuity under optical microscope.

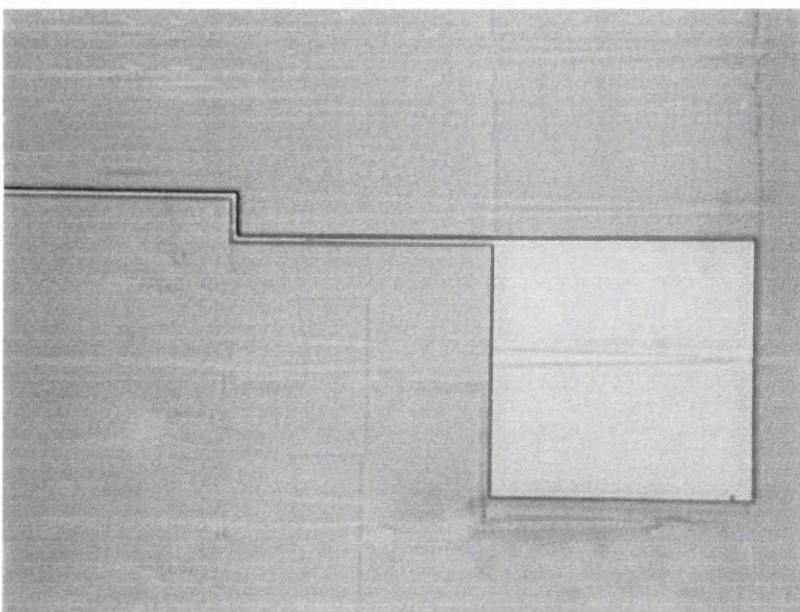


Figure 4.17 Photograph of the part of the 16 μm wide thin film heater located above one arm of the interferometer. The large square region is used as the contact region for the electrical probes. Just visible are the buried waveguide y-junctions.

The resistance of the thin film heater is measured by a four-point probe technique using a Hewlett Packard Parameter Analyser. In the device discussed in this section, the electrical resistance of the thin film was found to be $4.5\text{ k}\Omega$. The thin film heater is $16\text{ }\mu\text{m}$ wide, $5000\text{ }\mu\text{m}$ long (the length of the arm) and 200 nm thick.

Experimental Measurements

The insertion loss of the device was measured using a modulated semiconductor laser coupled into the waveguide device through a single-mode optical fibre. A multi-mode fibre took the output to a lock-in amplifier via a photo-detector, where the insertion loss was found to be -3.5 dB greater than similar straight waveguides ($\sim 1.5\text{ dB}$) at $1.55\text{ }\mu\text{m}$. This excess loss was attributed to poorly defined Y-junctions after using resist etch masks, where a wedge, rather than a point was typically observed.

Two electrical probes were used to apply a voltage to the electrode heater. The power supply was rated to give a maximum dc voltages of 100 V in 10 mV steps. The unit was programmable, but it was subsequently found that its programmed response time was much slower than the thermo-optic device under examination.

As a result, a custom circuit was constructed in order to apply ac signals to the interferometer. An amplifier circuit was constructed using a power MOSFET which could handle a maximum current of $\sim 100\text{ mA}$. The rise time of the FET was of the order of 100 ns , much faster than that of the thermo-optic response, thus sufficient for temporal measurements on the interferometer. The circuit was externally triggered using a standard lab variable power supply with variable pulse width, delay, frequency and voltage (max. 10 V). The minimum trigger voltage for the circuit was 7 V . The power supply unit was used to power the amplifier with the thin-film heater forming the collector load.

Spectral Response

The spectral response of the Mach-Zehnder interferometer was obtained as a function of the electrical power is shown in Fig. 4.18. The electrical power was applied using the amplifier in a steady state, where the power was increased by increasing the power supply voltage.

The optical response of the interferometer to applied electrical power was monitored at a wavelength of 1.3 and 1.55 μm using a photodetector and lock-in amplifier. The power required for a null (corresponding to a π phase change between the two arms of the interferometer) was 0.67 W and 0.94 W, for 1.3 and 1.55 μm respectively. These power levels correspond to applied voltages of 55 and 65 V (based on the electrical resistance of the heater, 4.5 k Ω), corresponding to a current of 12.2 and 14.45 mA, at 1.3 and 1.55 μm respectively. It has been suggested that the current density of these electrodes of these devices are well below the electro-migration threshold of NiCr, which implies that it may be possible to package the device in a non-hermetic housing. The extinction ratio was measured to be greater than 30 dB which represents the limit of the loss measurement system.

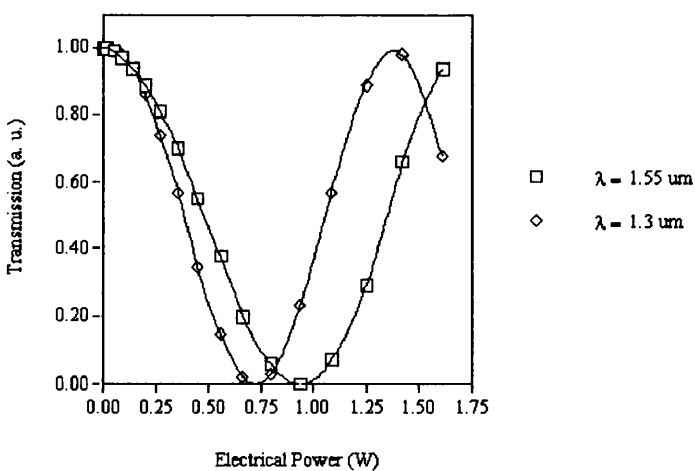


Figure 4.18 Spectral response of the Mach-Zehnder interferometer to applied electrical power. Of note is the power required for a null, 0.67 and 0.94 W at a wavelength of 1.3 and 1.55 μm respectively.

Caution must be used when taking optical measurements at high electrical powers as thermal crosstalk begins to take effect. The problem can be solved by ensuring that the measurements are taken quickly.

The electrical power required for a null are higher than those reported elsewhere [for example see [7, 27, 28, 29, 30]. However, it will be shown later in the finite element modelling section of this chapter, that a lower electrical power typically results in a slower response time, a characteristic which is shown to be favourable compared to other devices.. This illustrates that the electrical and optical response characteristics of a thermo-optic device must examined in association with each other, and not in isolation.

The results also confirm the explanation of Haruna et al [27] that the optical response is not linearly proportional to the applied voltage, but rather to the electrical power ($=V_{app}^2/R$), as was plotted in figure 4.18.

Temporal Response

As mentioned previously, an important factor in the operation of these devices is the speed of response to changes in the applied electrical power. The temporal response of the device was examined by applying a voltage pulse to the thin film heater. The applied voltage was 65 Volts (Power=0.94 W), corresponding to the null point of the interferometer. The output from the photo-detector was taken to a Gould digital oscilloscope where the optical response was analysed.

Figure 4.19 illustrates the response of the interferometer to the applied step voltage, where an analogy can be observed to that of an electrical RC circuit. Indeed it is possible to use this analogy to model the response of a thermo-optic interferometer, as will be demonstrated in the next section.

The optical signal was analysed by the rise time function of the oscilloscope, which calculated the 10:90% rise time, t_r , as 152 μ s. t_r varied from 148 μ s to 154 μ s during testing, however this can be attributed to the noise associated with the optical signal. The optical fall time , t_f , of the device was found to be the approximately the same as the t_r . Compared to other referenced devices, this device is nearly twice as fast as other devices, albeit at a slightly higher power. However Haruna et al [27] and Takato et al [7] are operating at a shorter wavelength which is obviously beneficial for low power operation, by reference to Figure 4.18.

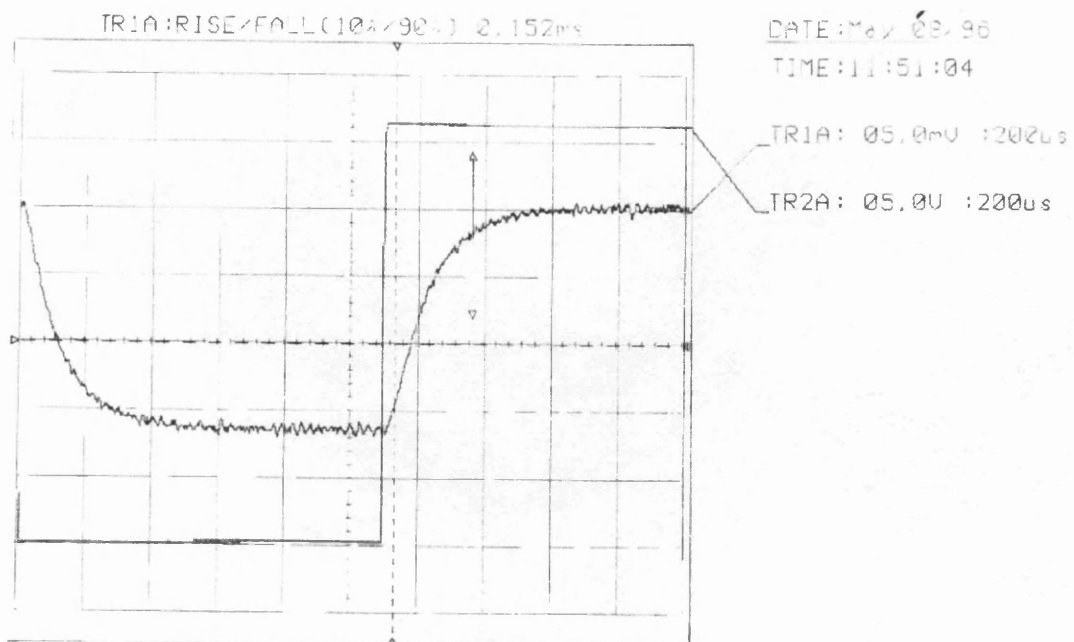


Figure 4.19 Response of waveguide interferometer to a step voltage input, t_r - 152 μ s

Using t_r as a figure of merit, it was estimated that the maximum operating frequency of this device was approximately 3 kHz. This is the maximum frequency at which the device will operate while still maintaining a maximum extinction ratio >30 dB. In the next section, the concept of overdriven switching is discussed, where faster operation can be achieved.

Finally, for this section, Figure 4.20 illustrates the response of the interferometer when used as a modulator. A modulated electrical signal, pulse width 600 μ s at a frequency of 833 Hz, was applied to the interferometer. Again, as before, a symmetrical pulse shape was obtained with a measured rise time of 148 μ s.

It has already been mentioned that the practical implementation of the waveguide interferometer would require the use of a phase locked loop. The thermo-optic modulation response presented here would be sufficient to supply a low frequency modulated reference signal, ~ 1 kHz, to one arm of the interferometer. The phase of the signal can be monitored through the use of a phase-locked loop (PLL), thus maintaining the phase quadrature points in a tandem configuration of interferometers.

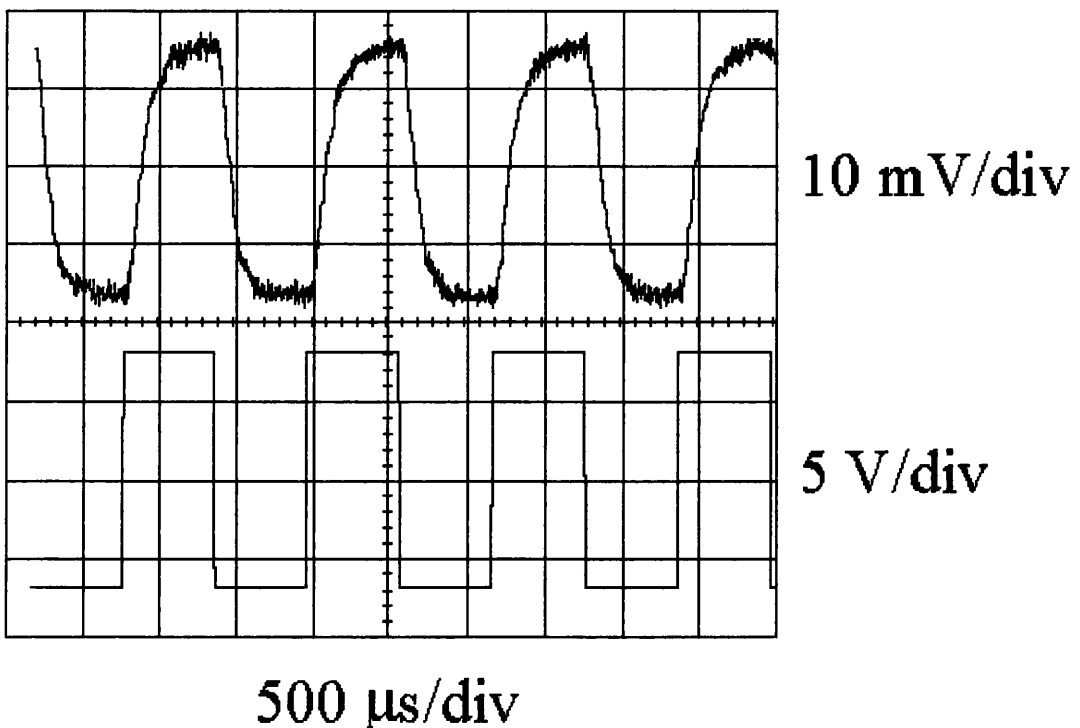


Figure 4.20 Reponse of interferometer (upper trace) to applied voltage signal (lower trace), pulse width 600 μ s and frequency 833 Hz.

4.6.3 Simulation of Overdriven Thermo-optic Modulators

Until this point, the thermo-optic response has been considered under the condition that the applied voltage signal had a pulselength longer than the response time of the thermo-optic device. Haruna et al [27, 31] examined the condition, where the pulselength is shorter than the response time of the device, and the necessary increase in the applied voltage signal. This condition is known as Overdriven Thermo-optic Switching.

In order to overdrive the device, a significant increase in the applied electrical signal is required. During the investigation, the thin-film heater was subjected to large currents, the effect of which is shown in Figure 4.21. As a result of the excessive current loads placed on the electrode heater, electrical breakdown of the device was observed.

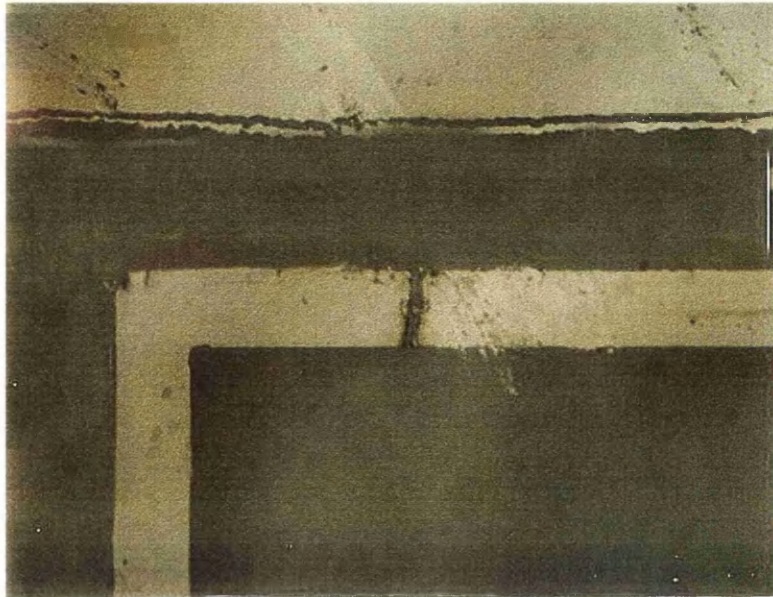


Figure 4.21 Photograph of the fused thin film heater, after application of 100V (2.2 W)

It is possible to model the response of a thermo-optic device using an analogy to an electrical RC circuit [32]. In such a model, the impedance is related to the ratio of the temperature swing to the heat flow and the heat capacity of the film is analogous to the capacitance, C. The voltage applied is analogous to the temperature applied by the thin film heater. R and C are chosen such that they gave the correct normally driven optical rise time as measured (148 μ s).

A simple model was defined based on a simple RC circuit, where the temperature applied was calculated from the applied electrical signal:

$$\text{Temp} = A_t \cdot \left(P_{\text{sig}} - P_{\text{sig}} \exp\left(\frac{-t}{10 \cdot RC}\right) \right) \quad (4.17)$$

where R and C were chosen to be 11.25 k Ω and 1 μ F respectively, A_t is defined here to be the electrical power to temperature coefficient, estimated to be 11.383 from the finite element modelling data in the next section, and t represents time. P_{sig} in the first instance, was defined as the power required for a null, 0.94 W. The data is input into the interferometer expression given by the following equation:

$$P_{\text{out}} = 0.5 \cdot \left(1 + \cos\left(\frac{2 \cdot \pi \cdot n_{\text{eff}} \cdot \frac{dn}{dT} \cdot \text{Temp} \cdot L}{\lambda}\right) \right) \quad (4.18)$$

where n_{eff} , dn/dT , L and λ are 1.448, 1×10^{-5} , 5000 μm and 1.55 μm respectively.

Figure 4.22 illustrates the change in the optical response of the interferometer for applied electrical powers. At 0.94 W, the rise time of the signal is 152 μs , and by subsequently increasing the applied power to 1.69 and 2.82 W, the rise time falls to just 52 and 27 μs respectively. We can also see that the number of cycles over the given time scale increases with increasing electrical power.

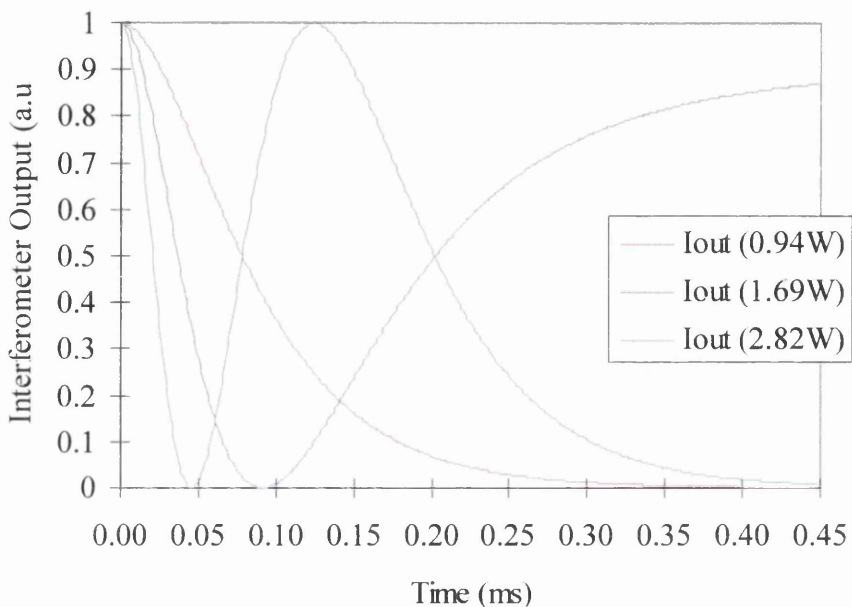


Figure 4.22 Model of influence of increasing electrical power on the interferometer response time

In summary, faster overdriven operation is obtainable by applying more energy than required, sufficient to take the device through more than one optical cycle, with a pulsewidth short enough to allow a single modulation.

Whilst it is interesting to be able to decrease the thermo-optic response time, it is only useful if continuous modulation is required. It would be more complex (to design the PLL control system) and unnecessary to use the overdriven regime to tune the phase of the interferometers. Similarly, the overdriven system would be difficult to control in transmitting a binary sequence of data, as exact electronic control would be required.

4.7 Finite element modelling of a thermo-optic modulator

It has been shown in previous sections, and by other authors, that it is possible to achieve reasonable response times at modest electrical drive powers through the use of the thermo-optic effect. The objective of this section is to examine the possibilities of using silica RIE and/or CVD diamond deposition to improve the temporal and electrical characteristics of a silica waveguide modulator [33].

The feasibility of implementing these techniques has been studied using a finite element analysis (FEA) model of the silica waveguide. FEA was used to estimate temperature changes arising from the application of electrical power to the thin film heater, where the data obtained was used in evaluating the temporal response of the interferometer.

Device Design

The interferometer under investigation is a symmetrical Mach-Zehnder interferometer as described in previous sections. Figure 4.23 illustrates the 3-D layout of the thermo-optic modulator structure.

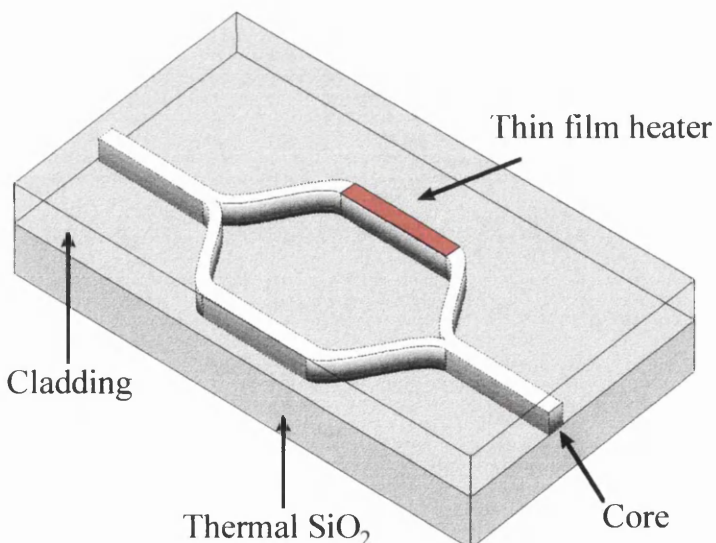


Figure 4.23 Schematic of silica based integrated optic Mach-Zehnder interferometer with thermo-optic phase control for use in low-coherence sensing applications.

4.7.1 Model Development

The output of a symmetrical two beam interferometer can be expressed as: [34]

$$I = 2I_0(1 + \cos\delta) \quad (4.19)$$

where δ is the phase difference between the two interferometer arms and I_0 is a constant intensity value. The phase difference, δ , can be expressed in terms of the optical path difference, L_{diff} , induced by the temperature difference, ΔT , between the two arms where from Equation 4.14:

$$\delta = \frac{2\pi}{\lambda_0} \cdot \left(n_{\text{eff}} \cdot \frac{\partial L}{\partial T} + L_{\text{phys}} \cdot \frac{\partial n}{\partial T} \right) \cdot \Delta T \quad (4.20)$$

where λ_0 is the free space wavelength, n_{eff} is the waveguide refractive index, L_{phys} is the length of the heated portion of the waveguide. The expressions $\partial L/\partial T$ and $\partial n/\partial T$ are the material thermal expansion and thermo-optic coefficients respectively.

Rogers et al [35] quote the fractional change in path length in an optical fibre due to a temperature change of 1°C as 6.3×10^{-6} . This value includes contributions from thermal expansion and the temperature dependence of refractive index, with the latter being the dominant term, a result of the origin of the thermo-optic effect.

In the case of planar waveguides, the substrate remains at room temperature throughout the experiments and therefore will limit free-expansion of the waveguide in the z-direction [29]. Consequently the thermal expansion coefficient of $5.5 \times 10^{-7} \text{ }^{\circ}\text{C}^{-1}$ [32] can be ignored. Subtracting this from the overall effect gives a value for $\partial n/\partial T$ of $5.75 \times 10^{-6} \text{ }^{\circ}\text{C}^{-1}$. These values are quoted for a wavelength of 633 nm, whereas at 1.3 and 1.55 μm they are lower [18].

Thus the optical output can be re-expressed as:

$$I = 2I_0 \left(1 + \cos \left(\frac{2\pi}{\lambda_0} \cdot L \cdot \frac{\partial n}{\partial T} \cdot \Delta T \right) \right) \quad (4.21)$$

I_0 is a constant and setting it to a value of 0.25 will give a normalised response between a maximum intensity of 1 and a minimum of 0. The values for λ_0 and L are known. In order to solve this equation we use FEA to evaluate ΔT , by calculating the temperature of the waveguide core as a function of time.

In evaluating the thermal characteristics of waveguide devices, a solution must be found for the 3-D, time dependant, thermal diffusion equation:

$$\frac{\partial}{\partial x} \left(K_x \frac{\partial T}{\partial x} \right) + \left(K_y \frac{\partial T}{\partial y} \right) + \left(K_z \frac{\partial T}{\partial z} \right) + S = \rho C_p \frac{\partial T}{\partial t} \quad (4.22)$$

In this equation, T represents the temperature in Kelvin or $^{\circ}\text{C}$, where either unit is applicable as temperature is evaluated relative to ambient. K_x , K_y and K_z denote the thermal conductivity in the x , y and z directions respectively, measurable in $\text{Wm}^{-1}\text{K}^{-1}$. These coefficients allow the definition of thermal anisotropy, for example in laminates and CVD diamond. The heat source term, S , is non-zero in any heated regions, where it has units of Wm^{-3} . The specific heat, C_p ($\text{Jkg}^{-1}\text{K}^{-1}$), is multiplied by the material density, r (kgm^{-3}), to give the specific heat capacity ($\text{Jm}^{-3}\text{K}^{-1}$).

In this model, the time dependant solutions are required to evaluate the temporal response of a waveguide. However, in the case of solving for thermal crosstalk between waveguides, a steady state solution can be obtained by setting the time dependant term, $\partial T/\partial t$, to zero, thus simplifying the equation.

Assumptions

The thermo-optic modulator under investigation utilises a long, thin film heater to heat the optical system. It is assumed that no net heat flow occurs along the heater, i.e. it is in thermal equilibrium along its length. Thus the dT/dz term can be set to zero, and omitted from the thermal diffusion equation, which simplifies the problem from a 3-dimensional problem to that of a 2 dimensional case. Equation 4.22 is now re-written as:

$$\frac{\partial}{\partial x} \left(K_x \frac{\partial T}{\partial x} \right) + \left(K_y \frac{\partial T}{\partial y} \right) + S = \rho C_p \frac{\partial T}{\partial t} \quad (4.23)$$

This equation is now solvable using a commercially available 2-D finite element software package, PDEase [36]. The cross-section, A-A', in Figure 4.24 shows the 2-D region that is modelled.

Thin film heater

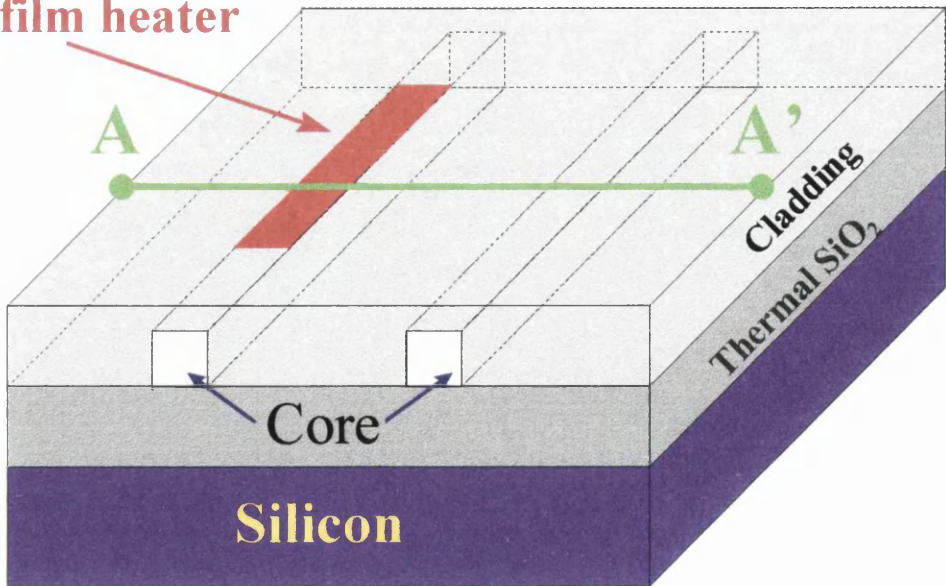


Figure 4.24: The 2D waveguide cross-section is defined in the model along the line (A-A')

It is assumed that cooling due to radiation can be ignored over the temperature range obtainable in this system, no more than 40°C above ambient. In fact, radiation loss is only influential if it is as large as cooling due to convection, which occurs when the temperature change in the system is >500°C [37]. Therefore, the major heat loss mechanism is that of thermal conduction. A similar assumption is described by Brown et al [32] in their consideration of the electrical circuit analogy of a thermal system.

It is also important to consider the conservation of energy, where power supplied by the thin film heater is linearly proportional to that of heat generated. Any proportional increase in power will manifest in the same proportional increase in heat generation. However, this condition only holds, subject to the condition of the previous paragraph.

Finally, the last assumption is that the modelled waveguide cross-section has the same geometrical and/or physical properties of that of the real as-fabricated device.

Material Properties

Table 4.4 shows some of the properties for the materials used in fabricating the thermo-optic modulator. All data was taken from data tables [38, 39] with the exception of NiCr. The composition of the evaporated NiCr films was unknown at the

time of investigation, thus the data used represents the average of the material properties of nickel and chrome.

Like NiCr, the thermal properties of the FHD produced glass films are not known with any certainty, thus the values used are likely values taken from the literature.

Material	Density (kg m ⁻³)	Heat Capacity (J m ⁻³ K ⁻¹)	Thermal Conductivity (W m ⁻¹ K ⁻¹)
Si	2328	1.636×10^6	149
Cr	7180	3.214×10^6	93.9
Ni	8902	3.948×10^6	90.9
¹ NiCr	8040	3.550×10^6	92.4
Fused SiO ₂	2210	1.657×10^6	1.318
Glass	2400-2800	1.740×10^6	2.20
² Diamond	3515	1.810×10^6	2000

Table 4.4 Selected material properties for common materials used in fabrication of silica based thermo-optic modulators. ¹Average of the material properties of Ni and Cr. Data from [38], except ², taken from [39].

From the data it is important to note the significance of the thermal conductivity of the materials. From the data it is clear that the thermal conductivity of fused SiO₂ and glass is significantly lower than that of silicon, thus highlighting the fact that thermal diffusion through the waveguide layers is the major constraint on the response speed of a thermo-optic modulator. Conversely, diamond possesses a very large thermal conductivity, which significantly improves the speed at which heat is dissipated.

The thermal properties of doped silica glass produced by flame hydrolysis deposition are unknown, despite a literature search on thermal effects in silica glass. Thus the data for silica glasses in general was used. It is not expected that the heat capacity of doped silica films would differ by much, as the bulk composition of FHD glass is typically 80-90 wt% silica. However, the inclusion of boron, germanium and phosphorous oxides in the glass system could make a difference to the thermal conductivity. It is also assumed that the thermal properties of the core and cladding are the same as the core, as there is unlikely to any significant variation.

In the original model, it was found that the optical response tended to overshoot the expected null point. As a result, it was necessary to vary the thermo-optic coefficient in order to help fit the model to the experimental data. This has the result of reducing the optical phase shift for the given predicted rise in waveguide temperature. As an alternative, the applied voltage could have been varied, thus reducing the temperature change in the waveguide. However, altering the applied voltage would further distance the model from reality.

4.7.2 Validation of the Finite Element Model

The FEA model was created and modified to fit the experimental results collected in previous sections. A summary of the experimental data is shown in Table 4.5 below. This data shows the electrical power required to null the interferometer at 1.3 and 1.55 μm , taken from Figure 4.19. Also shown is the temporal response for the normal and overdriven case. In the model, the time t_{fall} corresponds to the experimental t_{rise} .

Case Number	λ (μm)	$\delta n/\delta T$	V_{null} (V)	P_{null} (W)	t_{rise} (μs)	Model t_{fall} (μs)
1	1.3	5.0×10^{-6}	55	0.67	148	175
2	1.55	4.3×10^{-6}	65	0.94	148	175
3	1.3	5.0×10^{-6}	90	1.8	48	28

Table 4.5 Summary of experimental thermo-optic data, and corresponding FEA model results

Model 1 in Appendix II illustrates the basic data file used to define each of these experiments, where MZ1 specifically defines the conditions of Case 1. Case 2 and 3 were defined by modifying MZ1 to account for the different wavelength, λ , and respective null voltage, V_{null} . dn/dT was changed in Case 2 to account for wavelength [18] dispersion. The pulsewidth of the applied electrical signal in Case 1 and 2 was 1.2 ms, sufficiently long for one pulse, whereas in Case 3 it was reduced to 50 μs .

For the purposes of modelling ambient temperature is defined to be 20°C, where it was found that in all modelled cases the substrate temperature did not change.

Case Number 1

One of the critical factors in designing thermo-optic waveguide components is the problem of thermal crosstalk, described in Section 4.5.1. Ideally the arms of an integrated Mach-Zehnder interferometer should be sufficiently far apart that there is no thermal crosstalk. However, it is shown in Figure 4.25(a) that the predicted temperature rise at the designed core separation of 50 μm is 2°C, compared to 28°C at the core. In phase terms, a 2° rise in temperature amounts to ~ 0.25 radians compared to $\sim \pi$ radians at the heated core, raising the normalised null point to 0.03.

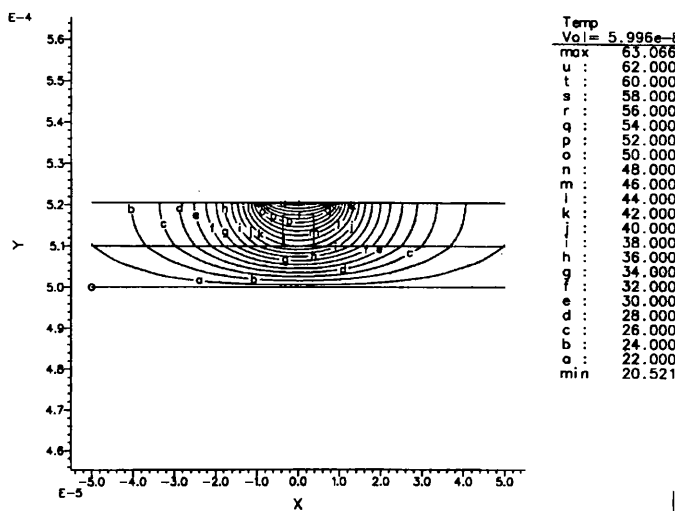


Figure 4.25 (a) Plot of thermal distribution through silica waveguide structure. Of note is the temperature at $\pm 50 \mu\text{m}$, indicating a thermal crosstalk of $< 2^\circ\text{C}$

Figure 4.25 (b) shows a close-up of the heated waveguide core where it can be observed that there is a temperature difference of 14°C between the top and bottom of the core. However, it is considered that the waveguide is singlemode, where the propagating optical mode has a gaussian like field distribution, thus placing the majority of the propagating field near the centre of the core, where the temperature change is 28°C, sufficient to null the interferometer. Also, it is noted that the maximum temperature is $\sim 63^\circ\text{C}$ at the heater, and that the heat diffuses away from the heater toward the substrate, at the ambient temperature of 20°C.

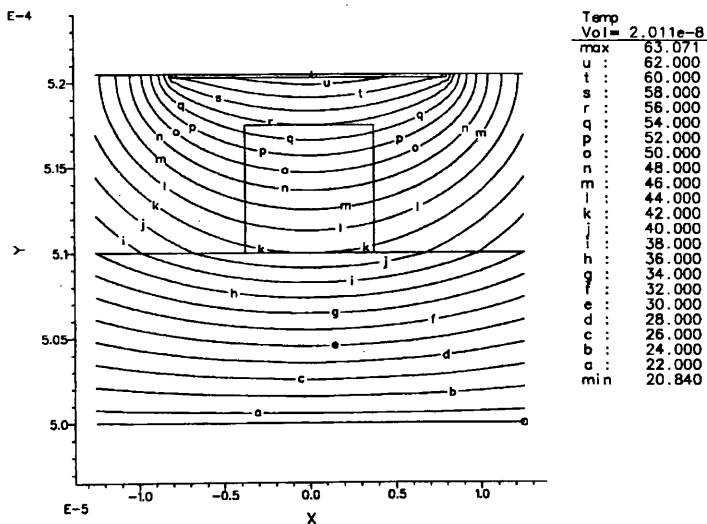


Figure 4.25 (b) Close-up of the waveguide core region of Figure 4.28 (a), showing a temperature difference of 14°C from the top to the bottom of the core.

The results described in the previous paragraphs describe the thermal condition at a given point in time, in this case after saturation of the thermal response. Figure 4.25 (c) shows the change in temperature with time, at the top, middle and bottom of the waveguide core. It is clear that the thermal response at each of these positions is the same, in that they exhibit the same rise and fall times. However, a small delay occurs between each point, due to the time taken to diffuse through the core.

Figure 4.25 (d) illustrates the change in the normalised optical output of the interferometer for the given change in temperature at the centre of the core as a function of time. From this we can see that the fall time is 175 μ s, compared to a rise time of 200 μ s, where the asymmetry in pulse shape arises from the asymmetric waveguide cross-section. The value of the fall time is in good agreement with the experimental case which exhibited a response time of 148 μ s.

Due to the cosine relationship between temperature and optical intensity, it is found that the thermal response is much slower than the optical response, as the thermal response takes longer to saturate, whereas the relatively small changes in temperature have little effect on the ultimate null point of the interferometer.

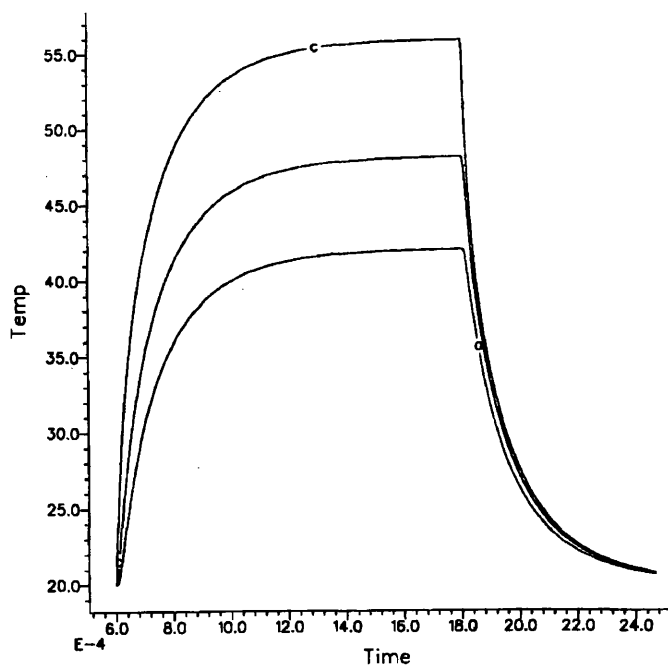


Figure 4.25 (c) Temporal *thermal* response of the thermo-optic interferometer at the top, middle and bottom of the core region. Note the time lag between the top and bottom due to thermal diffusion.

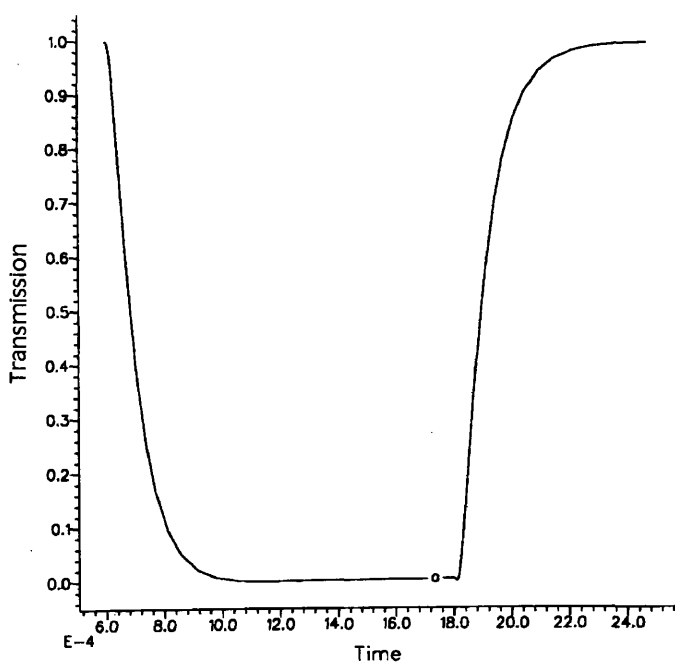


Figure 4.25 (d) Temporal *optical* response of the thermo-optic interferometer, calculated from the thermal response at the centre of the core. The optical fall time is found to be 175 μ s.

Case Number 2

The thermal crosstalk at $1.55 \mu\text{m}$ was found to be slightly higher, $\sim 3^\circ\text{C}$, than that of Case 1, attributable to the fact that a higher electrical power is required to null the interferometer. This increases the central core ΔT to $\sim 38^\circ\text{C}$, compared to the 28°C found in Case 1, which is sufficient to give an optical null from the interferometer.

The temporal response of the model at the slightly longer wavelength of $1.55\mu\text{m}$ was found to be exactly the same as that found at $1.3\mu\text{m}$, as expected. This is expected as the temporal response is restricted, not by the size of temperature change, but by the thermal conductivity and heat capacity, c.f. electrical RC circuit analogy.

Case Number 3

An advantage of overdriven thermo-optic modulation is that the applied electrical signals are very short. Figure 4.26 (a) illustrates that the lateral heat diffusion of the thermal signal is restricted, such that thermal crosstalk is reduced to zero. The predicted lateral heat diffusion is $\sim 20 \mu\text{m}$, less than half of that observed under normal operating conditions.

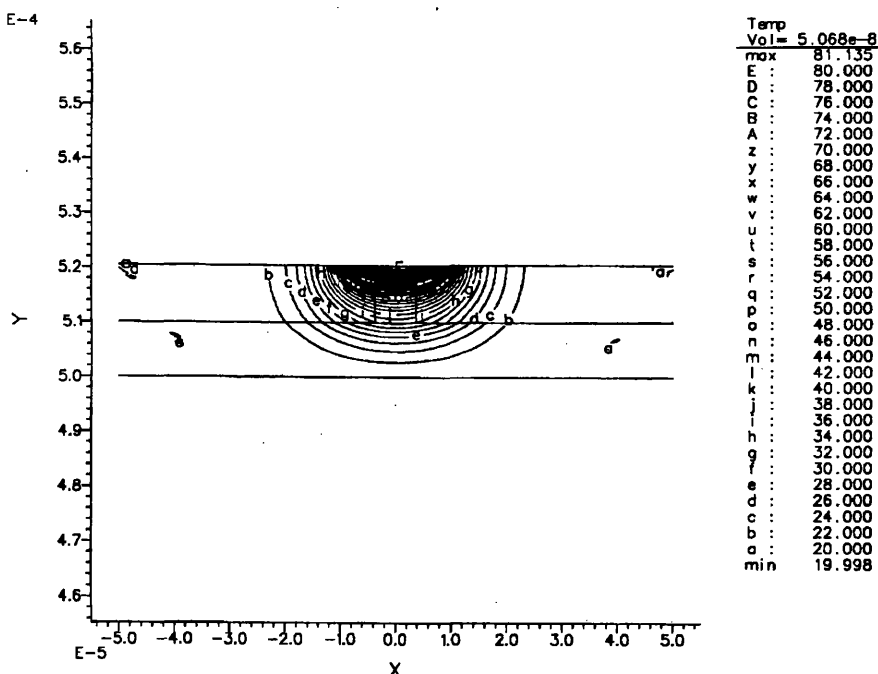


Figure 4.26 (a) Reduced thermal diffusion during overdriven operation, making thermal crosstalk 0.

As in Case 1, the predicted temperature change at the centre of the waveguide was approximately 28°C, again this is sufficient to null the optical output.

The optical output shown in Figure 4.26 (b) exhibits a fall time of 28 µs and a rise time of 152 µs. Again this is in reasonable agreement with the experimental case shown in Table 4.5. As in the previous cases, the rise time is slow due to the asymmetric cross-section of the waveguide.

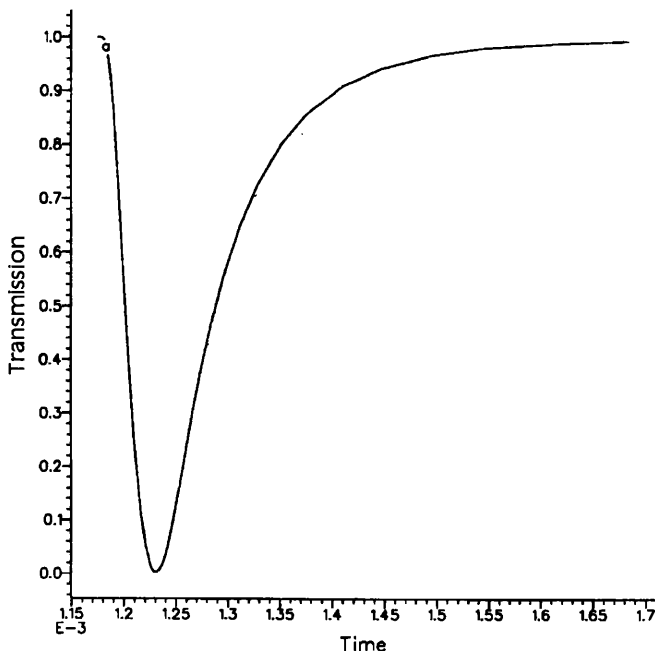


Figure 4.26 (b) Simulated overdriven response, with a 28 µs fall time.

Conclusions

Comparing the FEA and experimental data we can see that the modelled response times agreed with the experiment to within a factor of 1.2. These facts suggest that the thermal properties used in the model may not be optimised and the experimental structure may not have the exact same profile as the modelled one. However, the results are sufficiently close to the experimental case for these values of thermal properties to be used in qualitatively modelling novel structures.

4.7.3 Finite Element Analysis of Novel Thermo-optic Modulators

The finite element analysis technique has been shown to be a valuable tool in evaluating the thermo-optic response of a silica waveguide. Whilst the exact thermal properties of the glass systems are as yet unknown, it is reasonable to accept that this model would be sufficient to examine changes to cross-sectional device design. Until such point as precise material data is available it is clearly unwise to consider the effects of changing glass systems, for example through dopant addition.

As such, the model has been used to examine novel device structures which exhibit faster response times or reduced electrical power consumption.

Reduced Power Consumption

Case 4: Introduction of Thermal Anisotropy

Power consumption can be reduced by limiting the lateral heat spreading of the applied heat, i.e. reduce loss by thermal diffusion. This can be achieved by introducing a form of ‘thermal anisotropy’ into the waveguide structure by deep reactive ion etching of grooves into the over-cladding surrounding the waveguide, illustrated in Figure 4.27.

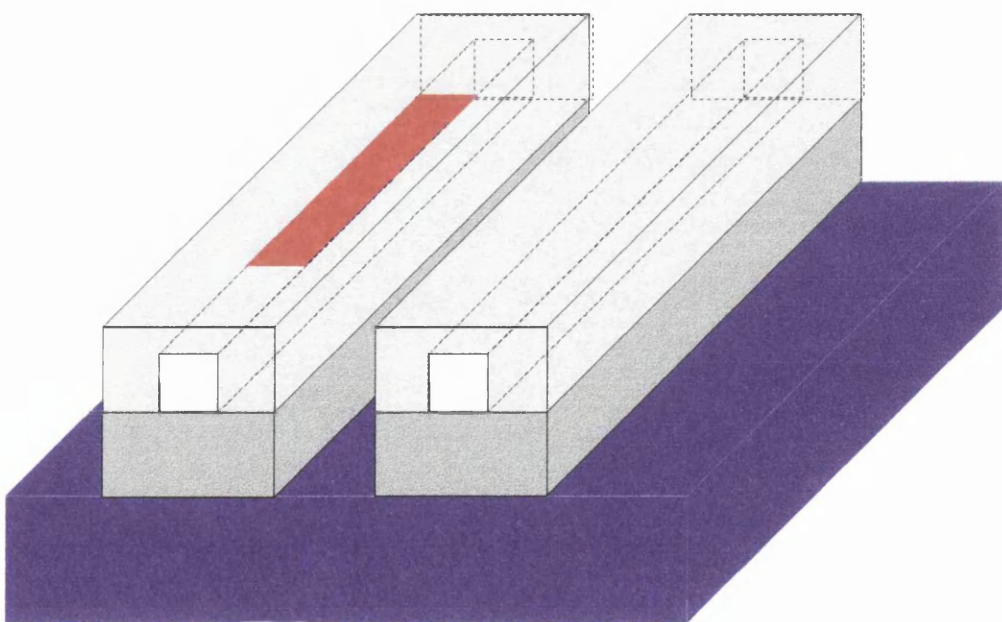


Figure 4.27 Schematic illustration of the introduction of thermal anisotropy through deep reactive ion etching of the waveguide buffer and cladding layers.

The advantage of this structure lies in the fact that air has a significantly lower thermal conductivity than that of the silica glass waveguide structure that it surrounds. As a result, the heat flow from the heater is restricted to the confines of the waveguide structure, thus reducing the lateral heat diffusion/loss.

The PDEase file describing the anisotropic device is shown as Model 2 in the Appendix, where MZTV2 specifically describes the situation where the device is surrounded by air.

Figure 4.28 (a) illustrates a reduction of the lateral heat diffusion, c.f. Figure 4.25(a), where it is obvious that thermal crosstalk is zero. Of note also is that the core temperature is 48°C, just as it was in Figure 4.25(a). The applied electrical power is where the major advantage of this structure is observed, where an applied voltage of 34 V is required to null the interferometer, equal to just 0.26 W, almost a third of that of the original device discussed in Case 1.

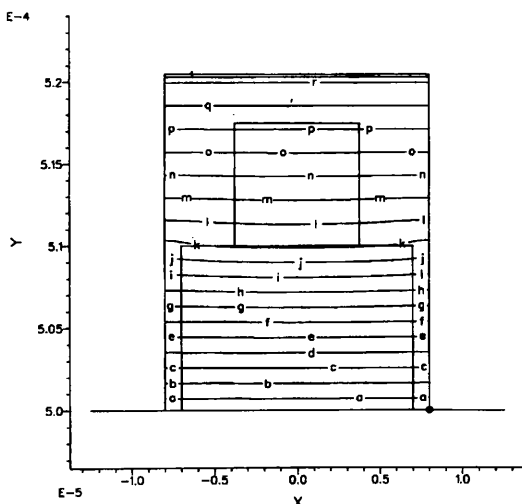


Figure 4.28 (a) Demonstration of the elimination of the thermal crosstalk through RIE anisotropy

However, Figure 4.28 (b) illustrates the **major** drawback of this device structure, where the response time of the device is 262 μ s, a significant increase on the 175 μ s of the original response illustrated in Figure 4.25 (d). Unfortunately, reducing the lateral heat diffusion also reduces the efficiency of heat removal when the device is switched off, as the heat in the core can only escape downwards toward the core.

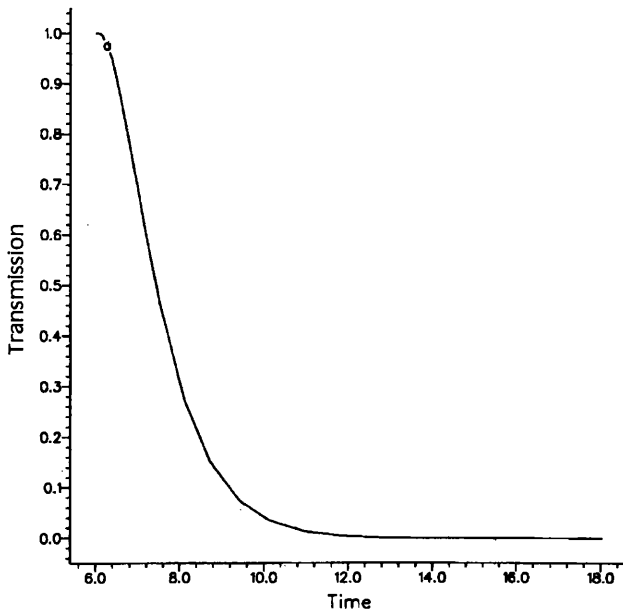


Figure 4.28 (b) Plot showing the slow temporal response after the introduction of thermal anisotropy

The configuration, and operation of this device is similar to that described by Inoue et al [29] where the authors examined the influence of deep grooves on the polarisation effects induced by thermal stress. The electrical power is less than the device described by Inoue, mainly due to the thinner glass layers used in this model.

Case 5: Uniform core heating through introduction of a second heater (Model 3)

One of the problems highlighted in Case 1, was that the temperature distribution across the core was not uniform, where a temperature drop of 14°C was quoted. A way of alleviating this problem would be to introduce a second heater under the core, thus simultaneously heating the waveguide from two directions. Of course, such a device remains purely hypothetical, as there are many difficulties involved in depositing FHD silica films onto metallic surfaces.

Model 2 of the Appendix was modified to include a thin film heater in the SiO_2 buffer layer (the modified file is shown as Model 3 in the Appendix). The heater was initially located between the silicon substrate and the buffer layer, however the heatsinking nature of the substrate ensured that the heater contributed little to the thermal response of the interferometer. Moving the heater improved matters as heat began to transfer to

the core. For the purposes of symmetry, the heater has been located 3 μm below the core, similar to the other heater position 3 μm above the core.

The expected reduction in temperature gradient across the core can be observed in Figure 4.29, where the difference in temperature is just 6°C. This is more than half than that of the planar device described in Case 1, and almost half that of the anisotropic device described in Case 4.

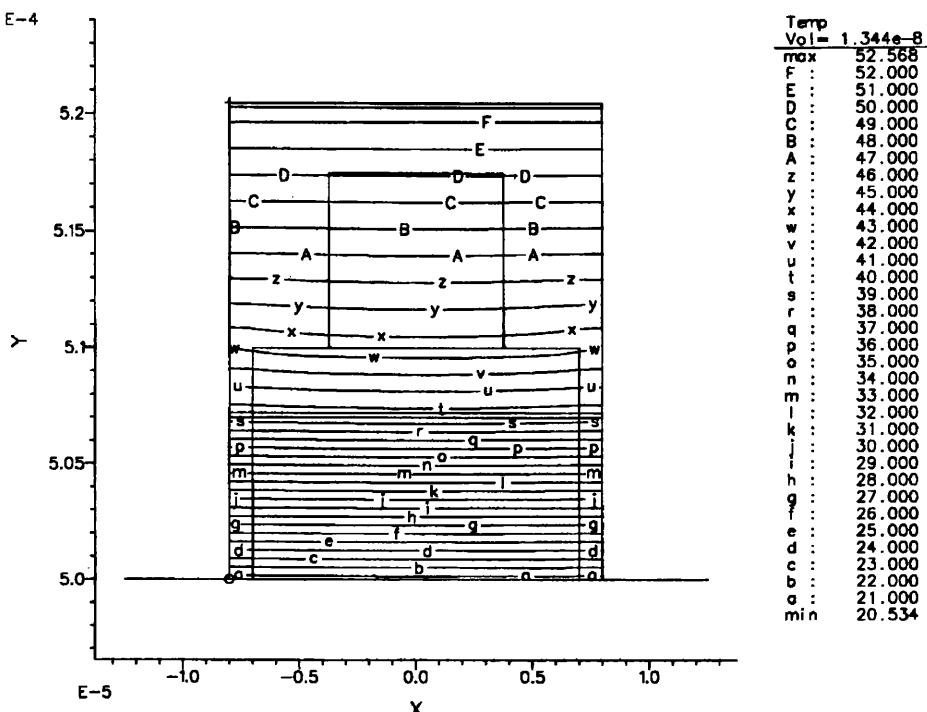


Figure 4.29 Reduced temperature facilitated by uniform heating using a surface and buried heater

Another advantage of secondary heating is that of reduced electrical power. As each heater would contribute to core heating, less heat is required from each heater. By reference to Figure 4.21, it is obvious that low power operation is advantageous, as it would prolong the life of the thin film heater.

The electrical power requirement for modulation is just 0.16 W in this device, however as two heaters are required the total power requirement is 0.32 W, which is greater than that of the single heater anisotropic device.

The thin film heater also restricts the thermal diffusion properties of the interferometer, thus limiting heat flow toward the silicon substrate. This causes a reduction in the response time to 282 μs , 20 μs slower than the device in Case 4.

Improved Temporal Response

The response time of thermo-optic components can be improved by adding and removing heat faster. Like the previous section, this can be achieved by introducing thermal anisotropy through the use of thinner layers and/or layers of higher thermal conductivity.

Case 6: Diamond Substrate (Model 1)

The basic planar structure as described in Case 1 (Model 1) was amended such that the silicon substrate was replaced by a higher thermal conductivity diamond substrate. (The properties of diamond are discussed in more detail in Chapter 6).

It was thought that the diamond substrate may improve the rate at which heat flows though the device, however it was found that the type substrate had no effect on the thermal response. The only effect was to slightly increase the response time to 182 μs .

Case 7: Reduction of Buffer Layer Thickness (Model 1)

Another way of making a thermo-optic device faster is by thinning the waveguide cladding and buffer regions. In this case, the buffer thickness of Model 1 was reduced to just 3 μm (an unrealistic value as the optical propagation loss would be excessive). This reduction resulted in a symmetrical waveguide cross-section with the distance from the heater to core centre to silicon heatsink equidistant.

Figure 4.30 illustrates the pulse symmetry arising from the thermal symmetry of the waveguide, where coupled with the thinner films through which the heat has to flow, results in a response time of 88 μs .

Case 8: Diamond filling of Anisotropic Structure

A reduction in the response time can be achieved by adding and removing heat faster. One way to do this, is through the selective area deposition of diamond films [40] by Chemical Vapour Deposition (CVD) into the grooved structure described in Case 4. A schematic illustration of how this would look is shown in figure 4.31.

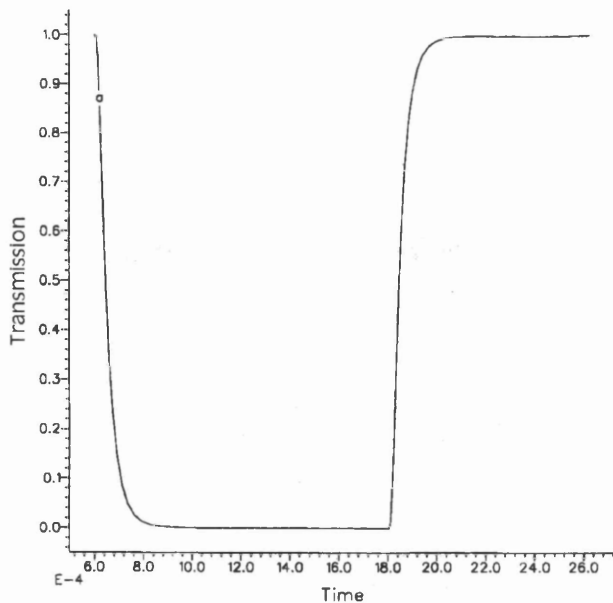


Figure 4.30 Improved pulse symmetry by making the buffer and clad thickness equal

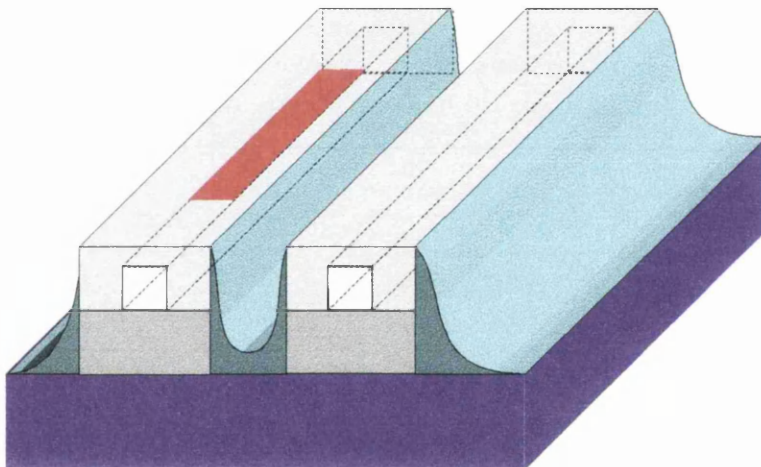


Figure 4.31 Schematic illustration of the introduction of thermal anisotropy through deep reactive ion etching of grooves and the subsequent filling with CVD diamond.

From the data in Table 4.4, CVD diamond films exhibit a thermal conductivity which is 1500 times greater than that of silica (2000 and $1.318 \text{ Wm}^{-1}\text{K}^{-1}$ respectively). This means that heat removal from a diamond coated waveguide structure will be far faster than that of the planar glass structure used in Cases 1 to 3.

Figure 4.32(a) illustrates the temperature distribution across the waveguide cross-section where it is obvious that the heat is removed laterally into the diamond films, rather than through to the silicon substrate. This means that the effective diffusion

distance from the heater to the heatsink is significantly reduced, i.e. the diamond acts as a short, c.f. an electrical connection to ground. The core temperature, as in previous devices was found to be $\sim 25^\circ\text{C}$ above ambient. However the temperature gradient across the device is significant at 35°C .

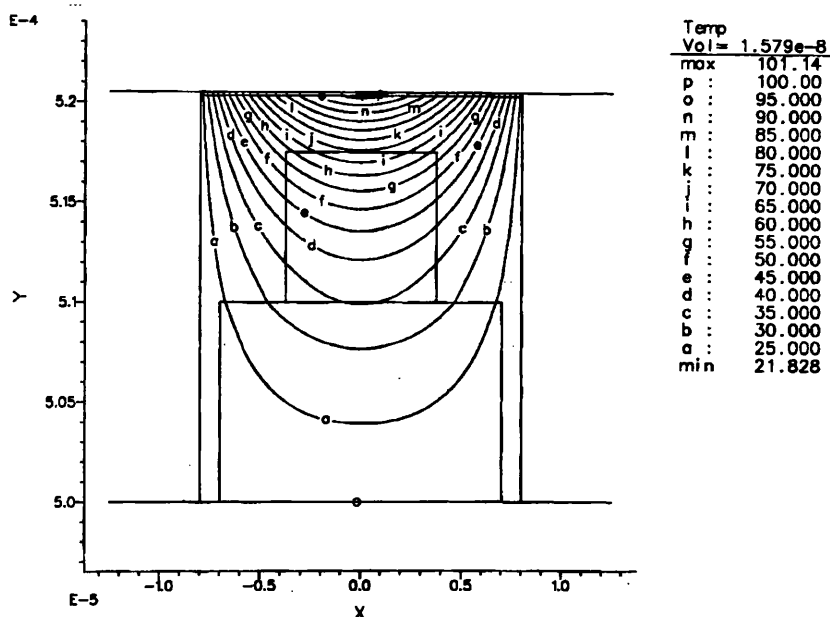


Figure 4.32 (a) Temperature distribution across core is greatly increased by the rapid removal of heat by the surrounding diamond regions.

The major advantage of the diamond shortcut is shown in Figure 4.32(b) where the response time has fallen significantly to just $25\mu\text{s}$. However, the drawback of removing heat faster is that the heater has to supply more energy to compensate, thus the applied voltage has risen to 166V, an increase in power to 6.1W.

Case 9: Introduction of second heater (Model 3)

The last case to be modelled is similar to the twin heater device of Case 5, with the exception that the device is surrounded by the CVD diamond film of Case 8. In this device it is found that the electrical power required to modulate the interferometer is reduced by 33% over that of the single heater Case 8. Also, unlike Case 5, there is an improvement in the response time as the core is heated quicker, but owing to the rapid removal of heat by the diamond film, the thermal properties of the heater are insignificant.

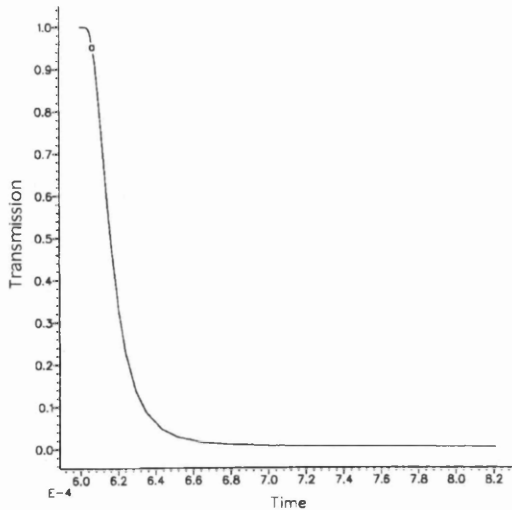


Figure 4.32 (b) Demonstration that diamond in-filling significantly reduces the response time

Summary

Case Number	Model Number	Power (W)	Response Time (μs)	Crosstalk ($^{\circ}\text{C}$ (@ 50 μm))	Core Temp Gradient ($^{\circ}\text{C}$)
1	1	0.67	175	2	14
2	1	0.94	175	3	20
3	1	1.8	28	0	28
4	2	0.26	262	N/A	10
5	3	0.16 (x2)	282	N/A	6
6	1	0.67	182	2	14
7	1	1.09	80	0	24
8	2	6.1	25	N/A	35
9	3	3.99 (x2)	20	N/A	8

It is clear, that if fabrication technology was capable, it would be possible to produce very fast, or very low power thermo-optic waveguide modulators.

4.8 Conclusions

Asymmetric integrated optical Mach-Zehnder interferometers with passive phase shifts have been designed and tested. The fabricated devices have been shown to agree reasonably well with the BPM simulations used in designing the devices. A fundamental constraint of these devices are that the phase shift is wavelength dependant.

A thermo-optic phase shifter has been developed such that it has a fast response time ($\sim 150 \mu\text{s}$) and a modest operating power ($< 0.9 \text{ W}$), which make it suitable for use in active tuning the phase of an unbalance interferometer in a low coherence sensing system. The low heater current densities are thought to be below the electro-migration thresholds for NiCr electrodes, a feature which makes packaging of the device easier.

Finite element modelling techniques have been used to predict the behaviour of a planar silica Mach-Zehnder modulator. By using a value of $5 \times 10^{-6} \text{ }^{\circ}\text{C}^{-1}$ for the thermo-optic coefficient we have been able to predict the experimental results for a device operating at $1.3 \mu\text{m}$. The modelling results have longer rise and fall times than the experimental ones suggesting that the structure modelled and the thermal constants used are not exactly the same as the fabricated device.

Comparing the FE and experimental data we can see that the optical response produced by the model is asymmetric, whereas experimentally the rise time and fall times were approximately the same. The modelled response agrees with experiment to a factor of 1.2. These results are sufficiently close to the experimental case for these values of thermal properties to be used in qualitatively modelling novel structures.

Using these thermal properties and device geometries we have been able to model structures which will operate at lower powers and structures which will have faster switching times. In general, to reduce the power consumption it is necessary to reduce the lateral heat spreading in the device by etching away unnecessary glass from beside the waveguides. To reduce the switching times it is necessary to reduce the thermal mass, this can be done by shrinking the lower buffer layer, and by adding high thermal conductivity regions around the waveguide to help extract the heat faster. Inevitably there is a trade-off between power and speed, faster devices will need more power and lower power devices will be slower.

References

- [1] Y. J. Rao, D. A. Jackson, *Meas. Sci. & Technol.*, 1996, **7**, 981.
- [2] A. Takagi, K. Jinguji, M. Kawachi, *J. Lightwave Tech.*, 1992, **10**, 1814
- [3] M. Izutsu, Y. Nakai and T. Sueta, *Opt. Lett.*, 1982, **7**, 136.
- [4] D. Marcuse, ‘Theory of Dielectric Optical Waveguides’, Academic Press, New York, 1974.
- [5] R. H. Rediker and F. J. Leonberger, *IEEE J. Quantum Electron.*, 1982, **10**, 1813.
- [6] F. S. Chu and P. L. Liu, *Optics Lett.*, 1991, **16**, 309.
- [7] N. Takato, K. Jinguji, M. Yasu, H. Toba and M. Kawachi, *J. Lightwave Technol.*, 1988, **6**, 1003.
- [8] D. L. Lee, “Electromagnetic Principles of Integrated Optics”, Wiley International, 1986.
- [9] R. G. Hunsperger, “Integrated Optics: Theory and Technology”, Springer-Verlag, 1995
- [10] T. Kitoh, N. Takato, M. Yasu and M. Kawachi, *J. Lightwave Technol.*, 1995, **13**, 555.
- [11] M. Kawachi, *Opt. Quantum Electron.*, 1990, **22**, 391.
- [12] BPM-CAD 3.0 Manual, Optiwave Corporation, 16 Concourse Gate, Suite 100, Nepean, Ontario, Canada, K2E 7S8.
- [13] W.K. Burns and A.F. Milton, *IEEE J. Quantum. Electron.*, 1975, **QE-11**, 32.
- [14] J. R. Bonar, *PhD Thesis*, University of Glasgow, 1995.
- [15] A. C. Liu, M. J. F. Digonnet and G. S. Kino, *Opt. Lett.*, 1991, **16**, 1732.
- [16] T. Fujiwara, D. Wong, Y. Zhao, S. Fleming, S. Poole and M. Sceats, *Electron. Lett.*, 1995, **31**, 573.
- [17] M. Abe, T. Kitagawa, K. Hattori, A. Himeno and Y. Ohori, *Electron. Lett.*, 1996, **32**, 893.

-
- [18] G. Ghosh, *Applied Optics*, 1997, **36**, 1540.
 - [19] W.-K Wang, H. J. Lee and P. J. Anthony, *J. Lightwave Technol.*, 1996, **14**, 429.
 - [20] J.-F. Tsay, B. Bendow and S. S. Mitra, *Phys. Rev. B*, 1973, **8**, 2688.
 - [21] J. Matsuoka, N. Kitamura, S. Fujinaga, T. Kitaoka and H Yamashita, *J. Non-Cryst. Solids*, 1991, **135**, 86.
 - [22] G. Ghosh, *IEEE Photon. Technol. Lett.*, 1994, **6**, 431.
 - [23] G. Ghosh, M. Endo and T. Iwasaki, *J. Lightwave Technol.*, 1994, **12**, 1338.
 - [24] A. J. McLaughlin, M. G. Jubber, J. R. Bonar, J. S. Aitchison and A.J. Jacobs-Cook, to be submitted for publication in *Appl. Phys. Lett.*
 - [25] M. Kawachi, M Yasu and T. Edahiro, *Electron. Lett*, 1983, **22**, 321.
 - [26] A. J. McLaughlin, J. R. Bonar, M. G. Jubber, P. V. S. Marques, S. E. Hicks, C. D. W. Wilkinson and J. S. Aitchison, *Conference on Lasers and Electro-Optics*, OSA Technical Digest Series, **11**, 1997, 508.
 - [27] M. Haruna and J. Koyama, *Appl. Opt.*, 1982, **21**, 3461.
 - [28] B. A. Moller, L. Jensen, C. Laurent-Lund and C. Thirstrup, *IEEE Photon. Technol. Lett.*, 1993, **5**, 1415.
 - [29] Y. Inoue, K. Katoh and M. Kawachi, *IEEE Photon. Technol. Lett.*, 1992, **4**, 36
 - [30] A. Sugita, K. Jinguiji, N. Takato, K. Katoh and M. Kawachi, *Trans. IEICE*, 1990, **E73**, 1990.
 - [31] N. Nishishara and M. Haruna, “Optical Integrated Circuits”, Prentice Hall, 1988.
 - [32] J.B. Brown, J.D.C. Jones, S.J. Rogers, R.K.Y. Chan and H.H. Wong, *Opt. Laser Technol.*, 1995, **27**, 335.
 - [33] A.J. McLaughlin, M.G. Jubber, J.R. Bonar, J.S. Aitchison and A.J. Jacobs-Cook, *Optoelectronic Integration and Switching*, IEE Colloquium, Glasgow, Nov. 1997.

-
- [34] E. Hecht, 'Optics', 2nd Edition, Addison Wesley Publishing Company, 1987.
 - [35] S.J. Rogers, J.B. Brown, J.D.C. Jones, R.K.Y. Chan and H.H. Wong, *Meas. Sci. Technol.*, 1996, **7**, 209.
 - [36] PDEase V 2.5, Reference Manual/Tutorial/Handbook, Macsyma Inc., 20 Academy Street, Arlington, MA 02174, USA.
 - [37] Private Communication with Dr M.G. Jubber, University of Glasgow.
 - [38] CRC Handbook of Chemistry and Physics, 62nd Edition, (1981-1982)
 - [39] Properties of Diamond, De Beers Industrial Diamond Division
 - [40] P.G. Roberts, D.K. Milne, P. John, M.G. Jubber and J.I.B. Wilson, *J. Materials Research*, 1996, **11**, 3128.

Chapter 5 IO interferometers for low-coherence sensing applications

5.1 Introduction

Optical fibre based low-coherence interferometric sensor systems have attracted a lot of interest recently, a review of which can be found in Rao & Jackson. [1]. Typically, these sensor systems employ a broadband optical source to illuminate a series arrangement of both a sensing, and interrogating interferometer, shown in Figure 5.1.

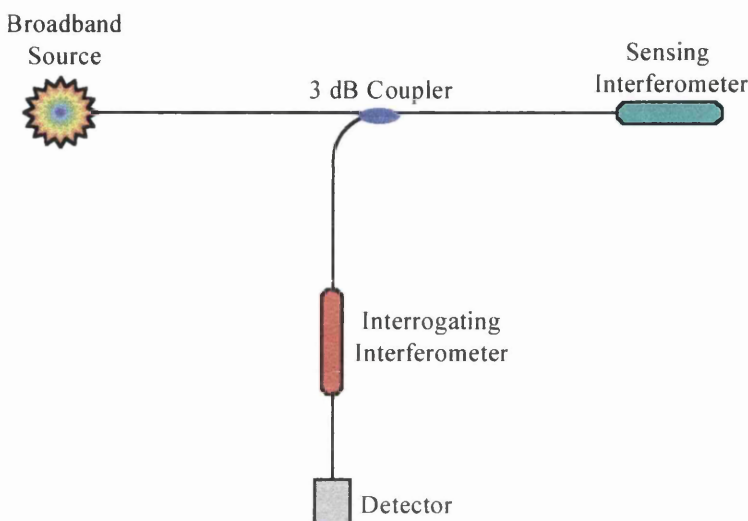


Figure 5.1 Schematic of a typical low coherence interferometric sensor system

In such systems, each interferometer has an optical path delay greater than the coherence length of the source, but equal to that of the other interferometer. Thus the optical beams derived from the sensing interferometer interfere in the interrogating interferometer, rather than at the sensing element. Systems based on these techniques have been developed to monitor a broad range of parameters, for example: displacement and temperature [2], and strain and temperature [3].

At present, most sensor systems are constructed using optical fibres or bulk optic interferometers. However, these interferometers can be impractical due to their sensitivity to environmental conditions such as vibration and temperature. In contrast, IO components offer increased performance and functionality in a robust, compact, mass producible format with a high degree of reproducibility. Recently, integrated optical (IO) components have been demonstrated as an alternative with reports of coherence modulated systems using LiNbO_3 interferometers [4, 5].

5.2 Basic Principles of Low Coherence Interferometry [1]

In the system demonstrated in Figure 5.1, light from a broadband source, for example a superluminescent diode (SLD), is coupled into an optical fibre system. The light propagates down the fibre to the sensing interferometer. The sensing interferometer of interest here consists of a Fabry-Perot interferometer, where the cavity is formed by the cleaved face of an optical fibre, and the underside of the micromachined silicon resonator [6] as shown in Figure 5.2 and Chapter 1, Figures 1.1-3.

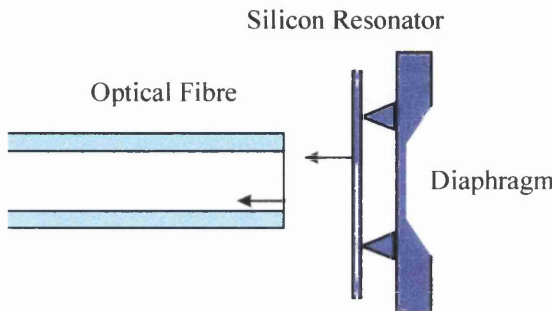


Figure 5.2 Schematic of the Fabry-Perot cavity formed between the optical fibre and resonator [6]

The coherence length of the source is chosen such that it is less than the optical path difference (OPD) of the interferometer. In the silicon sensor, this is twice the nominal cavity gap between the fibre and the resonator. In this case, no interference occurs at the sensor and the incoherent optical signals reflected from the fibre and the resonator propagate back along the optical fibre to the interrogating interferometer.

The OPD of the interrogating interferometer is equal to that of the sensing interferometer, where the reflected signals are brought back into coherence and interfere in the normal manner.

In general, the optical intensity observed at an interrogating interferometer can be described by the function ([1]):

$$I = I_0 \left[1 + \frac{1}{2} \exp \left(- \left(\frac{2\Delta x}{L_c} \right)^2 \right) \cos(k\Delta x) \right] \quad (5.1)$$

where I_0 is the total power detected, Δx is the OPD of the interferometer, L_c is the source coherence length and k is the wavenumber. Thus any change in the sensing interferometer OPD results in a change of both the phase and the fringe visibility of the signal.

5.3 Solutions for Signal Fading

The low coherence sensing system described in the previous section suffers from the effects of *signal fading*. Equation 5.1 can be simplified to:

$$I = I_0 [1 + \cos(\theta + \delta)] \quad (5.2)$$

where θ is a time varying function representing the movement of the resonator (~ 10 's nm) at a frequency w_r , given by:

$$\theta = R \cos(\omega_r t) \quad (5.3)$$

and δ describes the movement of the diaphragm (~ 100 's nm), given by

$$\delta = \frac{2\pi n d}{\lambda} \quad (5.3)$$

where d is the OPD of the sensor and λ is the centre wavelength of the source.

As the sensor operates, the OPD is modulated by a high frequency signal corresponding to the resonator movement (~ 200 kHz), and the relatively slow movement of the diaphragm. Thus as δ varies slowly with large amplitude, there are positions of the diaphragm which provide virtually zero sensitivity to the small changes of the OPD due to the resonator. This is the problem referred to as *signal fading*.

In order to alleviate this problem a number of schemes have been suggested:

- Passive quadrature interferometry employing dual interrogation interferometers
- Active quadrature interferometry where the interrogating interferometer is tuned
- A mixture of both schemes

Both of these schemes involve introducing a $\pi/2$ phase shift between the propagating optical beams, shifting the operating point of the interrogating interferometer to a point of maximum sensitivity. The techniques for implementing these schemes is described in Chapter 4.

In passive quadrature dual interferometers are used to interrogate the sensor, where one of the interferometers has one arm $\lambda/4$ longer than the other. Even as the OPD of the sensor changes due to the diaphragm movement, there is always an output from one interferometer. The outputs of both interferometers are processed electronically to extract the resonance frequency. A drawback of this system is that the quadrature

point is defined during fabrication for a particular wavelength, thus any changes in the operating wavelength of the source results in a different phase difference between the interferometers.

In active quadrature, the operating point of the interferometer is tuned using an effect such as the thermo-optic or electro-optic effect. The interferometer is controlled by applying a low frequency ac signal to one electrode, which is detected and processed electronically using a Phase Locked Loop (PLL). The interferometer is locked to a particular operating point by adjusting the dc bias applied to the device. A drawback of this system is that electrical power needs to be applied most of the time to bias the device, making the device energy inefficient.

A mixture of both techniques can be employed where the static phase shift reduces the electrical power required to adjust the interferometer, and the active phase shift compensates for any changes in the source wavelength.

5.4 Device Design

Multimode interferometers have been designed which possess an OPD equal to that of a resonant silicon sensor. The main design features of these devices are shown in Table 5.1.

	Core Size (μm)	Bend Radius (μm)	Δn (%)	OPD (μm)
Mask 1	8	7500	0.75	0
Mask 2	8	7500	0.75	250
Mask 3	20	7500	0.75	250

Table 5.1 Design features of multimode low coherence IO interferometers

The masks consist of a single waveguide input, a large branching angle Y-junction, a parallel configuration of interferometers and two output waveguides. Each arc of the S-bends passes through 90°, and the extra optical path difference (OPD) is inserted within the S-bend perpendicular to the direction of propagation (with respect to the input waveguide). The devices were normally separated after fabrication and tested

individually due to problems obtaining a suitable optical source. A schematic of the basic device is shown in Figure 5.3.

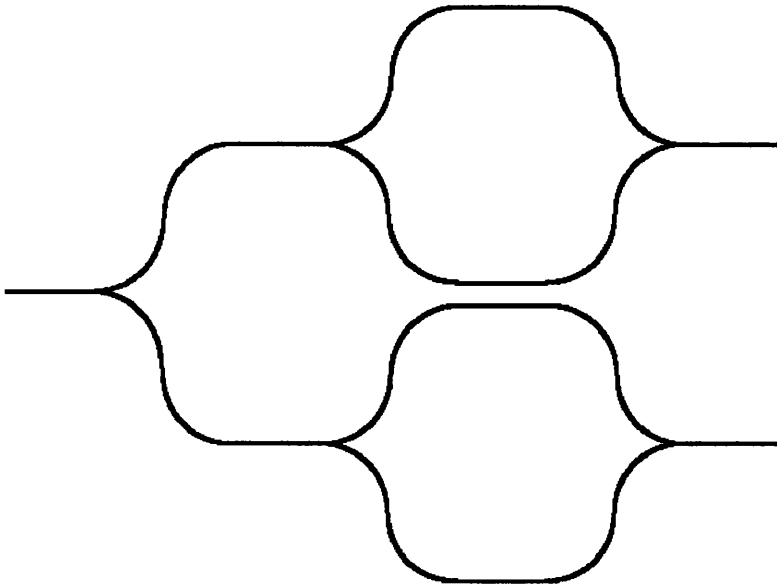


Figure 5.3 Layout of phase quadrature interferometers

Unfortunately these devices could not be simulated, as BPM software only considers the propagation of monochromatic light through a device. BPM also simulates in the forward propagating direction, but in this device the S-bends extend in a perpendicular direction to the forward propagation.

Single interferometers were tested at a wavelength of $1.55 \mu\text{m}$ where it was found that the insertion loss of the devices made with Mask 1 was 4.5 dB. It is thought that the major source of loss occurs as the light propagates through the S-Bends.

5.5 Low Coherence Optical Sources

In order to test the path imbalanced interferometers it became necessary to fabricate a superluminescent diode (SLD). The SLD produced here followed from the design of Camacho [7] who used bent waveguide lasers to produce external cavity lasers. The bent waveguide forms an angle of 8° with the normal of the cleaved facet which reduces the facet reflectivity to less than 0.01% [7]. Such designs have been used previously by Lin et al [8] to produce SLDs.

The devices were fabricated on a GaAs/AlGaAs substrate using the “self alignment” fabrication process as used for producing laser diodes. This process was devised by P.

Cusumano, formerly of the Optoelectronics Research Group, to minimise the number of photolithography steps required in defining electrode patterns in ridge waveguide lasers. The SLD was 500 μm long, with a similar sized single electrical contact, as opposed to the two section contact used for modelocking [7], thus increasing the length of the gain region, and therefore the maximum optical power from the device.

The optical power from the tilted facet was typically found to be in excess of 2.5 mW at a current of 80 mA. Figure 5.4 illustrates the optical spectrum from the device where it can be seen that the spectral width ($\Delta\lambda$) of the device is about 22 nm. The source coherence length was estimated using the relationship, $L_c = \lambda^2/\Delta\lambda$, to be 35 μm .

The light from the SLD was coupled to the interferometer via a “lensed” multimode fibre. The “lensing” of the fibre was created by exposing the cleaved fibre end to an electric arc using a fusion splicer.

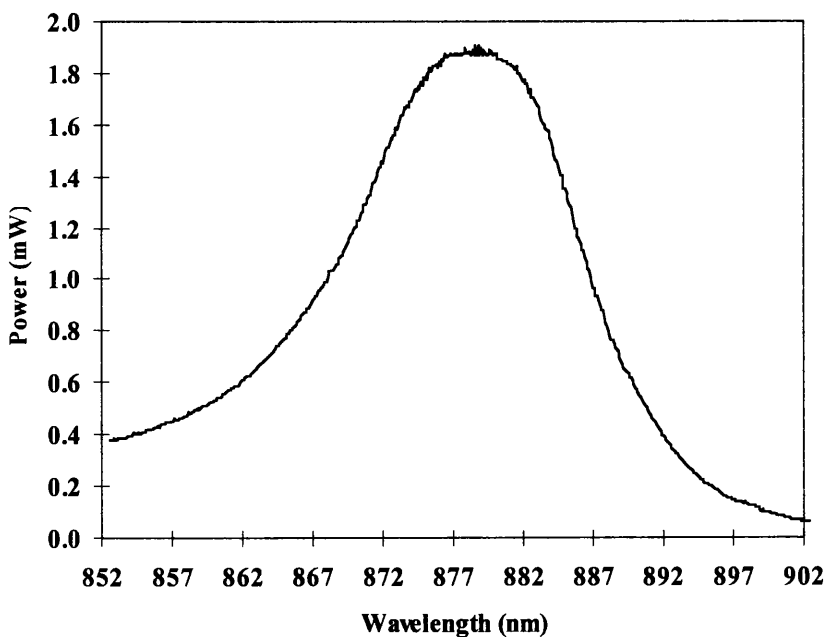


Figure 5.4 Optical spectrum from a fibre coupled bent waveguide SLD

5.6 Interferometer Performance [9, 10]

Symmetrical interferometers were fabricated using Mask 1 and tested to evaluate the tuning range and stability of the large path length devices at a pre-defined bias point. The path imbalanced devices were fabricated using Mask 2 and tested to estimate the group OPD, and hence the optical path imbalance, from the channelled spectra through the interferometer.

5.6.1 Tuning Range and Stability

Using the techniques described in Chapter 4, a thin film NiCr heater was fabricated over one arm of the interferometer. The tuning range was investigated by applying a large dc bias across the heater and monitoring the optical response on an Optical Spectrum Analyser. Figure 5.5 illustrates that the tuning range of the device is approximately 4π , where the power required for a π phase change was 0.22 W at the source wavelength of 878 nm. The fringe visibility was measured to be in excess of 30 dB using an optical spectrum analyser.

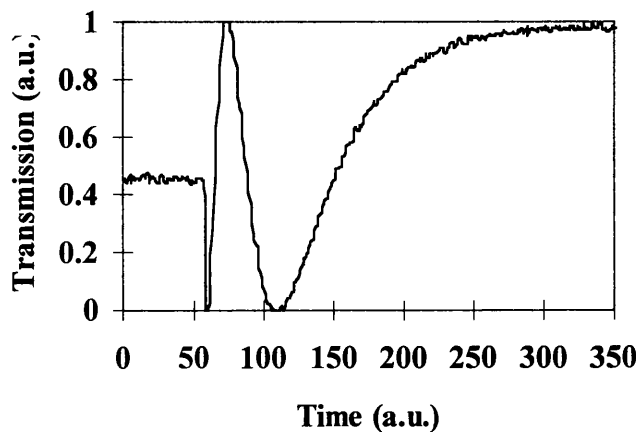


Figure 5.5 Illustration of the tuning range of the thermally tuned interferometer

The stability of the device was monitored over a short period of time, in this case approximately 30 minutes. Initially the device was left unbiased, where it was found that the background drift due to the source and the fibre coupling was less than 1%. The device was biased at its quadrature point, corresponding to an optical output of 50% and the drift was again found to be less than 1%. The temporal response of the device can be observed in Figure 5.6.

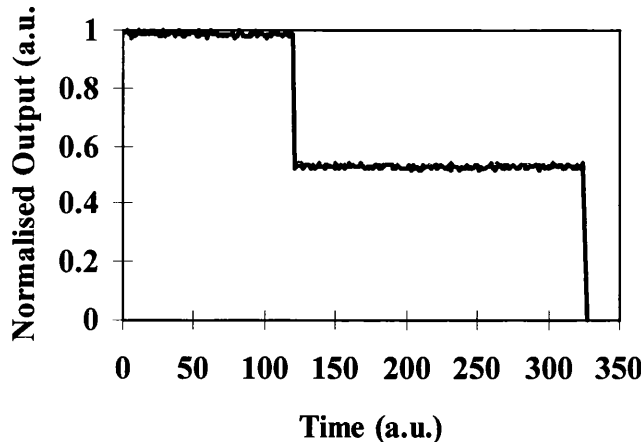


Figure 5.6 Device stability over time, unbiased and at the quadrature point

From these results it can be concluded that the thermally controlled device is reasonably stable with no noticeable degradation of performance over time.

5.6.2 Estimation of Optical Path Difference (OPD)

Figure 5.7 shows the channelled spectrum produced by the unbalanced interferometer. The fringe spacing in the channelled spectra is approximately $\Delta\lambda = 2.8 \text{ nm}$ at the centre wavelength, which gives a static group optical path difference of $279 \mu\text{m}$. This is in reasonable agreement with the designed optical path difference which was $250 \mu\text{m}$. It is thought that the error is due to the noise on the signal due to the relatively high insertion loss of the interferometer, $>4\text{dB}$, and the low optical power from the source. The fringe contrast was typically less than 3 dB , which is lower than expected. In this particular device there was a 1 dB excess loss in one arm of the interferometer due to a defect created during fabrication, leading to a power imbalance between the arms.

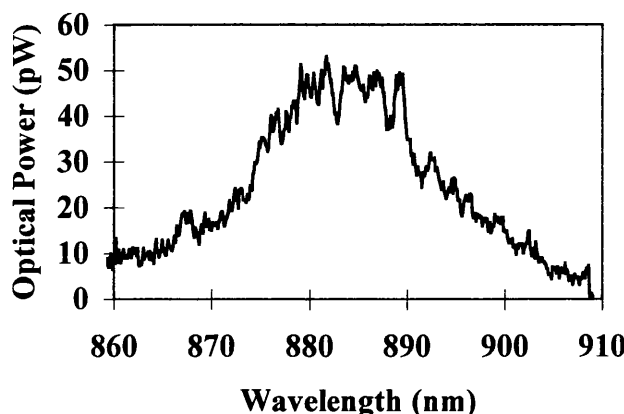


Figure 5.7 Channelled spectrum indicating a static group OPD of $279 \mu\text{m}$.

5.7 Conclusions

Interferometers with an optical path difference (OPD) equal to that of the cavity formed in a resonant silicon sensor have been fabricated and assessed. Active tuning of the devices has been shown to be stable over short periods of time. The maximum controllable tuning range of the devices has been shown to be of the order of 4π . Preliminary channelled spectra results have been obtained which indicate that the calculated static group OPD is in reasonable agreement with the initial device design. It is clear from these results that further development is required as the channelled spectrum obtained has a particularly low fringe visibility, <3dB, indicating problems relating to the insertion loss, and possibly the polarisation sensitivity, of the device.

References

- [1] Y.J. Rao & D.A. Jackson, *Meas. Sci. & Technol.*, 1996, **7**, 981.
- [2] L.A. Ferreira, A.B.L. Lobo Ribiero, J.L. Santos and F. Farahi, *IEEE Photon. Technol. Lett.*, 1996, **11**, 1519.
- [3] S.E. Kanellopoulos, V.A. Handerek & A.J. Rogers, *Opt. Lett.*, 1995, **20**, 333
- [4] J. Hauden, H. Porte & J.-P. Goedgebuer, *IEEE J. Quantum Electron.*, 1994, **30**, 2330.
- [5] H. Porte, J.-P. Goedgebuer, W. Elflein, A. Terras, F. Ledventec & N. Butterlin, *IEEE J. Sel. Top. Quantum Electron.*, 1996, **2**, 319.
- [6] Private communication with A.J. Jacobs-Cook, Lucas Electrical & Electronic Systems, Technical Centre - Advanced Product Development, Solihull, UK.
- [7] F. Camacho Páez, *PhD Thesis*, University of Glasgow, 1997.
- [8] C.F. Lin & C.S. Juang, *IEEE Photon. Technol. Lett.*, 1996, **8**, 206.
- [9] A.J. McLaughlin, J.R. Bonar, M.G. Jubber, A.J. Jacobs-Cook & J.S. Aitchison, *Conference on Lasers and Electro-optics*, **6**, OSA Technical Digest Series, 328, 1998
- [10] A.J. McLaughlin, J.R. Bonar, M.G. Jubber, F. Camacho, J.S. Aitchison, *to be presented at CLEO/EQEC '98*, Glasgow, CWE6, 1998.

Chapter 6. Hybrid Integration of Optoelectronic Components

In aerospace sensing applications it is advantageous to integrate many components into a single robust, functional, and modular unit [1]. This can be important where extreme conditions are to be found, as the operating environment of a single module is more controllable than a number of distributed discrete components.

In this chapter, the development of a hybrid optoelectronic planar lightwave circuit (PLC) is described, where new, or novel techniques have been used to solve some of the problems associated with integrating optoelectronic components onto a single substrate. Particularly where the problems arise due to the different, and at times incompatible, technologies used in packaging optoelectronic components. Table 6.1 lists some components used in optoelectronic applications and some of the associated techniques and problems encountered when integrating them with other components.

Component	Integration Technique	Typical Problems
Silica waveguide	Silicon host substrate	Thick cladding, polishing
Laser diode	'p or n-type' bonding	Alignment, thermal stability, contacts
Optical fibre	Micro-machining of silicon	Alignment, mechanical stability
Heatsink	CVD deposition of diamond	Incompatibility of process with FHD

Table 6.1 Techniques and Problems with Optoelectronic Integration

6.1 A Review of Common Integration Techniques

Various authors have investigated a number of techniques for hybrid packaging of optoelectronic components. A number of papers using some popular techniques can be found in reference [2], a colloquium on "Planar Silicon Hybrid Optoelectronics".

Robust integration of components, can be defined by the following criteria:

- Low-loss optical coupling between components
- Thermal stability (wavelength stability and device longevity),
- Mechanical stability (bond strength and alignment accuracy)
- Self-alignment, rather than active alignment of components,
- Simplicity of construction.

Yamada et al [3] described the integration of laser and photo-diodes with silica waveguides on a silicon substrate. Vertical alignment of the optical components was achieved by *mechanically* placing the diodes on the substrate, whereas lateral alignment was achieved by actively optimising the coupling efficiency between the components. Once aligned, the devices were bonded by melting pre-patterned electrode metal on the substrate. Alignment of this type resulted in a quoted alignment accuracy of $\pm 1 \mu\text{m}$.

A feature of silica waveguide devices, is the common use of silicon as the host substrate [4]. Silicon has been exploited as a substrate for optoelectronic integration through micromachining technology[5, 6], where the formation of V & U-grooves for alignment of optical fibres is now commonplace. *V-grooves* are a typical feature of optical fibre alignment, where the grooves hold fibres in a predetermined position, with another technique used for the optical interconnection. Two examples of other techniques are described here in [7], and in [8], [9].

Wale et al [7] examined the application of *flip-chip solder bump* technology, taken from the semiconductor industry, to the self-alignment of silica waveguides and optical fibres. The optical fibres are held in place by micromachined V-grooves on the silicon substrate. The silica waveguides are flip-chip aligned to fibres through the use of self aligning solder bump pads. A overall precision of $\pm 1 \mu\text{m}$ was achieved, with a typical excess loss of 1 dB attributable to this misalignment. The technique can also be applied to other devices such as laser diodes and photodetectors.

Another example, Cassidy et al [8], and latterly C.A. Jones et al [9], describe the use of *precision machined metal pins* which plug into V-grooves on the silicon motherboard, and act as locating pins for a fibre ribbon connector. This technique, subject to optical mode matching between the fibre and waveguides, can result in an alignment accuracy of $\pm 1 \mu\text{m}$, where the excess loss attributable to misalignment is just 0.7 dB. The same group report on the integration of a laser diode, where *an etched ridge* is formed on the laser substrate, which is flip-chip aligned to an etched V-groove on the silicon motherboard, thus achieving lateral alignment. Longitudinal alignment is achieved by pushing the device against *silica stops*. Again, like [3], bonding is achieved by reflow of the electrical contact on the substrate.

Another technique, although similar, is the use of *U-grooves* by Sugita et al [10] to align the optical fibres. A combination of RIE and photolithography was used to etch vertically through the silica waveguide layers, such that a U-groove was formed. The RIE stage is controlled such that the core of the fibre and the waveguide are aligned with each other. The authors quote an accuracy of $\pm 2\mu\text{m}$ giving an interface loss of 0.6 dB. However, by the authors own admission this technique is dependant on the lateral alignment accuracy at the photolithography stage, (a problem characteristic of FHD devices as described in the next section). The overall accuracy is also dependant on the precise depth control at the RIE stage. In all this technique is potentially the easiest to implement from a process point of view, however it is prone to variation.

An important consideration for optoelectronic integration, particularly for aerospace applications, is that of environmental sensitivity. In an aerospace environment extremes of temperature can be experienced, which coupled with mechanical vibration could lead to a degradation in the performance of an optical system. Differences in the thermal properties of materials used in packaging, can result in differing degrees in thermal expansion, thus altering optical coupling.

Wale et al [7] Sugita et al [10] also examined the reliability of their respective integration techniques, where the main area of investigation was temperature cycling. Wale found that the insertion loss had permanently changed by just 0.1 dB over the start value, although during the tests it was found that the maximum was 1.6 dB (Range -55°C to 85°C). Sugita reported 0.3 dB variation during cycling with no permanent change evident(Range -10°C to 60°C).

Recently, Hibino et al [11]examined a wide range of environmental conditions and their effects on UV bonded optical fibres. Investigated conditions included:

- Low and High (Dry and Damp) Storage Temperatures (-40 °C to 85°C)
- Temperature Cycling (Dry and Humid) (-40°C to 75°C)
- Water immersion, salt spray and airborne contaminants
- Vibration (10 - 2 kHz)

The average loss change after these tests was typically less than 0.05 dB, however damp conditions led to a higher loss, 0.09 dB. The typical transient loss was ~0.3 dB.

6.2 Hybrid packaging of FHD silica waveguides, laser diodes and optical fibres

The objective of this work is the development of an Application Specific Optoelectronic Circuit (ASOC) for low coherence optical sensing in automotive applications. The specification of the ASOC circuit is as follows:

- Integrated optic, phase tuneable Mach-Zehnder interferometers, for low-coherence detection of optical signals derived from silicon micro-resonant pressure and temperature sensors
- Optical interconnects for single/multimode optical fibre
- Integrated low-coherence laser diodes (or super luminescent diodes)
- Integral heatsink for thermal management of components

It is also intended that the final hybrid component be self-aligning such that the diodes and fibres can be integrated with the silica waveguides, reducing complexity.

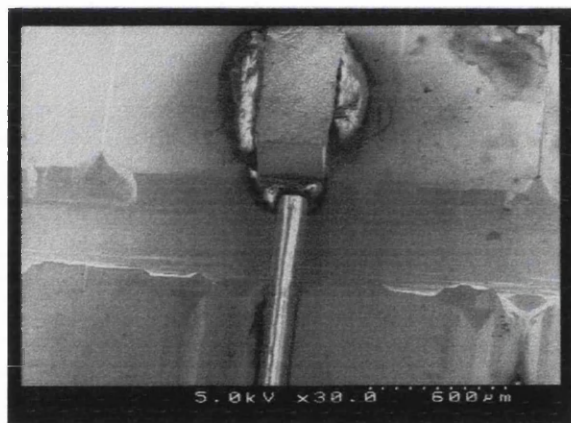


Figure 6.1 Illustration of a laser diode integrated bonded to a patterned silicon substrate with an integral optical fibre interface.

Problems arise in integrating these optical components due the different techniques involved in integrating each device. The different steps required are described below:

- Cutting and polishing of silica waveguides,
- Photolithography for V-groove mask definition,
- Anisotropic etching of silicon to form V-grooves,
- CVD diamond deposition for heatsink,
- Fibre bonding with UV curing adhesive,
- Au/Sn bonding of laser diode.

Obscured alignment marks

A fundamental constraint of silica based integrated optics is that the waveguide core is covered by a thick cladding layer. Photolithography is arguably the most important stage of fabrication, as errors typically jeopardise the performance of an optoelectronic component. The accuracy of multilevel photolithography relies on the use of alignment features where a small pattern is used in each mask level for positional alignment. Typically, the thickness of the cladding layer is greater than 10 microns, rendering alignment marks almost invisible thus making accurate microscope alignment difficult. The photograph of Figure 6.2 illustrates this problem where the diffuse alignment mark beneath the surface is apparent.



Figure 6.2 Diffuse appearance of alignment marks under the cladding.

6.2.1 Mask proximity to silicon surface

Prior to silicon micromachining, it is necessary to remove the silica layers to expose the underlying silicon substrate. However, as the mask is out of contact with the silicon surface, the transferred feature size will be different from that of the original mask pattern. A schematic of this problem is shown in Figure 6.3.

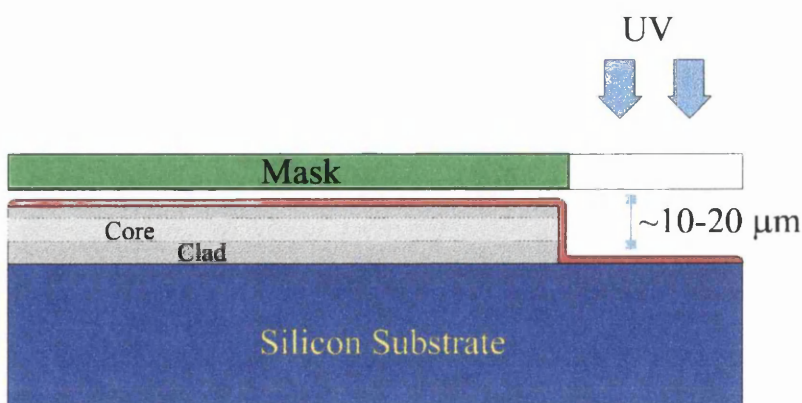


Figure 6.3 Schematic of the photolithography problem imposed by FHD technology

6.2.2 Waveguide Polishing

In order to minimise insertion loss it is necessary to polish the edge of the waveguides, thus removing any imperfections/roughness which may create scatter loss. It obvious that this task is difficult to perform, as it is necessary to retain the silicon substrate, such that it is available for micromachining purposes.

It is conceivable that the ends of the waveguides could be prepared by dry etch processing similar to that of Sugita et al [10], however as shown in Chapter 3, without the correct technology this can be a time and resource intensive process.

6.3 Integration (1) Silicon Partition Lightwave Integration Technology (SPLIT)

Reference [8] and [9] describe the use of precision machined metal alignment pins to align silicon motherboards with commercially available fibre ribbon connectors. This alignment technique provides the thrust for the work described in this section.

It is recognised that cylindrical objects, when placed in a V-groove structure, can be used to align optoelectronic components with a high degree of accuracy. Given that the surfaces of the aligning objects are sufficiently accurate, it is indeed conceivable that perfect lateral and vertical alignment is achievable, with the third direction being aligned by pushing components together along the alignment pins.

In fact, as Wale et al [7] describe, optical fibre manufacturers often pessimistically quote the tolerances of standard fibre concentricity and outside diameter to be $\pm 1\mu\text{m}$ $\pm 2\mu\text{m}$ respectively. However in the opinion of the referenced authors, such fibres are accurate to within $0.5\mu\text{m}$, which given a maximum micromachined sidewall roughness of less than $0.25\mu\text{m}$, suggests that high accuracy alignment is perfectly feasible using standard components. This data of course, is circa 1990.

In this project, it was established that it is possible to split and recombine a silicon wafer to sub-micron accuracy using crude workshop technology. The SPLIT wafer technique is therefore of use in dividing a wafer into multiple pieces such that each piece can be processed in a different way, such as CVD diamond deposition, silicon micromachining and end polishing of FHD prepared silica waveguides.

6.3.1 SPLIT Process

In this section, the simple technique for dividing and recombining a silicon wafer are described. SPLIT'ing a wafer requires a two stage wafer division process, an intermediate processing stage and a two stage realignment process.

Stage 1: V-groove definition

In this work V-grooves were machined using a mechanical grinding machine of the sort used to machine slots into metal surfaces. The grinding face and sides of the grinding wheel are impregnated with a fine diamond grit, where the face and sides are at 90° to each other.

The wafer to be grooved is placed on a metal clamp at an angle of 45° to the horizontal, and placed onto the grinding machine. The machine can be programmed to grind to a specific depth, a depth which is determined by the re-alignment pins. A schematic of this set-up is shown in Figure 6.4.

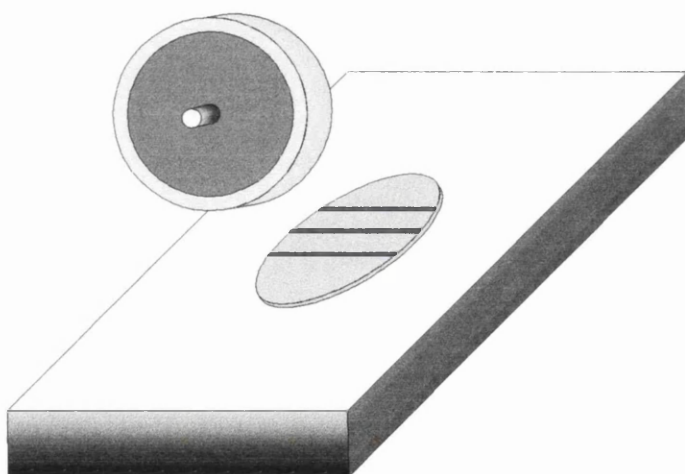


Figure 6.4 Illustration of a silicon wafer clamped at 45° to the horizontal, and subject to grinding. The dark lines on the substrate illustrate of the size of the grooves relative to the substrate.

The position and direction of the V-grooves are not important, as long as the groove runs almost perpendicular to the cut used to dice the wafer. A minimum of two grooves are required to realign the substrate. The grooves can be defined on the working face or the back of the wafer, however in order to maximise device yield it is recommended that the cut be made on the back.

Stage 2: Wafer Splitting

The wafer is split using a standard Loadpoint cutting machine. The cut should be made perpendicular to the V-grooves in order to maximise the alignment accuracy. The splitting stage is relatively straightforward, with the exception that the wafer must be cut on a smooth surface, for example a polished quartz plate. If the sample is sloped along the direction of the cut, the blade will run deeper, making the cut wider at the end than the beginning. This creates a gap at the wider end after realignment.

Stage 3: Intermediate Stage

At this point the individual pieces can be taken away and processed accordingly. Reasonable care must be taken not to damage the grooves. However, it is only during silicon micromachining that extreme caution must be used in protecting the grooves from the silicon etchant solution.

Stage 4: Wafer Realignment

Precision machined metal pins are used to realign the silicon substrate. Best results were used using 1mm ϕ metal blanks suitable for fabrication of high speed drill bits, although reasonable results were obtained using the high speed drill bits themselves.

The drill blanks are placed on a polished quartz plate, suitable for use as photolithography mask plates. The wafer pieces are flipped and placed groove down onto the pins. Pressure is applied to the back of the pieces, in the simplest case using small metal blocks such as those used in contact printing. Care must be taken to ensure that the blocks are evenly distributed to maintain an even force across the back of the realigning pieces. The alignment technique is illustrated schematically in Figure 6.5.

Stage 5: Wafer Bonding

At the time of writing, no specific technique of permanently bonding the individual pieces had been established. In order to demonstrate the alignment principle, pieces were bonded using a sticky photoresist coated silicon wafer as a support. The photoresist was hardened by baking the whole assembly at 90°C for an hour.

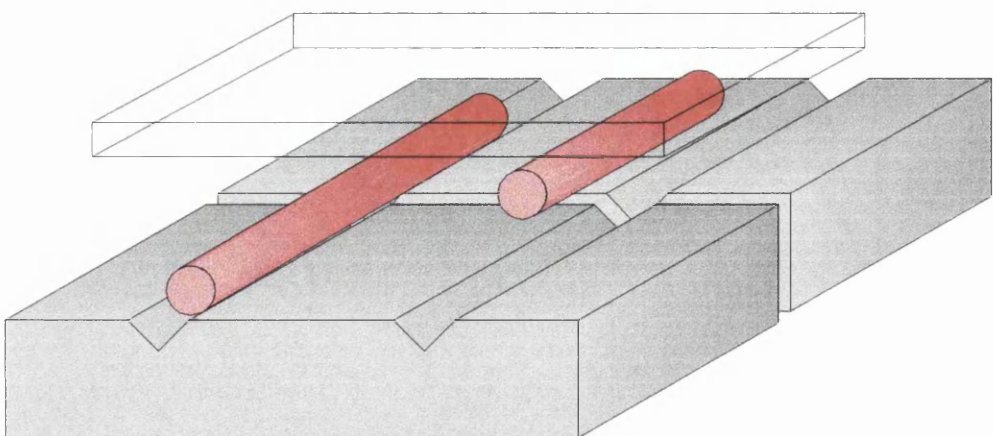


Figure 6.5 Schematic of self aligning process using precision machined metal pins inserted into mechanically ground V-grooves. Pins are placed on an optically flat quartz plate, and pressure is applied to the back of the substrate. Illustration inverted to for ease of understanding.

6.3.2 Demonstration of SPLIT Wafer Technique (Part 1)

The alignment accuracy of this technique was demonstrated using a quartered 3" silicon wafer. Figure 6.6 shows the divided substrate, where each piece has three machined grooves along its length. The grooves were formed by grinding to a depth of 1 mm at an angle of 45°. The sidewall angle of the groove was estimated using a DekTak surface profiler to be 45°. Also shown in Figure 6.6 is a 1.5 mm ϕ drill bit for demonstration purposes only.

The quarter pieces were aligned using the technique described in the previous section, and bonded in position under applied pressure using a photoresist coated half silicon wafer as a support. The aligned pieces are shown on the left of the photograph shown in Figure 6.6. Figure 6.7 shows a close-up of these aligned quarter pieces.

In order to evaluate the alignment precision of the technique, the bonded pieces were examined under an optical microscope. Figure 6.8 shows the bottom of one of the machined V-grooves, where there is alignment of the damage features of the grinding process. The vernier measurement tool on the microscope was used to measure the lateral alignment, which was estimated to be $\pm 2\mu\text{m}$. Talystep profiling showed the vertical alignment to vary from $1.6\mu\text{m}$ to $2.5\mu\text{m}$ across the sample. This inaccuracy was due to the use of drill bits, rather than smooth drill blanks at this stage.

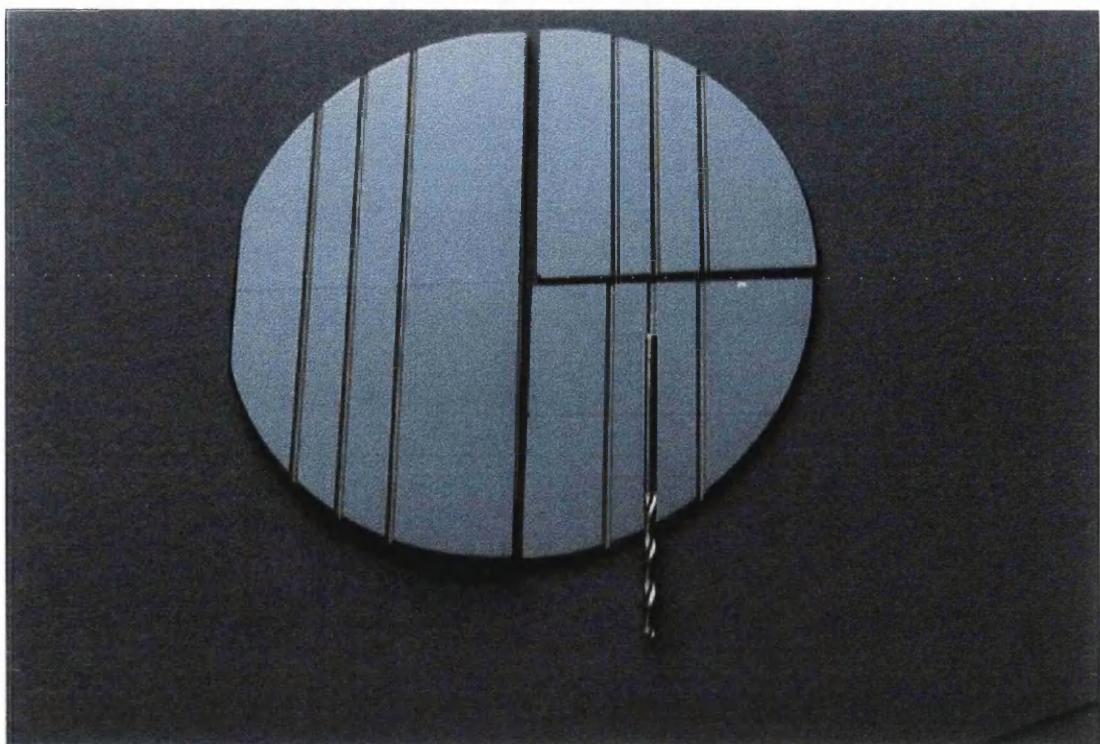


Figure 6.6 Photograph of a divided substrate, with SPLIT processed pieces on the left.

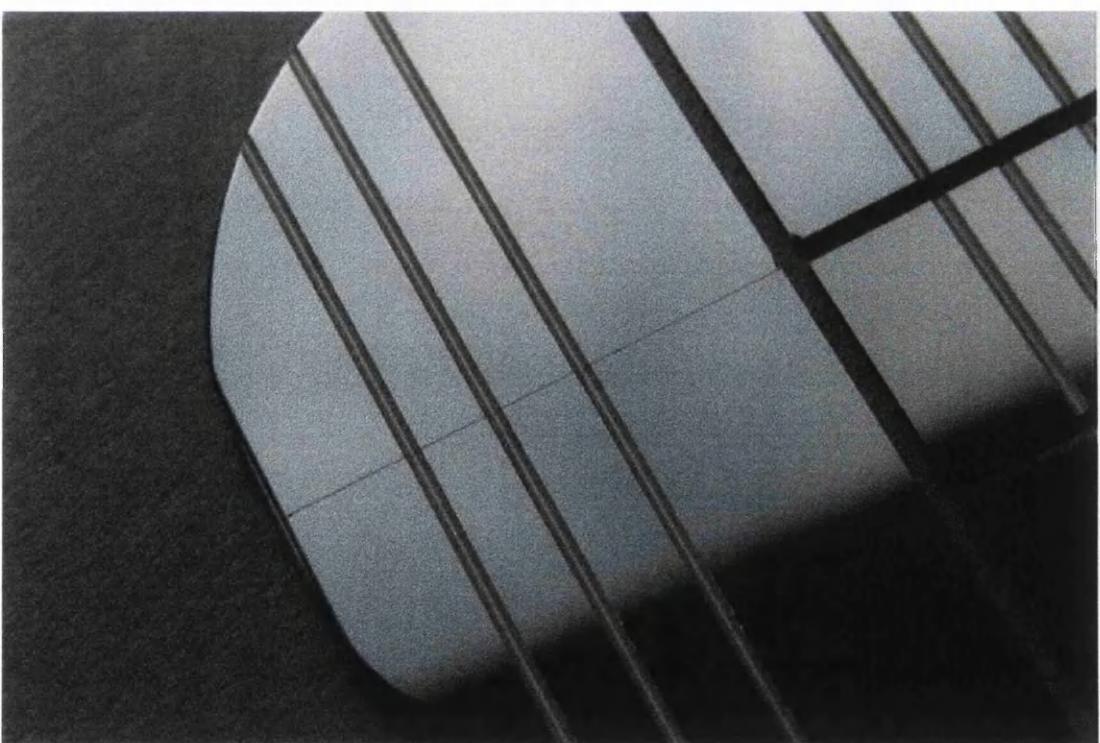


Figure 6.7 Photograph of quarter pieces after alignment by the SPLIT process

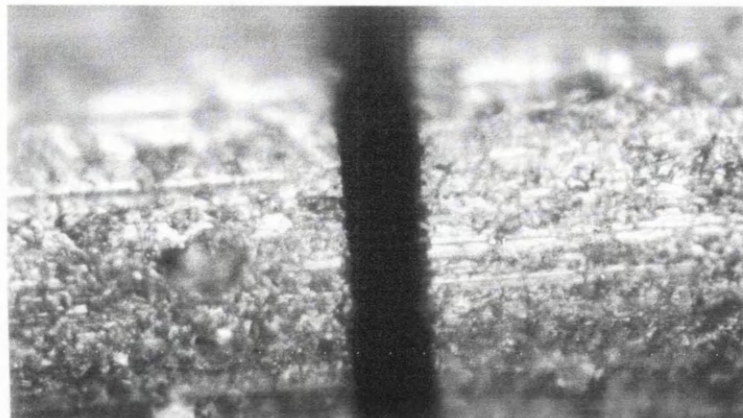


Figure 6.8 Close-up of machined V-groove after alignment by the SPLIT process

6.3.3 Demonstration of SPLIT Wafer Technique (Part 2)

The technique was applied to planar silica waveguides, as a means of better estimating the lateral alignment accuracy. The process was repeated with unclad RIE processed silica waveguides using 1 mm ϕ drill blanks as the alignment pins.

The resulting aligned structure is illustrated by the image shown in Figure 6.9. The lateral alignment was estimated using the optical microscope where the misalignment of the waveguides was found to be on the order of 0.5 μm . Talystep measurements showed that the vertical alignment had improved on the previous measurements where the edge to edge variation ranged from 0.32 to 0.5 μm across the sample. Figure 6.10 shows a Talystep scan of the vertical alignment.

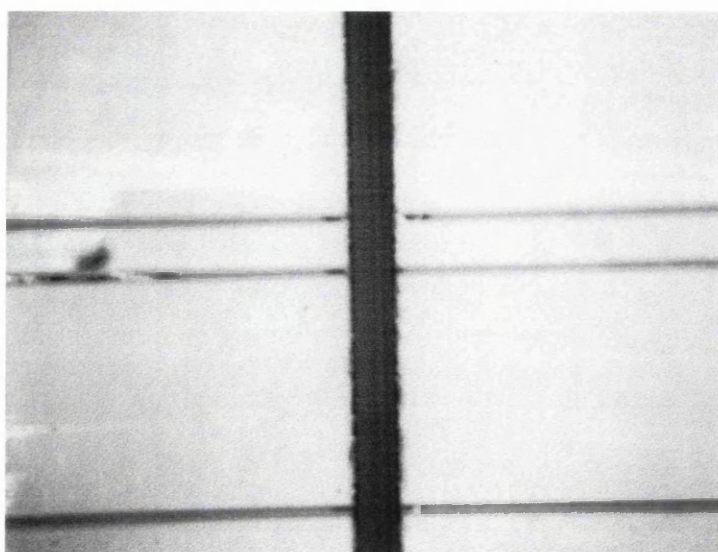


Figure 6.9 Photograph showing the alignment between waveguides. The two centre waveguides are 50 μm apart, with a linewidth of 7.5 μm . The dark band is the split in the wafers.

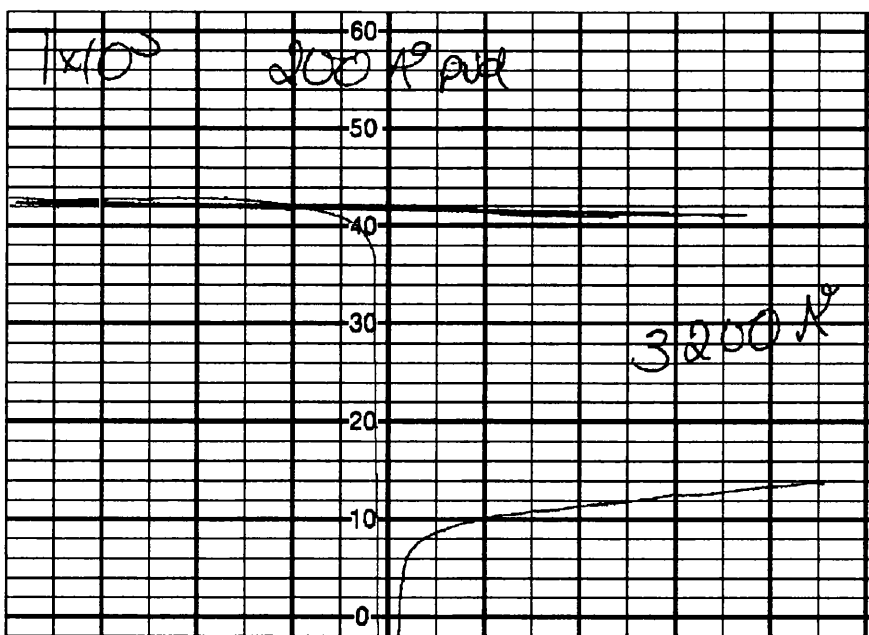


Figure 6.10 Talystep trace showing the vertical alignment of the sample to be $0.32 \mu\text{m}$.

It is clear from the results presented here that the SPLIT technique is a simple and accurate technique of realigning a partitioned silicon wafer. Higher accuracy could be achieved by using silicon micromachining to define the V-grooves.

6.4 Hybrid Processing for Optoelectronic Integration

In the previous section it was described how a silicon wafer could be split into different sections and recombined with accuracy such that each section could be processed in a different way. In the following sections some of this processing is described: firstly silicon micromachining, followed by a section on CVD diamond shaping. The work is intended primarily for the fabrication of self-aligning interfaces for V-grooves and laser diodes, although the technology described easily adapts to planar silica waveguides.

6.4.1 Thermal management of optoelectronic components

One of the major products to have been developed from CVD diamond technology is the diamond heat spreader. Diamond has two optimal properties, namely its thermal conductivity and thermal expansion coefficient, which make it an ideal material for heatsink applications. At room temperature, the thermal conductivity of diamond is much greater than that of any other material. The thermal expansion coefficient of diamond is $\approx 1 \times 10^{-6} \text{ }^{\circ}\text{C}^{-1}$, close to the values for both silicon and silica. The thermal properties for diamond and other packaging materials topic are listed in Table 6.2.

Material	Thermal Conductivity (W m ⁻¹ K ⁻¹)	Specific Heat (J kg ⁻¹ K ⁻¹)	Coefficient of Thermal Expansion (x 10 ⁶ °C ⁻¹)
Al ₂ O ₃	25 - 30	800	5.5 - 9.1
Au	296	132	14.2
Cu	385	385	16.8
Diamond (Natural)	2000	525	0.8 - 1.0
Diamond (CVD)	700 - 2000	525	1.0 - 2.0
GaAs	46 - 56	327	5.4 - 5.9
Silica	1.4	840	0.4
Silicon	149	702	2.6 - 4.7

Table 6.2 Selected thermal properties for materials used in optoelectronic integration

Whilst diamond is a superb thermal conductor, it has a lower heat capacity than copper, $1.85 \times 10^6 \text{ J m}^{-3}\text{K}^{-1}$ for diamond and $3.44 \times 10^6 \text{ J m}^{-3}\text{K}^{-1}$ for copper. Thus diamond can best described as a heat spreader, which requires further heatsinking to remove the heat. Consequently, by combining the heat spreading ability of diamond and the heatsinking performance of copper, more efficient thermal management of laser diodes can be achieved.

The heat spreading ability of diamond has been exploited for some time. However, until now these heat spreaders have been planar in nature, having been cut from larger crystals or fabricated from CVD diamond films. Although planar diamond pieces can be cut and polished it is difficult to produce complex shapes. In the following sections, the fabrication of diamond heat spreading layers on non-planar substrates is described.

By micromachining a silicon substrate and CVD coating it with diamond, features can be fabricated with tolerances sufficient to give precise alignment between laser diodes and optical fibres. These need to be positioned accurately on a micron scale in order to optimise optical coupling from a laser into the fibre. The low thermal expansion coefficient is also beneficial as it is much lower than that of Al₂O₃, a widely used packaging material. As described elsewhere, (see Ref. [7] and [10]) the thermal properties of different packaging materials place a constraint on reliability during temperature cycling. Matched thermal expansion coefficients are required in order to

maintain alignment of the optical components as the package temperature varies. Japanese researchers have recently investigated the use of athermal materials, that is, materials which have a negative expansion coefficient which compensates for the changes in the waveguide layers [12].

The failure rate of microelectronic devices is strongly related to the device temperature [13], often showing an exponential relationship. A 10-20°C increase in temperature can cause a doubling of the failure rate. Whilst the complexity of optoelectronic systems is far from that of microelectronics, applications are being developed, for example where arrays of high power lasers are integrated. The heat generated and the thermal gradients induced by these components may influence not just the device lifetime but also its emission wavelength and spectral width. For example, in AlGaAs double heterojunction lasers the dependence of wavelength with temperature ($\Delta\lambda/\Delta T$) is 0.25 nm/°C [14]. Optimised heatsinking is therefore essential for successful production of a stable integrated optical package.

In the following sections a description is given for the production of micromachined silicon substrates and the subsequent diamond coating of these structures to produce heatsinks with micron tolerance features. Figure 6.11 shows a schematic diagram of the envisaged integrated package with a laser diode (yellow-green), optical fibre, diamond heat spreading layer (blue), substrate heatsink (grey) and thermoelectric cooler (red).

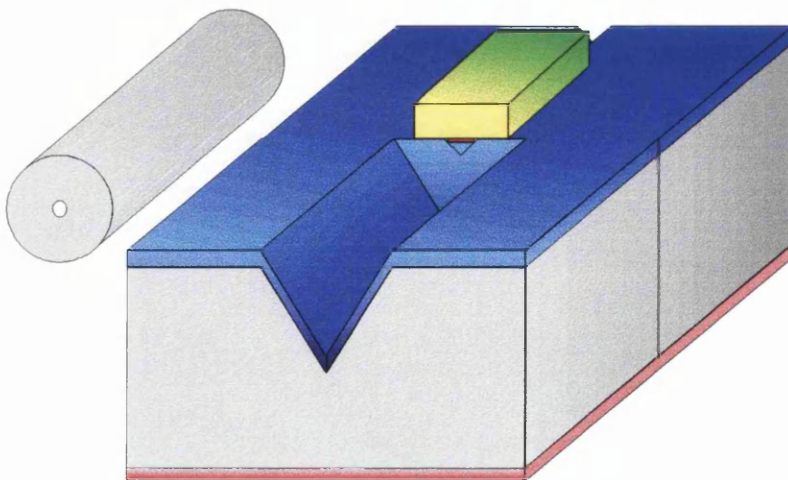


Figure 6.11 Envisaged integrated package, with integral heatsink and optical alignment features, c.f. Figure 6.1.

6.5 Integration (2): Silicon Micromachining

Silicon micromachining has long been an interesting process for fabricating microstructures for various applications [15]. The term, silicon micromachining, refers to any process in which the surface of a single crystal silicon substrate is modified. This can be achieved through bulk micromachining of the silicon substrate itself [5, 6], either through anisotropic wet etching, or surface micromachining by etching thin sacrificial layers on the surface. A review can be found in Gardner [16].

The most common optoelectronic application of bulk micromachining is the silicon V-groove used for holding optical fibres. Other structures include integrated optic interferometric pressure sensors [17], where an etched diaphragm under one arm introduces a phase shift, and the optically addressed microresonant pressure and temperature sensors to which this work is applied [18].

Arguably the most attractive application of silicon micromachining, is through surface micromachining to form micro-optical benches incorporating lenses and micro-positioners (Berkeley Refs. from CLEO). Surface micromachining can also be found in the fabrication of spatial light modulators [19], optical choppers [20] and fast mechanical modulators for fibre-to-the-home applications [21]. Motamedi [22] presents a short review of some micro-opto-electro-mechanical systems.

6.5.1 Anisotropic Wet Etching of Single Crystal Silicon

Silicon can be wet etched in two ways: isotropically or anisotropically. In isotropic etching, solutions of nitric, acetic and hydrofluoric acid are commonly used [16]. However it is difficult to control the etch rate and the rate is quite often diffusion dependant therefore making systematic etching difficult.

Anisotropic etch processes by contrast, offer a higher degree of control. Single crystal silicon substrates can be anisotropically etched in inorganic alkaline solutions such as potassium hydroxide (KOH) and caesium hydroxide (CsOH) to accurately produce features of micron dimension and tolerance. The rate at which etching takes place depends strongly on the crystallographic orientation and the doping level (for example the boron diffused etch stops used in cantilever fabrication, Chapter 1).

Potassium hydroxide etches preferentially in the $<100>$ and $<110>$ directions for both (100) and (110) orientated substrates. In (100) substrates, the ratio of the etch rate between the $<100>$ and $<111>$ direction can be greater than 100:1, where the intersection angle between the planes is 54.74° . Similar ratios exist in (110) orientated wafers where the etch ratio between the $<110>$ and $<111>$ directions can also be greater than 100:1, where the angle between the intersecting planes is 90° . An illustration of the etch geometry is shown in Figure 6.12.

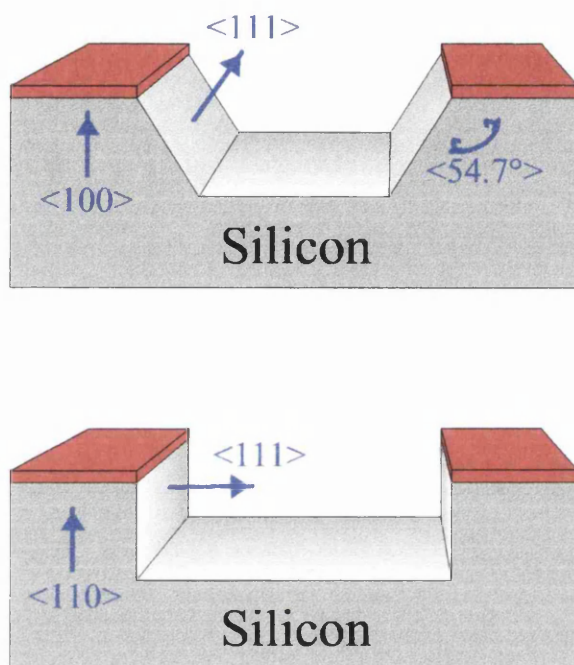


Figure 6.12 Top illustration shows the result of etching a (100) silicon substrate, mask aligned to the $<110>$ direction. The lower illustration shows a etched (110) substrate, $<100>$ alignment.

V-groove Fabrication

For the purposes of producing V-shaped grooves and ridges, etching is restricted to (100) silicon substrates. A V-groove can be produced by etching through a window in the etch mask, whereas a V-shaped ridge can be produced by etching the area surrounding a strip of mask as shown in Figure 6.13.

V-grooves are self limiting, terminating on the (111) planes, whilst ridge etching must be accurately timed as the etch will continue through the wafer. As mentioned previously, the angle between the (100) surface and the (111) sloping plane is 54.74° .

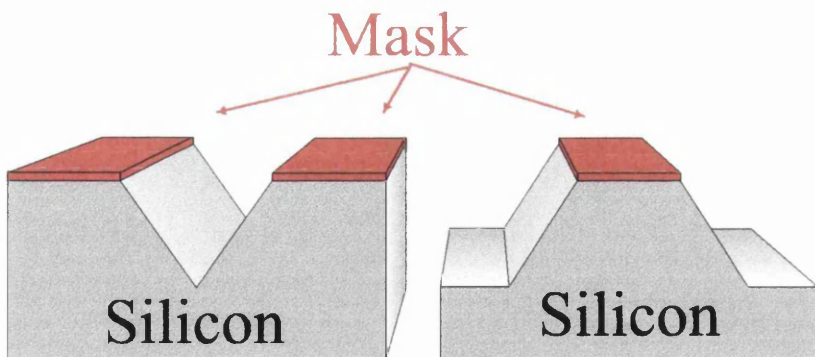


Figure 6.13 Illustration of V-groove (left) and V-ridge (right) formation using a windowed and strip etch mask. V-groove is self limiting as the etch terminates at the intersection of the (111) planes.

The Process - Figure 6.14 (a-g) on the following page

A (100) single crystal silicon wafer (a) is coated with a mask material to a thickness of 500 nm by plasma enhanced chemical vapour deposition (PECVD)(b). For silicon micromachining using potassium hydroxide (KOH), this mask could be either SiO_2 or Si_3N_4 . In practice Si_3N_4 makes a better etch mask as its etch rate in KOH is much lower than that of SiO_2 . The mask material is spin coated with photoresist, typically Shipley S1818 and pre-baked at 90°C for 30 minutes.

The sample is exposed through a photomask (c) using either a mask aligner or a contact printer and developed (d). Anisotropic etching will take place when the photomask is aligned with the <110> directions in the silicon wafer with an angular accuracy of <0.1°. Pattern transfer to the etch mask uses either wet etching in buffered HF, or dry etching in a CHF_3 plasma. Wet etching is faster, but being isotropic in nature, results in lateral widening of the mask window. Dry etching is recommended where greater dimensional control is required.

After etching the mask (e) the remaining photoresist is removed and the sample is placed in a 30 wt. % aqueous solution of KOH at 70°C for anisotropic etching (f). The etching is carried out in a quartz beaker with a reflux condenser attached. Quartz is required since KOH attacks glass, and the reflux condenser prevents the concentration of the solution from changing during the etch process. The final process in fabricating V-grooves is the removal of the etch mask (g).

A photograph off the KOH wet etch equipment is shown in Figure 6.15.

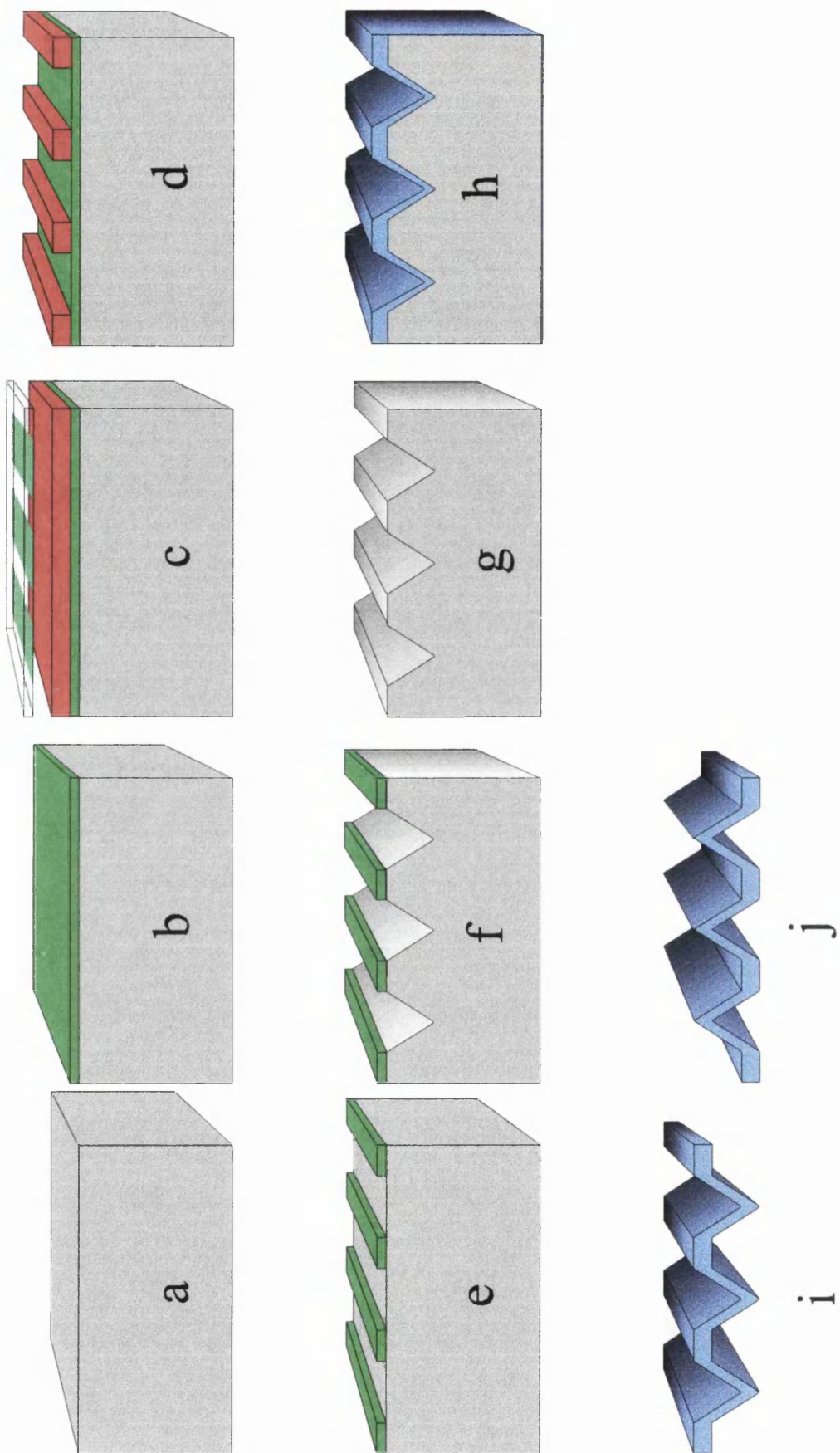


Figure 6.14 The process steps in fabricating V-grooves, and patterned free standing diamond.



Figure 6.15 Water bath, condenser and quartz beaker for KOH etching of silicon

Results of Anisotropic Wet Etching

The micrograph shown in Figure 6.16 illustrates the effect of etching through a window into (100) orientated silicon. On the left of the image the (111) etch plane can be seen quite clearly, with its characteristic 54.74° etch angle. The roughness at the bottom of the groove is thought to have arisen due to angular misalignment. Similarly, ridge etching is shown in the micrograph shown in Figure 6.17 where the etch is clearly progressing through the substrate, c.f. Figure 6.12 & 6.13.

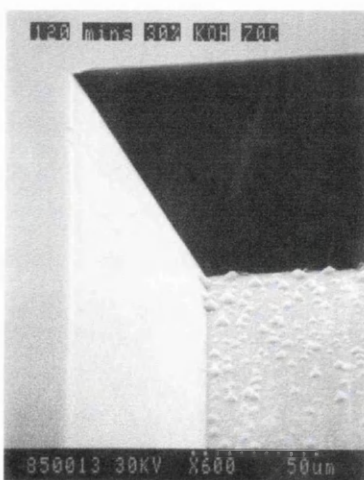


Figure 6.16 Micrograph of etched pit in silicon

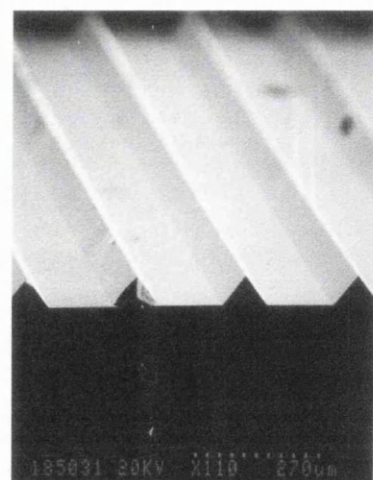


Figure 6.17 Micrograph of V-ridges

The results of micromachining v-grooves in silicon are shown in Figure 6.18. These V-grooves are 150 µm wide and 106 µm deep. The etch can clearly be seen to have terminated where the two (111) planes defining the walls of the V-groove meet. The etch rate was 0.5 µm min⁻¹ in the <100> direction and approximately two orders of magnitude lower in the <111> direction. The crystallographic nature of this etch produced accurately angled walls with low surface roughness.

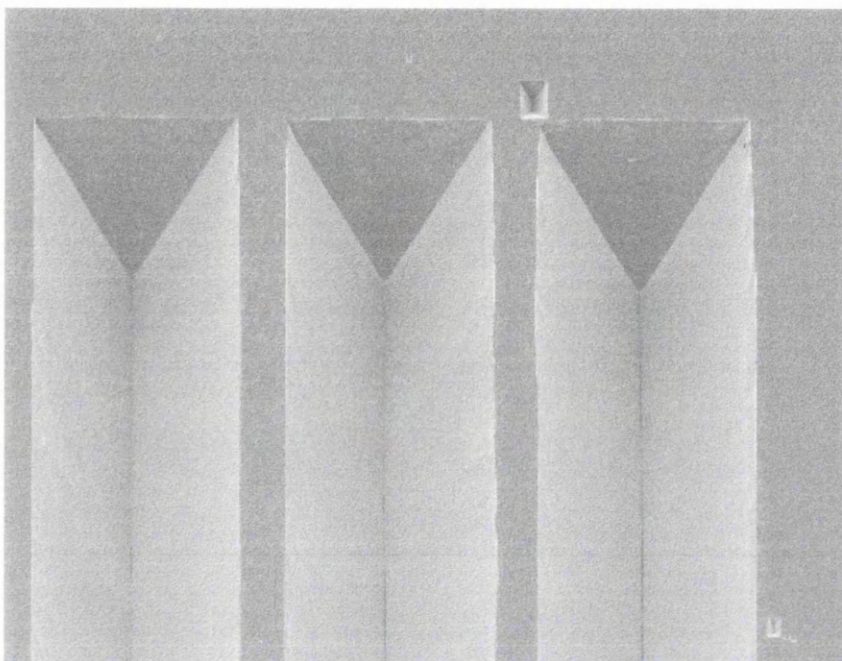


Figure 6.18 SEM of micromachined silicon V-grooves (150 µm wide and 106 µm deep)

At this point the silicon is ready for use in aligning optical fibres with other components. Alternatively, the silicon can be thoroughly cleaned and prepared for CVD diamond deposition, Figure 6.14 (h).

6.6 Integration (3) Micromachined Pattern transfer into CVD diamond [23 ,24]

Micromachined silicon substrates, were sent for diamond coating in *the* Heriot-Watt University Microwave Plasma CVD Reactor [25]. A three step process was used, as described on the following page:

- *Pre-treatment:* The pre-treatment step aids the removal of native oxide and coats the sample with a carbonaceous layer which is subtly altered during the bias induced nucleation step [26],

- *Bias induced nucleation*: This step is used to ‘seed’ the substrates for diamond growth. This method was chosen over mechanical abrasion techniques because of the need to coat complex geometries and provide a high nucleation density without damaging the accurately machined silicon structures,
- *Growth*: The conditions for the growth step are chosen to give a high rate of diamond deposition and to produce epitaxially orientated material.

The conditions used for each step of the process are listed in Table 6.3.

	(1) Pre-treatment	(2) Bias	(3) Growth
Pressure (mbar)	40	25	45
Temperature (°C)	850	850	700
Microwave Power (W)	500	175	800
Applied Bias (V)	0	-320	0
Duration (hr)	1	0.5	2 - 24
H ₂ Flow (sccm)	500	500	85
CH ₄ Flow (sccm)	6	6	2.5
CO (sccm)	0	0	70

Table 6.3: Process parameters used for CVD diamond deposition (Data courtesy of Dr M.G. Jubber)

After 24 hours of diamond deposition, the centre of the sample was uniformly coated to a thickness of 25 µm. The photograph shown in Figure 6.19 shows the greyish appearance of the diamond coating as deposited on the silicon substrate. Under SEM examination, the diamond layer has a much different appearance. The micrograph of Figure 6.20 shows conformal coating of the diamond film, following the contour of the micromachined silicon substrate, without any apparent variation of thickness.

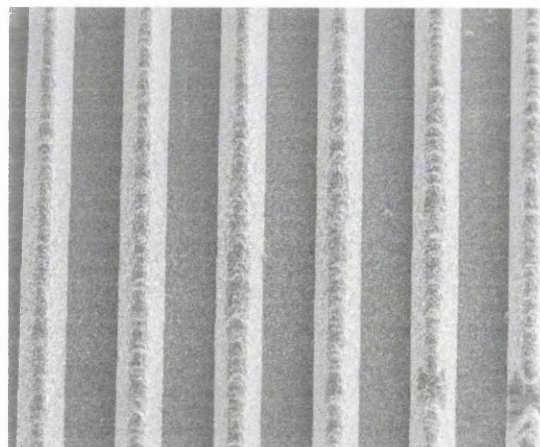


Figure 6.19 Photograph of diamond coated silicon substrate

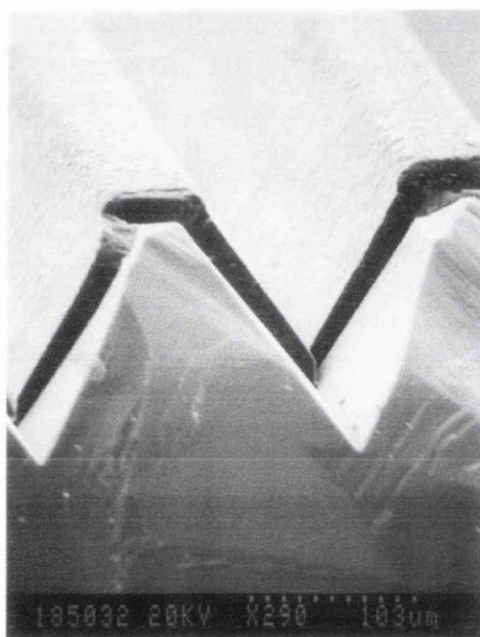


Figure 6.20 SEM Micrograph of conformal coating of silicon substrate with diamond film

Progression from this point very much depends on the diamond film requirements. For example, if only a thin layer of diamond is required, then it is possible to leave the diamond on the silicon substrate Figure 6.14 (h). The upper (growth) side of the diamond film is relatively smooth and conformal to the underlying silicon substrate.

For thicker layers ($>20 \mu\text{m}$) or where low surface roughness is essential, a free standing diamond film (i) can be created by sacrificially etching away the silicon in KOH. This can be turned over (j) to reveal the smooth surfaces which were in contact with the micromachined silicon substrate.

Figure 6.21 shows the free standing 25 μm thick diamond layer, after sacrificial etching in KOH. Two features to note are the thickness uniformity of the diamond coating over the V-shaped profile, and the smoothness of the surface which had been in contact with the micromachined silicon substrate.



Figure 6.21 Free standing diamond layer after sacrificial etching of silicon substrate.

The micrograph shown in Figure 6.22 shows localised epitaxially orientated growth on top of the V-shaped ridge. The diamond facets have formed epitaxially with the (100) orientated silicon substrate.

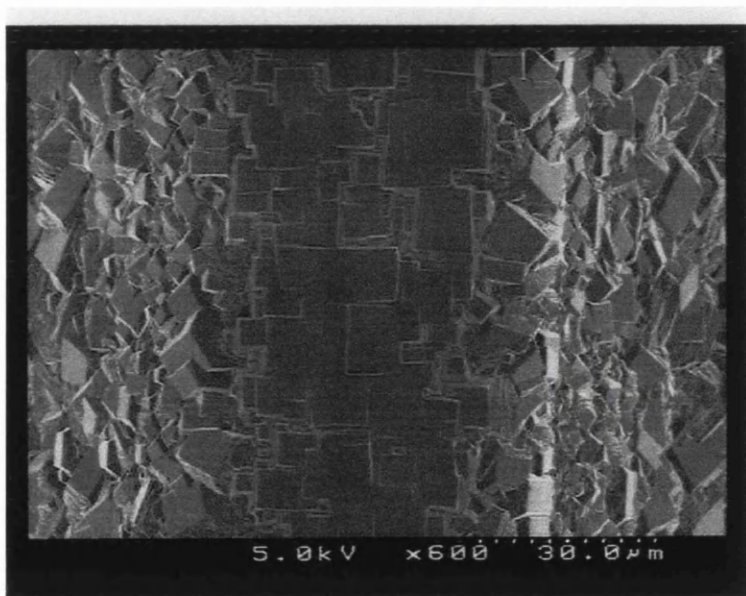


Figure 6.22 Demonstration of localised epitaxial growth on top of V-shaped ridges

Diamond deposition in rectangular trenches etched in silicon by reactive plasma etching has been previously investigated [27]. The authors found that the nucleation density was 3-5 orders of magnitude lower on vertical walls than on surfaces normal to the ion bombardment during bias assisted nucleation.

By contrast, in this work, V-grooves located near the centre of the deposited film were uniformly coated with diamond. However, near the edge of the deposited area there was a reduction in the nucleation density with increasing distance from the centre of the deposit. In some cases nucleation was entirely suppressed whilst growth on the top surface remained continuous.

Examination of etched holes in the silicon, shows that nucleation can clearly be seen on the surface, but that no nuclei are visible within the pyramid structure. This suggests that the electric field gradient, at the surface of the silicon structure, applied during the bias induced nucleation step is important in determining the nucleation density.

6.6.1 The case for CVD diamond films - Finite Element Modelling

The advantages of CVD diamond films in optoelectronic heatsink applications have been evaluated through the use of finite element modelling by Dr. M.G. Jubber. The work focused on a 2-dimensional model of the thermal performance of a simplified laser amplifier structure [28]. Models examined devices bonded p-side up (active region away from the heatsink) and p-side down (active region close to the heatsink). The heatsink was formed from an integrated diamond heat spreader and copper heatsink. The anisotropic thermal conductivity of CVD diamond was used in the models [29].

The modelling showed that optimum results can be obtained by bonding the devices p-side down, as summarised in Table 6.4. Increasing the diamond thickness from 0-200 μm would cause a 30% reduction in device temperature due to lateral heatspreading. However, thicker films are detrimental to device performance due to increased thermal resistance. Due to the slow rate of change of temperature with increasing diamond thickness above 100 μm , and the relatively long CVD process times for thick films, the optimum practical heatsink arrangement is to bond the device p-side down on a 100 μm thick diamond heat spreader on a copper heatsink.

	Temperature Rise p-side down (K)	Temperature Rise n-side down (K)
Ideal Heatsink	2.9	20.3
Copper Heatsink	6.3	22.4
Copper Heatsink with diamond heat spreader	5.4	22.7

Table 6.4 Influence of sample orientation and heatsink type upon device operating temperature.

6.7 Conclusions

A novel technique of integrating optoelectronic components onto a single silicon motherboard has been presented. The technique has been shown in principle to be capable of passively re-aligning multiple pieces of a divided silicon substrate to sub-micron accuracy using basic workshop technology. A combination of silicon micromachining and CVD diamond deposition has been used to fabricate patterned diamond structures which can in principle be used for aligning optical components such as laser diodes and optical fibres, whilst providing a means for efficient thermal management. Finite element modelling has been used to study the influence of semiconductor device orientation during bonding processes, and the relationship with the type of heatsink used. It is found that the operating temperature of optical components is strongly dependant on this orientation.

References

- [1] The SBAC Technology Committee, "Applications of Photonics in Avionics", Issue 1, February 1996.
- [2] Papers within IEE Colloquium on "Planar Silicon Hybrid Technology", IEEE Digest No. 1994/198, 1994.
- [3] Y. Yamada, M. Yamada, H Terui & M Kobayashi, *Opt. Eng.*, 1989, **28**, 1281
- [4] M. Kawachi, *Opt. & Quant. Elec.*, 1991, **22**, 331.
- [5] D.B. Lee, *J. Appl. Phys.*, 1969, **40**, 4569
- [6] K. E. Bean, *IEEE Trans. Electron. Dev.*, 1978, **ED-25**, 1185
- [7] M.J. Wale and C. Edge, *IEEE Trans. Components., Hybrids & Manuf. Technol.*, 1990, **13(4)**, 780.
- [8] S.A. Cassidy, F. MacKenzie, C.J. Beaumont, G.D. Maxwell, B.J. Ainslie, C.A. Jones, D. Rush and A. Thurlow, *BT Technol. J.*, 1993, **11(2)**, 137.
- [9] C.A. Jones, M.W. Nield, K. Cooper and J.D. Rush, Paper 12, in Reference [2].
- [10] A. Sugita, K. Onose, Y. Ohmori and M. Yasu, *Fiber & Integr. Opt.*, 1993, **12**, 347.
- [11] Y. Hibino, F. Hanawa, H. Nakagome, M. Ishii and N. Takato, *J. Lightwave Technol.*, 1995, **13**, 1728.
- [12] Y. Inoue, A. Kaneko, F. Hanawa, H. Takahashi, K Hattori and S. Sumida, *Electron. Lett.*, 1997, **33**, 1945.
- [13] A. Bar-Cohen, in R.C. Dorf (ed.), *The Electrical Engineering Handbook*, CRC Press Inc., Boca Raton, Florida, USA, 1993, Chapter 32 - "Thermal Management of Electronics" and references therein.
- [14] H. Kressel and M. Ettenberg, in M.J. Weber (ed.), *CRC Handbook of Laser Science and Technology, Volume 1, Lasers and Masers*, CRC Press Inc., Boca Raton, Florida, USA, 1982, Chapter 2.2 - "Semiconductor Lasers", p. 199.

- [15] K. Petersen, *IEEE Trans. on Electron Devices*, 1982.
- [16] J.W. Gardner, *Microsensors: Principles and Applications*, John Wiley & Sons, 1994.
- [17] M. Ohkawa, M. Izutsu and T. Sueta, *Appl. Opt.*, 1989, **28**, 5153.
- [18] A. J. Jacobs-Cook, *Sensors & Actuators A*, 1993, **37-38**, 540.
- [19] T.-H. Lin, *Opt. Eng.*, 1994, **33(11)**, 3643
- [20] M.T. Ching, R.A. Brennan and R.M. White, as reference 19, 3634
- [21] J.A. Walker, K.W. Goossen and S.C. Arney, *J. Microelectromech. Syst.*, 1996, **5(1)**, 45.
- [22] M.E. Motamedi, as reference 19, 3505.
- [23] M.G. Jubber, A.J. McLaughlin, J.H. Marsh, J.S. Aitchison, P. John, C.E. Troupe and J.I.B. Wilson, *Diamond 1996*, Tours, France, Sept. 1996.
- [24] M.G. Jubber, A.J. McLaughlin, J.H. Marsh, J.S. Aitchison, P. John, C.E. Troupe and J.I.B. Wilson, *Dia. and Rel. Mats.*, 1998, **7**, 1148.
- [25] M.G. Jubber, J.I.B. Wilson, I.C. Drummond, P. John and D.K. Milne, *Vacuum*, 1994, **45(5)**, 499.
- [26] P. John, C. Graham, D.K. Milne, M.G. Jubber and J.I.B. Wilson, *Dia. and Rel. Mats.*, 1996, **5**, 256.
- [27] A. Flöter, G. Schaarschmidt, B. Mainz, S. Laufer, S. Deutschmann and H.-J. Hinneberg, *Dia. and Rel. Mats.*, 1995, **4**, 930.
- [28] M.G. Jubber, K. McIlvaney, A.J. McLaughlin, J.H. Marsh, J.S. Aitchison, C.E. Troupe, P. John, J.I.B. Wilson, *to be presented at CLEO/EQEC '98*, Glasgow, CTuL41, 1998.
- [29] J.E. Graebner, S. Jin, G.W. Kammlot, Y.-H. Wong, J.A. Herb and C.F. Gardinier, *Dia. and Rel. Mats.*, 1993, **2**, 1059.

Chapter 7 Conclusions and Suggestions for Future Work

7.1 Conclusions

This thesis has been concerned with development of the techniques used to produce planar silica waveguide interferometers suitable for use in low coherence sensing applications. Principally this has involved the development of high rate, high selectivity, reactive ion etch processes, both to increase device throughput and to enable the fabrication of large core, multimode waveguide devices.

During the course of this work, the Flame Hydrolysis Deposition (FHD) facility has been improved through the upgrade of the deposition area to cleanroom standard. Roof mounted 'hepafilter' units were installed to proved a positive pressure within the room. The room was sealed, and painted with a cleanroom paint to reduce the level of contaminants within the room. At the outset of the work the room was classified as Class 100,000, but after renovation the room is now close to Class 100 standard. An observed reduction in the defect count on samples was observed, where the typical defect count is now less than 1 per cm^2 . Defects are also minimised by restricting the level of contact with wafers, as new, after deposition and during photolithography.

The glass system, $\text{SiO}_2\text{-GeO}_2\text{-B}_2\text{O}_3$, was investigated for the first time within the department. Initial studies examined the influence of the GeCl_4 flow rate upon the refractive index of the glass films, for a fixed SiCl_4 and BCl_3 flow rate. A reproducible, linear increase in refractive index was observed. Visual inspection of the samples indicated that complete sintering of the deposited oxide 'soot' had not been achieved, high levels of in, and out of plane scatter were observed. It was concluded that sintering temperature of the glass system was higher than the furnace maximum.

A new mass flow controller (MFC) was installed to increase the range of the BCl_3 flow rate (0-100 sccm). Inspection of samples produced with higher BCl_3 flow rates exhibited higher degrees of sintering with less observed scattering. An increase in the B_2O_3 content of the glass was confirmed by a decrease in the glass refractive index of approximately 0.1%.

Electron Microprobe analysis of the glass films indicated a linear increase of the GeO₂ content from 7.08 wt% to 16.23 wt% with increasing GeCl₄ flow rate. Analysis of the B₂O₃ content was also performed, but in general the levels measured were found to be below the quoted accuracy of the Microprobe. The analysis also showed the dopant homogeneity across 2 cm samples also to be less than the quoted Microprobe accuracy. EDS analysis of glass films prepared during different depositions shows the dopant homogeneity to be of the order of 0.38 wt% from one deposition to another. In the authors experience, the film thickness varied by less than $\pm 5\%$ from deposition to deposition and across a 3" wafer. Refractive index measurements have shown the birefringence to be 3.9×10^{-4} . The germanosilicate glass system has been shown to be photosensitive through the formation of UV written gratings on waveguide cores.

A difference in waveguide quality has been observed which has been attributed to the technique used to prepare NiCr etch masks. Thermally evaporated NiCr has been shown to result in smoother sidewalls, compared to those prepared by electron gun evaporation.

Reactive ion etch processing (RIE) of the germanosilicate glass system has been extensively investigated. The etch processes have been assessed in terms of glass etch rate, glass to mask selectivity, and qualitative assessments of the etch quality.

The implications for deep etching ($>10 \mu\text{m}$) of flame hydrolysis deposited silica glass using CHF₃, C₂F₆ and SF₆ as etchant gases have been presented. From the experimental data obtained, CHF₃ presents the most versatile etch process, in terms of FHD glass etch rate and high selectivity over both photoresist and nichrome. However higher etch rates are obtainable with the other etchant gases at the expense of selectivity and, in the case of SF₆, sidewall quality. Furthermore, it has been illustrated that SF₆ has a high selectivity over nichrome, which could be exploited by using a CF_X generating gas for increased sidewall protection. The experimental data also illustrates that doped silica glasses prepared by FHD have higher etch rates compared to pure fused silica.

The CHF₃ plasma process was investigated further through the inclusion of small amounts of O₂ in the etch process. It has been shown that the inclusion of O₂ results in

a reduction in sidewall roughness and that, in principle, sidewall roughness can be controlled by the controlled addition of O₂. However, O₂ has also been shown to increase lateral sidewall erosion with a reasonable amount of undercut observed.

Experimental design techniques were applied to study the influence of the main RIE process parameters in CHF₃/O₂ etching on the glass etch rate, mask etch rate and chamber cleanliness. The greatest variation in the glass etch rate was obtained under RF power and O₂ flow rate variation. It is generally thought that O₂ addition helps increase the number of etching species, as does an increase of RF Power. Mask etch rate variation was found to be greatest under RF power variation, followed closely by O₂ flow rate). In the case of RF power it is thought that this is largely due to the self bias voltage of the process, whereas in oxygen addition it is attributed to the decrease, and subsequent increase of polymer and reactive species respectively. The cleanliness of the chamber sidewalls and the sample was found to improve with decreasing CHF₃ and increasing O₂. It is suggested that the Taguchi design technique used in this thesis should not be used in further development as the technique has a number of limitations, such as no indication of interactions between factors.

The developed CHF₃ process has been shown to be highly reproducible with a high glass etch rate and mask selectivity. The etch profile has been shown to be anisotropic. This process and NiCr etch masks have now been adopted as the main silica waveguide fabrication technique.

Passive phase shifting in asymmetric Mach-Zehnder interferometers has been studied. A simple model has been demonstrated for selecting S-bend parameters when introducing small phase shifts, upto π , between the arms of an interferometer. BPM simulations were performed to precisely simulate optical propagation through the asymmetric interferometer. Interferometers were designed with 0, 80, 90, 100 and 180° phase shifts.

Asymmetric interferometers were fabricated and tested where it was found that the optical phase shifts were correct to within $\pm 2\%$ of the intended shift. However, it was highlighted that these phase shifts are dependant on fabrication reproducibility and the wavelength at which the devices operate.

Active phase control of these devices was investigated where control was facilitated through the thermo-optic effect. Phase modulators were fabricated which exhibited fast response times (~ 150 μ s) and modest operating powers. The device has been tested at 0.85, 1.3 and 1.55 μ m, where typical On/Off ratios in excess of 30 dB were found. It is thought that the electrical current density is below that of the electro-migration threshold for NiCr electrodes making the device simple to package, i.e. in a non-hermetic housing. The operating powers could be reduced further by fabricating an asymmetric interferometer (90° shifted) and biasing both interferometer arms. An alternative application of the device could be as a variable attenuator.

A finite element model has been developed which can be used to simulate thermo-optic modulators with different geometries. Devices have been simulated which exhibit faster response times or lower power consumption. Inevitably, there is a trade-off between speed and power. Devices have been simulated where the thermal mass of the interferometer cross-section has been reduced by RIE, and high conductivity diamond has been inserted about the core. The optical response time was observed to fall to just to 25 μ s, albeit at an power of 6W. Lower power devices been simulated where the electrical power is less than 0.26W, although the response time is 262 μ s.

Path imbalanced interferometers have been fabricated for low coherence sensing applications where the optical path difference (OPD) of the device is 250 μ m. Low coherence optical sources with a coherence length of <35 μ m and an average output power of 2.5 mW have been fabricated. The interferometers have been shown to be reasonably stable at a constant bias point, where the typical drift at the quadrature bias point was less than 1% over 30 minutes. The tuning range has been found to be controllable over 4π , with a nominal π shift power of 0.22 W at 878 nm. Preliminary channelled spectra measurements have been made, where the static group OPD has been shown to be approximately 279 μ m.

A novel technique for aligning optoelectronic components has been demonstrated. The technique involves splitting a silicon substrate into pieces which can then be processed using different techniques, e.g. FHD, RIE, silicon micromachining and electrode patterning. Accurate alignment of the pieces is ensured after re-alignment by

machining alignment grooves on the back of the substrate prior to division. Preliminary results indicate that this technique possess submicron accuracy.

A combination of silicon micromachining and CVD diamond deposition has been used to fabricate patterned diamond heatsinks with integral fibre alignment grooves. By machining ridges in the silicon, and depositing diamond films on the surface, a conformal diamond coating can be obtained. Sacrificial etching of the silicon results in a V-grooved diamond heatsink. This can be used for thermal management of laser diodes whilst facilitating alignment with optical fibres.

7.2 Suggestions for Future Work

During the course of this work it could be observed that there was a constant minimum sidewall roughness on RIE processed waveguides (~ 100 nm). This is a problem as sidewall roughness is a major source of loss in silica waveguides. Pattern transfer to metal masks during photolithography and the influence of O₂ in the etch process seem to have some bearing on the final sidewall roughness. Development work still needs to be performed to isolate the origin of the sidewall roughness.

An investigation into the relationship between glass doping levels, and dopant types, and RIE processing should be performed. Increasing tolerances in waveguide devices necessitates a clear understanding of the fabrication processes. It has already been highlighted that there is a 37% difference in etch rate between GeO₂ doped glass and quartz when etching in CHF₃. It is also known that there is a small difference when etching P₂O₅ doped glass.

The development of RIE processing should be taken further with a detailed analysis of new etch chemistries. The problems of etching in CHF₃, C₂F₆ and SF₆ have been highlighted earlier in thesis, however it is known that combinations of etch gases can yield successful etch process. Some suggestions for investigation include CHF₃/C₂F₆, CHF₃/SF₆, and SF₆/O₂. The inclusion of C₂F₆ in CHF₃ processes has been studied by previous authors and has been shown to increase the glass etch rate at the expense of the mask etch rate. Re-examination using experimental design techniques could provide new information regarding this etch process. The combination of SF₆ and CHF₃ can be looked upon from two points of view: either SF₆ improves the glass etch

rate, or CHF_3 improves the selectivity. Either way the combination of a fluorine producing gas and a CF_x producing gas could provide an interesting etch process. O_2 addition to SF_6 is suggested as a means of reducing the sidewall erosion characteristic of deep SF_6 etching.

It is suggested that the novel lower power and faster response thermo-optic modulators designs described in Chapter 4 are investigated. BPM simulation of the waveguide cross-sections after RIE removal of the excess cladding material, and after infilling of high conductivity materials needs to be performed to minimise optical loss and polarisation sensitivity.

With the developments made in the $\text{SiO}_2\text{-GeO}_2\text{-B}_2\text{O}_3$ glass system, particularly with the work of P.V.S. Marques on the photosensitive aspects of the glass, it is suggested that UV trimming of the interferometer path lengths be investigated. This can take the form of trimming the OPD to quadrature, trimming the OPD to match the cavity length of a sensing interferometer or generating the OPD completely using UV trimming. The stability of UV trimmed regions at high and low temperatures would need to be assessed before successful implementation in a sensor system such as those found on aircraft.

Related to the photosensitive $\text{SiO}_2\text{-GeO}_2\text{-B}_2\text{O}_3$ glass is the use of poling to introduce an electro-optic effect into the glass. This could be used in place of the slower thermo-optic effect as a means of tuning the interferometers.

Much work still has to be performed on the low-coherence applications of the interferometers. Firstly, a higher power, and stable low-coherence source needs to be obtained, before accurate measurements of the OPD can be obtained. The interferometers can then be tested in series, where one device is modulated as a sensor and the other tracks the phase. If the devices can be poled successfully, they could be potentially used as voltage/current sensors.

Finally, the alignment accuracy of the SPLIT processing of silicon wafers and the integral diamond heatspreaders needs to be assessed with real optical components. A robust bonding technique needs to be obtained to re-combine the devices.

Publication List

- [1] J.R. Bonar, M.V.D. Vermelho, P.V.S. Marques, A.J. McLaughlin and J.S. Aitchison, *Opt. Comms.*, 1998, **149**, 22.
- [2] J.R. Bonar, M.V.D. Vermelho, A.J. McLaughlin, P.V.S. Marques, J.S. Aitchison, J.F. Martins-Filho, A.G. Bezerra, A.S.L. Gomes and C.B. deAraujo, *Proc. ECIO'97.*, Stockholm, 1997
- [3] J.R. Bonar, M.V.D. Vermelho, A.J. McLaughlin, P.V.S. Marques, J.S. Aitchison, J.F. Martins-Filho, A.G. Bezerra, A.S.L. Gomes and C.B. deAraujo, *Opt. Comms.*, 1997, **141**, 137.
- [4] P.V.S. Marques, J.R. Bonar, A.J. McLaughlin, A.M.P. Leite and J.S. Aitchison, *Fisica '98*, 11th National Physics Conference, Porto, Sept. 1998.
- [5] P.V.S. Marques, J.R. Bonar, A. Glidle, A.J. McLaughlin, A.M.P. Leite and J.S. Aitchison, *Proc. QE-13*, Cardiff, 1997.
- [6] P.V.S. Marques, J.R. Bonar, A. Glidle, A.J. McLaughlin, A.M.P. Leite and J.S. Aitchison, *OSA Topical Meeting - "Bragg gratings, photosensitivity and poling in glass waveguides and fibres; applications and fundamentals"*, Virginia, 1997
- [7] A.J. McLaughlin, J.R. Bonar, M.G. Jubber, P.V.S. Marques, S.E. Hicks, C.D.W. Wilkinson and J.S. Aitchison, *Conference on Lasers and Electro-optics*, **11**, OSA Technical Digest Series, 1997, 508.
- [8] A.J. McLaughlin, J.R. Bonar, M.G. Jubber, P.V.S. Marques, S.E. Hicks, C.D.W. Wilkinson and J.S. Aitchison, *J. Vac. Sci. Technol. B*, 1998, **16**, 1860.
- [9] J.M. Ruano, D.Ortega, J.R. Bonar, A.J. McLaughlin, M.G. Jubber, J.M. Cooper and J.S. Aitchison, to be presented at *MNE'98*, Belgium, 1998.
- [10] A.J. McLaughlin, M.G. Jubber, J.R. Bonar, J.S. Aitchison and A.J. Jacobs-Cook, to be submitted for publication in *Appl. Phys. Lett.*

- [11] A.J. McLaughlin, M.G. Jubber, J.R. Bonar, J.S. Aitchison and A.J. Jacobs-Cook, *Optoelectronic Integration and Switching*, IEE Colloquium, Glasgow, Nov. 1997.
- [12] A.J. McLaughlin, J.R. Bonar, M.G. Jubber, A.J. Jacobs-Cook and J.S. Aitchison, *Conference on Lasers and Electro-optics*, 6, OSA Technical Digest Series, 1998, 328.
- [13] A.J. McLaughlin, J.R. Bonar, M.G. Jubber, F. Camacho and J.S. Aitchison, to be presented at *CLEO/EQEC'98*, Glasgow, CWE6, 1998.
- [14] M.G. Jubber, A.J. McLaughlin, J.H. Marsh, J.S. Aitchison, P. John, C.E. Troupe and J.I.B. Wilson, *Diamond 1996*, Tours, France, Sept. 1996.
- [15] M.G. Jubber, A.J. McLaughlin, J.H. Marsh, J.S. Aitchison, P. John, C.E. Troupe and J.I.B. Wilson, *Dia. and Rel. Mats.*, 1998, 7, 1148.
- [16] M.G. Jubber, K. McIlvaney, A.J. McLaughlin, J.H. Marsh, J.S. Aitchison, C.E. Troupe, P. John, J.I.B. Wilson, to be presented at *CLEO/EQEC '98*, Glasgow, CTuL41, 1998.
- [17] J.F. Martins-Filho, A.G. Bezerra-Jr., A.S.L. Gomes, Cid. B. de Araujo, J.R. Bonar, M.V.D. Vermelho, A.J. McLaughlin, P.V.S. Marques, J.S. Aitchison, *EFNNE '96*, Aracajú, Brasil, Nov 23-30, 1996.

Appendix

I. Selected Orthogonal Tables

Run	Input Number		
	1	2	3
1	1	1	1
2	1	2	2
3	2	1	2
4	2	2	1

Orthogonal Table designated L₄2³, for 3 factors, 2 level settings and 4 runs.

Run	Input Number				
	1	2	3	4	5
1	1	1	1	1	1
2	1	2	2	2	2
3	1	3	3	3	3
4	1	4	4	4	4
5	2	1	2	3	4
6	2	2	1	4	3
7	2	3	4	1	2
8	2	4	3	2	1
9	3	1	3	4	2
10	3	2	4	3	1
11	3	3	1	2	4
12	3	4	2	1	3
13	4	1	4	2	3
14	4	2	3	1	4
15	4	3	2	4	1
16	4	4	1	3	2

Orthogonal Table designated L₁₆4⁵, for 5 factors, 4 level settings and 16 runs.

Tables taken from:

G.Z. Yin and D.W. Jillie, *Solid State Technol.*, 1987, 127.

II. Finite Element Models

Model 1

```

{mz1.pde}
{new version to calculate the optical response}
{tidied up general version which will accept input parameters more easily}
{lower thermal conductivities for the silica layers}
{Time dependent version}
{this problem represents a thin film heater on a silica waveguide}

title
  "Mach-Zehnder, 55 volts, 1.2 ms pulse 1.3 microns"

select
  deltat=1E-8    {initial time step is 1E-8 seconds}
  errlim=0.001    {PDE error must be less than 0.0001}
  displaygrid=off {suppress the screen display of re-gridding}

variables
  Temp(100)    {Variable is "Temp", expected order of magnitude =100}
  {Do NOT set this to 10!!}

initial values
  Temp = 20    {start from ambient temperature}

definitions

Cp          {Specific heat will be set to one of the following later}
CpSi = 1.636E6 {J m^-3 K^-1}
CpSiO2 = 1.657E6 {J m^-3 K^-1}
CpCr = 3.55E6   {J m^-3 K^-1}
Cpglass = 1.74E6 {J m^-3 K^-1}

K          {Thermal Conductivity will be set to one of the following later}
KSi = 149     {W/m/K}
KSiO2 = 1.318 {W/m/K}
KCr = 92.5    {W/m/K}
Kglass = 2.2  {W/m/K}

A = 0        {Source Switch, A = 1 in Heater}
Ta = 20      {Ambient Temperature}

{***** Calculate the source power density *****}

Heaterlength = 5.2E-3    {Length of strip heater in metres}
Heaterwidth = 16E-6       {Width of heater in metres}
Heaterthickness = 200E-9   {Heater thickness in metres}
HeaterResistance = 4500    {Resistance of heater in ohms}
HeaterVoltage = 55         {Voltage being applied, in volts}
HeaterVolume = Heaterlength * Heaterwidth * Heaterthickness {cubic metres}
Power = HeaterVoltage * HeaterResistance / HeaterResistance {Watts}
PowerDensity = Power / HeaterVolume {Watts per cubic metre}

{***** Calculate the pulse parameters *****}

Period = 2.4E-3        {Time between pulses in seconds}
Frequency = 1/Period     {Pulse frequency in Hz}
PulseWidth = 1.2E-3      {Pulse width in seconds}
PulseFactor = 2 * Pi * (PulseWidth / 2) * (1 / Period) {offset cos term to give pulse width}

source = PowerDensity * ustep(-cos(Frequency*2*Pi*t)-cos(PulseFactor)) {W m^-3}

{***** Calculate the time parameters *****}

Delay = 1E-8
DelayFactor = 1
InitialTime = (Period / 2) - (PulseWidth / 2) - Delay
FinalTime = (Period / 2) + (PulseWidth * DelayFactor)

{***** optical parameters *****}

LengthofGuide = 4.8e-3   {metres}
dndT = 5.00E-6           {Change of index with temperature, from Julian Jones, et al:- 5.475E-6 @ 633nm}
lambda = 1.3E-6          {metres}

```

```

MaxIntensity = 0.25      {arbitrary units}

equations
dx(K*dx(Temp)) + dy(K*dy(Temp)) + A*source = Cp*dt(Temp)

boundaries

region 1    {Defines the maximum extent of the system}
Cp = Cpglass
K = Kglass

start(-0.00025,0.0005205)
value(Temp) = 20 {assume heater not on long enough to raise temp of substrate}
line to (-0.00025,0) to (0.00025,0) to (0.00025,0.0005205)
natural(Temp) = (Ta-Temp) {convective cooling}
line to (-0.00025,0.0005205) to finish

region 2 {thin film heater}
Cp = CpCr
K = KCr {W/m/K}
A = 1 {turns source on in this region}
start(-0.000008,0.0005205)
line to (-0.000008,0.0005203) to (0.000008,0.0005203) to (0.000008,0.0005205)
to finish

region 3 {Waveguide}
Cp = Cpglass
K = Kglass {W/m/K}
start(-0.00000375,0.000510)
line to (0.00000375,0.000510) to (0.00000375,0.0005175) to (-0.00000375,0.0005175)
to finish

region 4 {Silica}
Cp = CpSiO2
K = KSiO2 {W/m/K}
start(-0.00025,0.0005)
line to (0.00025,0.0005) to (0.00025,0.00051) to (-0.00025,0.00051)
to finish

region 5 {Silicon}
Cp = CpSi
K = KSi {W/m/K}
start(-0.00025,0)
line to (0.00025,0) to (0.00025,0.0005) to (-0.00025,0.0005)
to finish

time InitialTime to FinalTime

{ **** Output Sections ****}

monitors

{ For Cycle = 5
elevation(Temp) from (0,0.000510) to (0,0.0005175)
grid(x,y) zoom(-0.00025,0.0005,0.0005,0.0005)
contour(Temp) pause
contour(Temp) zoom(-0.00005,0.0005,0.0001,0.0005) pause
contour(Temp) zoom(-0.0000125,0.0005,0.000025,0.000025) pause
}

plots
for t=1.7e-3
contour(Temp) pause
contour(Temp) zoom(-0.00005,0.0005,0.0001,0.0005) pause
contour(Temp) zoom(-0.0000125,0.0005,0.000025,0.000025) pause

histories

history(Temp) at (0.0,0.000510) (0.0,0.00051375) (0.0,0.0005175)
history(2*MaxIntensity*(1+cos(2*pi*LengthofGuide*dndT*(Temp-Ta)/lambda))) at (0.0,0.00051375)

end { **** of file ****}

```

Model 2

```

{mztv2.pde}
{new version to calculate the correct optical response}
{tidied up general version which will accept input parameters more easily}
{lower thermal conductivities for the silica layers}
{Time dependent version}
{this problem represents a thin film heater on a silica waveguide}

title
  "Mach-Zehnder, 34 volts, 1.2 ms pulse 1.3 microns"

select
  deltat=1E-8    {initial time step is 1E-8 seconds}
  errlim=0.001    {PDE error must be less than 0.0001}
  displaygrid=off {suppress the screen display of re-gridding}

variables
  Temp(100)    {Variable is "Temp", expected order of magnitude =100}
  {Do NOT set this to 10!!}
initial values
  Temp = 20     {start from ambient temperature}

definitions

Cp      {Specific heat will be set to one of the following later}
CpSi = 1.636E6 {J m^-3 K^-1}
CpSiO2 = 1.657E6 {J m^-3 K^-1}
CpCr = 3.55E6 {J m^-3 K^-1}
Cpglass = 1.74E6 {J m^-3 K^-1}
Cpdiamond = 1.81E6 {J m^-3 K^-1}
CpCu = 3.45E6 {J m^-3 K^-1}

K       {Thermal Conductivity will be set to one of the following later}
KSi = 149   {W/m/K}
KSiO2 = 1.318 {W/m/K}
KCr = 92.5  {W/m/K}
Kglass = 2.2 {W/m/K}
Kdiamond = 2000 {W/m/K}
KCu = 398   {W/m/K}

A = 0      {Source Switch, A = 1 in Heater}
Ta = 20    {Ambient Temperature}

{***** Calculate the source power density *****}

Heaterlength = 5.2E-3 {Length of strip heater in metres}
Heaterwidth = 16E-6 {Width of heater in metres}
Heaterthickness = 200E-9 {Heater thickness in metres}
HeaterResistance = 4500 {Resistance of heater in ohms}
HeaterVoltage = 34 {Voltage being applied, in volts}
HeaterVolume = Heaterlength * Heaterwidth * Heaterthickness {cubic metres}
Power = HeaterVoltage * HeaterVoltage / HeaterResistance {Watts}
PowerDensity = Power / HeaterVolume {Watts per cubic metre}

{***** Calculate the pulse parameters *****}

Period = 2.4E-3 {Time between pulses in seconds}
Frequency = 1/Period {Pulse frequency in Hz}
PulseWidth = 1.2E-3 {Pulse width in seconds}
PulseFactor = 2 * Pi * (PulseWidth / 2) * (1 / Period) {offset cos term to give pulse width}

source = PowerDensity * ustep(-cos(Frequency*2*Pi*t)-cos(PulseFactor)) {W m^-3}

{***** Calculate the time parameters *****}

Delay = 1E-8
DelayFactor = 1
InitialTime = (Period / 2) - (PulseWidth / 2) - Delay
FinalTime = (Period / 2) + (PulseWidth * DelayFactor)

{***** optical parameters *****}

LengthofGuide = 4.8e-3 {metres}
dndT = 5.00E-6 {Change of index with temperature, from Julian Jones, et al:- 5.475E-6 @ 633nm}

```

```

lambda = 1.3E-6      {metres}
MaxIntensity = 0.25  {arbitrary units}

equations
dx(K*dx(Temp)) + dy(K*dy(Temp)) + A*source = Cp*dt(Temp)

boundaries

region 1  {Defines the maximum extent of the system}
Cp = Cpglass
K = Kglass

start(-0.00025,0.0005)
value(Temp) = 20 {assume heater not on long enough to raise temp of substrate}
line to (-0.00025,0) to (0.00025,0) to (0.00025,0.0005)
natural(Temp) = (Ta-Temp) {convective cooling}
line to (0.000008,0.0005) to (0.000008,0.0005205) to (-0.000008,0.0005205)
to (-0.000008,0.0005)
to finish

region 2  {thin film heater}
Cp = CpCr
K = KCr {W/m/K}
A = 1 {turns source on in this region}
start(-0.000008,0.0005205)
line to (-0.000008,0.0005203) to (0.000008,0.0005203) to (0.000008,0.0005205)
to finish

region 3  {Waveguide}
Cp = Cpglass
K = Kglass {W/m/K}
start(-0.0000375,0.000510)
line to (0.0000375,0.000510) to (0.0000375,0.0005175) to (-0.0000375,0.0005175)
to finish

region 4  {Silica}
Cp = CpSiO2
K = KSiO2 {W/m/K}
start(-0.000007,0.0005)
line to (0.000007,0.0005) to (0.000007,0.00051) to (-0.000007,0.00051)
to finish

region 5  {Silicon}
Cp = CpSi
K = KSi {W/m/K}
start(-0.00025,0)
line to (0.00025,0) to (0.00025,0.0005) to (-0.00025,0.0005)
to finish

time InitialTime to 1.8E-3 {changed from FinalTime}

{ **** Output Sections ****}

monitors

{ For Cycle = 5
elevation(Temp) from (0,0.000510) to (0,0.0005175)
grid(x,y) zoom(-0.00025,0.0005,0.0005,0.0005)
contour(Temp) pause
contour(Temp) zoom(-0.00005,0.0005,0.0001,0.0005) pause
contour(Temp) zoom(-0.0000125,0.0005,0.000025,0.000025) pause
}

plots
for t=1.7e-3
contour(Temp) pause
contour(Temp) zoom(-0.00005,0.0005,0.0001,0.0005) pause
contour(Temp) zoom(-0.0000125,0.0005,0.000025,0.000025) pause

histories

history(Temp) at (0.0,0.000510) (0.0,0.00051375) (0.0,0.0005175)

```

```
history(2*MaxIntensity*(1+cos(2*pi*LengthofGuide*dndT*(Temp-Ta)/lambda))) at (0.0,0.00051375)
```

```
end {***** of file *****}
```

Model 3

```
{mztv7.pde}
{new version to calculate the correct optical response}
{tidied up general version which will accept input parameters more easily}
{lower thermal conductivities for the silica layers}
{Time dependent version}
{this problem represents a thin film heater on a silica waveguide}

title
"Mach-Zehnder, 27 volts, 1.2 ms pulse 1.3 microns"

select
deltat=1E-8 {initial time step is 1E-8 seconds}
errlim=0.001 {PDE error must be less than 0.0001}
displaygrid=off {suppress the screen display of re-gridding}

variables
Temp(100) {Variable is "Temp", expected order of magnitude =100}
{Do NOT set this to 10!!}
initial values
Temp = 20 {start from ambient temperature}

definitions

Cp {Specific heat will be set to one of the following later}
CpSi = 1.636E6 {J m^-3 K^-1}
CpSiO2 = 1.657E6 {J m^-3 K^-1}
CpCr = 3.55E6 {J m^-3 K^-1}
Cpglass = 1.74E6 {J m^-3 K^-1}
Cpdiamond = 1.81E6 {J m^-3 K^-1}
CpCu = 3.45E6 {J m^-3 K^-1}

K {Thermal Conductivity will be set to one of the following later}
KSi = 149 {W/m/K}
KSiO2 = 1.318 {W/m/K}
KCr = 92.5 {W/m/K}
Kglass = 2.2 {W/m/K}
Kdiamond = 2000 {W/m/K}
KCu = 398 {W/m/K}

A = 0 {Source Switch, A = 1 in Heater}
Ta = 20 {Ambient Temperature}

{***** Calculate the source power density *****}

Heaterlength = 5.2E-3 {Length of strip heater in metres}
Heaterwidth = 16E-6 {Width of heater in metres}
Heaterthickness = 200E-9 {Heater thickness in metres}
HeaterResistance = 4500 {Resistance of heater in ohms}
HeaterVoltage = 27 {Voltage being applied, in volts}
HeaterVolume = Heaterlength * Heaterwidth * Heaterthickness {cubic metres}
Power = HeaterVoltage * HeaterVoltage / HeaterResistance {Watts}
PowerDensity = Power / HeaterVolume {Watts per cubic metre}

{***** Calculate the pulse parameters *****}

Period = 2.4E-3 {Time between pulses in seconds}
Frequency = 1/Period {Pulse frequency in Hz}
PulseWidth = 1.2E-3 {Pulse width in seconds}
PulseFactor = 2 * Pi * (PulseWidth / 2) * (1 / Period) {offset cos term to give pulse width}

source = PowerDensity * ustep(-cos(Frequency*2*Pi*t)-cos(PulseFactor)) {W m^-3}

{***** Calculate the time parameters *****}

Delay = 1E-8
DelayFactor = 1
InitialTime = (Period / 2) - (PulseWidth / 2) - Delay
FinalTime = (Period / 2) + (PulseWidth * DelayFactor)
```

```

{***** optical parameters *****}

LengthofGuide = 4.8e-3      {metres}
dndT = 5.00E-6      {Change of index with temperature, from Julian Jones, et al:- 5.475E-6 @ 633nm}
lambda = 1.3E-6      {metres}
MaxIntensity = 0.25      {arbitrary units}

equations
dx(K*dx(Temp)) + dy(K*dy(Temp)) + A*source = Cp*dt(Temp)

boundaries

region 1      {Defines the maximum extent of the system}
Cp = Cpglass
K = Kglass

start(-0.00025,0.0005)
value(Temp) = 20  {assume heater not on long enough to raise temp of substrate}
line to (-0.00025,0) to (0.00025,0) to (0.00025,0.0005)
natural(Temp) = (Ta-Temp)  {convective cooling}
line to (0.00008,0.0005) to (0.00008,0.0005205) to (-0.00008,0.0005205)
to (-0.00008,0.0005)
to finish

region 2  {thin film heater}
Cp = CpCr
K = KCr  {W/m/K}
A = 1    {turns source on in this region}
start(-0.000008,0.0005205)
line to (-0.000008,0.0005203) to (0.000008,0.0005203) to (0.000008,0.0005205)
to finish

region 3  {Waveguide}
Cp = Cpglass
K = Kglass  {W/m/K}
start(-0.00000375,0.000510)
line to (0.00000375,0.000510) to (0.00000375,0.0005175) to (-0.00000375,0.0005175)
to finish

region 4  {Silica}
Cp = CpSiO2
K = KSiO2  {W/m/K}
start(-0.000007,0.0005)
line to (0.000007,0.0005) to (0.000007,0.00051) to (-0.000007,0.00051)
to finish

region 5  {Silicon}
Cp = CpSi
K = KSi  {W/m/K}
start(-0.00025,0)
line to (0.00025,0) to (0.00025,0.0005) to (-0.00025,0.0005)
to finish

region 6  {thin film heater}
Cp = CpCr
K = KCr  {W/m/K}
A = 1    {turns source on in this region}
start(-0.000008,0.000507)
line to (-0.000008,0.0005072) to (0.000008,0.0005072) to (0.000008,0.000507)
to finish

time InitialTime to 1.8E-3 {changed from FinalTime}

{***** Output Sections *****}

monitors

{ For Cycle = 5
elevation(Temp) from (0,0.000510) to (0,0.0005175)
grid(x,y) zoom(-0.00025,0.0005,0.0005,0.0005)
contour(Temp) pause
contour(Temp) zoom(-0.00005,0.0005,0.0001,0.0005) pause
contour(Temp) zoom(-0.0000125,0.0005,0.000025,0.000025) pause
}

plots

```

```
for t=1.7e-3
    contour(Temp) pause
    contour(Temp) zoom(-0.00005,0.0005,0.0001,0.0005) pause
    contour(Temp) zoom(-0.0000125,0.0005,0.000025,0.000025) pause

histories

history(Temp) at (0.0,0.000510) (0.0,0.00051375) (0.0,0.0005175)
history(2*MaxIntensity*(1+cos(2*pi*LengthofGuide*dndT*(Temp-Ta)/lambda))) at (0.0,0.00051375)

end {***** of file *****}
```

III. Data for Designing Asymmetric Mach-Zehnder Interferometers

W	r	L	ΔL_{phys}
25.00	40000.00	1999.84	0.00000
25.25	39603.94	1999.84	0.00838
25.50	39215.79	1999.84	0.01683
25.75	38835.18	1999.84	0.02538
26.00	38461.88	1999.84	0.03400
26.25	38095.71	1999.84	0.04271
26.50	37736.44	1999.84	0.05150
26.75	37383.88	1999.84	0.06038
27.00	37037.86	1999.84	0.06933
27.25	36698.19	1999.84	0.07838
27.50	36364.69	1999.84	0.08750
27.75	36037.21	1999.84	0.09671
28.00	35715.57	1999.84	0.10600
28.25	35399.63	1999.84	0.11538
28.50	35089.23	1999.84	0.12484
28.75	34784.23	1999.84	0.13438
29.00	34484.49	1999.84	0.14400
29.25	34189.88	1999.84	0.15371
29.50	33900.26	1999.84	0.16350
29.75	33615.50	1999.84	0.17338
30.00	33335.50	1999.84	0.18333
30.25	33060.12	1999.84	0.19338
30.50	32789.26	1999.84	0.20350
30.75	32522.81	1999.84	0.21371
31.00	32260.65	1999.84	0.22400
31.25	32002.75	1999.84	0.23438
31.50	31748.83	1999.84	0.24483
31.75	31498.96	1999.84	0.25538
32.00	31253.00	1999.84	0.26600
32.25	31010.85	1999.84	0.27671
32.50	30722.43	1999.84	0.28807
32.75	30537.65	1999.84	0.29837
33.00	30306.43	1999.84	0.30933
33.25	30078.69	1999.84	0.32037
33.50	29854.35	1999.84	0.33150
33.75	29633.33	1999.84	0.34271
34.00	29415.56	1999.84	0.35400
34.25	29200.97	1999.84	0.36537
34.50	28989.49	1999.84	0.37683
34.75	28781.06	1999.84	0.38837
35.00	28575.61	1999.84	0.40000
35.25	28373.07	1999.84	0.41170
35.50	28173.38	1999.84	0.42349
35.75	27976.49	1999.84	0.43537
36.00	27782.33	1999.84	0.44733
36.25	27590.86	1999.84	0.45937
36.50	27402.00	1999.84	0.47149
36.75	27215.72	1999.84	0.48370
37.00	27031.95	1999.84	0.49599
37.25	26850.65	1999.84	0.50837
37.50	26671.78	1999.84	0.52082

37.75	26495.26	1999.84	0.53336
38.00	26321.08	1999.84	0.54599
38.25	26149.17	1999.84	0.55870
38.50	25979.50	1999.84	0.57149
38.75	25812.01	1999.84	0.58436
39.00	25646.67	1999.84	0.59732
39.25	25483.44	1999.84	0.61036
39.50	25322.28	1999.84	0.62348
39.75	25163.15	1999.84	0.63669
40.00	25006.00	1999.84	0.64998

